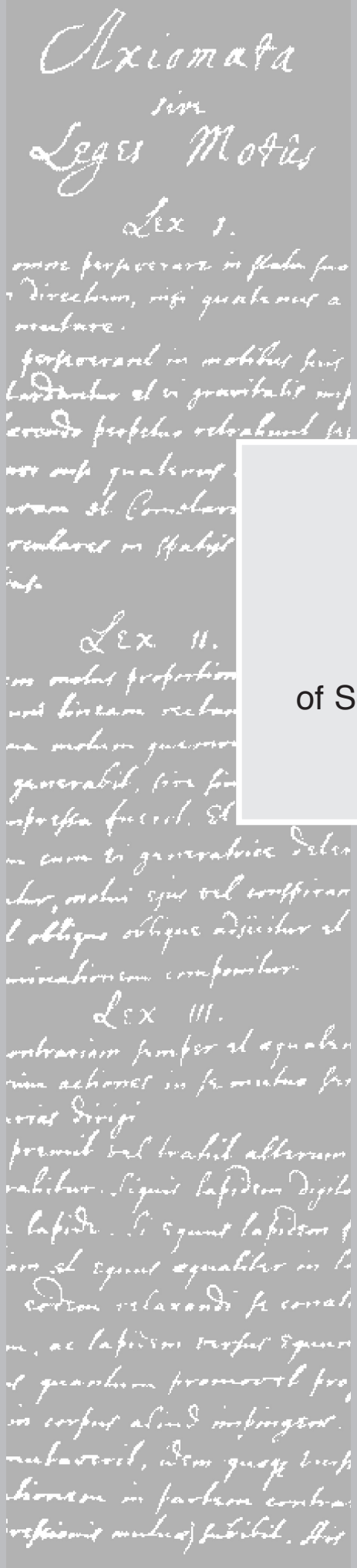

TECHNISCHE UNIVERSITÄT
KAISERSLAUTERN

Johannes Utzinger

Analysis and Computation of Solid Interfaces on the Meso Scale

UKL/LTM T 08-05 Juli 2008
Lehrstuhl für Technische Mechanik

Bibliografische Information Der Deutschen Bibliothek
Die Deutsche Bibliothek verzeichnet diese Publikation in der Deutschen Nationalbibliografie; detaillierte bibliografische Daten sind im Internet über **http://dnb.ddb.de** abrufbar.

Bibliographic information published by Die Deutsche Bibliothek
Die Deutsche Bibliothek lists this publication in the Deutsche Nationalbibliografie; detailed bibliographic data is available in the Internet at **http://dnb.ddb.de.**

Farbig erschienen auf http://kluedo.ub.uni-kl.de

Herausgeber: Fachbereich Maschinenbau und Verfahrenstechnik
Lehrstuhl für Technische Mechanik
Postfach 3049
Technische Universität Kaiserslautern
D-67653 Kaiserslautern

Verlag: Technische Universität Kaiserslautern

Druck: Technische Universität Kaiserslautern
ZBT – Abteilung Foto-Repro-Druck

D-386

Als Manuskript gedruckt. Printed in Germany.

ISSN 1610-4641
ISBN 978-3-939432-85-2

Analysis and Computation of Solid Interfaces on the Meso Scale

vom Fachbereich Maschinenbau und Verfahrenstechnik
der Technischen Universität Kaiserslautern
zur Verleihung des akademischen Grades

Doktor-Ingenieur (Dr.-Ing.)

genehmigte Dissertation
von

Dipl.-Ing. Johannes Utzinger

aus
Zweibrücken

Hauptreferent:	Prof. Dr.-Ing. P. Steinmann
Korreferenten:	Prof. Dr.-Ing. A. Menzel
	Prof. Dr.-Ing. J. Schröder
	Prof. Dr.-Ing. M. Maier
Vorsitzender:	Prof. Dr.-Ing. D. Eifler
Dekan:	Prof. Dr.-Ing. S. Ripperger

Tag der Einreichung:	28. Mai 2008
Tag der mündl. Prüfung:	18. Juli 2008

Kaiserslautern, Juli 2008
D 386

Preface

The work presented in this thesis has been carried out between October 2004 and May 2008 at the Chair of Applied Mechanics in the Department of Mechanical and Process Engineering at the University of Kaiserslautern. Located in the context of the DFG Research Unit 524 “Manufacturing, Characterisation and Simulation of Welded Lightweight Structures of Metal/Fibre-Reinforced Polymer Composites”, the related project “Modelling and Simulation of Laminar Welded Metal/Fibre-Reinforced Polymer Composites” (DFG STE 544/21) is funded by the Deutsche Forschungsgemeinschaft (DFG), which is gratefully acknowledged.

First, I would like to dedicate my gratefulness to Prof. Paul Steinmann, who provided any support as my doctoral supervisor and referee. The stimulating, special atmosphere he created at the Chair of Applied Mechanics was a fundament for the success of this work. I am especially thankful to Prof. Andreas Menzel for his willingness to be a referee for this thesis and for the time he spent with me in scientific discussion. Furthermore, I would like to express my gratitude to Prof. Jörg Schröder and to Prof. Martin Maier for their interest in my work and for acting as referees, as well as to Prof. Dietmar Eifler, representing the head of the committee.

Providing the basic network for scientific exchange, I would like to thank all my colleagues for the pleasant collaboration, especially Michael Scherer, Rouven Mohr and Stefan Uhlar. Finally, I would like to thank my family for the continuous support and encouragement.

Kaiserslautern, July 2008 Johannes Utzinger

Abstract

The present thesis is concerned with the simulation of the loading behaviour of both hybrid lightweight structures and piezoelectric mesostructures, with a special focus on solid interfaces on the meso scale. Furthermore, an analytical review on bifurcation modes of continuum-interface problems is included. The inelastic interface behaviour is characterised by elastoplastic, viscous, damaging and fatigue-motivated models. For related numerical computations, the Finite Element Method is applied. In this context, so-called interface elements play an important role. The simulation results are reflected by numerous examples which are partially correlated to experimental data.

Keywords: solid interfaces, bifurcation, ferroelectric fatigue, hybrid lightweight structures

Contents

1 Introduction

Progressive developments in technology demand materials and engineering structures with increasing application potential and complexity. In this context, solid interfaces play a decisive role (Butt et al. [30]). They inhere major influences on the physical properties of both natural and artificially manufactured materials.

An example for a modern engineering structure is given by means of hybrid joints of metals and fibre-reinforced polymers, which are investigated in the DFG Research Unit 524 “Manufacturing, Characterisation and Simulation of Welded Lightweight Structures of Metal/Fibre-Reinforced Polymer Composites”. By the combination of metals and polymers, a very large application field is developed, including the automotive and aerospace industry. Related, the incorporation of such lightweight materials contributes to both the economy and the ecology. In contrast to other joining methods, welding has advantages concerning the surface pretreatment and manufacturing time.

Materials that have one or more properties that can be significantly changed in a controlled fashion by external stimuli, such as stress, temperature, moisture, pH, electric or magnetic fields, are called “smart materials”. They constitute another field of modern engineering materials with many applications, e.g. in sensor or medical technology. One subarea of smart materials is represented by ferroelectric ceramics. Applied as sensors, actuators or storage segments, they are present in everyday life.

The simulation of such modern engineering structures is economically imperative. By the application of adequate physical models and subsequent mathematical treatment, several benefits are achieved. If a structure can successfully be simulated, the number of related experiments can be reduced and a prediction of, e.g., the mechanical behaviour becomes possible. Furthermore, related scientific fields as, for example, material science can profit from ideas and results generated in the environment of modelling and simulation.

In view of numerical simulations, solid interfaces can be related to the meso scale. In this respect, they constitute a link between some macroscopic surrounding materials, which are called the bulk materials, and some microscopic matter which is resident in the interior of the interface domain. Generally, compared to the surrounding bulk materials, solid interfaces are discontinuities with respect to their geometrical and physical properties. Concerning mechanics, jumps of stiffnesses or other model-dependent parameters have to be considered. In order to describe the failure of such discontinuities, so-called *traction-separation-laws* or *cohesive laws* can be applied, tracing back to the work of Dugdale [48] and Barenblatt [7].

Concerning Finite Element Methods (FEM), diverse possibilities to account for solid interfaces are known. A first possibility is given by an embedded discontinuity approach. There, discontinuities are inserted by means of additional degrees of freedom on the element level, see, e.g., Ortiz et al. [131], Belytschko et al. [15], Klisinski et al. [80], Lofti and Shing [96], Simo and Armero [162] and Simo et al. [163]. Though arbitrary orientation is permitted, the discontinuities are incompatible

over the element boundaries. Another method is known as the “Extended Finite Element Method” – (XFEM), introduced by Belytschko and Black [14] and Moës et al. [121]. It is based on the partition of unity concept (Melenk and Babuška [109]). Here, the approximated displacement field is enriched at the nodes by additional discontinuous functions. Therefore, discontinuities are compatible with the element boundaries, see also Sukumar et al. [172], Dolbow et al. [46] and Wells and Sluys [186]. The XFEM is applicable to any finite element type but all nodes have to be equipped with the additional degrees of freedom. Some related methods are discussed in, e.g., Hansbo and Hansbo [61, 60], Mergheim and Steinmann [115], Mergheim [113] and Mergheim et al. [114].

In view of predefined failure zones, so-called interface elements can be applied (see, e.g., Beer [13], Needleman [125], Gens et al. [58], Xu and Needleman [193], Camacho and Ortiz [31] and others). Combined with the appropriate material modelling, interface elements are systematically used for the discretisation of zones which are expected to fail. Though being very inflexible compared to the other methods, they inhere decisive advantages concerning the simplicity and the numerical handling if the failure zone is known a priori. For the example of a purely mechanical problem, the energetically conjugated quantities are then given by the interfacial traction vector as known from Cauchy’s Lemma and Theorem, and the displacement jump over the interface. In the scope of this work, solid interfaces are reviewed by means of welding zones of tensile specimens and grain boundaries of piezoelectric ceramics. For both cases, interfaces are predefined zones of failure. Consequently, in view of related numerical computations, interface elements are applied.

Goals of the Study and Modus Operandi

The goals of this study can be structured into three parts.

The first part is concerned with the modelling, the numerics and the simulation of welded lightweight structures of metal/fibre-reinforced polymer composites as investigated in the context of the DFG Research Unit 524. Based on local and integral experimental data sets, tensile tests of the related hybrid lightweight structures shall be simulated. This is achieved under quasistatic and fatigue-type loading boundary conditions on the meso scale by means of FEM. In this context, the welding zone is an a priori known zone of failure and is consequently discretised by the above mentioned interface elements, whereas the bulk material is discretised by continuum elements. Under the assumption that most of the nonlinear constitutive behaviour stems from the interface, adequate material models for both the bulk and the interface have to be developed. Related, a nonlinear finite element programme has to be applied to implement these models. As in this case, the process of interfacial delamination is of quite brittle nature, only geometrically linear formulations are accounted for. Interfacial modelling parameters are verified by data comparison of experiments and numerical simulation. Related, all experimental data is provided by partner projects connected to the DFG Research Unit 524.

The second part deals with the academic simulation of fatigued piezoelectric mesostructures. Concerning piezoelectric materials, fatigue is a very common loading type. For this reason, the prediction of the fatigue behaviour is a very important issue. Related, a granular piezoelectric mesostructure is discretised by continuum elements for the grains and by interface elements for the grain boundaries. The fatigue behaviour is completely assigned to the interfaces, while the grains are modelled by a linear ferroelectric material law. In the future, nonlinear effects as switching can be added to the grain bulk behaviour, such that the considered meso-mechanics serves as a physical sound input

for multiscale computations on the macro level. For now, it is solely focussed on the inelastic grain boundary behaviour which shall be triggered by low- and high-cycle fatigue boundary conditions. Related results have to be discussed and evaluated.

The third part concerns investigations on surface-wave type bifurcation modes in a two-dimensional non-coherent (cohesive) interface, connecting a semi-infinite three-dimensional linear bulk with a rigid substrate. This part serves as an additional activity with respect to the other goals of the study. If an infinite number of bifurcation modes occurs for a certain combination of interfacial and bulk-related material constitutions, a numerical solution of the boundary value problem would be considered to be mesh-dependent. For the uncoupled problem, a linear elastic bulk and different inelastic interfaces are considered. For the coupled problem, both the interface and the bulk are assumed to inhere linear ferroelectric behaviour.

The goals of the study are aspired by the subsequent modus operandi.

Chapter 2 begins with a recapitulation of the mechanical and electrical boundary value problem. This is followed by a reiteration of all constitutive bulk modelling aspects which are of relevance in the scope of this work. Where necessary, algorithmic aspects are discussed.

Chapter 3 deals with the constitutive modelling and algorithmic aspects of solid interfaces. This includes elastic, linear ferroelectric, plastic and Lemaitre-type-damaging behaviour as well as low- and high-cycle-fatigue-related models for both coupled and uncoupled problems. Additionally, viscoelastic and viscoplastic cohesive laws coupled to Lemaitre-type damage are discussed as a preliminary work in the context of the DFG Research Unit 524. Furthermore, mechanical and electrical interface conditions are introduced in the beginning of the chapter, thus complementing the boundary value problem as discussed in chapter 2. Finally, a penalty formalism is presented which prevents the interface from some unphysical self-penetration.

Chapter 4 is concerned with the bifurcation analysis of the uncoupled problem. First, an incremental boundary value problem (IBVP) is formulated. Thereafter, a stationary wave-type ansatz is applied to the IBVP. The results are exploited with respect to an elastic bulk and inelastic interfacial traction-separation-laws related to chapter 3. A subsequent bifurcation analysis reveals a finite number of bifurcation modes for all constitutive cases considered.

Chapter 5 deals with the bifurcation analysis for a coupled problem, whereby the strategy of chapter 4 is adopted. As a result for a linear ferroelectric bulk and interface, no surface wave-type bifurcation modes occur. However, if interfacial stiffnesses are chosen negative, a finite number of bifurcations is possible.

Chapter 6 includes the discretisation of the weak forms of the uncoupled and the coupled problem by finite elements. Furthermore, the linearisations of the discretised weak forms are briefly discussed. An outline on the issue of interface elements is included.

Chapter 7 contains the simulation of welded lightweight structures of metal/fibre-reinforced polymer composites. First, manufacturing and measuring methods as applied in the context of the DFG Research Unit 524 are introduced. This is followed by the presentation of the simulation results concerning quasistatic tensile tests. This includes the simulation of thermal impact welded as well as ultrasonic metal welded tensile specimens. For both manufacturing methods, good qualitative and quantitative agreements of experimental and numerical data has been achieved. Both local and integral data sets have been compared. Subsequently, local and integral data of preliminary tensile fatigue tests on ultrasonic metal welded specimens are compared to simulations.

Chapter 8 begins with a literature survey concerning the issues of piezoelectric fatigue, grain boundaries and piezoelectric modelling. This is followed by some remarks with respect to the interfacial modelling in the present elaboration. Subsequently, a discretisation of a rectangular PZT mesostructure which is adopted from a micrograph is presented, serving as an implementation framework for the interfacial fatigue models. Next, results are presented. Different low- and high-cycle-fatigue motivated boundary conditions are applied considering both mechanical and electrical cycling. Finally, a detailed discussion deals with the accomplished results.

Chapter 9 closes the work with conclusions and an outlook on possible future activities.

Zusammenfassung

Die progressive technologische Entwicklung benötigt Materialien und Strukturen mit geeignetem Potential und ausreichender Komplexität. In diesem Zusammenhang spielen Festkörpergrenzschichten eine entscheidende Rolle (Butt et al. [30]). Die physikalischen Eigenschaften von natürlichen und künstlich hergestellten Materialien werden von solchen Grenzschichten in hohem Maße beeinflusst.

Ein Beispiel für eine moderne Ingenieursstruktur stellen hybride Verbindungen von Metallen und faserverstärkten Kunststoffen dar. Diese werden im Rahmen der DFG-Forschergruppe 524 "Herstellung, Eigenschaftsanalyse und Simulation geschweißter Leichtbaustrukturen aus Metall/Faser-Kunststoff-Verbunden" betrachtet. Durch die Kombination von Metallen und Polymeren werden sehr breite Anwendungsfelder möglich, insbesondere in der Automobilindustrie und der Luft- und Raumfahrttechnik. Ökonomische und ökologische Aspekte spielen dabei eine maßgebende Rolle.

Ein weiteres Beispiel sind sogenannte intelligente Materialien, welche mannigfaltige Anwendungsmöglichkeiten, z.B. in der Sensor- und Medizintechnik, bieten. Eine Untergruppe der intelligenten Materialien stellen ferroelektrische Keramiken dar. Als Sensoren, Aktuatoren oder Speicherelemente haben sie in den Alltag Einzug gehalten.

Die Simulation solcher Ingenieursstrukturen ist, ökonomisch gesehen, zwingend erforderlich. Die Anwendung geeigneter physikalischer Modelle und deren mathematische Umsetzung ist in vielerlei Hinsicht von Vorteil. So können durch Simulationen Experimente reduziert werden, und Vorhersagen, z.B. bezüglich des mechanischen Verhaltens, werden möglich. Des Weiteren können verwandte wissenschaftliche Gebiete von Ideen und Resultaten profitieren, welche im Umfeld von Modellierung und Simulation generiert werden.

Bei numerischen Simulationen können Festkörpergrenzschichten auf eine Mesoskala bezogen werden. Im diesem Sinne stellen Sie ein Bindeglied zwischen makroskopischem Gesamtverhalten und dem mikroskopischen Inhalt der Grenzschicht selbst dar. Verglichen mit den umgebenden Materialien sind Festkörpergrenzschichten geometrische und physikalische Diskontinuitäten. In der Mechanik müssen deshalb Sprünge der Steifigkeiten oder anderer modellbezogener Parameter berücksichtigt werden. Um das Versagen solcher Diskontinuitäten zu beschreiben, werden sogenannte *Traktions-Separations-Gesetze* oder *kohäsive Gesetze* verwendet. Diese werden auf Dugdale [48] und Barenblatt [7] zurückgeführt.

Im Rahmen der Finiten Elemente Methode (FEM) sind verschiedene Möglichkeiten bekannt, um Festkörpergrenzschichten mesomechanisch zu berücksichtigen. Eine Möglichkeit besteht in einem eingebetteten Diskontinuitäten-Ansatz, wobei Diskontinuitäten durch zusätzliche Freiheitsgrade auf der Elementebene darstellbar sind, siehe Ortiz et al. [131], Belytschko et al. [15], Klisinski et al. [80], Lofti und Shing [96], Simo und Armero [162], und Simo et al. [163]. Beliebige Orientierungen der Diskontinuitäten sind erlaubt, jedoch sind sie inkompatibel bezüglich der Elementgrenzen. Eine weitere Methode ist als die Erweiterte Finite Elemente Methode (XFEM) bekannt, welche von Belytschko und Black [14] und Moës et al. [121] eingeführt wurde. Dabei wird das approximierte

Verschiebungsfeld an den Knoten durch zusätzliche diskontinuierliche Funktionen angereichert, sodass die Diskontinuitäten mit den Elementgrenzen kompatibel sind (Sukumar et al. [172], Dolbow et al. [46], Wells und Sluys [186]). Die XFEM ist bei beliebigen Elementtypen anwendbar, jedoch müssen alle Knoten mit Zusatzfreiheitsgraden ausgestattet sein. Damit verwandte Methoden sind z.B. in Hansbo und Hansbo [61, 60], Mergheim und Steinmann [115], Mergheim [113], und Mergheim et al. [114] zu finden.

Zur Diskretisierung vordefinierter Versagenszonen können sogenannte Grenzschichtelemente verwendet werden (Beer [13], Needleman [125], Gens et al. [58], Xu und Needleman [193], Camacho und Ortiz [31], und andere). Verglichen mit den oben erwähnten Methoden sind Grenzschichtelemente relativ unflexibel, allerdings sind sie von Vorteil hinsichtlich der einfachen numerischen Implementierung. In der vorliegenden Arbeit werden sowohl Grenzschichten geschweißter Hybridstrukturen als auch Korngrenzschichten piezoelektrischer Keramiken betrachtet. In beiden Fällen sind die Grenzschichten vordefinierte Versagenszonen. Für numerische Berechnungen werden deshalb Grenzschichtelemente verwendet.

Zielsetzung dieser Arbeit und Modus Operandi

Die Zielsetzung dieser Arbeit kann in drei Bereiche untergliedert werden.

Der erste Bereich beschäftigt sich mit der Modellierung, der Numerik und der Simulation von geschweißten Leichtbaustrukturen aus Metall/Faser-Kunststoff-Verbunden, wie sie in der DFG-Forschergruppe 524 untersucht werden. Basierend auf lokalen und integralen Datensätzen sollen Zug-Scher-Versuche bezüglich der genannten hybriden Strukturen simuliert werden. Dies wird unter quasistatischen und zyklischen Randbedingungen auf der Mesoskala mittels FEM umgesetzt. In diesem Zusammenhang ist die Schweißzone a priori als Versagenszone anzunehmen. Entsprechend wird sie mit Grenzschichtelementen diskretisiert, während die umgebenden Substrate mit Kontinuumselementen diskretisiert werden sollen. Unter der Annahme, dass nichtlineares Materialverhalten hauptsächlich von der Grenzschicht herrührt, werden geeignete Materialgesetze für die Grenzschicht und ihre Umgebung entwickelt. Diese kommen im Rahmen eines nichtlinearen FEM-Programmes zum Einsatz. Da der Delaminationsvorgang der Grenzschicht sehr spröde verläuft, werden nur geometrisch lineare Methoden verwendet. Die Modellparameter der Grenzschicht werden durch den Vergleich von Experimenten und numerischer Simulation verifiziert. Alle experimentelle Daten werden dabei von den Projektpartnern in der DFG-Forschergruppe 524 zur Verfügung gestellt.

Im zweiten Bereich soll die Ermüdung piezoelektrischer Mesostrukturen simuliert werden. Da bei piezoelektrischen Materialien zyklische Beanspruchungen häufig sind, ist die Vorhersage des Ermüdungsverhaltens von immenser Wichtigkeit. Eine durch Körner und Korngrenzen definierte piezoelektrische Struktur wird mit Kontinuumselementen für die Körner und Grenzschichtelementen für die Korngrenzen diskretisiert. Während das Ermüdungsverhalten gänzlich den Korngrenzen beigemessen wird, werden die Körner mittels eines linearen ferroelektrischen Materialgesetzes modelliert. Zukünftig sollen auch nichtlineare Effekte wie Domänenumklappprozesse berücksichtigt werden, und die hier betrachtete Mesomechanik soll als Grundlage für Multiskalenbetrachtungen herangezogen werden. Zunächst jedoch soll der Schwerpunkt auf der Simulation des Korngrenzenverhaltens liegen, wobei kleine und große Zyklenzahlen durch geeignete Modelle berücksichtigt werden. Die daraus hervorgehenden Resultate werden diskutiert und bewertet.

Der dritte Bereich betrifft Untersuchungen zu Bifurkationsmöglichkeiten vom Oberflächenwellentyp. Dabei wird eine zweidimensionale, nicht-kohärente (kohesive) Grenzschicht betrachtet, welche einen halbunendlichen dreidimensionalen linearen Festkörper mit einem starren Substrat verbindet. Dieser Bereich ist bezüglich der anderen Zielsetzungen als Zusatzaktivität einzuordnen. Falls für bestimmte Kombinationen von Festkörper- und Grenzschichtmaterialverhalten eine unendliche Anzahl solcher Bifurkationen möglich ist, wäre eine numerische Lösung des Randwertproblems netzabhängig.

Die Ziele der Arbeit werden durch den folgenden modus operandi angestrebt:

Kapitel 2 beginnt mit dem mechanischen und dem elektrischen Randwertproblem. Danach folgt eine Wiederholung von Modellierungsaspekten hinsichtlich der in dieser Arbeit relevanten, die Grenzschicht umgebenden Materialien. Wo notwendig, werden auch algorithmische Aspekte beleuchtet.

Kapitel 3 beschäftigt sich mit der konstitutiven Modellierung und den algorithmischen Aspekten von Festkörpergrenzschichten. Dabei wird elastisches, plastisches und schädigendes Verhalten vom Lemaitre-Typ betrachtet. Ermüdungsbezogene Modelle für kleine und große Zyklenzahlen werden sowohl für das nicht-gekoppelte als auch für das gekoppelte Problem vorgestellt. Des Weiteren werden viskoelastisch-schädigende und viskoplastisch-schädigende Modelle als Vorarbeit im Kontext der DFG-Forschergruppe 524 diskutiert. Zusätzlich werden mechanische und elektrische Grenzschichtbedingungen sowie ein sogenannter Penalty-Formalismus beleuchtet.

Kapitel 4 enthält die Bifurkationsanalyse für ein nicht-gekoppeltes Problem. Zunächst wird ein inkrementelles Randwertproblem formuliert, auf welches ein Ansatz für stehende Oberflächenwellen angewendet wird. Die daraus folgenden Resultate werden hinsichtlich eines linear elastischen Festkörpers und inelastischen Traktions-Separations-Gesetzen ausgewertet, die in Beziehung zu Kapitel 3 stehen. Die anschließende Bifurkationsanalyse zeigt, dass für alle eingearbeiteten konstitutiven Gesetze höchstens eine endliche Anzahl von Bifurkationsmöglichkeiten besteht.

Kapitel 5 enthält die Bifurkationsanalyse für ein gekoppeltes Problem, wobei das Vorgehen von Kapitel 4 übernommen wird. Für lineare ferroelektrische Festkörper und Grenzschichten treten keine Bifurkationsmoden auf.

Kapitel 6 betrifft die Finite-Elemente-Diskretisierung der schwachen Formen für nicht-gekoppelte und gekoppelte Probleme. Linearisierungsaspekte werden kurz diskutiert, und ein Abriss zum Thema der Grenzschichtelemente ist enthalten.

Kapitel 7 beginnt mit einer kurzen Darstellung der Herstellungs- und Messmethoden, die im Rahmen der DFG-Forschergruppe 524 angewendet werden. Anschließend werden die Simulationsergebnisse bezüglich quasistatischer Zug-Scher-Versuche an wärmeimpulsgeschweißten und ultraschallgeschweißten hybriden Proben besprochen. Eine gute qualitative und quantitative Übereinstimmung von Experimenten und Simulation konnte erreicht werden. Des Weiteren werden Datensätze von zyklischen Zug-Scher-Vorversuchen an ultraschallgeschweißten Proben mit Simulationen verglichen.

Kapitel 8 beginnt mit einer Literaturrecherche zu piezoelektrischer Ermüdung, Modellierung und Korngrenzen. Es folgen einige Anmerkungen zur Grenzschichtmodellierung, und die Diskretisierung eines rechteckigen Ausschnitts einer piezoelektrischen Mesostruktur wird vorgestellt. Die anschließend präsentierten Ergebnisse beziehen sich auf mechanische und elektrische Randbedingungen in kleinen und großen Zyklenzahlen. Die Resultate werden diskutiert und bewertet.

Kapitel 9 fasst die Arbeit zusammen, enthält Schlussfolgerungen und einen Ausblick auf mögliche zukünftige Aktivitäten.

2 Constitutive Modelling and Algorithmic Aspects of Selected Bulk Materials

In the following, some selected bulk material properties as well as related algorithmic aspects will be briefly investigated. Thus, the focus is set on materials which are important in the context of this work. All constitutive models are formulated geometrically linear, given in a standard continuum. By addressing appropriate energy contributions, the material laws are motivated and derived. Expressions for stresses and tangent moduli are obtained, and, in this regard, algorithmic methods are incorporated.

First of all, a Boundary Value Problem (BVP) is introduced, being splitted into a mechanical and an electrical BVP. Then, the material models are discussed. The starting point is the simple linear hyperelastic material modelling, adequate for many materials concerning small strains, e.g. for metals in the isotropic case. Otherwise, especially fibre-reinforced composites inhere an anisotropic material behaviour. In this regard and for small strains, transversal isotropic and orthotropic elasticity are presented. To overview the diverse field of elasticity, the textbooks of Ogden [130], Marsden and Hughes [105] and Ting [177] can be consulted. Next, small strain elastoplasticity with linear isotropic hardening is concisely described. This material model is used to describe inelastic behaviour of metals as a first approximation. Inelastic material modelling is discussed in detail in the textbooks of, e.g., Lemaitre [90], Lemaitre and Chaboche [91] as well as Simo and Hughes [164]. Finally, introducing coupled problems, linear ferroelectricity for bulk materials is described. In this context, switching effects are not addressed. In order to gain further knowledge on the issue of electrically-mechanically coupled problems, the books of Maugin [106], Eringen and Maugin [51], Ikeda [71] and Smith [165] are advocated.

2.1 Boundary Value Problem

Let $\mathcal{B} \subseteq \mathcal{R}^n$ be the configuration of a body of interest, subjected to small deformations, see Fig. 2.1 for an illustration. Then, position vectors pointing on $\mathcal{B}$ are denoted as $\boldsymbol{x} \in \mathcal{R}^n$, related displacements and the electrical potential shall be given as $\boldsymbol{u}$ and, respectively, Φ. Considering $\mathcal{B}$, inherent physical properties can be described as quasi-electrostatic and source-free, with body forces and external charges being neglected.

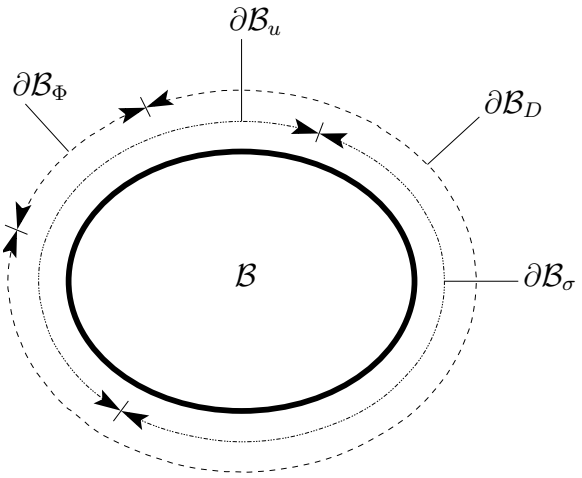

Figure 2.1: Configuration $\mathcal{B}$ and some boundary conditions

2.1.1 Mechanical Boundary Value Problem

The local format of the balance of linear momentum reads as

$$\text{div}\boldsymbol{\sigma} = \mathbf{0} \quad \text{in} \quad \mathcal{B} \tag{2.1}$$

with $\boldsymbol{\sigma}$ being the stress tensor. The boundary conditions, see also Fig. 2.1, are given as

$$\boldsymbol{u} = \boldsymbol{u}_p \quad \text{on} \quad \partial\mathcal{B}_u, \quad \boldsymbol{\tau} = \boldsymbol{\sigma} \cdot \boldsymbol{n}_\sigma = \boldsymbol{\tau}_p \quad \text{on} \quad \partial\mathcal{B}_\sigma \tag{2.2}$$

Here, $\boldsymbol{\tau}_p$ are prescribed tractions and $\boldsymbol{n}_\sigma$ is the outward normal with respect to $\partial\mathcal{B}_\sigma$. Moreover, the balance of angular momentum implies the symmetry of the stress tensor, i.e.

$$\boldsymbol{\sigma} = \boldsymbol{\sigma}^t \tag{2.3}$$

Stresses are dependent on strains $\boldsymbol{\varepsilon}$ and, optionally, other quantities, which are summarised in $[\bullet]$, being of special relevance in view of coupled problems. Consequently, until some constitutive relations are specified, stresses are given as

$$\boldsymbol{\sigma} = \boldsymbol{\sigma}(\boldsymbol{\varepsilon}, [\bullet]) \tag{2.4}$$

with the strains $\boldsymbol{\varepsilon}$ being the symmetric gradient of the displacement vector $\boldsymbol{u}$ which is the basic kinematic assumption.

$$\boldsymbol{\varepsilon} = \nabla^{sym}_{\boldsymbol{x}} \boldsymbol{u} \tag{2.5}$$

2.1.2 Electrical Boundary Value Problem

For the present configuration, mechanical and, moreover, electrical fluxes shall be considered. In this regard, a second balance law to be considered is the Gaussian law, resulting from Maxwell's equations, given as

$$\mathrm{div}\boldsymbol{D} = 0 \quad \text{in} \quad \mathcal{B} \tag{2.6}$$

wherein $\boldsymbol{D}$ is the dielectric displacement. Appropriate boundary conditions, see also Fig. 2.1, read as

$$\Phi = \Phi_p \quad \text{on} \quad \partial\mathcal{B}_\Phi, \quad \Lambda = -\boldsymbol{D}\cdot\boldsymbol{n}_D = \Lambda_p \quad \text{on} \quad \partial\mathcal{B}_D \tag{2.7}$$

with Λ_p denoting external surface charges and $\boldsymbol{n}_D$ being the outward normal with respect to $\partial\mathcal{B}_D$, compare also Kamlah [76], Schröder and Romanowski [158], Maugin [106] and Eringen and Maugin [51]. In order to close the system of equations, the dielectric displacement vector must be specified. Generally, it holds

$$\boldsymbol{D} = \boldsymbol{D}(\boldsymbol{E}, [\bullet]) \tag{2.8}$$

with $\boldsymbol{E}$ being the electric field vector. The choice of $[\bullet]$ depends on some material behaviour to be selected, especially in the case of electrical-mechanical coupling. Finally, the related kinematic assumption is expressed by

$$\boldsymbol{E} = -\nabla_{\boldsymbol{x}}\Phi \tag{2.9}$$

In the subsequent sections equations (2.4) and (2.8) will be specified, based on energetically motivated assumptions.

2.2 Linear Elasticity

In this section some linear hyperelastic material laws are presented. For this reason the associated boundary value problem is reduced to the mechanical case of equations (2.1)–(2.5). In the context of elasticity it may be noteworthy to address the difference between hypo- and hyperelasticity. For both cases stresses $\boldsymbol{\sigma}$ are solely dependent on the strains $\boldsymbol{\varepsilon}$, i.e.

$$\boldsymbol{\sigma} = \boldsymbol{\sigma}(\boldsymbol{\varepsilon}) \tag{2.10}$$

For the case of hypoelasticity, or rather Cauchy Elasticity, the relation of stress and strain rates is invertible, but no potential relation for the stresses can be specified. Consequently, Cauchy elastic materials may dissipate energy in closed strain cycles. For further details see for instance Truesdell [178] and Ogden [130]. In contrast to this, hyperelasticity – which is also called Green elasticity – inheres an invertible stress-strain rate relation, too, but additionally a potential by means of a strain energy function W is present. For such material behaviour the second law of thermodynamics results in

$$\mathcal{D} = \mathcal{D}_{loc} = \mathcal{W} - \dot{\Psi} = 0 \tag{2.11}$$

reflecting a reversible process, introducing the dissipation power $\mathcal{D}$, the stress power $\mathcal{W} = \dot{W}$ and the free energy power $\dot{\Psi}$. In this regard, it holds

$$\Psi = \Psi(\boldsymbol{\varepsilon}; [\bullet]), \quad [\bullet] = \text{const.} \tag{2.12}$$

The stress power is expressed by

$$\mathcal{W} = \boldsymbol{\sigma} : \dot{\boldsymbol{\varepsilon}} \tag{2.13}$$

The combination of equations (2.11) and (2.13) renders

$$\boldsymbol{\sigma} : \dot{\boldsymbol{\varepsilon}} - \dot{\Psi} = 0 \tag{2.14}$$

and, with equation (2.12) in mind, yields in

$$\left[\boldsymbol{\sigma} - \frac{\partial \Psi}{\partial \boldsymbol{\varepsilon}}\right] : \dot{\boldsymbol{\varepsilon}} = 0 \tag{2.15}$$

The Coleman-Noll Entropy Principle – for a detailed outline on this issue see, e.g., Coleman and Noll [41] as well as Truesdell and Noll [179] – directly implies

$$\boldsymbol{\sigma} = \frac{\partial \Psi}{\partial \boldsymbol{\varepsilon}} \tag{2.16}$$

with $\boldsymbol{\sigma}$ being symmetric as induced by the local form of balance of angular momentum. Furthermore, by

$$\dot{\boldsymbol{\sigma}} = \mathbb{C}^{el} : \dot{\boldsymbol{\varepsilon}} \tag{2.17}$$

with

$$\mathbb{C}^{el} = \frac{\partial^2 \Psi}{\partial \boldsymbol{\varepsilon} \otimes \partial \boldsymbol{\varepsilon}} = \frac{\partial \boldsymbol{\sigma}}{\partial \boldsymbol{\varepsilon}} = [\mathbb{C}^{el}]_{ijkl}\, \boldsymbol{e}_i \otimes \boldsymbol{e}_j \otimes \boldsymbol{e}_k \otimes \boldsymbol{e}_l \tag{2.18}$$

the rate relation of stresses and strains is founded on the fourth order Elastic Continuum Tangent Stiffness Tensor $\mathbb{C}^{el}$. As obvious from equations (2.5) and (2.18) $\mathbb{C}^{el}$ inheres some minor symmetries, i.e.

$$[\mathbb{C}^{el}]_{ijkl} = [\mathbb{C}^{el}]_{jikl} = [\mathbb{C}^{el}]_{jilk} \tag{2.19}$$

and, furthermore, major symmetries

$$[\mathbb{C}^{el}]_{ijkl} = [\mathbb{C}^{el}]_{klij} \tag{2.20}$$

Requesting a linear and positive definite relation of stresses and strains, the free energy is specified as

$$\Psi = \mathcal{W} = \frac{1}{2}\, \boldsymbol{\varepsilon} : \mathbb{C}^{el} : \boldsymbol{\varepsilon} \; > \; 0 \quad \forall\, \boldsymbol{\varepsilon} \neq \mathbf{0}, \quad [\mathbb{C}^{el}]_{ijkl} = \text{const.} \tag{2.21}$$

Consequently, the correlation of stresses and strains is rewritten as

$$\boldsymbol{\sigma} = \mathbb{C}^{el} : \boldsymbol{\varepsilon} \tag{2.22}$$

denoting the constitutive relation. The symmetry properties of $\mathbb{C}^{el}$ allow a reduction from 81 to 21 coefficients. This, together with the symmetries of the stress and strain tensors is exploited by applying

the so-called Voigt notation, giving a compact description of correlations. Accordingly, Voigt-notated strains $\boldsymbol{\varepsilon}^V$ and stresses $\boldsymbol{\sigma}^V$ are related by

$$\boldsymbol{\sigma}^V = \boldsymbol{C}^{el} \cdot \boldsymbol{\varepsilon}^V \tag{2.23}$$

with $\boldsymbol{C}^{el} = C^{el}_{ij}\, \boldsymbol{e}_i \otimes \boldsymbol{e}_j$ being the Voigt-notated Elastic Continuum Tangent Stiffness Tensor. Thereby, the sequence of indices corresponding to the Voigt notation shall be exemplified by

$$\underbrace{\begin{bmatrix} \sigma_{11} \\ \sigma_{22} \\ \sigma_{33} \\ \sigma_{12} \\ \sigma_{23} \\ \sigma_{13} \end{bmatrix}}_{\sigma^V_i} = \underbrace{\begin{bmatrix} [\mathbb{C}^{el}]_{1111} & [\mathbb{C}^{el}]_{1122} & [\mathbb{C}^{el}]_{1133} & [\mathbb{C}^{el}]_{1112} & [\mathbb{C}^{el}]_{1123} & [\mathbb{C}^{el}]_{1113} \\ [\mathbb{C}^{el}]_{2211} & [\mathbb{C}^{el}]_{2222} & [\mathbb{C}^{el}]_{2233} & [\mathbb{C}^{el}]_{2212} & [\mathbb{C}^{el}]_{2223} & [\mathbb{C}^{el}]_{2213} \\ [\mathbb{C}^{el}]_{3311} & [\mathbb{C}^{el}]_{3322} & [\mathbb{C}^{el}]_{3333} & [\mathbb{C}^{el}]_{3312} & [\mathbb{C}^{el}]_{3323} & [\mathbb{C}^{el}]_{3313} \\ [\mathbb{C}^{el}]_{1211} & [\mathbb{C}^{el}]_{1222} & [\mathbb{C}^{el}]_{1233} & [\mathbb{C}^{el}]_{1212} & [\mathbb{C}^{el}]_{1223} & [\mathbb{C}^{el}]_{1213} \\ [\mathbb{C}^{el}]_{2311} & [\mathbb{C}^{el}]_{2322} & [\mathbb{C}^{el}]_{2333} & [\mathbb{C}^{el}]_{2312} & [\mathbb{C}^{el}]_{2323} & [\mathbb{C}^{el}]_{2313} \\ [\mathbb{C}^{el}]_{1311} & [\mathbb{C}^{el}]_{1322} & [\mathbb{C}^{el}]_{1233} & [\mathbb{C}^{el}]_{1312} & [\mathbb{C}^{el}]_{1323} & [\mathbb{C}^{el}]_{1313} \end{bmatrix}}_{C^{el}_{ij}} \cdot \underbrace{\begin{bmatrix} \varepsilon_{11} \\ \varepsilon_{22} \\ \varepsilon_{33} \\ 2\varepsilon_{12} \\ 2\varepsilon_{23} \\ 2\varepsilon_{13} \end{bmatrix}}_{\varepsilon^V_j} \tag{2.24}$$

as found in, e.g., Mehlhorn [107], Simo and Hughes [164] and Haupt [64]. Other sequences are described in, for instance, the books of Voigt [184] and Spencer [166, 167]. Please note that for linear elasticity, due to given $\mathbb{C}^{el} = \text{const.}$, no further algorithmic procedures are necessary.

2.2.1 Isotropic Linear Elasticity

If, in addition to the demands of equation (2.21), directional independence for material properties is assumed, isotropy is at hand. This is the case for the elastic regime of, e.g., steel. Therefore, the free energy is given as

$$\Psi = \Psi(\boldsymbol{\varepsilon}) = \Psi(i_\varepsilon) \tag{2.25}$$

depending solely on the strains. This correlation is refined by introducing an irreducible set of invariants

$$i_\varepsilon = \{I_1, I_2, I_3\} = \{I^*_1, I^*_2, I^*_3\} = \{\varepsilon_1, \varepsilon_2, \varepsilon_3\} \quad \text{with} \quad I_m = \boldsymbol{\varepsilon}^m : \boldsymbol{I} \tag{2.26}$$

For $m = 1, 2, 3$, the so-called basic invariants are given by I_m, the so-called principal invariants are denoted as I^*_m, while ε_m are the eigenvalues of $\boldsymbol{\varepsilon}$. Straightforwardly, stresses can be computed as

$$\boldsymbol{\sigma} = \frac{\partial \Psi}{\partial \boldsymbol{\varepsilon}} = \frac{\partial \Psi}{\partial I_1}\boldsymbol{I} + 2\,\frac{\partial \Psi}{\partial I_2}\boldsymbol{\varepsilon} + 3\,\frac{\partial \Psi}{\partial I_3}\boldsymbol{\varepsilon}^2 = \Phi_1\,\boldsymbol{I} + \Phi_2\,\boldsymbol{\varepsilon} + \Phi_3\,\boldsymbol{\varepsilon}^2 \tag{2.27}$$

For the sake of linearity, with λ and μ being material parameters –the so-called Lamé-parameters– it shall be

$$\Phi_1 = \lambda\, I_1, \quad \Phi_2 = 2\mu, \quad \Phi_3 = 0 \tag{2.28}$$

and consequently, the stresses are given as

$$\boldsymbol{\sigma} = \lambda \boldsymbol{I}\,[\boldsymbol{\varepsilon} : \boldsymbol{I}] + 2\mu\,\boldsymbol{\varepsilon} \tag{2.29}$$

and the constant Elastic Continuum Tangent Stiffness Tensor for the isotropic case reads as

$$\mathbb{C}^{iso} = \frac{\partial \boldsymbol{\sigma}}{\partial \boldsymbol{\varepsilon}} = \lambda \, \boldsymbol{I} \otimes \boldsymbol{I} + 2\mu \, \mathbb{I}^{sym} \tag{2.30}$$

Concerning the Voigt notation, this is reflected by

$$C_{ij}^{iso} = \begin{bmatrix} 2\mu+\lambda & \lambda & \lambda & 0 & 0 & 0 \\ \lambda & 2\mu+\lambda & \lambda & 0 & 0 & 0 \\ \lambda & \lambda & 2\mu+\lambda & 0 & 0 & 0 \\ 0 & 0 & 0 & \mu & 0 & 0 \\ 0 & 0 & 0 & 0 & \mu & 0 \\ 0 & 0 & 0 & 0 & 0 & \mu \end{bmatrix} \tag{2.31}$$

2.2.2 Transversely Isotropic Linear Elasticity

Now, transversely isotropic material properties are highlighted. For this class of materials a direction of anisotropy, denoted by $\boldsymbol{m}_0$, $\|\boldsymbol{m}_0\| = 1$, and the structure tensor $\boldsymbol{M}_0 = \boldsymbol{m}_0 \otimes \boldsymbol{m}_0$ are introduced. A material example for this is found in the elastic regime of a fibre-reinforced composite where all fibres are aligned in one direction. The free energy allows a reduced representation of 5 invariants and reads as

$$\Psi = \Psi(\boldsymbol{\varepsilon}; \boldsymbol{m}_0) = \Psi(i_\varepsilon, i_{\varepsilon M_0}) = \Psi(I_1, I_2, I_3, I_4, I_5) \tag{2.32}$$

with

$$i_{\varepsilon M_0} = \{I_4, I_5\} = \{\boldsymbol{\varepsilon} : \boldsymbol{M}_0, \boldsymbol{\varepsilon}^2 : \boldsymbol{M}_0\} \tag{2.33}$$

Again, stresses are computed by differentiating the free energy with respect to basic invariants, yielding

$$\begin{aligned} \boldsymbol{\sigma} &= \frac{\partial \Psi}{\partial \boldsymbol{\varepsilon}} \\ &= \frac{\partial \Psi}{\partial I_1} \boldsymbol{I} + 2 \frac{\partial \Psi}{\partial I_2} \boldsymbol{\varepsilon} + 3 \frac{\partial \Psi}{\partial I_3} \boldsymbol{\varepsilon}^2 + \frac{\partial \Psi}{\partial I_4} \boldsymbol{M}_0 + \frac{\partial \Psi}{\partial I_5} 2 \, [\boldsymbol{\varepsilon} \cdot \boldsymbol{M}_0]^{sym} \\ &= \Phi_1 \boldsymbol{I} + \Phi_2 \boldsymbol{\varepsilon} + \Phi_3 \boldsymbol{\varepsilon}^2 + \Phi_4 \boldsymbol{M}_0 + \Phi_5 \, 2 \, [\boldsymbol{\varepsilon} \cdot \boldsymbol{M}_0]^{sym} \end{aligned} \tag{2.34}$$

Due to the assumption of linearity and the symmetry of the Elastic Continuum Tangent Stiffness Tensor, an adequate invariant formulation of the free energy is determined. Accordingly, for $i = 1, ..., 5$, Φ_i takes the format

$$\Phi_1 = \lambda \, I_1 + \alpha \, I_4, \quad \Phi_2 = 2\mu_\perp, \quad \Phi_3 = 0, \quad \Phi_4 = \alpha \, I_1 + \beta \, I_4, \quad \Phi_5 = 2[\mu_\parallel - \mu_\perp] \tag{2.35}$$

at which $\lambda, \mu_\perp, \mu_\parallel, \alpha$ and β denote adequate material constants, leading towards

$$\boldsymbol{\sigma} = [\lambda \, \boldsymbol{\varepsilon} : \boldsymbol{I} + \alpha \, \boldsymbol{\varepsilon} : \boldsymbol{M}_0] \boldsymbol{I} + 2\mu_\perp \, \boldsymbol{\varepsilon} + [\alpha \, \boldsymbol{\varepsilon} : \boldsymbol{I} + \beta \, \boldsymbol{\varepsilon} : \boldsymbol{M}_0] \boldsymbol{M}_0 + 2[\mu_\parallel - \mu_\perp] \, [\boldsymbol{\varepsilon} \cdot \boldsymbol{M}_0 + \boldsymbol{M}_0 \cdot \boldsymbol{\varepsilon}] \tag{2.36}$$

The constant Elastic Continuum Tangent Stiffness Tensor for the transversal isotropic case is then given as

$$\mathbb{C}^{tra} = \frac{\partial \boldsymbol{\sigma}}{\partial \boldsymbol{\varepsilon}} = \lambda\, \boldsymbol{I} \otimes \boldsymbol{I} + \alpha\, [\boldsymbol{I} \otimes \boldsymbol{M}_0 + \boldsymbol{M}_0 \otimes \boldsymbol{I}] + \beta \boldsymbol{M}_0 \otimes \boldsymbol{M}_0 + 2\mu_\perp\, \mathbb{I}^{sym} + 2[\mu_\parallel - \mu_\perp]\, \mathbb{M}_0 \quad (2.37)$$

A coefficient-explicit representation describes

$$\mathbb{M}_0 = \frac{1}{2}\, [\delta_{ik} M_{(0)jl} + \delta_{il} M_{(0)jk} + \delta_{jl} M_{(0)ik} + \delta_{jk} M_{(0)il}]\, \boldsymbol{e}_i \otimes \boldsymbol{e}_j \otimes \boldsymbol{e}_k \otimes \boldsymbol{e}_l \quad (2.38)$$

If the direction of anisotropy is identified as $\boldsymbol{m}_0 = \boldsymbol{e}_3$, the Voigt-notated equivalent to equation (2.37) is consequently found as

$$C_{ij}^{tra} = \begin{bmatrix} \lambda + 2\mu_\perp & \lambda & \lambda + \alpha & 0 & 0 & 0 \\ \lambda & \lambda + 2\mu_\perp & \lambda + \alpha & 0 & 0 & 0 \\ \lambda + \alpha & \lambda + \alpha & \lambda + 2\alpha + \beta - 2\mu_\perp + 4\mu_\parallel & 0 & 0 & 0 \\ 0 & 0 & 0 & \mu_\perp & 0 & 0 \\ 0 & 0 & 0 & 0 & \mu_\parallel & 0 \\ 0 & 0 & 0 & 0 & 0 & \mu_\parallel \end{bmatrix} \quad (2.39)$$

2.2.3 Orthotropic Linear Elasticity

Finally, let $\boldsymbol{m}_1, \|\boldsymbol{m}_1\| = 1$ and $\boldsymbol{m}_2, \|\boldsymbol{m}_2\| = 1$ be two orthogonal directions of anisotropy, with structure tensors $\boldsymbol{M}_1 = \boldsymbol{m}_1 \otimes \boldsymbol{m}_1$ and $\boldsymbol{M}_2 = \boldsymbol{m}_2 \otimes \boldsymbol{m}_2$. This orthotropic model is exemplary for many fibre-reinforced composites, e.g. for a carbon fibre – polyamide canvas. In this case the free energy can be represented by a reduced number of 7 invariants, reading as

$$\Psi = \Psi(\boldsymbol{\varepsilon}; \boldsymbol{m}_1, \boldsymbol{m}_2) = \Psi(i_\varepsilon, i_{\varepsilon M_1}, i_{\varepsilon M_2}) = \Psi(I_1, I_2, I_3, I_4, I_5, I_6, I_7) \quad (2.40)$$

with

$$i_{\varepsilon M_1} = \{I_4, I_5\} = \{\boldsymbol{\varepsilon} : \boldsymbol{M}_1, \boldsymbol{\varepsilon}^2 : \boldsymbol{M}_1\}, \quad i_{\varepsilon M_2} = \{I_6, I_7\} = \{\boldsymbol{\varepsilon} : \boldsymbol{M}_2, \boldsymbol{\varepsilon}^2 : \boldsymbol{M}_2\} \quad (2.41)$$

By differentiating the free energy with respect to basic invariants, stresses are computed as

$$\begin{aligned} \boldsymbol{\sigma} &= \frac{\partial \Psi}{\partial \boldsymbol{\varepsilon}} \\ &= \frac{\partial \Psi}{\partial I_1}\, \boldsymbol{I} + 2\, \frac{\partial \Psi}{\partial I_2}\, \boldsymbol{\varepsilon} + 3\, \frac{\partial \Psi}{\partial I_3}\, \boldsymbol{\varepsilon}^2 \\ &+ \frac{\partial \Psi}{\partial I_4}\, \boldsymbol{M}_1 + \frac{\partial \Psi}{\partial I_5}\, 2\, [\boldsymbol{\varepsilon} \cdot \boldsymbol{M}_1]^{sym} + \frac{\partial \Psi}{\partial I_6}\, \boldsymbol{M}_2 + \frac{\partial \Psi}{\partial I_7}\, 2\, [\boldsymbol{\varepsilon} \cdot \boldsymbol{M}_2]^{sym} \\ &= \Phi_1\, \boldsymbol{I} + \Phi_2\, \boldsymbol{\varepsilon} + \Phi_3\, \boldsymbol{\varepsilon}^2 + \Phi_4\, \boldsymbol{M}_1 + \Phi_5\, 2\, [\boldsymbol{\varepsilon} \cdot \boldsymbol{M}_1]^{sym} + \Phi_6\, \boldsymbol{M}_2 + \Phi_7\, 2\, [\boldsymbol{\varepsilon} \cdot \boldsymbol{M}_2]^{sym} \end{aligned} \quad (2.42)$$

Following from the assumption of linearity and the symmetry of the Elastic Continuum Tangent Stiffness Tensor, an appropriate free energy function determines Φ_i as

$$\Phi_1 = \lambda\, I_1 \,+\, \alpha_1\, I_4, + \alpha_2\, I_6, \quad \Phi_2 = 2\mu, \quad \Phi_3 = 0, \quad \Phi_4 = \alpha_1\, I_1 \,+\, \beta_1\, I_4 \,+\, \beta_3\, I_6,$$

$$\Phi_5 = 2\mu_1, \quad \Phi_6 = \alpha_2\, I_1 \,+\, \beta_3 I_4 \,+\, \beta_2 I_6, \quad \Phi_7 = 2\mu_2 \tag{2.43}$$

with $\lambda, \mu, \alpha_1, \alpha_2, \mu_1, \mu_2, \beta_1, \beta_2$ and β_3 being appropriate material parameters. With this in hand the stress tensor is rewritten as

$$\begin{aligned} \boldsymbol{\sigma} \;&=\; [\lambda\, \boldsymbol{\varepsilon} : \boldsymbol{I} + \alpha_1\, \boldsymbol{\varepsilon} : \boldsymbol{M}_1 + \alpha_2\, \boldsymbol{\varepsilon} : \boldsymbol{M}_2]\, \boldsymbol{I} \;+\; 2\mu\, \boldsymbol{\varepsilon} \\ &+\; [\alpha_1\, \boldsymbol{\varepsilon} : \boldsymbol{I} + \beta_1\, \boldsymbol{\varepsilon} : \boldsymbol{M}_1 + \beta_3\, \boldsymbol{\varepsilon} : \boldsymbol{M}_2]\, \boldsymbol{M}_1 \;+\; 2\mu_1\, [\boldsymbol{\varepsilon} \cdot \boldsymbol{M}_1 + \boldsymbol{M}_1 \cdot \boldsymbol{\varepsilon}] \\ &+\; [\alpha_2\, \boldsymbol{\varepsilon} : \boldsymbol{I} + \beta_3\, \boldsymbol{\varepsilon} : \boldsymbol{M}_1 + \beta_2\, \boldsymbol{\varepsilon} : \boldsymbol{M}_2]\, \boldsymbol{M}_2 \;+\; 2\mu_2\, [\boldsymbol{\varepsilon} \cdot \boldsymbol{M}_2 + \boldsymbol{M}_2 \cdot \boldsymbol{\varepsilon}] \end{aligned} \tag{2.44}$$

Here, the constant Elastic Continuum Tangent Stiffness Tensor reads as

$$\begin{aligned} \mathbb{C}^{ort} \;=\; \frac{\partial \boldsymbol{\sigma}}{\partial \boldsymbol{\varepsilon}} \;&=\; \lambda\, \boldsymbol{I} \otimes \boldsymbol{I} \;+\; \alpha_1\, \boldsymbol{I} \otimes \boldsymbol{M}_1 \;+\; \alpha_2\, \boldsymbol{I} \otimes \boldsymbol{M}_2 \;+\; 2\mu\, \mathbb{I}^{sym} \\ &+\; \alpha_1\, \boldsymbol{M}_1 \otimes \boldsymbol{I} \;+\; \beta_1\, \boldsymbol{M}_1 \otimes \boldsymbol{M}_1 \;+\; \beta_3\, \boldsymbol{M}_1 \otimes \boldsymbol{M}_2 \;+\; 2\mu_1\, \mathbb{M}_1 \\ &+\; \alpha_2\, \boldsymbol{M}_2 \otimes \boldsymbol{I} \;+\; \beta_3\, \boldsymbol{M}_2 \otimes \boldsymbol{M}_1 \;+\; \beta_2\, \boldsymbol{M}_2 \otimes \boldsymbol{M}_2 \;+\; 2\mu_2\, \mathbb{M}_2 \end{aligned} \tag{2.45}$$

A coefficient-explicit representation describes

$$\mathbb{M}_1 = \frac{1}{2}\, [\delta_{ik} M_{(1)jl} + \delta_{il} M_{(1)jk} + \delta_{jl} M_{(1)ik} + \delta_{jk} M_{(1)il}]\, \boldsymbol{e}_i \otimes \boldsymbol{e}_j \otimes \boldsymbol{e}_k \otimes \boldsymbol{e}_l \tag{2.46}$$

$$\mathbb{M}_2 = \frac{1}{2}\, [\delta_{ik} M_{(2)jl} + \delta_{il} M_{(2)jk} + \delta_{jl} M_{(2)ik} + \delta_{jk} M_{(2)il}]\, \boldsymbol{e}_i \otimes \boldsymbol{e}_j \otimes \boldsymbol{e}_k \otimes \boldsymbol{e}_l \tag{2.47}$$

Additionally, for $\boldsymbol{m}_1 = \boldsymbol{e}_1$ and $\boldsymbol{m}_2 = \boldsymbol{e}_2$ denoting the directions of anisotropy, the Elastic Continuum Tangent Stiffness Tensor in the Voigt notation is represented by

$$C_{ij}^{ort} = \begin{bmatrix} \lambda{+}2\alpha_1{+}\beta_1{+}2\mu{+}4\mu_1 & \lambda{+}\alpha_1{+}\alpha_2{+}\beta_3 & \lambda{+}\alpha_1 & 0 & 0 & 0 \\ \lambda{+}\alpha_1{+}\alpha_2{+}\beta_3 & \lambda{+}2\alpha_2{+}\beta_2{+}2\mu{+}4\mu_2 & \lambda{+}\alpha_2 & 0 & 0 & 0 \\ \lambda{+}\alpha_1 & \lambda{+}\alpha_2 & \lambda{+}2\mu & 0 & 0 & 0 \\ 0 & 0 & 0 & [\mu{+}\mu_1{+}\mu_2] & 0 & 0 \\ 0 & 0 & 0 & 0 & [\mu{+}\mu_2] & 0 \\ 0 & 0 & 0 & 0 & 0 & [\mu{+}\mu_1] \end{bmatrix} \tag{2.48}$$

2.3 Elastoplasticity with Linear Isotropic Hardening

Now, an elastoplastic material law with isotropic hardening will be presented. In this context an uncoupled problem is at hand and the boundary value problem described in section 2.1 is again reduced to equations (2.1)–(2.5), describing the pure mechanical case.

2.3.1 Constitutive Modelling

A kinematic assumption is introduced as

$$\boldsymbol{\varepsilon} = \boldsymbol{\varepsilon}^e + \boldsymbol{\varepsilon}^p \tag{2.49}$$

splitting the strains into an elastic part $\boldsymbol{\varepsilon}^e$ and a plastic part $\boldsymbol{\varepsilon}^p$. Stresses are given as

$$\boldsymbol{\sigma} = \boldsymbol{\sigma}(\boldsymbol{\varepsilon}^e, \alpha^p) \tag{2.50}$$

being dependent on the elastic strains and a plastic parameter α^p, accounting for irreversible plastic effects. Based on the free energy, the second law of thermodynamics also reflects the so-called principle of positive dissipation, reading as

$$\mathcal{D} = \mathcal{D}_{loc} = \mathcal{W} - \dot{\Psi} \geq 0 \tag{2.51}$$

with

$$\Psi = \Psi(\boldsymbol{\varepsilon}^e, \alpha^p) \tag{2.52}$$

and the stress power being given in equation (2.13). The combination of equations (2.49), (2.51), and (2.52) renders

$$\left[\boldsymbol{\sigma} - \frac{\partial \Psi}{\partial \boldsymbol{\varepsilon}^e}\right] : \dot{\boldsymbol{\varepsilon}}^e + \boldsymbol{\sigma} : \dot{\boldsymbol{\varepsilon}}^p - \frac{\partial \Psi}{\partial \alpha^p}\,\dot{\alpha}^p \geq 0 \tag{2.53}$$

The Coleman-Noll entropy principle, also known as the standard argument of rational thermodynamics, implies

$$\boldsymbol{\sigma} = \frac{\partial \Psi}{\partial \boldsymbol{\varepsilon}^e} \tag{2.54}$$

Next, by defining

$$R = -\frac{\partial \Psi}{\partial \alpha^p} \tag{2.55}$$

as the so-called internal stress, or, respectively, the hardening stress, a reduced dissipation inequality turns out to be

$$\mathcal{D}_{red} = \boldsymbol{\sigma} : \dot{\boldsymbol{\varepsilon}}^p + R\,\dot{\alpha}^p = \mathcal{S} \circ \dot{\mathcal{F}} \geq 0 \tag{2.56}$$

introducing the thermodynamic force $\mathcal{S} = \{\boldsymbol{\sigma}, R\}$ and the thermodynamic flux $\dot{\mathcal{F}} = \{\dot{\varepsilon}^p, \dot{\alpha}^p\}$. Up to now, this does not contain any statement concerning the constitutive relations – in this regard, an evolution equation is needed. In order to give consideration to the separation of an elastic and a plastic range, which is present for loads above the yielding point, a yield function is proposed as

$$\Phi^p = \Phi^p(\mathcal{S}) \leq 0 \tag{2.57}$$

The yield function is supposed to be negative in the elastic range and is zero if plasticity evolves. Let $\mathcal{E}$ be a closure of the elastic range, defined as

$$\mathcal{E} := \{\mathcal{S} \mid \Phi^p(\mathcal{S}) \leq 0\} \tag{2.58}$$

The crucial assumption to be incorporated is the well-known postulate of maximum dissipation, see, e.g., Hill [65] and Lubliner [98], given as

$$\mathcal{D}_{red}(\mathcal{S}) \geq \mathcal{D}_{red}(\mathcal{S}^*) \; \forall \; \mathcal{S}^* \; \in \; \mathcal{E} \tag{2.59}$$

and constituting a constraint maximisation problem, see Simo and Hughes [164]. Therewith, the so-called associative evolution equations or flow rules

$$\dot{\boldsymbol{\varepsilon}}^p \;\; = \;\; \dot{\gamma} \, \frac{\partial \Phi^p(\mathcal{S})}{\partial \boldsymbol{\sigma}} \tag{2.60}$$

$$\dot{\alpha}^p \;\; = \;\; \dot{\gamma} \, \frac{\partial \Phi^p(\mathcal{S})}{\partial R} \tag{2.61}$$

are derived, together with some loading- and unloading conditions which are also called Kuhn-Tucker optimality conditions, reading as

$$\dot{\gamma} \geq 0, \quad \Phi^p(\mathcal{S}) \leq 0, \quad \dot{\gamma} \, \Phi^p(\mathcal{S}) = 0 \tag{2.62}$$

In equation (2.62), $\dot{\gamma}$ denotes a Lagrange multiplier. Moreover, related to the postulate of maximum dissipation, the closure of the elastic range $\mathcal{E}$ gets convex. Please note that the principle of maximum dissipation does not include the principle of positive dissipation, which has to be checked separately. In the case of maximum dissipation the so-called plastic potential is identified with the yield function $\Phi^p(\mathcal{S})$. If this associative case is not indicated, some non-associative evolution equations or flow rules

$$\dot{\boldsymbol{\varepsilon}}^p \;\; = \;\; \dot{\gamma} \, \frac{\partial \Phi^{p,\star}(\mathcal{S})}{\partial \boldsymbol{\sigma}} \tag{2.63}$$

$$\dot{\alpha}^p \;\; = \;\; \dot{\gamma} \, \frac{\partial \Phi^{p,\star}(\mathcal{S})}{\partial R} \tag{2.64}$$

may decide the constitutive behaviour, where $\Phi^{p,\star}(\mathcal{S})$ denotes the plastic potential with $\Phi^{p,\star}(\mathcal{S}) \neq \Phi^p(\mathcal{S})$.

The rate relation concerning stresses is expressed by

$$\dot{\boldsymbol{\sigma}} = \frac{\partial^2 \Psi}{\partial \boldsymbol{\varepsilon}^e \otimes \partial \boldsymbol{\varepsilon}^e} : \dot{\boldsymbol{\varepsilon}}^e + \frac{\partial^2 \Psi}{\partial \boldsymbol{\varepsilon}^e \, \partial \alpha^p} \, \dot{\alpha}^p \tag{2.65}$$

Otherwise, the rate relation for the hardening stress yields in

$$\dot{R} = -\frac{\partial^2 \Psi}{\partial \alpha^p \, \partial \boldsymbol{\varepsilon}^e} : \dot{\boldsymbol{\varepsilon}}^e - \frac{\partial^2 \Psi}{\partial \alpha^p \, \partial \alpha^p} \, \dot{\alpha}^p \tag{2.66}$$

Now, a further constitutive assumption is declared by an additive split of the free energy function.

$$\Psi(\boldsymbol{\varepsilon}^e, \alpha^p) = \Psi^{el}(\boldsymbol{\varepsilon}^e) + \Psi^{ep}(\alpha^p) = \Psi^{el}(i_\varepsilon) + \Psi^{ep}(\alpha^p) \tag{2.67}$$

For an isotropic linear behaviour in the elastic range, this results straightforwardly in

$$\dot{\boldsymbol{\sigma}} = \mathbb{C}^{iso} : \dot{\boldsymbol{\varepsilon}}^e, \quad \mathbb{C}^{iso} = \frac{\partial^2 \Psi}{\partial \boldsymbol{\varepsilon}^e \otimes \partial \boldsymbol{\varepsilon}^e} \tag{2.68}$$

and, concerning the rate of the hardening stress, it is found

$$\dot{R} = -H^p \, \dot{\alpha^p}, \quad H^p = \frac{\partial^2 \Psi}{\partial \alpha^p \, \partial \alpha^p} \tag{2.69}$$

with H^p denoting the hardening modulus. Demanding linear relations, a quadratic format of the free energy is introduced by

$$\Psi(\boldsymbol{\varepsilon}^e, \alpha^p) = \frac{1}{2} \, \boldsymbol{\varepsilon}^e : \mathbb{C}^{iso} : \boldsymbol{\varepsilon}^e + \frac{1}{2} \, H^p \, [\alpha^p]^2 \tag{2.70}$$

rendering

$$\boldsymbol{\sigma} = \mathbb{C}^{iso} : \boldsymbol{\varepsilon}^e, \quad R = -H^p \, \alpha^p \tag{2.71}$$

Moreover, the so-called Prandtl-Reuss tensor $\mathbb{C}^{ep}$ pulls together the stresses and overall strains, i.e.

$$\dot{\boldsymbol{\sigma}} = \mathbb{C}^{ep} : \dot{\boldsymbol{\varepsilon}}, \quad \mathbb{C}^{ep} = \mathbb{C}^{iso} - \aleph^{-1} \left[\mathbb{C}^{iso} : \frac{\partial \Phi^p}{\partial \boldsymbol{\sigma}} \right] \otimes \left[\frac{\partial \Phi^p}{\partial \boldsymbol{\sigma}} : \mathbb{C}^{iso} \right] \tag{2.72}$$

with

$$\aleph = \frac{\partial \Phi^p}{\partial \boldsymbol{\sigma}} : \mathbb{C}^{iso} : \frac{\partial \Phi^p}{\partial \boldsymbol{\sigma}} + H^p \left[\frac{\partial \Phi^p}{\partial R} \right]^2 \tag{2.73}$$

The Prandtl-Reuss tensor $\mathbb{C}^{ep}$ is in general non-symmetric. Only for associative evolution equations it inheres minor and major symmetries, see equations (2.19) and (2.20).

A further constitutive assumption comprises plastic incompressibility. That means, only the deviatoric part of the stress tensor initiates plastic behaviour. This is reflected by the von Mises yield function

$$\Phi^p(\mathcal{S}) = \varphi(\boldsymbol{\sigma}) - [Y_0 - R], \quad \varphi(\boldsymbol{\sigma}) = \sqrt{3/2} \| \, \boldsymbol{\sigma}^{dev} \| \tag{2.74}$$

being motivated by a one dimensional tension setting, introducing the initial yield stress Y_0. In view of the evolution equations, equation (2.74-1) multiplied by $\sqrt{2/3}$ yields in

$$\dot{\boldsymbol{\varepsilon}^p} = \dot{\gamma} \, \boldsymbol{N}, \quad \boldsymbol{N} = \frac{\boldsymbol{\sigma}^{dev}}{\| \boldsymbol{\sigma}^{dev} \|} \quad \Rightarrow \quad \boldsymbol{\varepsilon}^p = [\boldsymbol{\varepsilon}^p]^{dev} \tag{2.75}$$

$$\dot{\alpha}^p = \dot{\gamma} \sqrt{2/3} \tag{2.76}$$

2.3.2 Algorithmic Aspects

For the given problem please consider the overall strains $\boldsymbol{\varepsilon}$ to be a known quantity. In order to generate explicit expressions for stresses $\boldsymbol{\sigma}$, it is necessary to integrate the evolution equations numerically. Here, this is accomplished by the Euler backward method. A time increment $\Delta t = t_{n+1} - t_n$ between two discrete points of time t_{n+1} and t_n shall be given. The related evolution equations then read as

$$\boldsymbol{\varepsilon}^p_{n+1} = \boldsymbol{\varepsilon}^p_n + \Delta\gamma_{n+1}\,\boldsymbol{N}_{n+1} \tag{2.77}$$

$$\alpha^p_{n+1} = \alpha^p_n + \Delta\gamma_{n+1}\,\sqrt{2/3} \tag{2.78}$$

Recalling that only the deviatoric part of the stresses is incorporated into plastic evolution, and, consequently, the plastic strain tensor is deviatoric itself, see equation (2.75), with equation (2.71-1) it holds

$$\begin{aligned}\boldsymbol{\sigma} &= [\lambda\,\boldsymbol{I}\otimes\boldsymbol{I} + 2\mu\,\mathbb{I}^{sym}] : [\boldsymbol{\varepsilon} - \boldsymbol{\varepsilon}^p] = 3\lambda\,\boldsymbol{\varepsilon}^{sph} + 2\mu\,[\boldsymbol{\varepsilon} - \boldsymbol{\varepsilon}^p] \\ &= [3\lambda + 2\mu]\boldsymbol{\varepsilon}^{sph} + 2\mu\,[\boldsymbol{\varepsilon}^{dev} - \boldsymbol{\varepsilon}^p] = \boldsymbol{\sigma}^{sph} + \boldsymbol{\sigma}^{dev}\end{aligned} \tag{2.79}$$

In view of equation (2.77) and for the point of time t_{n+1}, this yields in

$$\boldsymbol{\sigma}^{dev}_{n+1} = 2\mu\,[\boldsymbol{\varepsilon}^{dev}_{n+1} - \boldsymbol{\varepsilon}^p_n] - 2\mu\,\Delta\gamma_{n+1}\,\boldsymbol{N}_{n+1} \tag{2.80}$$

and, furthermore, it holds

$$\boldsymbol{\sigma}^{sph}_{n+1} = [3\,\lambda + 2\,\mu]\,\boldsymbol{\varepsilon}^{sph}_{n+1} = [\lambda + 2/3\mu]\,[\boldsymbol{I} : \boldsymbol{\varepsilon}_{n+1}]\,\boldsymbol{I} \tag{2.81}$$

With

$$\boldsymbol{\sigma}^{dev}_{trial} = 2\mu\,[\boldsymbol{\varepsilon}^{dev}_{n+1} - \boldsymbol{\varepsilon}^p_n], \quad \boldsymbol{N}_{trial} = \frac{\boldsymbol{\sigma}^{dev}_{trial}}{\|\boldsymbol{\sigma}^{dev}_{trial}\|} = \boldsymbol{N}_{n+1} \tag{2.82}$$

the double contraction of equation (2.80) with $\boldsymbol{N}_{n+1}$ renders the so-called radial return, given as

$$\|\boldsymbol{\sigma}^{dev}_{n+1}\| = \|\boldsymbol{\sigma}^{dev}_{trial}\| - 2\mu\,\Delta\gamma_{n+1} \tag{2.83}$$

Furthermore, together with equations (2.71-2), (2.78) and (2.83), the von Mises yield function (2.74-1) renders

$$\Delta\gamma_{n+1} = \Phi^p_{trial}\,[2H^p/3 + 2\mu]^{-1}, \quad \Phi^p_{trial} = \|\boldsymbol{\sigma}^{dev}_{trial}\| - \sqrt{2/3}\,[Y_0 - R_n], \quad R_n = -H^p\,\alpha^p_n \tag{2.84}$$

This, together with equation (2.77), can be reiterated in order to compute $\boldsymbol{\varepsilon}^p_{n+1}$ and in combination with equations (2.79) and (2.80) to compute $\boldsymbol{\sigma}_{n+1} = \boldsymbol{\sigma}^{sph}_{n+1} + \boldsymbol{\sigma}^{dev}_{n+1}$. Please note that for von Mises plasticity with isotropic linear hardening the Lagrange multiplier $\Delta\gamma_{n+1}$ can directly be computed. Taking equation (2.78) into account, the hardening stress then follows as $R_{n+1} = -H^p\,\alpha^p{}_{n+1}$. In the case of non-linear hardening an iteration has to be accomplished in order to find some $\Delta\gamma_{n+1}$ with $\Phi^p(\Delta\gamma_{n+1}) = 0$. To solve the boundary value problem at hand, Newton's method is applied. In this

context the so-called algorithmic tangent modulus has to be computed. In general, it is not identical to the Prandtl-Reuss tensor and is given by

$$\mathbb{C}^{ep}_{alg} = \frac{\partial \boldsymbol{\sigma}_{n+1}}{\partial \boldsymbol{\varepsilon}_{n+1}} = [\lambda + 2\mu]\, \boldsymbol{I} \otimes \boldsymbol{I} + c_I\, \mathbb{I}^{dev} + c_{II}\, \boldsymbol{N}_{n+1} \otimes \boldsymbol{N}_{n+1} \tag{2.85}$$

with

$$c_I = 2\mu \left[1 - \frac{2\mu \Delta\gamma_{n+1}}{\|\boldsymbol{\sigma}^{dev}_{trial}\|}\right] \tag{2.86}$$

$$c_{II} = 4\mu^2 \left[\frac{\Delta\gamma_{n+1}}{\|\boldsymbol{\sigma}^{dev}_{trial}\|} - [2\mu + 2H^p/3]^{-1}\right] \tag{2.87}$$

It inheres minor and major symmetries, see equations (2.19) and (2.20). For a non-associative flow rule such symmetry would be lost. The aforementioned considerations are only valid in the plastic range. In contrast, for loads in the elastic range the algorithmic procedure above is replaced by setting

$$\boldsymbol{\varepsilon}^p_{n+1} = \boldsymbol{\varepsilon}^p_n, \quad \boldsymbol{\sigma}_{n+1} = \mathbb{C}^{iso} : [\boldsymbol{\varepsilon}_{n+1} - \boldsymbol{\varepsilon}^p_{n+1}] \tag{2.88}$$

where $\mathbb{C}^{iso}$ denotes the tangent modulus. The Voigt notation of $\mathbb{C}^{iso}$ has been given in equation (2.31). Finally, the algorithmic procedure is concisely comprehended in Tab. 2.1.

2.4 Linear Ferroelectricity

In the following, a linear ferroelectric material law is introduced, being relevant for, e.g., ferroelectric ceramics as lead zirconate titanate (PZT) close to saturation polarisation. Consequently, the operating point of the ferroelectric ceramic is located on a linear regime of the hysteresis loop. Switching effects are therefore neglected. Therefore, the material behaviour is not explicitly ferroelectric anymore, but in view of future work, including nonlinear effects as switching, the name is retained. For the given electrical-mechanical coupling the electromechanical boundary value problem as described in equations (2.1)–(2.9) has to be solved. Stresses, given as

$$\boldsymbol{\sigma} = \boldsymbol{\sigma}(\boldsymbol{\varepsilon}, \boldsymbol{E}) \tag{2.89}$$

as well as the dielectric displacements

$$\boldsymbol{D} = \boldsymbol{D}(\boldsymbol{\varepsilon}, \boldsymbol{E}) \tag{2.90}$$

shall depend on the strains $\boldsymbol{\varepsilon}$ and the electric field vector $\boldsymbol{E}$. Here, the strain energy function W_{mech} and the complementary electric field energy function W^*_{elec} constitute mechanical and electrical potentials to be incorporated in the second law of thermodynamics, resulting in

$$\mathcal{D} = \mathcal{D}_{loc} = \mathcal{W}_{mech} - \mathcal{W}^*_{elec} - \dot{H} = 0 \tag{2.91}$$

Changes of state are reversible since in this case all mechanical and electrical forces are assumed to be derived from potentials. In equation (2.91) $\mathcal{W}_{mech}$ denotes the stress power while $\mathcal{W}^*_{elec}$ is identi-

given:	$\boldsymbol{\varepsilon}_{n+1},\ \boldsymbol{\varepsilon}^p_n,\ \alpha^p_n$		
1. trial value:	compute $\|\boldsymbol{\sigma}^{dev}_{trial}\| \ \Rightarrow\ \Phi^p_{trial}$		
2. check yield function:	if $\Phi^p_{trial} \leq 0$: goto 3.a), else: goto 3.b)		
3.a) elastic update:	$\bullet^p_{n+1}$	$=$	$\bullet^p_n$
	$\boldsymbol{\sigma}_{n+1}$	$=$	$\mathbb{C}^{iso} : [\boldsymbol{\varepsilon}_{n+1} - \boldsymbol{\varepsilon}^p_{n+1}]$
	$\mathbb{C}^{iso}$		tangent modulus
3.b) plastic update:	$\Delta\gamma^p_{n+1} = \dfrac{\Phi^p_{trial}}{2/3H^p + 2\mu} \ \Rightarrow\ \boldsymbol{\varepsilon}^p_{n+1}, \alpha^p_{n+1}$		
	$\boldsymbol{\sigma}^{sph}_{n+1}$	$=$	$[\lambda + 2/3\mu]\,[\boldsymbol{I} : \boldsymbol{\varepsilon}_{n+1}]\,\boldsymbol{I}$
	$\boldsymbol{\sigma}^{dev}_{n+1}$	$=$	$\boldsymbol{\sigma}^{dev}_{trial} - 2\mu\Delta\gamma^p_{n+1}\boldsymbol{N}_{n+1}$
	$\boldsymbol{\sigma}_{n+1}$	$=$	$\boldsymbol{\sigma}^{sph}_{n+1} + \boldsymbol{\sigma}^{dev}_{n+1}$
	$\mathbb{C}^{ep}_{alg}$		tangent modulus

Table 2.1: Algorithmic procedure for bulk elastoplasticity with linear isotropic hardening

fied with the complementary dielectric displacement power. For ferroelectricity a widely applicable potential is provided by introducing the electric enthalpy function H. It allows that the polarisation can be specified due to fixed electric field inputs as well as stresses due to fixed strains, compare Smith [165]. For temperature-independent problems the electric enthalpy function is equivalent to the electric Gibbs function. By application of the Legendre-transformation, the electric enthalpy can be correlated to other potentials, e.g. the free energy.

$$H = H(\boldsymbol{\varepsilon}, \boldsymbol{E}; \boldsymbol{m}_0) = \inf_{\boldsymbol{D}}(\Psi - \boldsymbol{E}\cdot\boldsymbol{D}), \quad \boldsymbol{m}_0 = \text{const.} \tag{2.92}$$

Corresponding to section 2.2.2, ferroelectric materials inhere one direction of anisotropy, denoted by $\boldsymbol{m}_0, \|\boldsymbol{m}_0\| = 1$. The structure tensor is given as $\boldsymbol{M}_0 = \boldsymbol{m}_0 \otimes \boldsymbol{m}_0$. The stress power and the

complementary dielectric displacement power are expressed by

$$\mathcal{W}_{mech} = \boldsymbol{\sigma} : \dot{\boldsymbol{\varepsilon}}, \quad \mathcal{W}^{*}_{elec} = \boldsymbol{D} \cdot \dot{\boldsymbol{E}} \tag{2.93}$$

Equations (2.91) and (2.93) together yield

$$\boldsymbol{\sigma} : \dot{\boldsymbol{\varepsilon}} - \boldsymbol{D} \cdot \dot{\boldsymbol{E}} - \dot{H} = 0 \tag{2.94}$$

and, incorporating equation (2.92), renders

$$\Big[\boldsymbol{\sigma} - \frac{\partial H}{\partial \boldsymbol{\varepsilon}}\Big] : \dot{\boldsymbol{\varepsilon}} + \Big[- \boldsymbol{D} - \frac{\partial H}{\partial \boldsymbol{E}}\Big] \cdot \dot{\boldsymbol{E}} = 0 \tag{2.95}$$

Due to the Coleman-Noll Entropy Principle, it follows

$$\boldsymbol{\sigma} = \frac{\partial H}{\partial \boldsymbol{\varepsilon}}, \quad \boldsymbol{D} = -\frac{\partial H}{\partial \boldsymbol{E}} \tag{2.96}$$

The rate relations of stresses and dielectric displacements with respect to the strains and the electric field are given by

$$\dot{\boldsymbol{\sigma}} = \mathbb{C}^{fer,el} : \dot{\boldsymbol{\varepsilon}} - \mathfrak{e}^{\triangle} \cdot \dot{\boldsymbol{E}}, \quad \dot{\boldsymbol{D}} = \mathfrak{e} : \dot{\boldsymbol{\varepsilon}} + \boldsymbol{\epsilon} \cdot \dot{\boldsymbol{E}} \tag{2.97}$$

The associated Ferroelectric Continuum Tangent Tensors read as

$$\begin{aligned} &\mathbb{C}^{fer,el} = \frac{\partial^2 H}{\partial \boldsymbol{\varepsilon} \otimes \partial \boldsymbol{\varepsilon}} = [\mathbb{C}^{fer,el}]_{ijkl} \boldsymbol{e}_i \otimes \boldsymbol{e}_j \otimes \boldsymbol{e}_k \otimes \boldsymbol{e}_l, \quad \mathfrak{e}^{\triangle} = -\frac{\partial^2 H}{\partial \boldsymbol{\varepsilon} \otimes \partial \boldsymbol{E}} = [\mathfrak{e}^{\triangle}]_{ijk} \boldsymbol{e}_i \otimes \boldsymbol{e}_j \otimes \boldsymbol{e}_k, \\ &\mathfrak{e} = -\frac{\partial^2 H}{\partial \boldsymbol{E} \otimes \partial \boldsymbol{\varepsilon}} = [\mathfrak{e}]_{kij} \boldsymbol{e}_k \otimes \boldsymbol{e}_i \otimes \boldsymbol{e}_j, \qquad \boldsymbol{\epsilon} = -\frac{\partial^2 H}{\partial \boldsymbol{E} \otimes \partial \boldsymbol{E}} = \epsilon_{ij} \boldsymbol{e}_i \otimes \boldsymbol{e}_j \end{aligned} \tag{2.98}$$

The symmetric properties of $\mathbb{C}^{fer,el}$ are equivalent to properties stated in equations (2.19) and (2.20). In order to achieve a linear relation of energetically conjugated quantities, the electric enthalpy is formulated as

$$H = \frac{1}{2}\, \boldsymbol{\varepsilon} : \mathbb{C}^{fer,el} : \boldsymbol{\varepsilon} - \boldsymbol{E} \cdot \mathfrak{e} : \boldsymbol{\varepsilon} - \frac{1}{2}\, \boldsymbol{E} \cdot \boldsymbol{\epsilon} \cdot \boldsymbol{E} \tag{2.99}$$

Accordingly, the correlations

$$\boldsymbol{\sigma} = \mathbb{C}^{fer,el} : \boldsymbol{\varepsilon} - \mathfrak{e}^{t} \cdot \boldsymbol{E}, \quad \boldsymbol{D} = \mathfrak{e} : \boldsymbol{\varepsilon} + \boldsymbol{\epsilon} \cdot \boldsymbol{E} \tag{2.100}$$

follow straightforwardly. Concerning the other Ferroelectric Continuum Tangent Tensors, it holds

$$[\mathfrak{e}]_{kij} = [\mathfrak{e}]_{kji}, \quad \epsilon_{ij} = \epsilon_{ji} \tag{2.101}$$

as well as

$$\mathfrak{e} = [\mathfrak{e}]_{kij} \boldsymbol{e}_k \otimes \boldsymbol{e}_i \otimes \boldsymbol{e}_j, \quad \mathfrak{e}^{t} = \mathfrak{e}^{\triangle} = [\mathfrak{e}]_{kij} \boldsymbol{e}_i \otimes \boldsymbol{e}_j \otimes \boldsymbol{e}_k \tag{2.102}$$

Here, $\mathfrak{e}$ is called the third order piezoelectric tensor and $\boldsymbol{\epsilon}$ denotes the second-order tensor of permittivity. As found in equation (2.101), symmetric properties allow $\mathfrak{e}$ to be represented by 18 piezoelectric

constants while 6 dielectric or permittivity constants are sufficient for a complete description of $\boldsymbol{\epsilon}$. Together with the Voigt representations of $\boldsymbol{\sigma}^V$ and $\boldsymbol{\varepsilon}^V$ as stated in equation (2.24) it holds

$$\boldsymbol{\sigma}^V = \boldsymbol{C}^{fer,el} \cdot \boldsymbol{\varepsilon}^V - \boldsymbol{e}^t \cdot \boldsymbol{E}, \quad \boldsymbol{D} = \boldsymbol{e} \cdot \boldsymbol{\varepsilon}^V + \boldsymbol{\epsilon} \cdot \boldsymbol{E} \tag{2.103}$$

At the same time, an adequate Voigt notation of $\mathfrak{e}$, denoted as $\boldsymbol{e}$, is given as

$$e_{ij} = \begin{bmatrix} e_{111} & e_{122} & e_{133} & e_{112} & e_{123} & e_{131} \\ e_{211} & e_{222} & e_{233} & e_{212} & e_{223} & e_{231} \\ e_{311} & e_{322} & e_{333} & e_{312} & e_{323} & e_{331} \end{bmatrix} \tag{2.104}$$

Obviously, a Voigt notation of $\boldsymbol{\epsilon}$ and $\boldsymbol{E}$ is not indicated while the Voigt notation of $\mathbb{C}^{fer,el}$, identified with $\boldsymbol{C}^{fer,el}$, has already been given in equation (2.24). According to Schröder and Gross [155], an invariant representation of the electric enthalpy reads

$$\begin{aligned} H = H(\boldsymbol{\varepsilon}, \boldsymbol{E}; \boldsymbol{m}_0) &= H(i_\varepsilon, i_{Em_0}, i_{\varepsilon Em_0}) \\ &= H(I_1, I_2, I_3, I_4, I_5, J_1, J_2, K_1, K_2, K_3, K_4) \\ &= H_1(I_1, I_2, I_3, I_4, I_5) + H_2(J_1, J_2) + H_3(K_1, K_2, K_3, K_4) \end{aligned} \tag{2.105}$$

with

$$\begin{aligned} i_{Em_0} &= \{\boldsymbol{E}^2, \boldsymbol{E} \cdot \boldsymbol{m}_0\} = \{J_1, J_2\} \\ i_{\varepsilon Em_0} &= \{\boldsymbol{\varepsilon} : [\boldsymbol{E} \otimes \boldsymbol{m}_0], \boldsymbol{\varepsilon} : [\boldsymbol{E} \otimes \boldsymbol{E}], \boldsymbol{\varepsilon}^2 : [\boldsymbol{E} \otimes \boldsymbol{E}], \boldsymbol{\varepsilon}^2 : [\boldsymbol{E} \otimes \boldsymbol{m}_0]\} \\ &= \{K_1, K_2, K_3, K_4\} \end{aligned} \tag{2.106}$$

with K_3 being redundant but generally important as a natural quantity to model higher order effects, according to Schröder and Gross [155]. With this in hand, stresses are computed by differentiating the electric enthalpy with respect to the invariants depicted above:

$$\begin{aligned} \boldsymbol{\sigma} = \frac{\partial H}{\partial \boldsymbol{\varepsilon}} &= \frac{\partial H}{\partial I_1} \boldsymbol{I} + 2 \frac{\partial H}{\partial I_2} \boldsymbol{\varepsilon} + 3 \frac{\partial H}{\partial I_3} \boldsymbol{\varepsilon}^2 + \frac{\partial H}{\partial I_4} \boldsymbol{M}_0 + \frac{\partial H}{\partial I_5} 2 [\boldsymbol{\varepsilon} \cdot \boldsymbol{M}_0]^{sym} \\ &+ \frac{\partial H}{\partial K_1} [\boldsymbol{E} \otimes \boldsymbol{m}_0]^{sym} + \frac{\partial H}{\partial K_2} \boldsymbol{E} \otimes \boldsymbol{E} + \frac{\partial H}{\partial K_3} 2 [\boldsymbol{\varepsilon} \cdot [\boldsymbol{E} \otimes \boldsymbol{E}]]^{sym} \\ &+ \frac{\partial H}{\partial K_4} [[\boldsymbol{\varepsilon} \cdot [\boldsymbol{E} \otimes \boldsymbol{m}_0]]^{sym} + [[\boldsymbol{E} \otimes \boldsymbol{m}_0] \cdot \boldsymbol{\varepsilon}]^{sym}] \end{aligned} \tag{2.107}$$

This is further developed, yielding

$$\begin{aligned}\boldsymbol{\sigma} &= \Phi_1\,\boldsymbol{I} + \Phi_2\,\boldsymbol{\varepsilon} + \Phi_3\,\boldsymbol{\varepsilon}^2 + \Phi_4\,\boldsymbol{M}_0 + \Phi_5\,2\,[\boldsymbol{\varepsilon}\cdot\boldsymbol{M}_0]^{sym} \\ &+ \Phi_6\,[\boldsymbol{E}\otimes\boldsymbol{m}_0]^{sym} + \Phi_7\,\boldsymbol{E}\otimes\boldsymbol{E} + \Phi_8\,2\,[\boldsymbol{\varepsilon}\cdot[\boldsymbol{E}\otimes\boldsymbol{E}]]^{sym} \\ &+ \Phi_9\,[[\boldsymbol{\varepsilon}\cdot[\boldsymbol{E}\otimes\boldsymbol{m}_0]]^{sym} + [[\boldsymbol{E}\otimes\boldsymbol{m}_0]\cdot\boldsymbol{\varepsilon}]^{sym}] \end{aligned} \tag{2.108}$$

Analogously, dielectric displacements are expressed as

$$\begin{aligned}\boldsymbol{D} &= -\frac{\partial H}{\partial \boldsymbol{E}} \\ &= -2\,\frac{\partial H}{\partial J_1}\,\boldsymbol{E} - \frac{\partial H}{\partial J_2}\,\boldsymbol{m}_0 - \frac{\partial H}{\partial K_1}\,\boldsymbol{\varepsilon}\cdot\boldsymbol{m}_0 - 2\,\frac{\partial H}{\partial K_2}\,\boldsymbol{\varepsilon}\cdot\boldsymbol{E} - 2\,\frac{\partial H}{\partial K_3}\,\boldsymbol{\varepsilon}^2\cdot\boldsymbol{E} - \frac{\partial H}{\partial K_4}\,\boldsymbol{\varepsilon}^2\cdot\boldsymbol{m}_0 \\ &= -\Phi_{10}\,\boldsymbol{E} - \Phi_{11}\,\boldsymbol{m}_0 - \Phi_6\,\boldsymbol{\varepsilon}\cdot\boldsymbol{m}_0 - \Phi_7\,\boldsymbol{\varepsilon}\cdot\boldsymbol{E} - \Phi_8\,\boldsymbol{\varepsilon}^2\cdot\boldsymbol{E} - \Phi_9\,\boldsymbol{\varepsilon}^2\cdot\boldsymbol{m}_0 \end{aligned} \tag{2.109}$$

The constitutive relations are considered to be linear. Consequently, in order to create constant symmetric Ferroelectric Continuum Tangent Tensors, the evaluation of an appropriate quadratic enthalpy function renders

$$\Phi_1 = \lambda\,I_1 + \alpha\,I_4 + \zeta_1\,J_2, \quad \Phi_2 = 2\mu_\perp, \quad \Phi_3 = 0, \quad \Phi_4 = \alpha\,I_1 + \beta\,I_4 + \zeta_2\,J_2, \quad \Phi_5 = 2\,[\mu_\parallel - \mu_\perp]$$

$$\Phi_6 = \zeta_3, \quad \Phi_7 = \Phi_8 = \Phi_9 = 0, \quad \Phi_{10} = 2\gamma_1, \quad \Phi_{11} = \zeta_1\,I_1 + \zeta_2\,I_4 + 2\gamma_2\,J_2 \tag{2.110}$$

with λ, $\mu_\perp$, $\mu_\parallel$, α, β, ζ_1, ζ_2, ζ_3, γ_1 and γ_2 indicating material parameters. Consequently, this leads to

$$\begin{aligned}\boldsymbol{\sigma} &= [\lambda\,I_1 + \alpha\,I_4 + \zeta_1\,J_2]\,\boldsymbol{I} + 2\mu_\perp\,\boldsymbol{\varepsilon} + [\alpha\,I_1 + \beta\,I_4 + \zeta_2\,J_2]\,\boldsymbol{M}_0 \\ &+ 4\,[\mu_\parallel - \mu_\perp]\,[\boldsymbol{\varepsilon}\cdot\boldsymbol{M}_0]^{sym} + \zeta_3\,[\boldsymbol{E}\otimes\boldsymbol{m}_0]^{sym} \end{aligned} \tag{2.111}$$

$$\boldsymbol{D} = -2\gamma_1\,\boldsymbol{E} - (\zeta_1\,I_1 + \zeta_2\,I_4 + 2\gamma_2 J_2)\,\boldsymbol{m}_0 - \zeta_3\,\boldsymbol{\varepsilon}\cdot\boldsymbol{m}_0 \tag{2.112}$$

Hence, the Ferroelectric Continuum Tangent Tensors are given as

$$\mathbb{C}^{fer,el} = \mathbb{C}^{tra} \tag{2.113}$$

$$\boldsymbol{\mathfrak{e}} = \frac{\partial \boldsymbol{D}}{\partial \boldsymbol{\varepsilon}} = -\zeta_1 \boldsymbol{m}_0 \otimes \boldsymbol{I} - \zeta_2\,\boldsymbol{m}_0 \otimes \boldsymbol{M}_0 - \zeta_3\,\boldsymbol{\mathfrak{e}}^* \tag{2.114}$$

$$\boldsymbol{\epsilon} = \frac{\partial \boldsymbol{D}}{\partial \boldsymbol{E}} = -2\gamma_1\,\boldsymbol{I} - 2\gamma_2\,\boldsymbol{M}_0 \tag{2.115}$$

with

$$\mathfrak{e}^* = \frac{1}{2}\left[m_{(0)i}\delta_{kj} + m_{(0)j}\delta_{ki}\right] \boldsymbol{e}_k \otimes \boldsymbol{e}_i \otimes \boldsymbol{e}_j \tag{2.116}$$

Finally, if the direction of anisotropy is identified as $\boldsymbol{m}_0 = \boldsymbol{e}_3$ the Voigt notated piezoelectric tensor reads as

$$e_{ij} = \begin{bmatrix} 0 & 0 & 0 & 0 & 0 & e_{15} \\ 0 & 0 & 0 & 0 & e_{15} & 0 \\ e_{31} & e_{31} & e_{33} & 0 & 0 & 0 \end{bmatrix} \tag{2.117}$$

with

$$e_{31} = -\zeta_1, \quad e_{33} = -\zeta_1 - \zeta_2 - \zeta_3, \quad e_{15} = -\frac{1}{2}\zeta_3 \tag{2.118}$$

Due to the fact that the Ferroelectric Continuum Tangent Tensors as well as the stresses $\boldsymbol{\sigma}$ and the dielectric displacements $\boldsymbol{D}$ can be directly computed, no further algorithmic methods have to be dealt within this section.

3 Constitutive Modelling and Algorithmic Aspects of Solid Interfaces

Subsequently, several geometrically linear interfacial constitutive models, also referred to as traction-separation-laws or cohesive laws, are introduced. Such material models are supposed to be sufficient to simulate the behaviour of laminar welding interfaces of metal-/fibre-reinforced polymer composites under diverse loading conditions as well as grain boundaries of ferroelectric materials under fatigue loading. Solid interfaces are –approximately– one geometrical dimension smaller than the surrounding continuum. They normally inhere significant differences in material behaviour when compared to the bulk material. The fact that an interface is bordered by surfaces belonging to the surrounding material implies the idea of constitutively connecting traction vectors and displacement jumps related to those surfaces. Accordingly, for a coupled problem, the relation of dielectric displacements and potential jumps has to be considered additionally.

Constitutive originators are, once more, energy considerations with respect to the free energy or the electric enthalpy function, bearing in mind the second law of thermodynamics. Stresses and Continuum Tangent Stiffness Tensors are derived, under special consideration of algorithmic aspects. For the bigger part of the traction-separation-laws introduced in this work the constitutive behaviour is decoupled with respect to an interfacial orthonormal base system $\{\boldsymbol{s}, \boldsymbol{t}, \boldsymbol{n}\}$. It is localised on some average surface in between the surrounding surfaces, with $\boldsymbol{s}$ and $\boldsymbol{t}$ being tangential vectors. Such decoupling is considered to be adequate if the debonding processes are largely dominated by one failure mode. Due to the fact that many interfacial constitutive relations are strongly kindred to bulk material laws, for further insight, it shall be referred to the textbooks already stated in chapter 2. Applications of uncoupled cohesive material laws are found in, e.g., Tijssens et al. [176], Tijssens et al. [175], Hanson et al. [62] and Li et al. [94], [93]. In contrast, coupled material laws are introduced in e.g., Xu and Needleman [193], Ortiz and Pandolfi [132], Falk et al. [54], Jin et al. [73], Kroon and Faleskog [86] and Van den Bosch et al. [45].

Before going into detail concerning such traction-separation-laws, some mechanical and electrical complementing conditions with respect to the interface are stated, in addition to the boundary value problem discussed above. The first interfacial material law to be introduced, i.e. linear elasticity, provides something of a fundament for subsequent traction-separation-laws. Next, this framework is extended by taking viscous effects into account. Furthermore, elastoplasticity with Lemaitre-type damage is introduced, being sufficient for the simulation of, e.g., thermal impact welded tensile specimens. A further viscous material law, viscoplasticity with Lemaitre-type damage, is discussed thereafter. The incorporation of viscous interfaces is considered to capture relaxation and creep characteristics. Subsequently, interfacial fatigue is modelled by adequate traction-separation-laws distinguishing

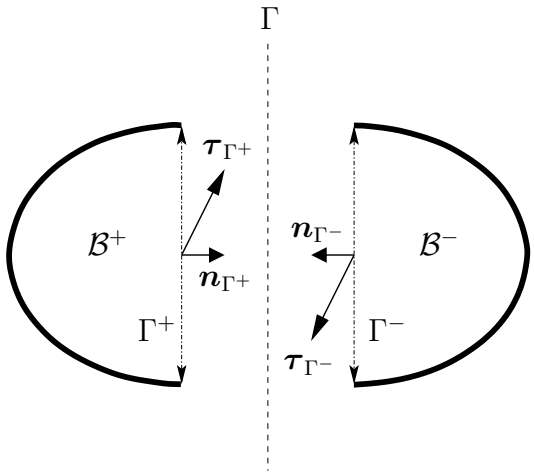

Figure 3.1: Configurations $\mathcal{B}^+$, $\mathcal{B}^-$, interface Γ and some interface conditions

between small and large cycle numbers. In this regard, so-called time- and cycle-based fatigue laws are introduced. By reviewing linear ferroelectricity for the interface, the coupled problem is taken into account. Finally, this is extended by time- and cycle-based fatigue laws. To emphasise the functionality of the mentioned constitutive relations, prototype examples of relevant quantities are included where adequate, pointing out the basic constitutive behaviour.

3.1 Interface Conditions

Without loss of generality let $\mathcal{B}$ be splitted into two parts, denoted as $\mathcal{B}^+$ and $\mathcal{B}^-$. These are bonded by an interface, with Γ denoting the related centre line. Adequate interface-related position vectors $\boldsymbol{x}$ are only considered to point onto Γ. Furthermore, towards the interface, let $\mathcal{B}^+$ and $\mathcal{B}^-$ be closed by boundaries Γ^+ and Γ^-, see Fig. 3.1 for a visualisation. With respect to both $\mathcal{B}^+$ and $\mathcal{B}^-$, the aforementioned equations (2.1)–(2.9), constituting the boundary value problem, retain all their validity.

3.1.1 Mechanical Interface Conditions

An interface-related traction equilibrium condition reads as

$$\boldsymbol{\tau}_{\Gamma^+} + \boldsymbol{\tau}_{\Gamma^-} = \boldsymbol{0}, \quad \text{with} \quad \boldsymbol{\tau}_{\Gamma^+} = \boldsymbol{\sigma} \cdot \boldsymbol{n}_{\Gamma^+}, \quad \boldsymbol{\tau}_{\Gamma^-} = \boldsymbol{\sigma} \cdot \boldsymbol{n}_{\Gamma^-} \quad \text{and} \quad [\![\boldsymbol{\sigma}]\!] \cdot \boldsymbol{n}_{\Gamma^-} = \boldsymbol{0} \tag{3.1}$$

see also Fig. 3.1 for illustration. A displacement compatibility condition is given as

$$\boldsymbol{u}_{\Gamma^+} - \boldsymbol{u}_{\Gamma^-} = [\![\boldsymbol{u}]\!] \tag{3.2}$$

where $[\![\boldsymbol{u}]\!]$ denotes the so-called displacement jump.

3.1.2 Electrical Interface Conditions

Furthermore, a dielectrical displacement equilibrium condition takes the representation

$$\Lambda_{\Gamma^+} + \Lambda_{\Gamma^-} = 0, \quad \text{with} \quad \Lambda_{\Gamma^+} = -\boldsymbol{D} \cdot \boldsymbol{n}_{\Gamma^+}, \quad \Lambda_{\Gamma^-} = -\boldsymbol{D} \cdot \boldsymbol{n}_{\Gamma^-} \quad \text{and} \quad [\![\boldsymbol{D}]\!] \cdot \boldsymbol{n}_{\Gamma^-} = \boldsymbol{0} \tag{3.3}$$

while the potential compatibility condition reads as

$$\Phi_{\Gamma^+} - \Phi_{\Gamma^-} = [\![\Phi]\!] \tag{3.4}$$

In what follows, it will be identified $\boldsymbol{n}_{\Gamma^-} \equiv \boldsymbol{n}$.

3.2 Linear Elasticity

The linear hyperelastic traction-separation behaviour described in this section refers to the uncoupled boundary value problem. An adequate relation of tractions and displacement jumps therefore reads as

$$\boldsymbol{\tau} = \boldsymbol{\tau}([\![\boldsymbol{u}]\!]) \tag{3.5}$$

Though the traction vector $\boldsymbol{\tau}$ inheres the same units as the stress tensor, the energetically conjugate quantity is chosen to inhere the unit of meter, i.e. the displacement jump. This is due to the fact that strains are given as length differences divided by an initial length. In the case of an interface the initial distance between the bordering surfaces is supposed to be very small or even zero. Division by zero is avoided by only taking the separation of the bordering surfaces into account. Consequently, for the sake of units, a division by an internal length must be inherent in the constitutive relations. With W being a displacement jump energy function and $\mathcal{W} = \dot{W}$ denoting the traction power, identical to equation (2.11), the second law of thermodynamics for an interface reads as

$$\mathcal{D} = \mathcal{D}_{loc} = \mathcal{W} - \dot{\Psi} = 0 \tag{3.6}$$

Please note that here and in all following sections the second law of thermodynamics, represented by the Clausius-Duhem inequality (3.6), shall be separately fullfilled for the bulk continuum and the interface. The free energy of the interface is given as

$$\Psi = \Psi([\![\boldsymbol{u}]\!]; \boldsymbol{s}, \boldsymbol{t}, \boldsymbol{n}), \quad \boldsymbol{s}, \boldsymbol{t}, \boldsymbol{n} = \text{const.} \tag{3.7}$$

where $\{\boldsymbol{s}, \boldsymbol{t}, \boldsymbol{n}\}$ is the orthonormal interface base system, with $\boldsymbol{s}$ and $\boldsymbol{t}$ denoting orthogonal tangential vectors of the interface. In what follows, as all further interfacial material laws include elasticity, the dependency on the constant orthogonal tangential vectors is tacitly assumed and not explicitly stated anymore. The traction power is expressed by

$$\mathcal{W} = \boldsymbol{\tau} \cdot \dot{[\![\boldsymbol{u}]\!]} \tag{3.8}$$

Equations (3.6) and (3.8) together yield

$$\boldsymbol{\tau} \cdot [\![\dot{\boldsymbol{u}}]\!] - \dot{\Psi} = 0 \tag{3.9}$$

Considering equation (3.7), it holds

$$\Big[\boldsymbol{\tau} - \frac{\partial \Psi}{\partial [\![\boldsymbol{u}]\!]}\Big] \cdot [\![\dot{\boldsymbol{u}}]\!] = 0 \tag{3.10}$$

Application of the Coleman-Noll Entropy Principle then gives

$$\boldsymbol{\tau} = \frac{\partial \Psi}{\partial [\![\boldsymbol{u}]\!]} \tag{3.11}$$

The rate relation of tractions and displacement jumps then reads as

$$\dot{\boldsymbol{\tau}} = \boldsymbol{C}^{if,el} \cdot [\![\dot{\boldsymbol{u}}]\!] \tag{3.12}$$

where the second order Elastic Interfacial Tangent Stiffness Tensor is given by

$$\boldsymbol{C}^{if,el} = \frac{\partial^2 \Psi}{\partial [\![\boldsymbol{u}]\!] \otimes \partial [\![\boldsymbol{u}]\!]} = \frac{\partial \boldsymbol{\tau}}{\partial [\![\boldsymbol{u}]\!]} = C_{ij}^{if,el}\, \boldsymbol{e}_i \otimes \boldsymbol{e}_j \tag{3.13}$$

Regarding equation (3.13), symmetric properties follow as

$$C_{ij}^{if,el} = C_{ji}^{if,el} \tag{3.14}$$

The free energy is specified by

$$\Psi = \mathcal{W} = \frac{1}{2}\, [\![\boldsymbol{u}]\!] \cdot \boldsymbol{C}^{if,el} \cdot [\![\boldsymbol{u}]\!] > 0 \quad \forall\, [\![\boldsymbol{u}]\!] \neq \boldsymbol{0}, \quad C_{ij}^{if,el} = \text{const.} \tag{3.15}$$

assuming a linear and positive definite relation of tractions and displacement jumps which is given by

$$\boldsymbol{\tau} = \boldsymbol{C}^{if,el} \cdot [\![\boldsymbol{u}]\!] \tag{3.16}$$

The traction-separation correlation regarded here shall be linear and decoupled with respect to the interfacial orthonormal system $\{\boldsymbol{s}, \boldsymbol{t}, \boldsymbol{n}\}$. This is clearly a simplification of the general case where the constitutive answer is coupled with respect to $\{\boldsymbol{s}, \boldsymbol{t}, \boldsymbol{n}\}$. An adequate formulation of the free energy function is given as

$$\Psi = \Psi([\![\boldsymbol{u}]\!]; \boldsymbol{s}, \boldsymbol{t}, \boldsymbol{n}) = \Psi(i_{[\![u]\!]}) \tag{3.17}$$

where the coefficients $i_{[\![u]\!]}$ compare to the irreducible set of invariants of the tensorial case, reading as

$$i_{[\![u]\!]} = \{I_s^{if}, I_t^{if}, I_n^{if}\} \quad \text{with} \quad I_i^{if} = [[\![\boldsymbol{u}]\!] \cdot \boldsymbol{i}]^2 \tag{3.18}$$

Consequently, tractions are computed by

$$\boldsymbol{\tau} = \frac{\partial \Psi}{\partial [\![\boldsymbol{u}]\!]} = 2\frac{\partial \Psi}{\partial I_s^{if}} [[\![\boldsymbol{u}]\!] \cdot \boldsymbol{s}] \, \boldsymbol{s} + 2\frac{\partial \Psi}{\partial I_t^{if}} [[\![\boldsymbol{u}]\!] \cdot \boldsymbol{t}] \, \boldsymbol{t} + 2\frac{\partial \Psi}{\partial I_n^{if}} [[\![\boldsymbol{u}]\!] \cdot \boldsymbol{n}] \, \boldsymbol{n}$$

$$= \Phi_s [[\![\boldsymbol{u}]\!] \cdot \boldsymbol{s}] \, \boldsymbol{s} + \Phi_t [[\![\boldsymbol{u}]\!] \cdot \boldsymbol{t}] \, \boldsymbol{t} + \Phi_n [[\![\boldsymbol{u}]\!] \cdot \boldsymbol{n}] \, \boldsymbol{n} \tag{3.19}$$

Therewith, interfacial material constants are introduced via

$$\Phi_i = c_i = \frac{c_i^*}{l_i}, \quad i = s, t, n \tag{3.20}$$

with c_i^* being elastic stiffnesses, l_i denoting some constant and inherent lengths, as already mentioned, and c_i being the interfacial stiffness parameters. This renders the tractions straightforwardly as

$$\boldsymbol{\tau} = \sum_i c_i [[\![\boldsymbol{u}]\!] \cdot \boldsymbol{i}] \, \boldsymbol{i}, \quad i = s, t, n \tag{3.21}$$

The second order Elastic Interfacial Tangent Stiffness Tensor then reads

$$\boldsymbol{C}^{if,el} = \sum_i \boldsymbol{C}_i^{if,el}, \quad i = s, t, n \tag{3.22}$$

with

$$\boldsymbol{C}_i^{if,el} = c_i \, \boldsymbol{i} \otimes \boldsymbol{i} \tag{3.23}$$

Please note that if the distance between the bordering interfaces is greater than zero, it can be identified with l_n. Then, c_n^* can be correlated to the Young's modulus of the bulk. Even if the distance between the bordering interfaces is close to zero, some $l_n \neq 0$ can be applied to map the bulk properties on the interface. Nevertheless, it has to be considered that an orthotropic elastic bulk cannot completely be compared to the interface because the orthonormal decoupled interface is in lack of any transversal contraction stiffnesses. Otherwise, it can also be set $l_n = 1$ as a default. Then, the interfacial normal stiffness c_n is exempt from any comparison with the bulk, and numerical difficulties resulting from very small l_i are excluded. Regarding the tangential directions a correlation with bulk shear moduli is in principle possible. For further remarks on these issues, see, e.g. Willam et al. [188]. In further examinations it is set $l_s = l_t = l_n = 1$ for convenience, except where explicitly stated otherwise.

3.3 Viscoelasticity with Damage

The computational modelling of viscous interfaces is of special interest since adhesive connections gain more and more importance, e.g. in the field of fibre-reinforced polymer composites. In the case of viscoelasticity, material behaviour is rate-dependent without equilibrium hysteresis. First theories have been developed by e.g. Coleman and Noll [39], [40], Coleman and Mizel [38] and Mizel and Wang [120]. For more recent reviews concerning the field of viscoelasticity, see, e.g., Kaliske and Rothert [75], Reese and Govindjee [147, 148], and Kaliske [74]. Concerning general textbooks, once

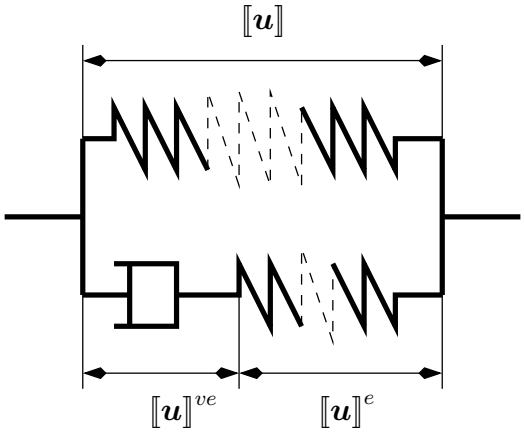

Figure 3.2: One-dimensional model of viscoelasticity with Lemaitre-type damage, consisting of a generalised Maxwell element

more, the book of Simo and Hughes [164] is recommended. In our case, a generalised Maxwell element is chosen as a material model, compare Fig. 3.2.

3.3.1 Constitutive Modelling

As illustrated in Fig. 3.2 the displacement jump $[\![\boldsymbol{u}]\!]$ is split into an elastic part $[\![\boldsymbol{u}]\!]^e$ and a viscous part $[\![\boldsymbol{u}]\!]^{ve}$ i.e.

$$[\![\boldsymbol{u}]\!] = [\![\boldsymbol{u}]\!]^e + [\![\boldsymbol{u}]\!]^{ve} \tag{3.24}$$

This is the basic kinematic assumption. Furthermore, the parallel spring shall induce a traction τ_i^∞ while the spring serial to the damper induces the traction τ_i^m. This is the case for all interfacial orthonormal directions $\boldsymbol{i} \in \{\boldsymbol{s}, \boldsymbol{t}, \boldsymbol{n}\}$. Again, related material behaviour is decoupled. The overall traction then reads as

$$\boldsymbol{\tau} = \boldsymbol{\tau}^\infty + \boldsymbol{\tau}^m \tag{3.25}$$

The dependencies of the tractions are given as

$$\boldsymbol{\tau}^\infty = \boldsymbol{\tau}^\infty([\![\boldsymbol{u}]\!], d_i), \quad \boldsymbol{\tau}^m = \boldsymbol{\tau}^m([\![\boldsymbol{u}]\!]^e, d_i), \quad i = s, t, n \tag{3.26}$$

In equation (3.26) the damage parameter $d_i \in [0, 1[$ is introduced, with $\dot{d}_i > 0$ and healing effects being excluded. It is incorporated in a Lemaitre-type damage context, see Lemaitre [90] and Lemaitre and Chaboche [91]. For $d_i \to 1$, some regarded material tends to be fully damaged and not to be able to bear any load. The Clausius-Duhem inequality reads as

$$\mathcal{D} = \mathcal{D}_{loc} = \mathcal{W} - \dot{\Psi} \geq 0 \tag{3.27}$$

where the free energy of the interface occupies the dependencies

$$\Psi = \Psi([\![\boldsymbol{u}]\!], [\![\boldsymbol{u}]\!]^e, d_i) \tag{3.28}$$

The traction power is given as

$$\mathcal{W} = \boldsymbol{\tau} \cdot \dot{[\![\boldsymbol{u}]\!]} = \boldsymbol{\tau}^{\infty} \cdot \dot{[\![\boldsymbol{u}]\!]} + \boldsymbol{\tau}^{m} \cdot \dot{[\![\boldsymbol{u}]\!]}^{e} + \boldsymbol{\tau}^{m} \cdot \dot{[\![\boldsymbol{u}]\!]}^{ve} \tag{3.29}$$

In view of the second law of thermodynamics, represented by equation (3.27), it follows

$$\boldsymbol{\tau}^{\infty} \cdot \dot{[\![\boldsymbol{u}]\!]} + \boldsymbol{\tau}^{m} \cdot \dot{[\![\boldsymbol{u}]\!]}^{e} + \boldsymbol{\tau}^{m} \cdot \dot{[\![\boldsymbol{u}]\!]}^{ve} - \dot{\Psi} \geq 0 \tag{3.30}$$

being equivalent to

$$\left[\boldsymbol{\tau}^{\infty} - \frac{\partial \Psi}{\partial [\![\boldsymbol{u}]\!]}\right] \cdot \dot{[\![\boldsymbol{u}]\!]} + \left[\boldsymbol{\tau}^{m} - \frac{\partial \Psi}{\partial [\![\boldsymbol{u}]\!]^{e}}\right] \cdot \dot{[\![\boldsymbol{u}]\!]}^{e} + \boldsymbol{\tau}^{m} \cdot \dot{[\![\boldsymbol{u}]\!]}^{ve} - \sum_{i} \frac{\partial \Psi}{\partial d_i}\, \dot{d}_i \geq 0 \tag{3.31}$$

With the Coleman-Noll Entropy Principle in mind, also known as the standard argument of rational thermodynamics, it is concluded

$$\boldsymbol{\tau}^{\infty} = \frac{\partial \Psi}{\partial [\![\boldsymbol{u}]\!]}, \quad \boldsymbol{\tau}^{m} = \frac{\partial \Psi}{\partial [\![\boldsymbol{u}]\!]^{e}} \tag{3.32}$$

Furthermore, the damage driving force shall be defined as

$$\bar{\mu}_i = -\frac{\partial \Psi}{\partial d_i} \tag{3.33}$$

This yields the reduced dissipation inequality, reading as

$$\mathcal{D}_{red} = \boldsymbol{\tau}^{m} \cdot \dot{[\![\boldsymbol{u}]\!]}^{ve} + \sum_{i} \bar{\mu}_i\, \dot{d}_i \geq 0 \tag{3.34}$$

The constitutive assumption of viscoelasticity is given by the rate dependency

$$\dot{[\![u_i]\!]}^{ve} = \frac{\tau_i^m}{\eta_i}, \quad \boldsymbol{\tau}^{m} = \sum_{i} \tau_i^m\, \boldsymbol{i} \tag{3.35}$$

where $\eta_i > 0$ denotes the viscosity in $\boldsymbol{i}$-direction. The tractions induced by the spring serial to the damper are supposed to be constituted by

$$\tau_i^m = [1 - d_i]\, c_i^m\, [\![u_i]\!]^e \tag{3.36}$$

The bracket term containing d_i becomes zero if $d_i \to 1$. Such damaging behaviour is indicated by the dotted line in Fig. 3.2. The rate of this traction is straightforwardly computed as

$$\dot{\tau}_i^m = [1 - d_i]\, c_i^m \left[\dot{[\![u_i]\!]} - \dot{[\![u_i]\!]}^{ve}\right] \tag{3.37}$$

Please note that damaging behaviour is computed independently such that d_i is treated as a constant in equation (3.36). Equations (3.35) and (3.37) together yield the differential equation for the damper-

serial tractions

$$\dot{\tau}_i^m + [1 - d_i]\,\frac{c_i^m}{\eta_i}\,\tau_i^m = [1 - d_i]\,c_i^m\,\dot{[\![u_i]\!]} \tag{3.38}$$

Additionally, combining equations (3.24), (3.35) and (3.36), an alternative differential equation for the viscoelastic displacement jump is derived, reading as

$$\dot{[\![u_i]\!]}^{ve} = \frac{1 - d_i}{T_i}\,[[\![u_i]\!] - [\![u_i]\!]^{ve}], \quad T_i = \frac{\eta_i}{c_i^m} \tag{3.39}$$

Therein, the relaxation time T_i has been introduced. The free energy is now split into two parts, given as

$$\Psi([\![\boldsymbol{u}]\!], [\![\boldsymbol{u}]\!]^e, d_i) = \Psi^\infty([\![\boldsymbol{u}]\!]) + \Psi^m([\![\boldsymbol{u}]\!]^e, d_i) \tag{3.40}$$

$$= \frac{1}{2}\,[\![\boldsymbol{u}]\!] \cdot \Big[\sum_i [1 - d_i]\,\boldsymbol{C}_i^{if,el,\infty}\Big] \cdot [\![\boldsymbol{u}]\!]$$

$$+ \frac{1}{2}\,[\![\boldsymbol{u}]\!]^e \cdot \Big[\sum_i [1 - d_i]\,\boldsymbol{C}_i^{if,el,m}\Big] \cdot [\![\boldsymbol{u}]\!]^e \tag{3.41}$$

and incorporating the Elastic Interfacial Tangent Stiffness Tensors with respect to the parallel spring $\boldsymbol{C}_i^{if,el,\infty}$ and the damper-serial spring $\boldsymbol{C}_i^{if,el,m}$, both at hand for the $\boldsymbol{i}$-direction. Here, synchronal damage is assumed for both springs, dependent on d_i. Certainly, an alternative and more general description is possible if the spring damage evolutions are kept distinctly. Because the displacement jump $[\![\boldsymbol{u}]\!]$ is considered to be available for direct computation, a non-incremental expression for $\boldsymbol{\tau}^\infty$ is possible, which is given as

$$\boldsymbol{\tau}^\infty = \Big[\sum_i [1 - d_i]\,\boldsymbol{C}_i^{if,el,\infty}\Big] \cdot [\![\boldsymbol{u}]\!] \tag{3.42}$$

In order to compute $\boldsymbol{\tau}^m$, algorithmic procedures have to be incorporated, a topic of which will be discussed later on.

The phenomenological Lemaitre-type-damage approach, see also Lemaitre [90], Lemaitre and Chaboche [91], Jansson and Larsson [72] as well as Larsson and Jansson [88], relies on the idea that the load capacity of some specimen is related to the effective cross-sectional area or rather effective volume. This is expressed by means of the interfacial damage parameters $d_i \in [0, 1[$. If $d_i \to 1$, the material tends to be fully damaged. With respect to the interfacial orthonormal base system $\{\boldsymbol{s}, \boldsymbol{t}, \boldsymbol{n}\}$ three different damage parameters d_s, d_t, d_n are distinguished. For the decoupled damage parameters d_i exponential relations are chosen, reading as

$$d_i = 1 - \exp(j_i[\mu_{i(0)} - \mu_i]) \tag{3.43}$$

The variable μ_i, accountable for the progression of damage in $\boldsymbol{i}$-direction, is computed according to

$$\mu_i = \max\{\bar{\mu}_i([\![\boldsymbol{u}]\!], [\![\boldsymbol{u}]\!]^e), \mu_{i(0)}\} \tag{3.44}$$

and the so-called damage driving force is given by

$$\bar{\mu}_i \;=\; -\partial_{d_i}\Psi \;=\; \frac{1}{2}[\![\boldsymbol{u}]\!]^e \cdot \boldsymbol{C}_i^{if,el,m} \cdot [\![\boldsymbol{u}]\!]^e + \frac{1}{2}[\![\boldsymbol{u}]\!] \cdot \boldsymbol{C}_i^{if,el,\infty} \cdot [\![\boldsymbol{u}]\!] \tag{3.45}$$

By equation (3.44) the actual elastic relative displacement energy is compared to the prior state what serves as a criterion on whether damage proceeds or not. Please note that the values of the damage parameters either remain zero or increase monotonically. The fixed material parameters $\mu_{i(0)}$ are damage thresholds, determining the initiation of damage, where j_i represent the intensity of the damage evolution.

In view of the reduced dissipation inequality (3.34) the first summand of this inequality can be reformulated by applying equation (3.35), rendering

$$\boldsymbol{\tau}^m \cdot [\![\dot{\boldsymbol{u}}]\!]^{ve} = \Big[\sum_i [\![\dot{u_i}]\!]^{ve}\, \eta_i\, \boldsymbol{i}\Big] \cdot \Big[\sum_i [\![\dot{u_i}]\!]^{ve}\, \boldsymbol{i}\Big] = \sum_i \eta_i \big[[\![\dot{u_i}]\!]^{ve}\big]^2 \tag{3.46}$$

Obviously, this is always positive or zero. In order to fulfil inequality (3.34), also the second summand must be positive or zero. With a closer look on equation (3.45) it always holds $\bar{\mu}_i \geq 0$. Consequently, together with $\dot{d}_i > 0$, the second term of equation (3.34) is positive or zero, too, and the reduced dissipation inequality is fulfilled, providing thermodynamical consistency.

3.3.2 Algorithmic Aspects

To allow for an easy algorithmic treatment, the evolutions of viscous and damaging effects are separated. Firstly, viscous effects are computed, incorporating damage parameters $d_{i(n)}$, given from the last computational step, which is denoted by index n. For the computation of $\boldsymbol{\tau}^m$ the starting point is given by equation (3.39). By multiplication with the time increment Δt an algorithmic-incremental version of equation (3.39) in the sense of the Euler backward method is obtained, reading as

$$\Delta[\![u_i]\!]^{ve} = \frac{\Delta t\,[1-d_{i(n)}]}{T_i}\,[\![u_i]\!]^e_{n+1} = \frac{\Delta t\,[1-d_{i(n)}]}{T_i}\,[[\![u_i]\!]^e_n + \Delta[\![u_i]\!] - \Delta[\![u_i]\!]^{ve}] \tag{3.47}$$

This equation is solved with respect to the viscoelastic displacement jump increment, yielding

$$\Delta[\![u_i]\!]^{ve} = \frac{\Delta t\,[1-d_{i(n)}]}{T_i + \Delta t\,[1-d_{i(n)}]}\,[[\![u_i]\!]^e_n + \Delta[\![u_i]\!]] \tag{3.48}$$

with

$$\Delta[\![u_i]\!] = [\![u_i]\!]_{n+1} - [\![u_i]\!]_n \tag{3.49}$$

The damper-serial tractions are then computed as

$$\tau^m_{i(n+1)} = c_i^m\,[1-d_{i(n)}][[\![u_i]\!]_{n+1} - [\![u_i]\!]^{ve}_{n+1}] \tag{3.50}$$

with

$$[\![u_i]\!]^{ve}_{n+1} = [\![u_i]\!]^{ve}_n + \Delta[\![u_i]\!]^{ve} \tag{3.51}$$

given:	$[\![\boldsymbol{u}]\!]_{n+1},\ [\![\boldsymbol{u}]\!]_n^{ve},\ d_{i(n)}$	
1. viscous update:	compute $\Delta[\![\boldsymbol{u}]\!]^{ve}\ \Rightarrow\ [\![\boldsymbol{u}]\!]_{n+1}^{ve}$	
2. traction update:	$\boldsymbol{\tau}_{n+1}^{m}$	$= \sum_i c_i^m[1-d_{i(n)}]\,[[\![\boldsymbol{u}_i]\!]_{n+1} - [\![\boldsymbol{u}_i]\!]_{n+1}^{ve}]$
	$\boldsymbol{\tau}_{n+1}^{\infty}$	$= \sum_i c_i^\infty[1-d_{i(n)}]\,[\![\boldsymbol{u}_i]\!]_{n+1}$
	$\boldsymbol{\tau}_{n+1}$	$= \boldsymbol{\tau}_{n+1}^{m} + \boldsymbol{\tau}_{n+1}^{\infty}$
3. damage update:	compute $\bar{\mu}_{i(n+1)}\ \Rightarrow\ d_{i(n+1)}$	
4. tangent modulus:	$\boldsymbol{C}_{alg}^{if,ved}$	

Table 3.1: Algorithmic procedure for interfacial viscoelasticity with damage

The traction components are then given as

$$\boldsymbol{\tau}_{n+1}^{\infty} = \sum_i \tau_{i(n+1)}^{\infty}\,\boldsymbol{i}, \quad \tau_{i(n+1)}^{\infty} = c_i^{\infty}\,[1-d_{i(n)}]\,[\![u_i]\!]_{n+1}, \quad \boldsymbol{\tau}_{n+1}^{m} = \sum_i \tau_{i(n+1)}^{m}\,\boldsymbol{i} \tag{3.52}$$

Consequently, the overall traction is computed as

$$\boldsymbol{\tau}_{n+1} = \boldsymbol{\tau}_{n+1}^{\infty} + \boldsymbol{\tau}_{n+1}^{m} \tag{3.53}$$

With the current viscoelastic displacement jump in hand the damage parameter $d_{i(n+1)}$ is computed. It is based on the elastic part of the relative displacements $[\![\boldsymbol{u}]\!]_{n+1}^{e} = [\![\boldsymbol{u}]\!]_{n+1} - [\![\boldsymbol{u}]\!]_{n+1}^{ve}$ and inheres the straightforward update

$$d_{i(n+1)} = 1 - \exp(j_i[\mu_{i(0)} - \mu_{i(n+1)}]) \tag{3.54}$$

with

$$\mu_{i(n+1)} = \max\{\bar{\mu}_{i(n+1)}([\![\boldsymbol{u}]\!]_{n+1}, [\![\boldsymbol{u}]\!]_{n+1}^{e}), \mu_{i(n)}, \mu_{i(0)}\} \tag{3.55}$$

and

$$\bar{\mu}_{i(n+1)} \;=\; -\partial_{d_i}\Psi_{n+1} \;=\; \frac{1}{2}[\![\boldsymbol{u}]\!]_{n+1}^{e} \cdot \boldsymbol{C}_i^{if,el,m} \cdot [\![\boldsymbol{u}]\!]_{n+1}^{e} + \frac{1}{2}[\![\boldsymbol{u}]\!]_{n+1} \cdot \boldsymbol{C}_i^{if,el,\infty} \cdot [\![\boldsymbol{u}]\!]_{n+1} \tag{3.56}$$

If damage evolves, it is essential that

$$\mu_{i(n+1)} = \bar{\mu}_{i(n+1)}(\llbracket \boldsymbol{u} \rrbracket_{n+1}, \llbracket \boldsymbol{u} \rrbracket^{e}_{n+1}) \tag{3.57}$$

The such computed damage parameter then serves as input for the next computation step. The present boundary value problem shall be solved by Newton's method. Therefore, the interfacial algorithmic tangent modulus is needed. It is given as

$$\boldsymbol{C}^{if,ved}_{alg} = \frac{\partial \boldsymbol{\tau}_{n+1}}{\partial \llbracket \boldsymbol{u} \rrbracket_{n+1}} = \sum_i \boldsymbol{C}^{if,el,\infty}_i \left[1 - d_{i(n)}\right] + \sum_i c^m_i \left[1 - d_{i(n)}\right] \left[\boldsymbol{i} \otimes \boldsymbol{i} - \frac{\partial \llbracket \boldsymbol{u}_i \rrbracket^{ve}_{n+1}}{\partial \llbracket \boldsymbol{u} \rrbracket_{n+1}}\right] \tag{3.58}$$

With

$$\frac{\partial \llbracket \boldsymbol{u}_i \rrbracket^{ve}_{n+1}}{\partial \llbracket \boldsymbol{u} \rrbracket_{n+1}} = \frac{\Delta t \left[1 - d_{i(n)}\right]}{T_i + \Delta t \left[1 - d_{i(n)}\right]} \boldsymbol{i} \otimes \boldsymbol{i} \tag{3.59}$$

the algorithmic tangent finally results in

$$\boldsymbol{C}^{if,ved}_{alg} = \sum_i \boldsymbol{C}^{if,el,\infty}_i \left[1 - d_{i(n)}\right] + \sum_i \boldsymbol{C}^{if,el,m}_i \frac{T_i \left[1 - d_{i(n)}\right]}{T_i + \Delta t \left[1 - d_{i(n)}\right]} \tag{3.60}$$

The algorithmic procedure is reiterated in Tab. 3.1.

3.3.3 Prototype Examples

In this section some prototype examples are presented, demonstrating the functionality of the viscoelastic damage law, which has been discussed above. The plots have been created by a finite

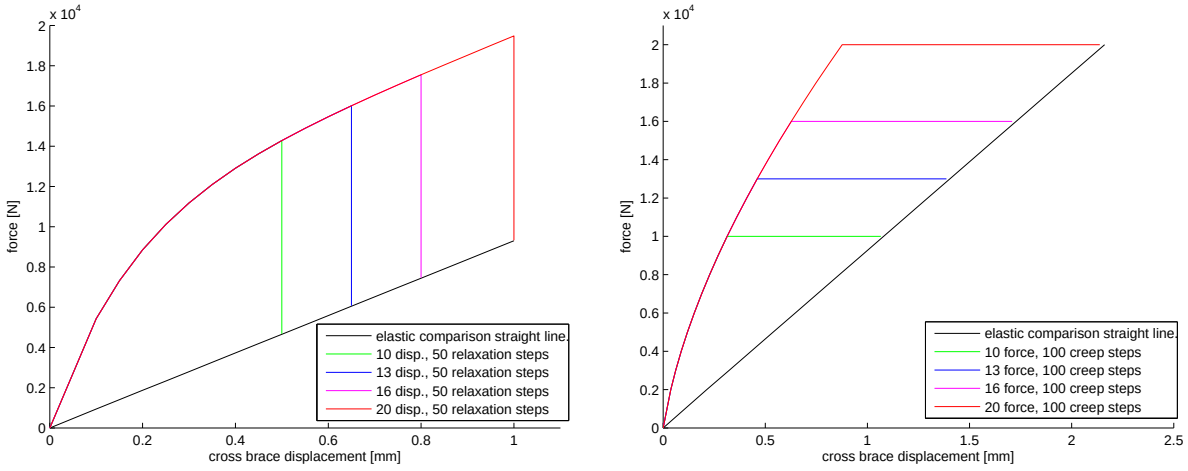

Figure 3.3: One-dimensional exemplary force-displacement plots of viscoelasticity. Left: displacement control. Relaxation behaviour, starting from different points of the loading history. Right: force control. Creep behaviour, starting from different points of the loading history

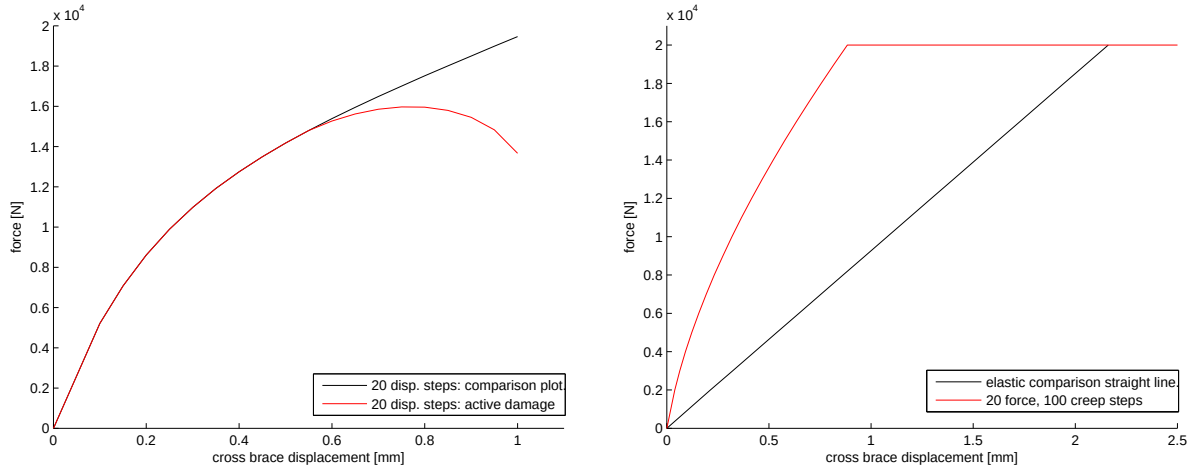

Figure 3.4: One-dimensional exemplary force-displacement plots of viscoelasticity with Lemaitre-type damage. Left: displacement control. Damage is activated at approx. 15 kN. Right: force control. Creep behaviour - the elastic straight line is exceeded because damage is active

element simulation of a single lap tensile specimen, with linear elasticity for the bulk and viscoelasticity (with damage) for the interfacial zone.

In Fig. 3.3 relaxation behaviour is shown on the left hand side, whereas creep behaviour is presented on the right hand side. In both cases, damage has been switched off to focus on the purely viscoelastic material law. Moreover, in both cases, an elastic comparison straight line has been plotted, which refers to the parallel spring. Concerning relaxation, different starting points have been chosen, rendering different lines. All lines end before they reach the elastic comparison straight line. This is due to the fact that the damper needs an infinite amount of time to relax, being parallel to some spring. For the similar reason, in the case of creep, the elastic comparison straight line is not reached either.

Damaging behaviour is presented in Fig. 3.4. On the left hand side, some displacement controlled viscoelastic behaviour is plotted with and without damage. Damage is activated at approx. 15 kN, being visible by the decreasing character of the red curve. On the right hand side, some creep behaviour already shown in Fig. 3.3 is extended by damage. The elastic comparison straight line is now exceeded due to the damaging influence on the parallel spring.

3.4 Elastoplasticity with Damage

In what follows, a traction-separation-law is introduced, representing elastoplasticity with linear hardening, coupled with Lemaitre-type damage. Again, the constitutive response is decoupled with respect to the interfacial orthonormal system. For elastoplasticity in an interfacial context, see, e.g., Miehe and Schröder [118]. Concerning damage, an interfacial adaption is given in, e.g., Willam et al. [188], Jansson and Larsson [72] and Larsson and Jansson [88]. The continuum case of elastoplasticity coupled to damage is discussed in, e.g., Lemaitre [89]. Moreover, the typical textbooks of Simo and

Hughes [164], Lemaitre [90] and Lemaitre and Chaboche [91] are recommended.

3.4.1 Constitutive Modelling

For geometrically linear elastoplasticity a split of kinematic quantities is proceeded. Translated to the interface, this would be a split of the (overall) displacement jump $[\![\boldsymbol{u}]\!]$ into an elastic part $[\![\boldsymbol{u}]\!]^e$ and a plastic part $[\![\boldsymbol{u}]\!]^p$.

$$[\![\boldsymbol{u}]\!] = [\![\boldsymbol{u}]\!]^e + [\![\boldsymbol{u}]\!]^p \tag{3.61}$$

Tractions are given as

$$\boldsymbol{\tau} = \boldsymbol{\tau}([\![\boldsymbol{u}]\!]^e, \alpha_i^p, d_i), \quad i = s, t, n \tag{3.62}$$

dependent on the elastic part of the displacement jump, plastic parameters α_i^p and damage parameters d_i (see also section 3.3). The second law of thermodynamics is given by the Clausius-Duhem inequality, reading as

$$\mathcal{D} = \mathcal{D}_{loc} = \mathcal{W} - \dot{\Psi} \geq 0 \tag{3.63}$$

where the free energy of the interface occupies the dependencies

$$\Psi = \Psi([\![\boldsymbol{u}]\!]^e, \alpha_i^p, d_i) \tag{3.64}$$

and $\mathcal{W}$ denotes the traction power, reading as

$$\mathcal{W} = \boldsymbol{\tau} \cdot [\![\dot{\boldsymbol{u}}]\!] = \boldsymbol{\tau} \cdot [[\![\dot{\boldsymbol{u}}]\!]^e + [\![\dot{\boldsymbol{u}}]\!]^p] \tag{3.65}$$

Accordingly, the Clausius-Duhem inequality can be rewritten as

$$\left[\boldsymbol{\tau} - \frac{\partial \Psi}{\partial [\![\boldsymbol{u}]\!]^e}\right] \cdot [\![\dot{\boldsymbol{u}}]\!]^e + \boldsymbol{\tau} \cdot [\![\dot{\boldsymbol{u}}]\!]^p - \sum_i \left[\frac{\partial \Psi}{\partial \alpha_i^p}\, \dot{\alpha}_i^p + \frac{\partial \Psi}{\partial d_i}\, \dot{d}_i\right] \geq 0 \tag{3.66}$$

The Coleman-Noll entropy principle implies

$$\boldsymbol{\tau} = \frac{\partial \Psi}{\partial [\![\boldsymbol{u}]\!]^e} \tag{3.67}$$

The so-called interfacial internal stress or, respectively, hardening traction in $\boldsymbol{i}$-direction is defined as

$$R_i = -\frac{\partial \Psi}{\partial \alpha_i^p} \tag{3.68}$$

while the so-called damage driving force shall be given once more as

$$\bar{\mu}_i = -\frac{\partial \Psi}{\partial d_i} \tag{3.69}$$

With this in hand, the reduced dissipation inequality is written as

$$\mathcal{D}_{red} = \boldsymbol{\tau} \cdot \dot{[\![\boldsymbol{u}]\!]}^p + \sum_i \Big[R_i \, \dot{\alpha}_i^p + \bar{\mu}_i \, \dot{d}_i \Big] \geq 0 \tag{3.70}$$

The thermodynamic force shall be given by $\mathcal{S}_i^{if} = \{\boldsymbol{\tau}, R_i, \bar{\mu}_i\}$. Then, constitutive relations are introduced by means of the interfacial yield function, reading as

$$\Phi_i^p = \Phi_i^p(\mathcal{S}_i^{if}) \leq 0 \tag{3.71}$$

The interfacial yield function is negative in the elastic range and zero if plasticity evolves. The elastic range shall therefore be defined by the closure

$$\mathcal{E}_i^{if} := \{\mathcal{S}_i^{if} \mid \Phi_i^p(\mathcal{S}_i^{if}) \leq 0\} \tag{3.72}$$

The postulate of maximum dissipation, as proposed by e.g. Hill [65] and Lubliner [98], can be adapted to the interface, reading as

$$\mathcal{D}_{red}(\mathcal{S}_i^{if}) \geq \mathcal{D}_{red}(\mathcal{S}_i^{if,*}) \; \forall \; \mathcal{S}_i^{if,*} \; \in \; \mathcal{E}_i^{if} \tag{3.73}$$

By the related constraint maximisation problem, see Simo and Hughes [164], the interfacial associated evolution equations or, respectively, flow rules follow as

$$\dot{[\![\boldsymbol{u}_i]\!]}^p = \frac{\dot{\gamma}_i^p}{1 - d_i} \frac{\partial \Phi_i^p(\mathcal{S}_i^{if})}{\partial \bar{\boldsymbol{\tau}}}, \quad \sum_i [\![\boldsymbol{u}_i]\!]^p = [\![\boldsymbol{u}]\!]^p \quad \text{with} \quad i = s, t, n \tag{3.74}$$

$$\dot{\alpha}_i^p = \frac{\dot{\gamma}_i^p}{1 - d_i} \frac{\partial \Phi_i^p(\mathcal{S}_i^{if})}{\partial \bar{R}_i} \tag{3.75}$$

being decoupled in the interfacial orthonormal base system $\boldsymbol{i} \in \{\boldsymbol{s}, \boldsymbol{t}, \boldsymbol{n}\}$. The Lagrange multipliers are denoted as $\dot{\gamma}_i^p$. The related Kuhn-Tucker optimality conditions of loading and unloading are given as

$$\dot{\gamma}_i^p \geq 0, \quad \Phi_i^p(\mathcal{S}_i^{if}) \leq 0, \quad \dot{\gamma}_i^p \, \Phi_i^p(\mathcal{S}_i^{if}) = 0 \tag{3.76}$$

The postulate of maximum dissipation does generally not imply that dissipation is positive. Thermodynamical consistency will be shown later. A quadratic format of the free energy is introduced as

$$\begin{aligned} \Psi([\![\boldsymbol{u}]\!]^e, \alpha_i^p, d_i) &= \Psi^{eld}([\![\boldsymbol{u}]\!]^e, d_i) + \Psi^{epd}(\alpha_i^p, d_i) \\ &= \frac{1}{2} \, [\![\boldsymbol{u}]\!]^e \cdot \Big[\sum_i [1 - d_i] \, \boldsymbol{C}_i^{if,el} \Big] \cdot [\![\boldsymbol{u}]\!]^e + \frac{1}{2} \sum_i [1 - d_i] \, H_i^p \, \alpha_i^{p2} \end{aligned} \tag{3.77}$$

introducing the plastic hardening moduli in $\boldsymbol{i}$-direction, H_i^p. This renders the tractions and the hardening tractions as

$$\boldsymbol{\tau} = \sum_i [1 - d_i]\, \boldsymbol{C}_i^{if,el} \cdot \left[[\![\boldsymbol{u}]\!] - [\![\boldsymbol{u}]\!]^p \right] \tag{3.78}$$

$$R_i = -[1 - d_i]\, H_i^p\, \alpha_i^p \tag{3.79}$$

The so-called effective tractions and effective hardening tractions, given in the undamaged part of the interface, are given as

$$\bar{\boldsymbol{\tau}} = \boldsymbol{C}^{if,el} \cdot \left[[\![\boldsymbol{u}]\!] - [\![\boldsymbol{u}]\!]^p \right] \tag{3.80}$$

$$\bar{R}_i = -H_i^p\, \alpha_i^p \tag{3.81}$$

The formulations for the damage related quantities d_i, μ_i and $\bar{\mu}_i$, compare section 3.3, are introduced as

$$d_i = 1 - \exp(j_i[\mu_{i(0)} - \mu_i]) \tag{3.82}$$

Being accountable for the progression of damage in $\boldsymbol{i}$-direction, the variable μ_i is computed according to

$$\mu_i = \max\{\bar{\mu}_i([\![\boldsymbol{u}]\!]^e, \alpha_i^p), \mu_{i(0)}\} \tag{3.83}$$

The damage driving force is given by

$$\bar{\mu}_i \;=\; -\partial_{d_i} \Psi \;=\; \frac{1}{2} [\![\boldsymbol{u}]\!]^e \cdot \boldsymbol{C}_i^{if,el} \cdot [\![\boldsymbol{u}]\!]^e + \frac{1}{2} H_i^p\, {\alpha_i^p}^2 \tag{3.84}$$

Before going into detail concerning algorithmic aspects, the directionally decoupled interfacial yield functions are specified, mainly inspired by Miehe and Schröder [118]:

$$\Phi_i^p \;= \mid \bar{\boldsymbol{\tau}} \cdot \boldsymbol{i} \mid - [Y_{i(0)} - \bar{R}_i] \leq 0 \tag{3.85}$$

with $Y_{i(0)}$ denoting the interfacial yield tractions. Equation (3.85), together with equations (3.74) and (3.75), then renders

$$[\![\dot{\boldsymbol{u}}_i]\!]^p = \frac{\dot{\gamma}_i^p}{1 - d_i}\, \text{sign}(\bar{\boldsymbol{\tau}} \cdot \boldsymbol{i})\, \boldsymbol{i} \tag{3.86}$$

$$\dot{\alpha}_i^p = \frac{\dot{\gamma}_i^p}{1 - d_i} \tag{3.87}$$

In section 2.3, the continuum tangent modulus is given by the Prandtl-Reuss Tensor. Accordingly, for the interfacial material law as discussed here, an interfacial tangent modulus is defined via

$$\dot{\boldsymbol{\tau}} = \boldsymbol{C}^{if,epd} \cdot [\![\dot{\boldsymbol{u}}]\!] \tag{3.88}$$

It is found by developing the traction rate as

$$\dot{\boldsymbol{\tau}} = \sum_i \left[[1 - d_i]\, \boldsymbol{C}_i^{if,el} \cdot [[\![\dot{\boldsymbol{u}}_i]\!] - [\![\dot{\boldsymbol{u}}_i]\!]^p] - \dot{d}_i\, \bar{\boldsymbol{\tau}}_i \right] \tag{3.89}$$

If damage evolution is active, it holds

$$\dot{d}_i = \underbrace{j_i \, \exp(j_i[\mu_{i(0)} - \mu_i])}_{d_i'} \left[\bar{\boldsymbol{\tau}}_i \cdot [[\![\dot{\boldsymbol{u}}_i]\!] - [\![\dot{\boldsymbol{u}}_i]\!]^p] + H_i^p \alpha_i^p \dot{\alpha}_i^p\right] \tag{3.90}$$

In order to further develop equations (3.89) and (3.90), the rates of the plastic displacement jump and the plastic parameter have to be found. During plastic evolution, the rate of the yield function is given by

$$\dot{\Phi}_i^p = \partial_{\bar{\boldsymbol{T}}} \Phi_i^p \cdot \dot{\bar{\boldsymbol{\tau}}} + \partial_{\bar{R}_i} \Phi_i^p \, \dot{\bar{R}}_i = 0 \tag{3.91}$$

The rates of the effective traction and effective hardening traction are given as

$$\dot{\bar{\boldsymbol{\tau}}} = \sum_i \boldsymbol{C}_i^{if,el} \cdot [[\![\dot{\boldsymbol{u}}_i]\!] - [\![\dot{\boldsymbol{u}}_i]\!]^p] \tag{3.92}$$

$$\dot{\bar{R}}_i = -H_i^p \dot{\alpha}_i^p \tag{3.93}$$

Incorporating this as well as the results from equations (3.86) and (3.87) in equation (3.91) renders after some manipulations the Lagrange multipliers in $\boldsymbol{i}$-direction as

$$\dot{\gamma}_i^p = \frac{1 - d_i}{1 + H_i^p / c_i} \, \text{sign}(\bar{\tau}_i) \, [\![\dot{\boldsymbol{u}}_i]\!] \tag{3.94}$$

Therewith, the rates of the plastic displacement jump and the plastic parameter are rewritten and inserted into equations (3.90) and (3.89). Consequently, the interfacial tangent modulus is computed as

$$\boldsymbol{C}^{if,epd} = \sum_i \underbrace{\left[[1 - d_i] c_i \left[1 - \frac{1}{1 + H_i^p / c_i}\right] - d_i' \left[\bar{\tau}_i^2 \left[1 - \frac{1}{1 + H_i^p / c_i}\right] - \frac{\bar{R}_i \, |\bar{\tau}_i|}{1 + H_i^p / c_i}\right]\right]}_{\rho_i^{epd}} \boldsymbol{i} \otimes \boldsymbol{i} \tag{3.95}$$

Now, the reduced dissipation inequality is regarded once more in order to check thermodynamical consistency. Equations (3.70), (3.78) and (3.80) render

$$\begin{aligned} \mathcal{D}_{red} &= \boldsymbol{\tau} \cdot [\![\dot{\boldsymbol{u}}]\!]^p + \sum_i [R_i \, \dot{\alpha}_i^p + \bar{\mu}_i \, \dot{d}_i] \\ &= \sum_i [[1 - d_i] \, \bar{\boldsymbol{\tau}}_i \cdot [\![\dot{\boldsymbol{u}}]\!]_i^p + R_i \, \dot{\alpha}_i^p + \bar{\mu}_i \, \dot{d}_i] \\ &= \sum_i [|\bar{\tau}_i| \dot{\gamma}_i^p + R_i \frac{\dot{\gamma}_i^p}{1 - d_i} + \bar{\mu}_i \dot{d}_i] \end{aligned} \tag{3.96}$$

By incorporating the yield function (3.85) and the Kuhn-Tucker optimality conditions (3.76), equation (3.96) is rewritten as

$$\mathcal{D}_{red} = \sum_i [\underbrace{\Phi_i^p \, \dot{\gamma}_i^p}_{=0} + \underbrace{Y_{i(0)} \, \dot{\gamma}_i^p}_{\geq 0} + \underbrace{\bar{\mu}_i \dot{d}_i}_{\geq 0}] \geq 0 \tag{3.97}$$

Accordingly, the dissipation inequality is fulfilled and thermodynamical consistency is given.

3.4.2 Algorithmic Aspects

Again, a staggered algorithm is used to compute plastic and damage-related quantities. First, the plastic update is proceeded. Accordingly, the damage parameter is assumed to be fixed, given from the previous computation step. For a discrete time step $\Delta t = t_{n+1} - t_n > 0$ the implicit Euler backward method is applied to the rate of the plastic displacement jump:

$$[\![\boldsymbol{u}]\!]^p_{n+1} = [\![\boldsymbol{u}]\!]^p_n + \Delta t \sum_i [\![\dot{u}_i]\!]^p_{n+1}\, \boldsymbol{i} = [\![\boldsymbol{u}]\!]^p_n + \sum_i \frac{\Delta\gamma^p_{i(n+1)}}{1-d_{i(n)}} \text{sign}(\bar{\tau}_{i(n+1)})\, \boldsymbol{i} \tag{3.98}$$

The effective tractions can, accordingly, be written as

$$\bar{\boldsymbol{\tau}}_{n+1} = \sum_i \Big[\underbrace{\boldsymbol{C}^{if,el}_i \cdot \big[[\![\boldsymbol{u}]\!]_{n+1} - [\![\boldsymbol{u}]\!]^p_n\big]}_{\bar{\boldsymbol{\tau}}_{i,trial}} - c_i \frac{\Delta\gamma^p_{i(n+1)}}{1-d_{i(n)}} \text{sign}(\bar{\tau}_{i(n+1)})\, \boldsymbol{i} \Big] \tag{3.99}$$

The effective traction in $\boldsymbol{i}$-direction is then given as

$$\bar{\boldsymbol{\tau}}_{i(n+1)} = \bar{\boldsymbol{\tau}}_{i,trial} - c_i \frac{\Delta\gamma^p_{i(n+1)}}{1-d_{i(n)}} \text{sign}(\bar{\tau}_{i(n+1)})\, \boldsymbol{i} \tag{3.100}$$

from which we conclude

$$\boldsymbol{i} = \boldsymbol{i}_{trial}, \quad \bar{\tau}_{i(n+1)} + c_i \frac{\Delta\gamma^p_{i(n+1)}}{1-d_{i(n)}} \text{sign}(\bar{\tau}_{i(n+1)}) = \bar{\tau}_{i,trial} \tag{3.101}$$

Equation $(3.101)_2$ is equivalent to

$$\frac{\bar{\tau}_{i,trial}}{|\bar{\tau}_{i,trial}|}\, |\bar{\tau}_{i,trial}| = \frac{\bar{\tau}_{i(n+1)}}{|\bar{\tau}_{i(n+1)}|}\, |\bar{\tau}_{i(n+1)}| + c_i \frac{\Delta\gamma^p_{i(n+1)}}{1-d_{i(n)}} \frac{\bar{\tau}_{i(n+1)}}{|\bar{\tau}_{i(n+1)}|} \tag{3.102}$$

Based on this relation, together with $c_i \geq 0$ and $\Delta\gamma^p_{i(n+1)} \geq 0$, we obtain after some transformation

$$|\bar{\tau}_{i(n+1)}| = |\bar{\tau}_{i,trial}| - c_i \frac{\Delta\gamma^p_{i(n+1)}}{1-d_{i(n)}} \quad \text{and} \quad \text{sign}(\bar{\tau}_{i(n+1)}) = \text{sign}(\bar{\tau}_{i,trial}) \tag{3.103}$$

During plastic evolution it is essential to satisfy the yield condition

$$\Phi^p_{i(n+1)} = |\bar{\tau}_{i(n+1)}| - [Y_{i(0)} - \bar{R}_{i(n+1)}] = 0 \tag{3.104}$$

Furthermore, the Euler backward method results in

$$\bar{R}_{i(n+1)} = \bar{R}_{i,trial} - H_i^p \frac{\Delta\gamma^p_{i(n+1)}}{1-d_{i(n)}}, \quad \bar{R}_{i,trial} = -H_i^p\, \alpha^p_{i(n)} \tag{3.105}$$

and

$$\alpha^p_{i(n+1)} = \alpha^p_{i(n)} + \frac{\Delta\gamma^p_{i(n+1)}}{1-d_{i(n)}} \tag{3.106}$$

Equations (3.103), (3.104) and (3.105) render the explicit update for the Lagrange multiplier.

$$\Delta\gamma^p_{i(n+1)} = \frac{\Phi^p_{i,trial}\,[1-d_{i(n)}]}{c_i + H_i^p} \quad \text{with} \quad \Phi^p_{i,trial} = |\bar{\tau}_{i,trial}| - [Y_{i(0)} - \bar{R}_{i,trial}] \tag{3.107}$$

Of course, only if $\Phi^p_{i,trial} > 0$, plasticity evolves. If $\Phi^p_{i,trial} \leq 0$, all plastic quantities remain unchanged. This is taken into account by introducing

$$\zeta_i^{ep} = \begin{cases} 0 & \text{if} \quad \Phi^p_{i,trial} \leq 0 \\ 1 & \text{if} \quad \Phi^p_{i,trial} > 0 \end{cases} \tag{3.108}$$

and setting

$$\Delta\gamma^p_{i(n+1)} = \zeta_i^{ep} \frac{\Phi^p_{i,trial}\,[1-d_{i(n)}]}{c_i + H_i^p} \tag{3.109}$$

Combining equations (3.100), (3.101), (3.103) and $(3.107)_1$, we end up with

$$\bar{\boldsymbol{\tau}}_{i(n+1)} = \bar{\boldsymbol{\tau}}_{i,trial} - \zeta_i^{ep} \frac{\Phi^p_{i,trial}}{1 + H_i^p/c_i}\, \text{sign}(\bar{\tau}_{i,trial})\, \boldsymbol{i} \tag{3.110}$$

The effective traction vector update $\bar{\boldsymbol{\tau}}_{n+1}$ is then given by assembling terms of all directions as well as the nominal traction vector update $\boldsymbol{\tau}_{n+1}$.

$$\bar{\boldsymbol{\tau}}_{n+1} = \sum_i \bar{\boldsymbol{\tau}}_{i(n+1)}, \quad \boldsymbol{\tau}_{n+1} = \sum_i [1-d_{i(n)}] \bar{\boldsymbol{\tau}}_{i(n+1)} \tag{3.111}$$

Concerning the damage quantities, the update is now consequently computed by incorporating the current plastic or, respectively, elastic displacement jump $[\![\boldsymbol{u}]\!]^e_{n+1} = [\![\boldsymbol{u}]\!]_{n+1} - [\![\boldsymbol{u}]\!]^p_{n+1}$, yielding

$$d_{i(n+1)} = 1 - \exp(j_i[\mu_{i(0)} - \mu_{i(n+1)}]) \tag{3.112}$$

with

$$\mu_{i(n+1)} = \max\{\bar{\mu}_{i(n+1)}([\![\boldsymbol{u}]\!]^e_{n+1}, \alpha^p_{i(n+1)}), \mu_{i(n)}, \mu_{i(0)}\} \tag{3.113}$$

and

$$\bar{\mu}_{i(n+1)} = -\partial_{d_i} \Psi_{n+1} = \frac{1}{2} [\![\boldsymbol{u}]\!]^e_{n+1} \cdot \boldsymbol{C}_i^{if,el} \cdot [\![\boldsymbol{u}]\!]^e_{n+1} + \frac{1}{2} H_i^p\, {\alpha^p_{i(n+1)}}^2 \tag{3.114}$$

given:	$[\![\boldsymbol{u}]\!]_{n+1},\ [\![\boldsymbol{u}]\!]^p_n,\ \alpha^p_{i(n)},\ d_{i(n)}$
1. trial value:	compute $\|\bar{\tau}_{i,trial}\| \ \Rightarrow\ \Phi^p_{i,trial}$
2. check yield function:	$\zeta^{ep}_i = \begin{cases} 0 & \text{if} \quad \Phi^p_{i,trial} \leq 0 \\ 1 & \text{if} \quad \Phi^p_{i,trial} > 0 \end{cases}$
3. traction update:	$\Delta\gamma^p_{i(n+1)} = \zeta^{ep}_i \dfrac{\Phi^p_{i,trial}[1-d_{i(n)}]}{c_i + H^p_i} \ \Rightarrow\ [\![\boldsymbol{u}]\!]^p_{n+1},\ \alpha^p_{i(n+1)}$
4. tangent modulus:	$\boldsymbol{C}^{if,epd}_{alg}$
5. damage update:	compute $\bar{\mu}_{i(n+1)} \ \Rightarrow\ d_{i(n+1)}$

Table 3.2: Algorithmic procedure for interfacial elastoplasticity with damage

When solving the obtained set of nonlinear equations with a classical Newton scheme, the so-called algorithmic tangent

$$\boldsymbol{C}^{if,epd}_{alg} = \frac{\partial \boldsymbol{\tau}_{n+1}}{\partial [\![\boldsymbol{u}]\!]_{n+1}} \tag{3.115}$$

is required to compute the global tangent matrix of the finite element code. Using equations (3.78) in the given algorithmic context together with (3.115) gives

$$\frac{\partial \boldsymbol{\tau}_{n+1}}{\partial [\![\boldsymbol{u}]\!]_{n+1}} = \sum_i [1-d_{i(n)}] \boldsymbol{C}^{if,el}_i \cdot \left[\boldsymbol{I} - \frac{\partial [\![\boldsymbol{u}]\!]^p_{n+1}}{\partial [\![\boldsymbol{u}]\!]_{n+1}} \right] \tag{3.116}$$

To further develop equation (3.116), we observe from equation (3.98)

$$\frac{\partial [\![\boldsymbol{u}]\!]^p_{n+1}}{\partial [\![\boldsymbol{u}]\!]_{n+1}} = \sum_i \left[\Delta\gamma^p_{i(n+1)} \frac{\partial [\text{sign}(\bar{\tau}_{i(n+1)})\, \boldsymbol{i}]}{\partial [\![\boldsymbol{u}]\!]_{n+1}} + [\text{sign}(\bar{\tau}_{i(n+1)})\, \boldsymbol{i}] \otimes \frac{\partial \Delta\gamma^p_{i(n+1)}}{\partial [\![\boldsymbol{u}]\!]_{n+1}} \right] [1-d_{i(n)}]^{-1} \tag{3.117}$$

Combining equations (3.101), (3.103) and (3.117) renders

$$\begin{aligned}
\frac{\partial \Delta\gamma^{p}_{i(n+1)}}{\partial [\![\boldsymbol{u}]\!]_{n+1}} &= \zeta_i^{ep}\,[1-d_{i(n)}]\,\frac{\partial\big[|\bar{\tau}_{i,trial}|/[c_i+H_i^p]\big]}{\partial [\![\boldsymbol{u}]\!]_{n+1}} \\
&= \zeta_i^{ep}\,[1-d_{i(n)}]\,\frac{\partial\big[\,|\,\big[\boldsymbol{C}^{if,el}\cdot[[\![\boldsymbol{u}]\!]_{n+1}-[\![\boldsymbol{u}]\!]_n^p]\big]\cdot\boldsymbol{i}\,|\,/[c_i+H_i^p]\big]}{\partial [\![\boldsymbol{u}]\!]_{n+1}} \\
&= \zeta_i^{ep}\,[1-d_{i(n)}]\,\frac{\text{sign}(\bar{\tau}_{i,trial})}{1+H_i^p/c_i}\,\boldsymbol{i}
\end{aligned} \tag{3.118}$$

where ζ_i^{ep} has been evaluated at the beginning of the algorithmic procedure. Furthermore, it holds

$$\frac{\partial[\text{sign}(\bar{\tau}_{i,trial})\,\boldsymbol{i}]}{\partial [\![\boldsymbol{u}]\!]_{n+1}} = \frac{\partial[\bar{\boldsymbol{\tau}}_{i,trial}/\|\bar{\boldsymbol{\tau}}_{i,trial}\|]}{\partial [\![\boldsymbol{u}]\!]_{n+1}} = \frac{\partial\,\boldsymbol{i}}{\partial [\![\boldsymbol{u}]\!]_{n+1}} = \boldsymbol{0} \tag{3.119}$$

Considering equations (3.118), (3.119) and (3.117) then gives

$$\frac{\partial [\![\boldsymbol{u}]\!]^p_{n+1}}{\partial [\![\boldsymbol{u}]\!]_{n+1}} = \sum_i \frac{\zeta_i^{ep}}{1+H_i^p/c_i}\,\boldsymbol{i}\otimes\boldsymbol{i} \tag{3.120}$$

Reinserting these results finally renders

$$\boldsymbol{C}^{if,epd}_{alg} = \sum_i [1-d_{i(n)}]\left[1-\frac{\zeta_i^{ep}}{1+H_i^p/c_i}\right]\boldsymbol{C}_i^{if,el} \tag{3.121}$$

The algorithmic procedure is once more reflected by Tab. 3.2.

3.4.3 Prototype Example

Now, a prototype example is presented which demonstrates the functionality of the elastoplastic damage law discussed above. The plot has been created by a finite element simulation of a single lap tensile specimen, with linear elasticity for the bulk and elastoplasticity with damage for the interfacial zone. In Fig. 3.5 the plastic behaviour begins at approx. 6300 N whereas damaging occurs at 7000 N. Obviously, the damage law induces some softening behaviour, which is also observed in the unloading behaviour.

3.5 Viscoplasticity with Damage

In this section the material model of interfacial viscoplasticity with Lemaitre-Type damage is discussed. This constitutive relation reflects rate-dependent interfacial material behaviour with equilibrium hysteresis. In our case the ansatz of Perzyna, see, e.g., Perzyna [142], Perzyna and Wojno [143] and Chaboche [34] is applied. In this context a yield surface separates an elastic and a viscoplastic domain. The framework of this theory includes classical plasticity as a special case. An adequate one-dimensional model is depicted in Fig. 3.6. Other approaches of viscoplasticity are given by an

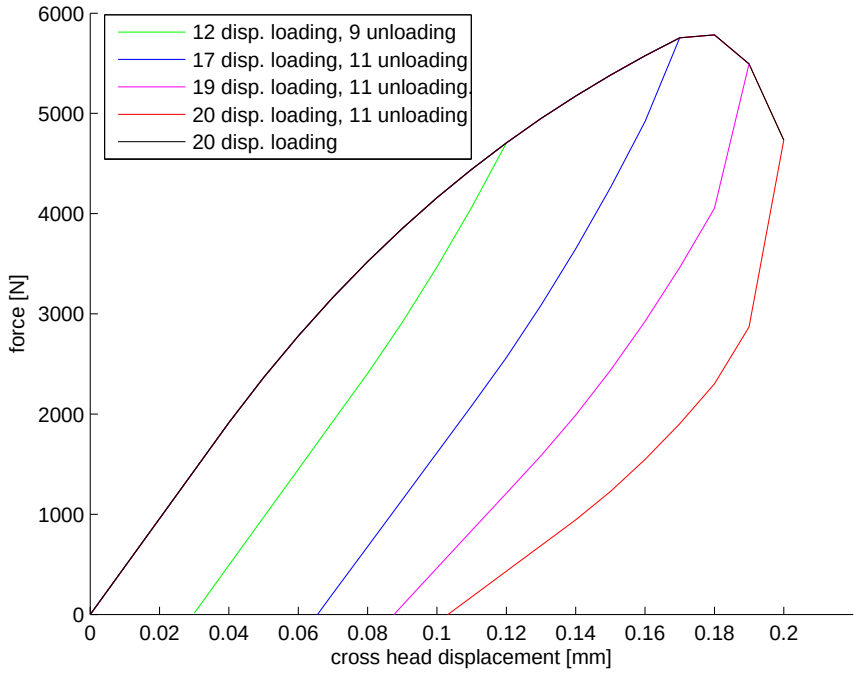

Figure 3.5: One-dimensional exemplary force-displacement plots of elastoplasticity with damage

abandonment of yield criteria and an uniform formulation of the viscoplastic evolution, see, e.g., Hart [63] and Miller [119], and a split of stresses into an rate-independent and a rate-dependent viscoplastic part as proposed by, e.g., Krempl [83] and Krempl and Bordonaro [84].

For some more recent achievements in the field of viscoplasticity see, e.g., Ortiz and Stainier [133] and Espinosa et al. [52].

3.5.1 Constitutive Modelling

Again, a split of the overall displacement jump into an elastic and a plastic part is carried out.

$$[\![\boldsymbol{u}]\!] = [\![\boldsymbol{u}]\!]^e + [\![\boldsymbol{u}]\!]^{vp} \tag{3.122}$$

The traction vector is given as

$$\boldsymbol{\tau} = \boldsymbol{\tau}([\![\boldsymbol{u}]\!]^e, \alpha_i^{vp}, d_i), \quad i = s, t, n \tag{3.123}$$

It depends on the elastic part of the displacement jump, some viscoplastic parameters α_i^{vp} and some damage parameters d_i. The Clausius-Duhem inequality reads as

$$\mathcal{D} = \mathcal{D}_{loc} = \mathcal{W} - \dot{\Psi} \geq 0 \tag{3.124}$$

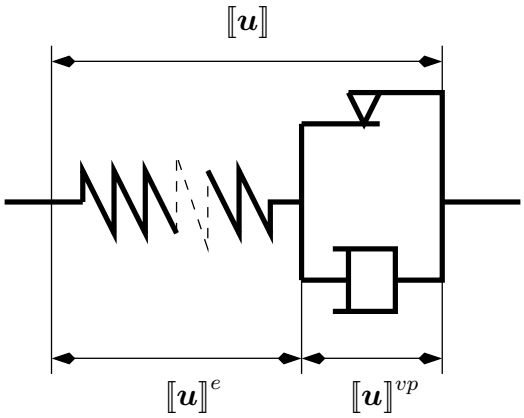

Figure 3.6: One-dimensional model of viscoplasticity

with the free energy of the interface, reading as

$$\Psi = \Psi([\![\boldsymbol{u}]\!]^e, \alpha_i^{vp}, d_i) \tag{3.125}$$

The traction power is denoted by

$$\mathcal{W} = \boldsymbol{\tau} \cdot \dot{[\![\boldsymbol{u}]\!]} = \boldsymbol{\tau} \cdot [\dot{[\![\boldsymbol{u}]\!]}^e + \dot{[\![\boldsymbol{u}]\!]}^{vp}] \tag{3.126}$$

The Clausius-Duhem inequality can then be reformulated as

$$\Big[\boldsymbol{\tau} - \frac{\partial \Psi}{\partial [\![\boldsymbol{u}]\!]^e}\Big] \cdot \dot{[\![\boldsymbol{u}]\!]}^e + \boldsymbol{\tau} \cdot \dot{[\![\boldsymbol{u}]\!]}^{vp} - \sum_i \Big[\frac{\partial \Psi}{\partial \alpha_i^{vp}}\, \dot{\alpha}_i^{vp} + \frac{\partial \Psi}{\partial d_i}\, \dot{d}_i\Big] \geq 0 \tag{3.127}$$

By taking the Coleman-Noll Entropy Principle into account, it is essential that

$$\boldsymbol{\tau} = \frac{\partial \Psi}{\partial [\![\boldsymbol{u}]\!]^e} \tag{3.128}$$

The hardening traction in $\boldsymbol{i}$-direction reads

$$R_i = -\frac{\partial \Psi}{\partial \alpha_i^{vp}} \tag{3.129}$$

The damage driving force, compare previous chapters, is given as

$$\bar{\mu}_i = -\frac{\partial \Psi}{\partial d_i} \tag{3.130}$$

Consequently, the reduced dissipation inequality is formulated as

$$\mathcal{D}_{red} = \boldsymbol{\tau} \cdot \left[\!\left[\dot{\boldsymbol{u}} \right]\!\right]^{vp} + \sum_i \left[R_i \, \dot{\alpha}_i^{vp} + \bar{\mu}_i \, \dot{d}_i \right] \geq 0 \tag{3.131}$$

With the thermodynamic force being given as $\mathcal{S}_i^{if} = \{\boldsymbol{\tau}, R_i, \bar{\mu}_i\}$, the interfacial viscoplastic yield function is introduced as

$$\Phi_i^{vp} = \Phi_i^{vp}(\mathcal{S}_i^{if}) \tag{3.132}$$

Please note that, compared to elastoplasticity with damage, this yield function shall not be restricted to negative or zero values. Nevertheless, some elastic range can be defined by the closure

$$\mathcal{E}_i^{if} := \{\mathcal{S}_i^{if} \mid \Phi_i^{vp}(\mathcal{S}_i^{if}) \leq 0\} \tag{3.133}$$

In the case of inelasticity some plastic threshold is overcome, and the so-called effective excess traction in $\boldsymbol{i}$-direction for the undamaged interfacial material fraction is given as

$$\bar{\tau}_i^{ex} = \left\{ \begin{array}{lllll} \bar{\tau}_i - [Y_{i(0)} - \bar{R}_i] & \text{if} & \bar{\tau}_i & \geq & Y_{i(0)} - \bar{R}_i \\ \bar{\tau}_i + [Y_{i(0)} - \bar{R}_i] & \text{if} & \bar{\tau}_i & < & -[Y_{i(0)} - \bar{R}_i] \end{array} \right\} = [|\bar{\tau}_i| - [Y_{i(0)} - \bar{R}_i]] \, \text{sign}(\bar{\tau}_i) \tag{3.134}$$

Motivated by equation (3.134), the viscoplastic yield function is then defined as

$$\Phi_i^{vp}(\bar{\tau}_i) = |\bar{\tau}_i| - [Y_{i(0)} - \bar{R}_i] \tag{3.135}$$

Incorporating the viscosity in $\boldsymbol{i}$-direction, an adequate constitutive relation concerning the rate of the viscoplastic displacement jump reads as

$$\left[\!\left[\dot{u}_i \right]\!\right]^{vp} = \frac{\bar{\tau}_i^{ex}}{\eta_i \, [1 - d_i]} \tag{3.136}$$

As already mentioned in the introduction, the ansatz of Perzyna, see, e.g., Perzyna [142], Perzyna and Wojno [143] and Chaboche [34] is applied. In this context, a yield function of the format as introduced in equations (3.134) and (3.135) enters equation (3.136) in the form

$$\left[\!\left[\dot{u}_i \right]\!\right]^{vp} = \frac{1}{\eta_i \, [1 - d_i]} \, \Phi_i^{vp}(\bar{\tau}_i) \, \text{sign}(\bar{\tau}_i) = \frac{1}{\eta_i \, [1 - d_i]} \, \Phi_i^{vp}(\bar{\tau}_i) \, \frac{\partial \Phi_i^{vp}}{\partial \bar{\tau}_i} \quad \text{if} \quad \Phi_i^{vp} > 0 \tag{3.137}$$

being equivalent to

$$\left[\!\left[\dot{u}_i \right]\!\right]^{vp} = \frac{\langle \Phi_i^{vp}(\bar{\tau}_i) \rangle}{\eta_i \, [1 - d_i]} \, \frac{\partial \Phi_i^{vp}}{\partial \bar{\tau}_i} = \frac{\dot{\gamma}_i^{vp}}{1 - d_i} \, \frac{\partial \Phi_i^{vp}}{\partial \bar{\tau}_i} = \frac{\dot{\gamma}_i^{vp}}{1 - d_i} \, \text{sign}(\bar{\tau}_i) \tag{3.138}$$

denoting the evolution equation for the rate of the viscoplastic displacement jump and introducing the penalty parameter $\dot{\gamma}_i^{vp}$. Accordingly, the rate of the viscoplastic parameter can be expressed by

$$\dot{\alpha}_i^{vp} = \frac{\langle \Phi_i^{vp}(\bar{\tau}_i) \rangle}{\eta_i \, [1 - d_i]} \, \frac{\partial \Phi_i^{vp}}{\partial \bar{R}_i} = \frac{\dot{\gamma}_i^{vp}}{1 - d_i} \tag{3.139}$$

Please note that for viscoplasticity the Kuhn-Tucker optimality conditions of plasticity are not legal. Nevertheless, some conditions with respect to the penalty parameter and the yield function can be defined:

$$\dot{\gamma}_i^{vp} \geq 0, \quad \dot{\gamma}_i^{vp}\, \Phi_i^{vp}(\mathcal{S}_i^{if}) \geq 0 \tag{3.140}$$

In view of the rate of the effective tractions, it has to be fulfilled

$$\dot{\bar{\tau}}_i = c_i \left[[\![\dot{\boldsymbol{u}}_i]\!] - [\![\dot{\boldsymbol{u}}_i]\!]^{vp} \right] = c_i \left[[\![\dot{\boldsymbol{u}}_i]\!] - \frac{\dot{\gamma}_i^{vp}}{1-d_i} \frac{\partial \Phi_i^{vp}}{\partial \bar{\tau}_i} \right] \tag{3.141}$$

The free energy is introduced by a quadratic format, reading as

$$\begin{aligned} \Psi([\![\boldsymbol{u}]\!]^e, \alpha_i^{vp}, d_i) &= \Psi^{eld}([\![\boldsymbol{u}]\!]^e, d_i) + \Psi^{vpd}(\alpha_i^{vp}, d_i) \\ &= \frac{1}{2}\, [\![\boldsymbol{u}]\!]^e \cdot \Big[\sum_i [1-d_i]\, \boldsymbol{C}_i^{if,el} \Big] \cdot [\![\boldsymbol{u}]\!]^e \\ &+ \frac{1}{2} \sum_i [1-d_i] H_i^{vp}\, \alpha_i^{vp\,2} \end{aligned} \tag{3.142}$$

introducing the viscoplastic hardening moduli in $\boldsymbol{i}$-direction, H_i^{vp}. Hence, tractions and hardening tractions follow as

$$\boldsymbol{\tau} = \sum_i [1-d_i]\, \boldsymbol{C}_i^{if,el} \cdot \left[[\![\boldsymbol{u}]\!] - [\![\boldsymbol{u}]\!]^{vp} \right] \tag{3.143}$$

$$R_i = -[1-d_i]\, H_i^{vp}\, \alpha_i^{vp} \tag{3.144}$$

Effective tractions and hardening tractions, which are present in the undamaged fraction of the interface material, are given as

$$\bar{\boldsymbol{\tau}} = \boldsymbol{C}^{if,el} \cdot \left[[\![\boldsymbol{u}]\!] - [\![\boldsymbol{u}]\!]^{vp} \right] \tag{3.145}$$

$$\bar{R}_i = -H_i^{vp}\, \alpha_i^{vp} \tag{3.146}$$

Concerning the quantities d_i, μ_i, $\bar{\mu}_i$ related to Lemaitre-type damage, expressions from section 3.4.1 can be adopted for viscoplastic quantities, see equations (3.82), (3.83) and (3.84). For computational treatment algorithmic expressions are derived in the next section, being closely related to the algorithmic aspects concerning elastoplasticity with damage as reviewed in section 3.4.2. Now, the reduced dissipation inequality is investigated for thermodynamical consistency. Following the investigations of section 3.4.1, it is found

$$\mathcal{D}_{red} = \sum_i [\underbrace{\Phi_i^{vp}\, \dot{\gamma}_i^{vp}}_{\geq 0} + \underbrace{Y_{i(0)}\, \dot{\gamma}_i^{vp}}_{\geq 0} + \underbrace{\bar{\mu}_i \dot{d}_i}_{\geq 0}] \geq 0 \tag{3.147}$$

Consequently, the dissipation inequality is fulfilled and the traction-separation-law is thermodynamically consistent.

3.5.2 Algorithmic Aspects

To get an update for the viscoplastic displacement jump, the implicit Euler backward method is once more applied:

$$[\![\boldsymbol{u}]\!]^{vp}_{n+1} = [\![\boldsymbol{u}]\!]^{vp}_{n} + \Delta t \sum_i \dot{[\![u_i]\!]}^{vp}_{n+1}\, \boldsymbol{i} = [\![\boldsymbol{u}]\!]^{vp}_{n} + \sum_i \frac{\Delta\gamma^{vp}_{i(n+1)}}{1-d_{i(n)}} \text{sign}(\bar{\tau}_{i(n+1)})\, \boldsymbol{i} \tag{3.148}$$

Effective tractions are then rewritten as

$$\bar{\boldsymbol{\tau}}_{n+1} = \sum_i \Big[\underbrace{\boldsymbol{C}^{if,el}_i \cdot \big[[\![\boldsymbol{u}]\!]_{n+1} - [\![\boldsymbol{u}]\!]^{vp}_{n}\big]}_{\bar{\boldsymbol{\tau}}_{i,trial}} - c_i \frac{\Delta\gamma^{vp}_{i(n+1)}}{1-d_{i(n)}} \text{sign}(\bar{\tau}_{i(n+1)})\, \boldsymbol{i} \Big] \tag{3.149}$$

In analogy to equations (3.100), (3.101) and (3.102) it holds

$$|\bar{\tau}_{i(n+1)}| = |\bar{\tau}_{i,trial}| - c_i \frac{\Delta\gamma^{vp}_{i(n+1)}}{1-d_{i(n)}} \quad \text{and} \quad \text{sign}(\bar{\tau}_{i(n+1)}) = \text{sign}(\bar{\tau}_{i,trial}) \tag{3.150}$$

The viscoplastic yield function is given as

$$\Phi^{vp}_{i(n+1)} = |\bar{\tau}_{i(n+1)}| - [Y_{i(0)} - \bar{R}_{i(n+1)}] \tag{3.151}$$

Concerning the hardening tractions the Euler backward method renders

$$\bar{R}_{i(n+1)} = \bar{R}_{i,trial} - H^{vp}_i \frac{\Delta\gamma^{vp}_{i(n+1)}}{1-d_{i(n)}}, \quad \bar{R}_{i,trial} = -H^{vp}_i\, \alpha^{vp}_{i(n)} \tag{3.152}$$

Accordingly, equation (3.151) is rewritten as

$$\begin{aligned} \Phi^{vp}_{i(n+1)} &= |\bar{\tau}_{i(n+1)}| - Y_{i(0)} + \bar{R}_{i,trial} - H^{vp}_i \frac{\Delta\gamma^{vp}_{i(n+1)}}{1-d_{i(n)}} \\ &= |\bar{\tau}_{i,trial}| - c_i \frac{\Delta\gamma^{vp}_{i(n+1)}}{1-d_{i(n)}} - Y_{i(0)} + \bar{R}_{i,trial} - H^{vp}_i \frac{\Delta\gamma^{vp}_{i(n+1)}}{1-d_{i(n)}} \\ &= \Phi^{vp}_{i,trial} - [c_i + H^{vp}_i] \frac{\Delta\gamma^{vp}_{i(n+1)}}{1-d_{i(n)}} \end{aligned} \tag{3.153}$$

with

$$\Phi^{vp}_{i,trial} = |\bar{\tau}_{i,trial}| - [Y_{i(0)} - \bar{R}_{i,trial}] \tag{3.154}$$

The time-discrete update of the viscoplastic penalty parameter is defined as

$$\Delta\gamma^{vp}_{i(n+1)} = \Delta t \frac{\Phi^{vp}_{i(n+1)}}{\eta_i} \tag{3.155}$$

where Δt denotes the time increment. Combining equations (3.153) and (3.155) yields

$$\frac{\Delta t}{\eta_i}\Big[\Phi^{vp}_{i,trial} - [c_i + H_i^{vp}]\,\frac{\Delta\gamma^{vp}_{i(n+1)}}{1-d_{i(n)}}\Big] - \Delta\gamma^{vp}_{i(n+1)} = 0 \tag{3.156}$$

This is further transformed into

$$\Delta\gamma^{vp}_{i(n+1)} = \frac{\Phi^{vp}_{i,trial}}{[c_i + H_i^{vp}]/[1-d_{i(n)}] + \eta_i/\Delta t} \tag{3.157}$$

giving the update of the viscoplastic penalty parameter. Certainly, this is only valid during viscoplastic evolution. If $\Phi^{vp}_{i,trial} \leq 0$, all plastic quantities remain unchanged, which has been expressed by Macaulay-brackets in section 3.5.1. Now, this is algorithmically taken into account by introducing

$$\zeta_i^{vp} = \begin{cases} 0 & \text{if} \quad \Phi^{vp}_{i,trial} \leq 0 \\ 1 & \text{if} \quad \Phi^{vp}_{i,trial} > 0 \end{cases} \tag{3.158}$$

The viscoplastic penalty parameter is then rewritten as

$$\Delta\gamma^{vp}_{i(n+1)} = \zeta_i^{vp}\,\frac{\Phi^{vp}_{i,trial}}{[c_i + H_i^{vp}]/[1-d_{i(n)}] + \eta_i/\Delta t} \tag{3.159}$$

Considering equations (3.100), (3.150) and (3.159) results in

$$\bar{\boldsymbol{\tau}}_{i(n+1)} = \bar{\boldsymbol{\tau}}_{i,trial} - \zeta_i^{vp}\,\frac{\Phi^{vp}_{i,trial}}{1 + H_i^{vp}/c_i + \eta_i\,[1-d_{i(n)}]/[c_i\,\Delta t]}\,\text{sign}(\bar{\tau}_{i,trial})\,\boldsymbol{i} \tag{3.160}$$

Assembling terms of all directions the effective traction vector update $\bar{\boldsymbol{\tau}}_{n+1}$ and the nominal traction vector update $\boldsymbol{\tau}_{n+1}$ read as

$$\bar{\boldsymbol{\tau}}_{n+1} = \sum_i \bar{\boldsymbol{\tau}}_{i(n+1)}, \quad \boldsymbol{\tau}_{n+1} = \sum_i [1-d_{i(n)}]\bar{\boldsymbol{\tau}}_{i(n+1)} \tag{3.161}$$

Now, the direct damage update is computed, in analogy to equations (3.112), (3.113) and (3.114), yielding

$$d_{i(n+1)} = 1 - \exp(j_i[\mu_{i(0)} - \mu_{i(n+1)}]) \tag{3.162}$$

with

$$\mu_{i(n+1)} = \max\{\bar{\mu}_{i(n+1)}(\llbracket\boldsymbol{u}\rrbracket^e_{n+1}, \alpha^{vp}_{i(n+1)}), \mu_{i(n)}, \mu_{i(0)}\} \tag{3.163}$$

and

$$\bar{\mu}_{i(n+1)} \;=\; -\partial_{d_i}\Psi_{n+1} \;=\; \frac{1}{2}\llbracket\boldsymbol{u}\rrbracket^e_{n+1}\cdot\boldsymbol{C}_i^{if,el}\cdot\llbracket\boldsymbol{u}\rrbracket^e_{n+1} + \frac{1}{2}H_i^{vp}\,{\alpha^{vp}_{i(n+1)}}^2 \tag{3.164}$$

given:	$[\![\boldsymbol{u}]\!]_{n+1},\ [\![\boldsymbol{u}]\!]_n^{vp},\ \alpha_{i(n)}^{vp},\ d_{i(n)}$
1. trial value:	compute $\|\bar{\tau}_{i,trial}\| \ \Rightarrow\ \Phi_{i,trial}^{vp}$
2. check yield function:	$\zeta_i^{vp} = \begin{cases} 0 & \text{if} \quad \Phi_{i,trial}^{vp} \leq 0 \\ 1 & \text{if} \quad \Phi_{i,trial}^{vp} > 0 \end{cases}$
3. traction update:	$\Delta\gamma_{i(n+1)}^{vp} = \zeta_i^{vp} \dfrac{\Phi_{i,trial}^{vp}}{[c_i + H_i^{vp}]/[1 - d_{i(n)}] + \eta_i/\Delta t} \ \Rightarrow\ [\![\boldsymbol{u}]\!]_{n+1}^{vp},\ \alpha_{i(n+1)}^{vp}$
4. tangent modulus:	$\boldsymbol{C}_{alg}^{if,vpd}$
5. damage update:	compute $\bar{\mu}_{i(n+1)} \ \Rightarrow\ d_{i(n+1)}$

Table 3.3: Algorithmic procedure for interfacial viscoplasticity with damage

where the elastic displacement jump $[\![\boldsymbol{u}]\!]_{n+1}^e = [\![\boldsymbol{u}]\!]_{n+1} - [\![\boldsymbol{u}]\!]_{n+1}^{vp}$ has been incorporated. Next, the algorithmic tangent modulus is computed. It is given by

$$\boldsymbol{C}_{alg}^{if,vpd} = \frac{\partial \boldsymbol{\tau}_{n+1}}{\partial [\![\boldsymbol{u}]\!]_{n+1}} \tag{3.165}$$

and will be incorporated into a Finite Element code. Equations (3.143) and (3.165) together yield

$$\frac{\partial \boldsymbol{\tau}_{n+1}}{\partial [\![\boldsymbol{u}]\!]_{n+1}} = \sum_i [1 - d_{i(n)}] \boldsymbol{C}_i^{if,el} \cdot \left[\boldsymbol{I} - \frac{\partial [\![\boldsymbol{u}]\!]_{n+1}^{vp}}{\partial [\![\boldsymbol{u}]\!]_{n+1}} \right] \tag{3.166}$$

For the further development of equation (3.166), equation (3.148) is incorporated, giving

$$\frac{\partial [\![\boldsymbol{u}]\!]_{n+1}^{vp}}{\partial [\![\boldsymbol{u}]\!]_{n+1}} = \sum_i \left[\Delta\gamma_{i(n+1)}^{vp} \frac{\partial [\text{sign}(\bar{\tau}_{i(n+1)})\, \boldsymbol{i}]}{\partial [\![\boldsymbol{u}]\!]_{n+1}} + [\text{sign}(\bar{\tau}_{i(n+1)})\, \boldsymbol{i}] \otimes \frac{\partial \Delta\gamma_{i(n+1)}^{vp}}{\partial [\![\boldsymbol{u}]\!]_{n+1}} \right] [1 - d_{i(n)}]^{-1} \tag{3.167}$$

Equations (3.150), (3.159) and (3.167) together render

$$\begin{aligned}\frac{\partial \Delta\gamma^{vp}_{i(n+1)}}{\partial [\![\boldsymbol{u}]\!]_{n+1}} &= \zeta_i^{vp}\,\frac{\partial\big[|\bar{\tau}_{i,trial}|/[[c_i+H_i^{vp}]/[1-d_{i(n)}]+\eta_i/\Delta t]\big]}{\partial [\![\boldsymbol{u}]\!]_{n+1}}\\ &= \zeta_i^{vp}\,\frac{\partial\big[\;|\;\big[\boldsymbol{C}^{if,el}\cdot[[\boldsymbol{u}]]_{n+1}-[\![\boldsymbol{u}]\!]_n^{vp}\big]\cdot\boldsymbol{i}\;|\;/[[c_i+H_i^{vp}]/[1-d_{i(n)}]+\eta_i/\Delta t]\big]}{\partial [\![\boldsymbol{u}]\!]_{n+1}}\\ &= \zeta_i^{vp}\,\frac{\mathrm{sign}(\bar{\tau}_{i,trial})}{[1+H_i^{vp}/c_i]/[1-d_{i(n)}]+\eta_i/[c_i\,\Delta t]}\,\boldsymbol{i}\end{aligned} \tag{3.168}$$

Considering equations (3.168), (3.119), $(3.150)_2$ and (3.167) renders

$$\frac{\partial [\![\boldsymbol{u}]\!]^{vp}_{n+1}}{\partial [\![\boldsymbol{u}]\!]_{n+1}} = \sum_i \frac{\zeta_i^{vp}}{1+H_i^{vp}/c_i+\eta_i\,[1-d_{i(n)}]/[c_i\,\Delta t]}\,\boldsymbol{i}\otimes\boldsymbol{i} \tag{3.169}$$

Reinserting this into equations (3.166) and (3.165), respectively, yields in the algorithmic tangent modulus, given by

$$\boldsymbol{C}^{if,vpd}_{alg} = \sum_i [1-d_{i(n)}]\left[1-\frac{\zeta_i^{vp}}{1+H_i^{vp}/c_i+\eta_i\,[1-d_{i(n)}]/[c_i\,\Delta t]}\right]\boldsymbol{C}_i^{if,el} \tag{3.170}$$

The most important algorithmic aspects are comprehended in Tab. 3.3.

3.5.3 Prototype Examples

Subsequently, demonstrating the functionality of the viscoelastic damage law introduced above, some prototype examples are presented. The plots have been created by a finite element simulation of a single lap tensile specimen, with linear elasticity for the bulk and viscoplasticity (with damage) for the interfacial zone.

In Fig. 3.7 relaxation behaviour is shown on the left hand side whereas creep behaviour is presented on the right hand side. In both cases damage has been switched off to focus on the purely viscoplastic material law. Additionally, in both cases, an elastic-plastic comparison curve has been plotted, referring to the case without damping. Concerning relaxation, different starting points have been chosen, rendering different lines. All lines end before they reach the elastic-plastic comparison curve. This is due to the fact that the damper needs an infinite amount of time to relax. In contrast, in the case of creep, the elastic-plastic comparison curve is exceeded for a very large number of creep steps. In contrast to viscoelasticity no parallel spring is at hand. Consequently, the model allows for infinite creep displacements.

In Fig. 3.8 damaging behaviour is presented. On the left hand side, some displacement controlled viscoelastic behaviour is plotted with and without damage. Damage is activated at approx. 4 kN, being visible by the decreasing character of the red curve. On the right hand side, 250 creep steps are extended by damage. Without it the elastic-plastic comparison curve would not be exceeded here.

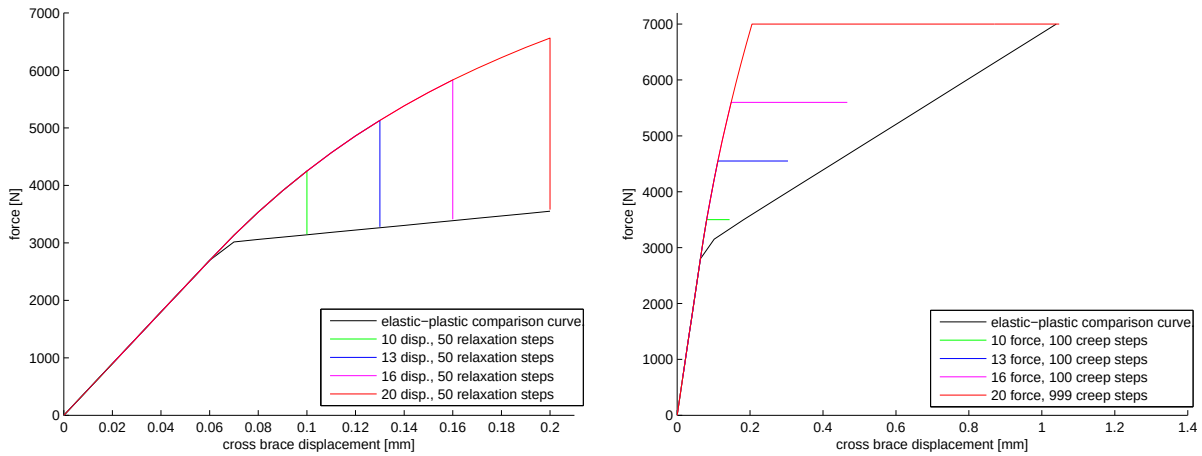

Figure 3.7: One-dimensional exemplary force-displacement plots of viscoplasticity. Left: displacement control. Relaxation behaviour, starting from different points of the loading history. Right: force control. Creep behaviour, starting from different points of the loading history

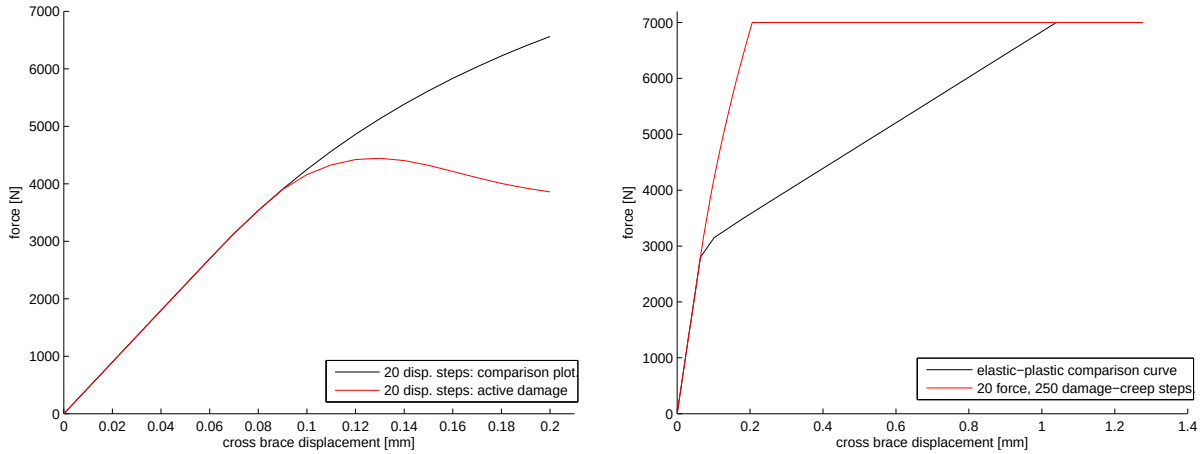

Figure 3.8: One-dimensional exemplary force-displacement plots of viscoplasticity with Lemaitre-type damage. Left: displacement control. Damage is activated at approx. 4 kN. Right: force control. Creep behaviour - the elastic straight line is exceeded because damage is active

3.6 Fatigue

Many technical products are subject to fatigue loading. Consequently, also material interfaces suffer from fatigue effects. This creates the need of adequate interfacial fatigue models. Generally, it is distinguished between low-cycle-fatigue and high-cycle-fatigue. Typical cycle numbers concerning

low-cycle-fatigue are resident in the range of $\mathcal{O}(10^0) - \mathcal{O}(10^3)$ while high-cycle-fatigue is on hand for higher cycle numbers. According to this distinction, different material models are supposable. Concerning high cycle numbers, a cycle-based formulation is mostly incorporated while for low cycle numbers a direct retracing of the loading history by resolving single cycles in several loading steps is practicable. Typical for both possibilities is the fatigue-related application of damage mechanics as proposed by Lemaitre [90] and Lemaitre and Chaboche [91]. In view of high-cycle-fatigue, fatigue damage evolution has often be defined to be stress dependent, see, e.g., Lemaitre and Plumtree [92], Hua and Socie [68] and Chaboche [35]. However, by further developing the formulation of Paas et al. [135], Peerlings et al. [140] proposed a strain based formalism being of the same form as the high-cycle part of the classical strain-based approach to fatigue as described in Manson and Hirschberg [104] or, respectively, Basquin's law, see Basquin [8]. It has been adopted in an interfacial context by, e.g., Robinson et al. [149], Munoz et al. [123] and Erinc et al. [50]. A cohesive low-cycle-fatigue formalism was developed by Nguyen et al. [127] and was further extended by Arias et al. [2] for coupled problems, however, without placing emphasis on its numerical implementation.

3.6.1 Constitutive Modelling: General Remarks

For the constitutive modelling of fatigue effects, we once more apply Lemaitre-type damage. It is assumed that by the influence of cyclic loading in the elastic regime of the interface, stiffnesses are decreased. This clearly leads towards a material modelling which is identical to elasticity with damage where the damage parameter is motivated specifically for the type of fatigue which is present. The nominal tractions depend on the displacement jump and the damage variable $d \in [0, 1[$ with $\dot{d} > 0$:

$$\boldsymbol{\tau} = \boldsymbol{\tau}(\llbracket \boldsymbol{u} \rrbracket, d) \tag{3.171}$$

Please note that, in contrast to the decoupled traction-separation laws of previous sections, the damage evolution is synchronal in all interfacial orthonormal directions. The second law of thermodynamics, represented by the Clausius-Duhem inequality, is given as

$$\mathcal{D} = \mathcal{D}_{loc} = \mathcal{W} - \dot{\Psi} \geq 0 \tag{3.172}$$

Concerning the free energy, dependencies are given as

$$\Psi = \Psi(\llbracket \boldsymbol{u} \rrbracket, d) \tag{3.173}$$

with $\mathcal{W}$ being the traction power. Equation (3.172) can consequently be reformulated, yielding

$$\left[\boldsymbol{\tau} - \frac{\partial \Psi}{\partial \llbracket \boldsymbol{u} \rrbracket}\right] \cdot \llbracket \dot{\boldsymbol{u}} \rrbracket - \frac{\partial \Psi}{\partial d}\, \dot{d} \geq 0 \tag{3.174}$$

Incorporating the Coleman-Noll Entropy Principle renders

$$\boldsymbol{\tau} = \frac{\partial \Psi}{\partial \llbracket \boldsymbol{u} \rrbracket} \tag{3.175}$$

The reduced dissipation inequality is computed straightforwardly and reads

$$\mathcal{D}_{red} = -\frac{\partial \Psi}{\partial d}\,\dot{d} \geq 0 \tag{3.176}$$

Again, the free energy relation is introduced in a quadratic format, reading as

$$\Psi(\llbracket \boldsymbol{u} \rrbracket, d) = \frac{1}{2}\,[1-d]\,\llbracket \boldsymbol{u} \rrbracket \cdot \boldsymbol{C}^{if,el} \cdot \llbracket \boldsymbol{u} \rrbracket \tag{3.177}$$

Simultaneously, nominal tractions follow as

$$\boldsymbol{\tau} = [1-d]\,\boldsymbol{C}^{if,el} \cdot \llbracket \boldsymbol{u} \rrbracket \tag{3.178}$$

The effective tractions are computed by the simple relation

$$\bar{\boldsymbol{\tau}} = \boldsymbol{C}^{if,el} \cdot \llbracket \boldsymbol{u} \rrbracket \tag{3.179}$$

The reduced dissipation inequality is consequently rewritten as

$$\mathcal{D}_{red} = \frac{1}{2}\,\llbracket \boldsymbol{u} \rrbracket \cdot \boldsymbol{C}^{if,el} \cdot \llbracket \boldsymbol{u} \rrbracket\ \dot{d} \geq 0 \tag{3.180}$$

Obviously, it is always positive and thermodynamical consistency is fulfilled.

In the following, two differently motivated fatigue damage evolution formulations will be presented. The first one is called “Time-Based Fatigue Formulation” and is appropriate for low-cycle-fatigue simulations while the second one, named “Cycle-Based Fatigue Formulation”, is capable of representing high-cycle-fatigue loadings. Both methods inhere a common ground which is given by an effective quantity δ, defined as

$$\delta = \sqrt{\beta_s^2\,\llbracket u_s \rrbracket^2 + \beta_t^2\,\llbracket u_t \rrbracket^2 + \beta_n^2\,\llbracket u_n \rrbracket^2} \tag{3.181}$$

with

$$\llbracket u_i \rrbracket = \llbracket \boldsymbol{u} \rrbracket \cdot \boldsymbol{i}, \quad i = s,t,n \tag{3.182}$$

and β_s, β_t and β_n denoting material parameters, controlling the influence of the projected displacement jumps on δ while $\boldsymbol{i} \in \{\boldsymbol{s}, \boldsymbol{t}, \boldsymbol{n}\}$ are the already known orthonormal unit vectors characterising the interface itself. This effective quantity approach is coupled in the interfacial orthonormal directions and similar to the approach introduced by, e.g., Pandolfi and Ortiz [137], Pandolfi et al. [136], Ortiz and Pandolfi [132], Cirak et al. [36], Corigliano et al. [42] and others.

3.6.2 Constitutive Modelling: Time-Based Fatigue Formulation

The Time-Based Fatigue Formulation traces a cyclic loading history not in cycle-by-cycle steps but in arbitrarily exact time intervals or, respectively, loading segments. One of the first elaborations concerning this matter, considering an unloading-reloading hysteresis for a traction-separation correlation, was published by Nguyen et al. [127]. Therein, loading stiffness rates have been constructed such that shakedown effects are prevented. An application to the prediction of fatigue-crack nucleation has been

provided by Serebrinsky and Ortiz [160] while Arias et al. [2] applied the same elaborations to the cohesive modelling of ferroelectric fatigue. The material law which is applied to capture low-cycle-fatigue shall be given as an exponential function, to be specific

$$d = \exp\Big(-\frac{\breve{\alpha}}{\tilde{\delta}}\Big) \tag{3.183}$$

with $\breve{\alpha}$ being a positive material parameter. Hereby, $\tilde{\delta}$ takes the interpretation as a history-dependent effective quantity.

3.6.3 Algorithmic Aspects: Time-Based Fatigue Formulation

An incremental update for the damage variable is accomplished, with index $n+1$ denoting the current loading step. It is given as

$$d_{n+1} = \exp\Big(-\frac{\breve{\alpha}}{\tilde{\delta}_{n+1}}\Big) \tag{3.184}$$

The related history-dependent effective quantity $\tilde{\delta}$ is updated as follows:

$$\tilde{\delta}_{n+1} \;=\; \tilde{\delta}_n + \langle \delta_{n+1} - \delta_n \rangle, \quad \tilde{\delta}_0 = 0 \tag{3.185}$$

For loading, the expression in the Macaulay-brackets is positive and the history-dependent effective quantity is updated whereas, for unloading, it will be retained. Consequently, only an increasing δ contributes to the damage evolution in this rather simple but efficient formulation. Nevertheless, all types of cycling, incorporating cyclic compressive, tensile and alternating loads, are time-explicitly reflected, contributing to the evolution of d in the same manner. Related, updates for the effective and nominal traction vectors are given as

$$\bar{\boldsymbol{\tau}}_{n+1} = \boldsymbol{C}^{if,el} \cdot [\![\boldsymbol{u}]\!]_{n+1}, \quad \boldsymbol{\tau}_{n+1} = [1 - d_{n+1}]\, \bar{\boldsymbol{\tau}}_{n+1} \tag{3.186}$$

The algorithmic tangent of the Time-Based Fatigue Formalism is defined as

$$\boldsymbol{C}^{if,tbf}_{alg} = \frac{\partial \boldsymbol{\tau}_{n+1}}{\partial [\![\boldsymbol{u}]\!]_{n+1}} \tag{3.187}$$

Equation (3.186), together with equation (3.187), yields

$$\frac{\partial \boldsymbol{\tau}_{n+1}}{\partial [\![\boldsymbol{u}]\!]_{n+1}} = [1 - d_{n+1}]\, \boldsymbol{C}^{if,el} - \bar{\boldsymbol{\tau}}_{n+1} \otimes \frac{\partial d_{n+1}}{\partial [\![\boldsymbol{u}]\!]_{n+1}} \tag{3.188}$$

For the further development of equation (3.188), equation (3.184) is exploited as

$$\frac{\partial d_{n+1}}{\partial [\![\boldsymbol{u}]\!]_{n+1}} = \exp\Big(-\frac{\breve{\alpha}}{\tilde{\delta}_{n+1}}\Big)\, \breve{\alpha}\, \tilde{\delta}^{-2}_{n+1}\, \frac{\tilde{\delta}_{n+1}}{[\![\boldsymbol{u}]\!]_{n+1}} \tag{3.189}$$

given:	$[\![\boldsymbol{u}]\!]_{n+1},\ d_n$
1. damage update:	$\tilde{\delta}_{n+1} = \tilde{\delta}_n + \langle \delta_{n+1} - \delta_n \rangle, \quad \tilde{\delta}_0 = 0$
	$d_{n+1} = \exp\Big(- \dfrac{\breve{\alpha}}{\tilde{\delta}_{n+1}} \Big)$
2. traction update:	$\boldsymbol{\tau}_{n+1} = [1 - d_{n+1}]\, \boldsymbol{C}^{if,el} \cdot [\![\boldsymbol{u}]\!]_{n+1}$
4. tangent modulus:	$\boldsymbol{C}^{if,tbf}_{alg}$

Table 3.4: Algorithmic procedure for interfacial time-based fatigue

In view of equation (3.185), it holds

$$\frac{\partial \langle \delta_{n+1} - \delta_n \rangle}{\partial \delta_{n+1}} = \zeta^{tbf} = \begin{cases} 1 & \text{if} \quad \delta_{n+1} - \delta_n > 0 \\ 0 & \text{if} \quad \delta_{n+1} - \delta_n \leq 0 \end{cases} \tag{3.190}$$

Furthermore, incorporating equations (3.255) and (3.182), it holds

$$\frac{\partial \tilde{\delta}_{n+1}}{\partial [\![\boldsymbol{u}]\!]_{n+1}} = \zeta^{tbf}\, \delta_{n+1}^{-1} \sum_i \beta_i^2\, [\![\boldsymbol{u}_i]\!]_{n+1}, \quad i = s,t,n \tag{3.191}$$

Inserting the result of equation (3.191) into equation (3.189) renders

$$\frac{\partial d_{n+1}}{\partial [\![\boldsymbol{u}]\!]_{n+1}} = \exp\Big(- \frac{\breve{\alpha}}{\tilde{\delta}_{n+1}} \Big)\, \breve{\alpha}\, \tilde{\delta}_{n+1}^{-2}\, \delta_{n+1}^{-1}\, \zeta^{tbf} \sum_i \beta_i^2\, [\![\boldsymbol{u}_i]\!]_{n+1} \tag{3.192}$$

This, together with equations (3.188) and (3.187), yields the algorithmic tangent

$$\boldsymbol{C}^{if,tbf}_{alg} = [1 - d_{n+1}]\, \boldsymbol{C}^{if,el} - \exp\Big(- \frac{\breve{\alpha}}{\tilde{\delta}_{n+1}} \Big)\, \breve{\alpha}\, \tilde{\delta}_{n+1}^{-2}\, \delta_{n+1}^{-1}\, \zeta^{tbf}\, \bar{\boldsymbol{\tau}}_{n+1} \otimes \sum_i \beta_i^2\, [\![\boldsymbol{u}_i]\!]_{n+1} \tag{3.193}$$

The concisely comprehended algorithmic aspects are given in Tab. 3.4.

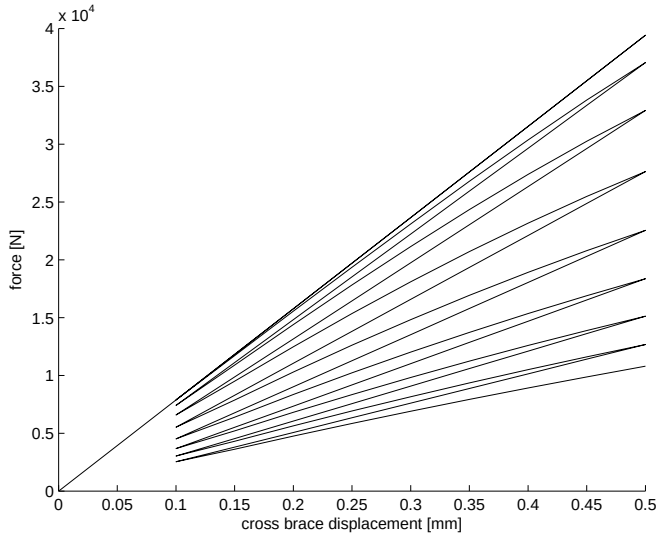

Figure 3.9: Force-displacement plot of time-based fatigue: displacement control

3.6.4 Prototype Example: Time-Based Fatigue Formulation

The exemplary force-displacement plot included here has been computed by applying cyclic displacements to a finite element discretisation of a single lap tensile specimen, with linear elasticity for the bulk and time-based fatigue for the interfacial zone. As Fig. 3.9 shows, the force decreases with continued cycling. This is due to the damaging influence, being driven by the history-dependent effective quantity $\tilde{\delta}$.

3.6.5 Constitutive Modelling: Cycle-Based Fatigue Formulation

The fatigue formulation for high-cycle-fatigue is based on a constitutive integration over many cycles by means of a cycle number N. This idea has first been implemented for continua by Paas et al. [135], Peerlings [139] and Peerlings et al. [140]. Concerning interfaces, similar formulations have been adopted for uncoupled problems by Robinson et al. [149], Munoz et al. [123] and Erinc et al. [50]. In the following, it is proceeded along the strategy described in Peerlings et al. [140], applying it to the interface. The damage variable is related to the deformation by means of a damage loading function

$$f(\delta, \kappa) = \delta - \kappa \tag{3.194}$$

where κ is a threshold. Thereby, damage evolution will be active if the given effective quantity δ exceeds κ. Here, the material law is given by the rate of the damage parameter d as

$$\dot{d} = \begin{cases} h(d,\delta)\,\dot{\delta} & \text{if} \quad f \geq 0, \quad \dot{f} \geq 0, \quad \text{and} \quad d < 1 \\ 0 & \text{else} \end{cases} \tag{3.195}$$

with the evolution function

$$h(d, \delta) = C \exp(\check{\gamma}\, d)\, \delta^{\check{\beta}} \tag{3.196}$$

and C, $\check{\beta}$ and $\check{\gamma}$ denoting material parameters.

3.6.6 Algorithmic Aspects: Cycle-Based Fatigue Formulation

Now, assume d_t, $d_{t+\Delta t}$ to be damage parameters corresponding to points in time t and $t + \Delta t$. For continued loading, integration of equation (3.195) then renders

$$d_{t+\Delta t} = d_t + \int_t^{t+\Delta t} \dot{d}(\tau)\, \mathrm{d}\tau \tag{3.197}$$

To avoid the influence of some highly varying $\dot{d}$, an approximation of this correlation is not advisable. Therefore, a sum notation with respect to single cycles in combination with a transformation of integration limits concerning time and cycle numbers is accomplished. With this in hand and the damage evolution being active, combining equations (3.195) and (3.197) renders

$$d_{N+\Delta N} = d_N + \sum_{k=N}^{N+\Delta N} \int_{\kappa}^{\delta_{a,k}} h(d_k, \delta_k)\, \mathrm{d}\delta_k \tag{3.198}$$

with N and $N + \Delta N$ being the number of performed cycles at points in time t and $t + \Delta t$. Moreover, $\delta_{a,k}$, δ_k and d_k denote the effective parameter amplitude at cycle k, the variable effective parameter and damage parameter during cycle k. It shall be mentioned that, again, only loading related δ shall contribute to the damage evolution. For the thus obtained expression for $d_{N+\Delta N}$ neither $\delta_{a,k}$ nor d_k would vary much within a sufficiently small increment ΔN. Hence, the sum expression in equation (3.198) can now be approximated. Application of the trapezoidal rule with respect to loading cycles N and $N + \Delta N$ is reasonable, which ends up with

$$d_{N+\Delta N} = d_N + \frac{1}{2}\, \zeta^{cbf} \left[Z(d_N, \delta_{a,N}) + Z(d_{N+\Delta N}, \delta_{a,N+\Delta N}) \right] \Delta N \tag{3.199}$$

wherein

$$Z = \Omega^{cbf} \int_{\kappa}^{\delta_a} h(d, \delta)\, \mathrm{d}\delta \tag{3.200}$$

In equation (3.199) an additional parameter is introduced to account for subthreshold loading.

$$\zeta^{cbf} = \begin{cases} 1 & \text{if} \quad \delta_a > \kappa \\ 0 & \text{else} \end{cases} \tag{3.201}$$

Furthermore, equation (3.200) contains the parameter Ω^{cbf}. It is defined as

$$\Omega^{cbf} = \begin{cases} 2 & \text{for alternating loads, mean load zero} \\ 1 & \text{for exclusively tensile or compressive loads} \end{cases} \tag{3.202}$$

Due to the positiveness of the effective displacement jump, $\Omega^{cbf} = 2$ implies that for alternating loads, the tensile and compressive loading parts have the same consequences on the damage evolution, assuming that both parts are equal in their norm. In other words, the effect of the tensile part of the load is put on par with the compressive part. In addition to this simplifying assumption, alternating loads with mean loads unequal zero are not included in this formulation. Next, according to Peerlings et al. [140], Heun's method enables to solve equation (3.199). This is accomplished by incorporating the Euler forward method. In detail, introducing a predictor value d_p, reading as

$$d_p = d_N + Z(d_N, \delta_{a,N})\,\Delta N \tag{3.203}$$

replaces $d_{N+\Delta N}$. Finally, equation (3.199) together with (3.203) render the damage update to take the format

$$d_{N+\Delta N} = d_N + \frac{1}{2}\,\zeta^{cbf}\left[Z(d_N, \delta_{a,N}) + Z(d_p, \delta_{a,N+\Delta N})\right]\Delta N \tag{3.204}$$

which nicely can be incorporated into a finite element context. The accuracy of this strategy is raised by diminishing ΔN. For $\kappa \neq 0$, either the range of cyclic compressive or tensile loads can be addressed, or a non-damaging zero-symmetric regime concerning δ is achieved for cyclic alternating loads. In view of numerical implementation, equation (3.204) is formulated in terms of computation steps $n+1$ and n, reading as

$$d_{n+1} = d_n + \frac{1}{2}\,\zeta^{cbf}\left[Z(d_n, \delta_{a,n}) + Z(d_p, \delta_{a,n+1})\right]\Delta N \tag{3.205}$$

Additionally, a so-called damage cut-off shall be defined via

$$d_{n+1} = 0.99 \quad \text{if} \quad d_n + \frac{1}{2}\,\zeta^{cbf}\left[Z(d_n, \delta_{a,n}) + Z(d_p, \delta_{a,n+1})\right]\Delta N > 0.99 \tag{3.206}$$

Thereby, the damage parameter d is prevented from exceeding its co-domain $[0, 1[$. Effective and nominal tractions follow straightforwardly as described in equation (3.186). According to equation (3.186) the tractions follow straightforwardly. The algorithmic tangent of the Cycle-Based Fatigue Formalism is defined as

$$\boldsymbol{C}_{alg}^{if,cbf} = \frac{\partial \boldsymbol{\tau}_{n+1}}{\partial [\![\boldsymbol{u}]\!]_{n+1}} \tag{3.207}$$

Equation (3.186), together with equation (3.207), yields in

$$\frac{\partial \boldsymbol{\tau}_{n+1}}{\partial [\![\boldsymbol{u}]\!]_{n+1}} = [1 - d_{n+1}]\,\boldsymbol{C}^{if,el} - \bar{\boldsymbol{\tau}}_{n+1} \otimes \frac{\partial d_{n+1}}{\partial [\![\boldsymbol{u}]\!]_{n+1}} \tag{3.208}$$

Equation (3.208) is computed by taking equation (3.205) into account:

$$\frac{\partial d_{n+1}}{\partial [\![\boldsymbol{u}]\!]_{n+1}} = \frac{1}{2}\,\zeta^{cbf}\,\Delta N \frac{\partial Z(D_p, \delta_{a,n+1})}{\partial [\![\boldsymbol{u}]\!]_{n+1}} \tag{3.209}$$

The appropriate Z is computed as

$$Z(d_p, \delta_{a,n+1}) = \Omega^{cbf} \int_{\kappa}^{\delta_{a,n+1}} h(d_p, \delta)\, \mathrm{d}\delta = \Omega^{cbf} \int_{\kappa}^{\delta_{a,n+1}} C \exp(\check{\gamma}\, d_p)\, \delta^{\check{\beta}}\, \mathrm{d}\delta$$

$$= \Omega^{cbf} \frac{C}{\check{\beta}+1} \exp(\check{\gamma}\, d_p) \left[\delta_{a,n+1}^{\check{\beta}+1} - \kappa^{\check{\beta}+1}\right] \tag{3.210}$$

Accordingly, it follows

$$\frac{\partial Z(d_p, \delta_{a,n+1})}{\partial [\![\boldsymbol{u}]\!]_{n+1}} = \Omega^{cbf}\, C\, \exp(\check{\gamma}\, d_p)\, \delta_{a,n+1}^{\check{\beta}} \frac{\partial \delta_{a,n+1}}{\partial [\![\boldsymbol{u}]\!]_{n+1}} \tag{3.211}$$

where

$$\frac{\partial \delta_{a,n+1}}{\partial [\![\boldsymbol{u}]\!]_{n+1}} = \delta_{a,n+1}^{-1} \sum_i \check{\beta}_i^2\, [\![\boldsymbol{u}_i]\!]_{n+1} \tag{3.212}$$

Equations (3.211) and (3.212) together yield

$$\frac{\partial Z(d_p, \delta_{a,n+1})}{\partial [\![\boldsymbol{u}]\!]_{n+1}} = \Omega^{cbf}\, C\, \exp(\check{\gamma}\, d_p)\, \delta_{a,n+1}^{\check{\beta}-1} \sum_i \check{\beta}_i^2\, [\![\boldsymbol{u}_i]\!]_{n+1} \tag{3.213}$$

Reinserting equation (3.213) into equation (3.209), the derivative of the damage parameter follows as

$$\frac{\partial d_{n+1}}{\partial [\![\boldsymbol{u}]\!]_{n+1}} = \frac{1}{2} \zeta^{cbf}\, \Delta N\, \Omega^{cbf}\, C\, \exp(\check{\gamma}\, d_p)\, \delta_{a,n+1}^{\check{\beta}-1} \sum_i \check{\beta}_i^2\, [\![\boldsymbol{u}_i]\!]_{n+1} \tag{3.214}$$

In the end, by inserting equation (3.214) into equation (3.208), the algorithmic tangent can be computed via equation (3.207) as

$$\boldsymbol{C}_{alg}^{if,cbf} = [1 - d_{n+1}]\, \boldsymbol{C}^{if,el} - \frac{1}{2} \zeta^{cbf}\, \Delta N\, \Omega^{cbf}\, C\, \exp(\check{\gamma}\, d_p)\, \delta_{a,n+1}^{\check{\beta}-1}\, \bar{\boldsymbol{\tau}}_{n+1} \otimes \sum_i \check{\beta}_i^2\, [\![\boldsymbol{u}_i]\!]_{n+1} \tag{3.215}$$

The most important algorithmic aspects are once more reflected by Tab. 3.5.

3.6.7 Prototype Example: Cycle-Based Fatigue Formulation

The exemplary force-cycle plot included here has been computed by applying a constant displacement amplitude to a finite element discretisation of a single lap tensile specimen, with linear elasticity for the bulk and cycle-based fatigue for the interfacial zone. On the left hand side, Fig. 3.10 shows the force over the cycle number. With growing cycle number, the force decreases due to the damaging influence of cycle-based fatigue. On the right hand side of Fig. 3.10, a Wöhler-diagram for one Gauss point is presented, where the life cycle is associated with a damage parameter value of $d = 0.99$, see equation (3.206). The stair-like patterns result from the constant cycle increment ΔN.

given: $[\![\boldsymbol{u}]\!]_{n+1},\ d_n$

1. damage update: $\zeta^{cbf} = \begin{cases} 1 & \text{if} \quad \delta_a > \kappa \\ 0 & \text{else} \end{cases}$

compute $d_p,\ Z(d_n, \delta_{a,n}),\ Z(d_p, \delta_{a,n+1})$

$$d_{n+1} = d_n + \frac{1}{2}\zeta^{cbf}[Z(d_n, \delta_{a,n}) + Z(d_p, \delta_{a,n+1})]$$

2. traction update: $\boldsymbol{\tau}_{n+1} = [1 - d_{n+1}]\, \boldsymbol{C}^{if,el} \cdot [\![\boldsymbol{u}]\!]_{n+1}$

4. tangent modulus: $\boldsymbol{C}^{if,cbf}_{alg}$

Table 3.5: Algorithmic procedure for interfacial cycle-based fatigue

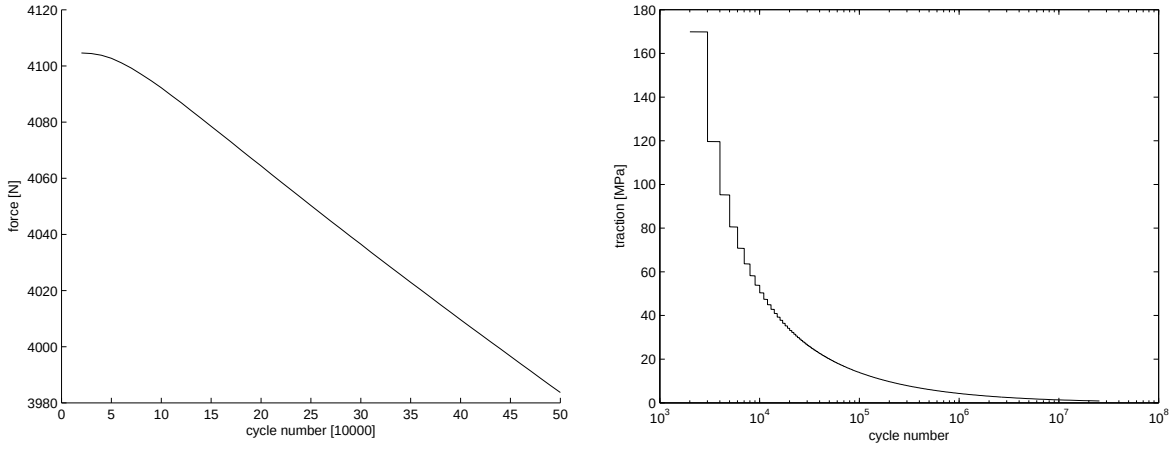

Figure 3.10: Left: force-cycle plot of cycle-based fatigue: displacement control. Right: Wöhler-diagram for one Gauss point, maximal traction over cycle number

3.7 Linear Ferroelectricity

Also in the context of ferroelectric ceramics as, e.g., PZT, interfaces play an important role. In view of the microstructure of such a material, grain boundaries are identified as interfaces between grains, inhering certain properties concerning stiffnesses, coupling phenomena and permittivity. As phase transformations are supposed to happen in the grain bulk, such effects are excluded concerning the interface. Furthermore, in accordance to section 2.4, the name of "linear ferroelectricity" shall be adopted for the present interfacial material law. At first, the tractions of a linear ferroelectric interface are given in the dependencies

$$\boldsymbol{\tau} = \boldsymbol{\tau}(\llbracket \boldsymbol{u} \rrbracket, E) \tag{3.216}$$

with E denoting the electric field strength in normal direction $\boldsymbol{n}$ of the interface. The current constitutive formulation assumes decoupled interfacial stiffnesses as proposed in section 3.2 while electrical and coupling processes are only assumed to happen in the above-mentioned $\boldsymbol{n}$-direction. As also described by equation (3.3), the dielectrical displacement of the interface is given with respect to the interfacial normal direction $\boldsymbol{n}$ and reads as

$$\Lambda = \Lambda(\llbracket \boldsymbol{u} \rrbracket, E) \tag{3.217}$$

Here, no dissipation occurs because changes of the interfacial state are reversible since the mechanical and electrical forces are supposed to be derived from potentials. Consequently, the second law of thermodynamics reads as

$$\mathcal{D} = \mathcal{D}_{loc} = \mathcal{W}_{mech} - \mathcal{W}^*_{elec} - \dot{H} = 0 \tag{3.218}$$

Again, due to the electrically coupled problem, the electric enthalpy function is incorporated:

$$H = H(\llbracket \boldsymbol{u} \rrbracket, E; \boldsymbol{s}, \boldsymbol{t}, \boldsymbol{n}) = \inf_{\Lambda}(\Psi - E\Lambda), \quad \boldsymbol{s}, \boldsymbol{t}, \boldsymbol{n} = \text{const.} \tag{3.219}$$

The traction power and the complementary dielectric displacement power are given as

$$\mathcal{W}_{mech} = \boldsymbol{\tau} \cdot \dot{\llbracket \boldsymbol{u} \rrbracket}, \quad \mathcal{W}^*_{elec} = \Lambda \dot{E} \tag{3.220}$$

Related, the second law of thermodynamics is rewritten as

$$\boldsymbol{\tau} \cdot \dot{\llbracket \boldsymbol{u} \rrbracket} - \Lambda \dot{E} - \dot{H} = 0 \tag{3.221}$$

Due to the dependencies described in equations (3.216) and (3.217), this is equivalent to

$$\left[\boldsymbol{\tau} - \frac{\partial H}{\partial \llbracket \boldsymbol{u} \rrbracket} \right] \cdot \dot{\llbracket \boldsymbol{u} \rrbracket} + \left[-\Lambda - \frac{\partial H}{\partial E} \right] \dot{E} = 0 \tag{3.222}$$

Incorporating the Coleman-Noll Entropy Principle renders the interfacial tractions and the dielectrical displacements as

$$\boldsymbol{\tau} = \frac{\partial H}{\partial \llbracket \boldsymbol{u} \rrbracket}, \quad \Lambda = -\frac{\partial H}{\partial E} \tag{3.223}$$

Consequently, thermodynamical consistency is trivially fulfilled. The rate relations of tractions and dielectrical displacements with respect to the rates of the displacement jumps and the electric field are given as

$$\dot{\boldsymbol{\tau}} = \boldsymbol{C}^{if,fer,el} \cdot [\![\dot{\boldsymbol{u}}]\!] - \boldsymbol{e}^{if,\triangle}\, \dot{E}, \quad \dot{\Lambda} = \boldsymbol{e}^{if} \cdot [\![\dot{\boldsymbol{u}}]\!] + \epsilon^{if}\, \dot{E} \tag{3.224}$$

The associated Ferroelectric Interface Tangent Tensors read as

$$\begin{aligned} \boldsymbol{C}^{if,fer,el} &= \frac{\partial^2 H}{\partial [\![\boldsymbol{u}]\!] \otimes \partial [\![\boldsymbol{u}]\!]} = C_{ij}^{if,fer,el} \boldsymbol{e}_i \otimes \boldsymbol{e}_j, \quad \boldsymbol{e}^{if,\triangle} = -\frac{\partial^2 H}{\partial [\![\boldsymbol{u}]\!]\, \partial E} = e_i^{if,\triangle} \boldsymbol{e}_i, \\ \boldsymbol{e}^{if} &= -\frac{\partial^2 H}{\partial E\, \partial [\![\boldsymbol{u}]\!]} = e_i^{if} \boldsymbol{e}_i, \qquad\qquad \epsilon^{if} = -\frac{\partial^2 H}{\partial E\, \partial E} \end{aligned} \tag{3.225}$$

By introducing an electric enthalpy function in a quadratic format, compare equation (2.99), reading as

$$H = \frac{1}{2}\, [\![\boldsymbol{u}]\!] \cdot \boldsymbol{C}^{if,fer,el} \cdot [\![\boldsymbol{u}]\!] - E\, \boldsymbol{e}^{if} \cdot [\![\boldsymbol{u}]\!] - \frac{1}{2}\, \epsilon^{if}\, E^2 \tag{3.226}$$

the tractions and dielectric displacements of the interface are rewritten as

$$\boldsymbol{\tau} = \boldsymbol{C}^{if,fer,el} \cdot [\![\boldsymbol{u}]\!] - \boldsymbol{e}^{if}\, E, \quad \Lambda = \boldsymbol{e}^{if} \cdot [\![\boldsymbol{u}]\!] + \epsilon^{if}\, E \tag{3.227}$$

In this case it holds

$$\boldsymbol{e}^{if} = \boldsymbol{e}^{if,\triangle} \tag{3.228}$$

The electric enthalpy shall also be expressed by a coefficient representation which compares to invariants of the tensorial case.

$$\begin{aligned} H &= H([\![\boldsymbol{u}]\!], E; \boldsymbol{s}, \boldsymbol{t}, \boldsymbol{n}) = H(i_{[\![u]\!]}, i_{En}, i_{[\![u]\!]En}) \\ &= H(I_s^{if}, I_t^{if}, I_n^{if}, J^{if}, K^{if}) = H_1(I_s^{if}, I_t^{if}, I_n^{if}) + H_2(J^{if}) + H_3(K^{if}) \end{aligned} \tag{3.229}$$

with

$$i_{En} = \{E^2\} = \{J^{if}\}, \quad i_{[\![u]\!]En} = \{[\![\boldsymbol{u}]\!] \cdot \boldsymbol{n}\, E\} = \{K^{if}\} \tag{3.230}$$

Thereby, the stiffness relations as introduced in section 3.2 are adopted and it holds $\boldsymbol{C}^{if,fer,el} = \boldsymbol{C}^{if,el}$. Now, tractions and dielectric displacements are expressed as derivatives with respect to coefficients comparing to the irreducible set of invariants of the tensorial case:

$$\begin{aligned} \boldsymbol{\tau} &= \frac{\partial H}{\partial [\![\boldsymbol{u}]\!]} = 2 \sum_i \frac{\partial H}{\partial I_i^{if}} \left[[\![\boldsymbol{u}]\!] \cdot \boldsymbol{i} \right] \boldsymbol{i} + \frac{\partial H}{\partial K^{if}}\, E\, \boldsymbol{n} \\ &= \sum_i \Phi_i \left[[\![\boldsymbol{u}]\!] \cdot \boldsymbol{i} \right] \boldsymbol{i} + \Phi_{[\![u]\!]En}\, E\, \boldsymbol{n}, \quad i = s, t, n \end{aligned} \tag{3.231}$$

$$\Lambda = -\frac{\partial H}{\partial E} = -\frac{\partial H}{\partial K^{if}}\, [\![\boldsymbol{u}]\!] \cdot \boldsymbol{n} - \frac{\partial H}{\partial J^{if}}\, 2E = -\Phi_{[\![u]\!]En}\, [\![\boldsymbol{u}]\!] \cdot \boldsymbol{n} - \Phi_{En}\, 2E \tag{3.232}$$

The evaluation of the quadratic electric enthalpy function implies linear constitutive relations. It holds

$$\Phi_{[\![u]\!]En} = -\frac{e^{if}}{l_e}, \quad \Phi_{En} = -\frac{1}{2}\,\frac{\epsilon_0\epsilon_r}{l_\epsilon} \tag{3.233}$$

leading towards

$$\boldsymbol{\tau} = \sum_i \frac{c_i}{l_i}\,[[\![\boldsymbol{u}]\!]\cdot\boldsymbol{i}]\,\boldsymbol{i} - \frac{e^{if}}{l_e}\,E\,\boldsymbol{n} \tag{3.234}$$

$$\Lambda = \frac{e^{if}}{l_e}\,[\![\boldsymbol{u}]\!]\cdot\boldsymbol{n} + \frac{\epsilon_0\epsilon_r}{l_\epsilon}\,E \tag{3.235}$$

The Ferroelectric Interface Tangent Tensors consequently read

$$\boldsymbol{e}^{if} = \frac{e^{if}}{l_e}\,\boldsymbol{n}, \quad \epsilon^{if} = \frac{\epsilon_0\epsilon_r}{l_\epsilon} \tag{3.236}$$

Hereby, the permittivity of the vacuum ϵ_0 and the relative permittivity ϵ_r are introduced. In what follows, characteristic lengths are again set as $l_e = l_\epsilon = 1$, see chapter 3.2. Furthermore, the interfacial relation of the electric field strength and the potential jump is now specified as

$$E = -[\![\Phi]\!] \tag{3.237}$$

Consequently, the tangent relations can then be comprehended as

$$\begin{bmatrix} \boldsymbol{\tau} \\ \Lambda \end{bmatrix} = \underbrace{\begin{bmatrix} \boldsymbol{C}^{if,el} & \boldsymbol{e}^{if} \\ \boldsymbol{e}^{if} & -\epsilon^{if} \end{bmatrix}}_{\boldsymbol{C}^{if,fer}} \cdot \begin{bmatrix} [\![\boldsymbol{u}]\!] \\ [\![\Phi]\!] \end{bmatrix} \tag{3.238}$$

3.8 Linear Ferroelectricity with Fatigue

Concerning fatigue in ferroelectric materials, switching effects in the grain bulk as well as grain boundary effects play an important role. In this work the fatigue-related degradation of grain boundaries is in focus. For a ferroelectric ceramic, depending on certain circumstances, e.g. geometric influences like notches, low-cycle-fatigue occurs, see for example Westram et al. [187]. Nevertheless, the most common fatigue type is high-cycle fatigue. As well as for the uncoupled problem time- and cycle based fatigue concepts will be distinguished, introducing the damage parameter $d \in [0, 1[$ as the crucial ingredient, see also Utzinger et al. [183, 182]. As a consequence, many details already described in section 3.6 are adopted.

3.8.1 Constitutive Modelling

The basic material behaviour, neglecting fatigue damage, shall be linear and equivalent to the constitutive relations as described in section 3.7. The dependencies of the fatigue-influenced tractions shall

be given as

$$\boldsymbol{\tau} = \boldsymbol{\tau}(\llbracket \boldsymbol{u} \rrbracket, E, d) \tag{3.239}$$

while the dielectric displacements read

$$\Lambda = \Lambda(\llbracket \boldsymbol{u} \rrbracket, E, d) \tag{3.240}$$

The Clausius-Duhem inequality is given as

$$\mathcal{D} = \mathcal{D}_{loc} = \mathcal{W}_{mech} - \mathcal{W}^{*}_{elec} - \dot{H} \geq 0 \tag{3.241}$$

For the electric enthalpy function, it holds

$$H = H(\llbracket \boldsymbol{u} \rrbracket, E, d; \boldsymbol{s}, \boldsymbol{t}, \boldsymbol{n}) = \inf_{\Lambda}(\Psi - E\Lambda), \quad \boldsymbol{s}, \boldsymbol{t}, \boldsymbol{n} = \text{const.} \tag{3.242}$$

Once more, traction power and the complementary dielectric displacement power read as

$$\mathcal{W}_{mech} = \boldsymbol{\tau} \cdot \dot{\llbracket \boldsymbol{u} \rrbracket}, \quad \mathcal{W}^{*}_{elec} = \Lambda \dot{E} \tag{3.243}$$

This, together with equation (3.241) yields in

$$\boldsymbol{\tau} \cdot \dot{\llbracket \boldsymbol{u} \rrbracket} - \Lambda \dot{E} - \dot{H} \geq 0 \tag{3.244}$$

In contrast to section 3.7 dissipation is at hand, yielding an additional term in the dissipation inequality.

$$\Big[\boldsymbol{\tau} - \frac{\partial H}{\partial \llbracket \boldsymbol{u} \rrbracket}\Big] \cdot \dot{\llbracket \boldsymbol{u} \rrbracket} + \Big[-\Lambda - \frac{\partial H}{\partial E}\Big] \dot{E} - \frac{\partial H}{\partial d}\, \dot{d} \geq 0 \tag{3.245}$$

By making use of standard arguments, the interfacial reduced dissipation inequality is given as

$$\mathcal{D}_{red} = -\frac{\partial H}{\partial d}\, \dot{d} \geq 0 \tag{3.246}$$

with the tractions and dielectric displacements reading as

$$\boldsymbol{\tau} = \frac{\partial H}{\partial \llbracket \boldsymbol{u} \rrbracket}, \quad \Lambda = -\frac{\partial H}{\partial E} \tag{3.247}$$

Inspired by equations (3.177), (3.226) and the results of section 3.7, the electric enthalpy is introduced as

$$H = \frac{1}{2}\,[1-d]\,\llbracket \boldsymbol{u} \rrbracket \cdot \boldsymbol{C}^{if,el} \cdot \llbracket \boldsymbol{u} \rrbracket - E\,\boldsymbol{e}^{if} \cdot \llbracket \boldsymbol{u} \rrbracket - \frac{1}{2}\,\epsilon_0 \epsilon_r(d)\, E^2 \tag{3.248}$$

see also Utzinger et al. [183, 182]. Fatigue damage shall, in this formulation, only affect stiffnesses and the interfacial permittivity. The tractions and dielectric displacements follow as

$$\boldsymbol{\tau} = [1-d]\,\boldsymbol{C}^{if,el} \cdot \llbracket \boldsymbol{u} \rrbracket - \boldsymbol{e}^{if}\, E, \quad \Lambda = \boldsymbol{e}^{if} \cdot \llbracket \boldsymbol{u} \rrbracket + \epsilon_0 \epsilon_r(d)\, E \tag{3.249}$$

whereas the tangents occurring in equation (3.249) have already been stated in equation (3.225).

The reduced format of the Clausius-Planck inequality is further specified as

$$\mathcal{D}_{red} = -\frac{\partial H}{\partial d}\,\dot{d} = \left[\frac{1}{2}\,[\![\boldsymbol{u}]\!]\cdot\boldsymbol{C}^{if,el}\cdot[\![\boldsymbol{u}]\!] \;+\; \frac{1}{2}\,\epsilon_0\,E^2\;\frac{\partial\epsilon_r(d)}{\partial d}\right]\,\dot{d} = Y\dot{d} \geq 0 \tag{3.250}$$

whereby the driving force is identified with Y. Here, healing processes of the damage are excluded. Consequently, the rate of the damage parameter is constrained by

$$\dot{d} \geq 0 \tag{3.251}$$

Due to the fact that the driving force constrains the kinetics of the damage parameter evolution, inequalities (3.250) and (3.251) indicate

$$\dot{d} > 0 \quad \text{for} \quad Y > 0 \tag{3.252}$$

$$\dot{d} = 0 \quad \text{for} \quad Y \leq 0 \tag{3.253}$$

providing thermodynamical consistency. The explicit relation concerning ϵ_r and d shall be linear, reading as

$$\epsilon_r(d) = \epsilon_r^{init} + [\epsilon_r^{end} - \epsilon_r^{init}]\,d \tag{3.254}$$

Here, ϵ_r^{init} denotes the relative permittivity at the beginning of a damaging process while ϵ_r^{end} is the relative permittivity at the end when $d = 1$. The fatigue damage evolution is either of the time-based or the cycle-based type as discussed in section 3.6, see also Utzinger et al. [183, 182]. The effective parameter ansatz described in section 3.6.1 is now expanded, incorporating the electric potential jump. This has first been done by Arias et al. [2]. Here, the effective parameter reads as

$$\delta = \sqrt{\beta_s^2\,[\![u_s]\!]^2 + \beta_t^2\,[\![u_t]\!]^2 + \beta_n^2\,[\![u_n]\!]^2 + \beta_\Phi^2\,[\![\Phi]\!]^2} \tag{3.255}$$

3.8.2 Algorithmic Aspects: Time-Based Fatigue Formulation

The updated traction vector and dielectric displacements of time-based fatigue read

$$\boldsymbol{\tau}_{n+1} = [1 - d_{n+1}]\,\boldsymbol{C}^{if,el}\cdot[\![\boldsymbol{u}]\!]_{n+1} - E_{n+1}\,\boldsymbol{e}^{if}, \quad \Lambda_{n+1} = \boldsymbol{e}^{if}\cdot[\![\boldsymbol{u}]\!]_{n+1} + \epsilon_0\epsilon_r(d_{n+1})\,E_{n+1} \tag{3.256}$$

The appropriate algorithmic tangent of the coupled problem at hand is given by

$$\boldsymbol{C}_{alg}^{if,fer,tbf} = \begin{bmatrix} \boldsymbol{C}_{uu}^{tbf} & \boldsymbol{c}_{u\Phi}^{tbf} \\ \\ \boldsymbol{c}_{\Phi u}^{tbf} & c_{\Phi\Phi}^{tbf} \end{bmatrix} \tag{3.257}$$

The components of $\boldsymbol{C}_{alg}^{if,fer,tbf}$ are stated in the below. To compute those components, some auxiliary computations are carried out:

$$\frac{\partial\epsilon_r}{\partial d_{n+1}} = \epsilon_r^{end} - \epsilon_r^{init} \tag{3.258}$$

given:	$[\![\boldsymbol{u}]\!]_{n+1},\ E_{n+1},\ d_n$
1. damage update:	$\tilde{\delta}_{n+1} = \tilde{\delta}_n + \langle \delta_{n+1} - \delta_n \rangle, \quad \tilde{\delta}_0 = 0$
	$d_{n+1} = \exp\Big(- \dfrac{\breve{\alpha}}{\tilde{\delta}_{n+1}} \Big)$
2. traction update:	$\boldsymbol{\tau}_{n+1} = [1 - d_{n+1}]\, \boldsymbol{C}^{if,el} \cdot [\![\boldsymbol{u}]\!]_{n+1} - E_{n+1} \boldsymbol{e}^{if}$
3. dielectric displacement update:	$\Lambda_{n+1} = \boldsymbol{e}^{if} \cdot [\![\boldsymbol{u}]\!]_{n+1} + \epsilon_0 \epsilon_r(d_{n+1})\, E_{n+1}$
4. tangent modulus:	$\boldsymbol{C}_{alg}^{if,fer,tbf}$

Table 3.6: Algorithmic procedure for interfacial ferroelectric time-based fatigue

$$\frac{\partial d_{n+1}}{\partial [\![\Phi]\!]_{n+1}} = \exp\Big(- \frac{\breve{\alpha}}{\tilde{\delta}_{n+1}} \Big)\, \breve{\alpha}\, \tilde{\delta}_{n+1}^{-2}\, \delta_{n+1}^{-1}\, \zeta^{tbf}\, \beta_\Phi^2\, [\![\Phi]\!]_{n+1} \tag{3.259}$$

Additionally, equations (3.188), (3.189) and (3.190) hold, as well as equations (3.191) and (3.192). Finally, it holds

$$\boldsymbol{C}_{uu}^{tbf} = \frac{\partial \boldsymbol{\tau}_{n+1}}{\partial [\![\boldsymbol{u}]\!]_{n+1}} = \boldsymbol{C}_{alg}^{if,tbf} \tag{3.260}$$

with the effective quantity as stated in equation (3.255). Moreover, it is

$$\begin{aligned} \boldsymbol{c}_{u\Phi}^{tbf} &= \frac{\partial \boldsymbol{\tau}_{n+1}}{\partial [\![\Phi]\!]_{n+1}} = -[\boldsymbol{C}^{if,el} \cdot [\![\boldsymbol{u}]\!]_{n+1}] \frac{\partial d_{n+1}}{\partial [\![\Phi]\!]_{n+1}} + \boldsymbol{e}^{if} \\ &= -\exp\Big(- \frac{\breve{\alpha}}{\tilde{\delta}_{n+1}} \Big)\, \breve{\alpha}\, \tilde{\delta}_{n+1}^{-2}\, \delta_{n+1}^{-1}\, \zeta^{tbf}\, \beta_\Phi^2\, [\![\Phi]\!]_{n+1}\, [\boldsymbol{C}^{if,el} \cdot [\![\boldsymbol{u}]\!]_{n+1}] + \boldsymbol{e}^{if} \end{aligned} \tag{3.261}$$

The third component is given by

$$\begin{aligned} \boldsymbol{c}_{\Phi u}^{tbf} &= \frac{\partial \Lambda_{n+1}}{\partial [\![\boldsymbol{u}]\!]_{n+1}} = \boldsymbol{e}^{if} - \epsilon_0\, [\![\Phi]\!]_{n+1} \frac{\partial \epsilon_{r,n+1}}{\partial d_{n+1}} \frac{\partial d_{n+1}}{\partial [\![\boldsymbol{u}]\!]_{n+1}} \\ &= \boldsymbol{e}^{if} - \epsilon_0\, [\epsilon_r^{end} - \epsilon_r^{init}]\, [\![\Phi]\!]_{n+1}\, \exp\Big(- \frac{\breve{\alpha}}{\tilde{\delta}_{n+1}} \Big)\, \breve{\alpha}\, \tilde{\delta}_{n+1}^{-2}\, \delta_{n+1}^{-1}\, \zeta^{tbf} \sum_i \beta_i^2\, [\![\boldsymbol{u}_i]\!]_{n+1} \end{aligned} \tag{3.262}$$

while the fourth component is computed as

$$\begin{aligned} c^{tbf}_{\Phi\Phi} &= \frac{\partial \Lambda_{n+1}}{\partial [\![\Phi]\!]_{n+1}} = -\epsilon_0 \epsilon_{r,n+1}(d_{n+1}) - \epsilon_0 \, [\![\Phi]\!]_{n+1} \, \frac{\partial \epsilon_{r,n+1}}{\partial d_{n+1}} \, \frac{\partial d_{n+1}}{\partial [\![\Phi]\!]_{n+1}} \\ &= -\epsilon_0 \epsilon_{r,n+1}(d_{n+1}) \\ &- \epsilon_0 \, [\epsilon_r^{end} - \epsilon_r^{init}] \, [\![\Phi]\!]_{n+1} \, \exp\Big(- \frac{\check{\alpha}}{\tilde{\delta}_{n+1}} \Big) \, \check{\alpha} \, \tilde{\delta}_{n+1}^{-2} \, \delta_{n+1}^{-1} \, \zeta^{tbf} \, \beta_\Phi^2 \, [\![\Phi]\!]_{n+1} \end{aligned} \tag{3.263}$$

Please note that, due to the non-associated character of the fatigue law incorporated, $\boldsymbol{C}^{if,fer,tbf}_{alg}$ turns out to be in general non-symmetric. A comprehension of the algorithmic procedure is given in Tab. 3.6.

3.8.3 Algorithmic Aspects: Cycle-Based Fatigue Formulation

Concerning cycle-based fatigue, the update of tractions and dielectric displacements is the same as for time-based fatigue, see equation (3.256). The algorithmic tangent is given by

$$\boldsymbol{C}^{if,fer,cbf}_{alg} = \begin{bmatrix} \boldsymbol{C}^{cbf}_{uu} & \boldsymbol{c}^{cbf}_{u\Phi} \\ \boldsymbol{c}^{cbf}_{\Phi u} & c^{cbf}_{\Phi\Phi} \end{bmatrix} \tag{3.264}$$

For the subsequent tangent computation, an auxiliary computation is performed as

$$\frac{\partial d_{n+1}}{\partial [\![\Phi]\!]_{n+1}} = \frac{1}{2} \, \zeta^{cbf} \, \Delta N \, \Omega^{cbf} \, C \, \exp(\check{\gamma} \, d_p) \, \delta_{a,n+1}^{\check{\beta}-1} \, \beta_\Phi^2 \, [\![\Phi]\!]_{n+1} \tag{3.265}$$

In view of equations (3.207)–(3.215), the first component is computed as

$$\boldsymbol{C}^{cbf}_{uu} = \frac{\partial \boldsymbol{\tau}_{n+1}}{\partial [\![\boldsymbol{u}]\!]_{n+1}} = \boldsymbol{C}^{if,cbf}_{alg} \tag{3.266}$$

The second component reads as

$$\begin{aligned} \boldsymbol{c}^{cbf}_{u\Phi} &= \frac{\partial \boldsymbol{\tau}_{n+1}}{\partial [\![\Phi]\!]_{n+1}} = -[\boldsymbol{C}^{if,el} \cdot [\![\boldsymbol{u}]\!]_{n+1}] \, \frac{\partial d_{n+1}}{\partial [\![\Phi]\!]_{n+1}} + \boldsymbol{e}^{if} \\ &= -\frac{1}{2} \, \zeta^{cbf} \, \Delta N \, \Omega^{cbf} \, C \, \exp(\check{\gamma} \, d_p) \, \delta_{a,n+1}^{\check{\beta}-1} \, \beta_\Phi^2 \, [\![\Phi]\!]_{n+1} \, [\boldsymbol{C}^{if,el} \cdot [\![\boldsymbol{u}]\!]_{n+1}] + \boldsymbol{e}^{if} \end{aligned} \tag{3.267}$$

given:	$[\![\boldsymbol{u}]\!]_{n+1},\ E_{n+1},\ d_n$
1. damage update:	$\zeta^{cbf} = \begin{cases} 1 & \text{if} \quad \delta_a > \kappa \\ 0 & \text{else} \end{cases}$
	compute $d_p,\ Z(d_n, \delta_{a,n}),\ Z(d_p, \delta_{a,n+1})$
	$d_{n+1} = d_n + \frac{1}{2}\zeta^{cbf}[Z(d_n, \delta_{a,n}) + Z(d_p, \delta_{a,n+1})]$
2. traction update:	$\boldsymbol{\tau}_{n+1} = [1 - d_{n+1}]\, \boldsymbol{C}^{if,el} \cdot [\![\boldsymbol{u}]\!]_{n+1} - E_{n+1}\boldsymbol{e}^{if}$
3. dielectric displacement update:	$\Lambda_{n+1} = \boldsymbol{e}^{if} \cdot [\![\boldsymbol{u}]\!]_{n+1} + \epsilon_0\epsilon_r(d_{n+1})\, E_{n+1}$
4. tangent modulus:	$\boldsymbol{C}^{if,fer,cbf}_{alg}$

Table 3.7: Algorithmic procedure for interfacial ferroelectric cycle-based fatigue

The third component is computed by

$$\begin{aligned} \boldsymbol{c}^{cbf}_{\Phi u} &= \frac{\partial \Lambda_{n+1}}{\partial [\![\boldsymbol{u}]\!]_{n+1}} = \boldsymbol{e}^{if} - \epsilon_0\, [\![\Phi]\!]_{n+1}\, \frac{\partial \epsilon_{r,n+1}}{\partial d_{n+1}}\, \frac{\partial d_{n+1}}{\partial [\![\boldsymbol{u}]\!]_{n+1}} \\ &= \boldsymbol{e}^{if} - \epsilon_0\, [\epsilon_r^{end} - \epsilon_r^{init}]\, [\![\Phi]\!]_{n+1}\, \frac{1}{2}\, \zeta^{cbf}\, \Delta N\, \Omega^{cbf}\, C\, \exp(\check{\gamma}\, d_p)\, \delta_{a,n+1}^{\check{\beta}-1} \sum_i \beta_i^2\, [\![\boldsymbol{u}_i]\!]_{n+1} \end{aligned} \tag{3.268}$$

Finally, the fourth component is given as

$$\begin{aligned} c^{cbf}_{\Phi\Phi} &= \frac{\partial \Lambda_{n+1}}{\partial [\![\Phi]\!]_{n+1}} = -\epsilon_0\epsilon_{r,n+1}(d_{n+1}) - \epsilon_0\, [\![\Phi]\!]_{n+1}\, \frac{\partial \epsilon_{r,n+1}}{\partial d_{n+1}}\, \frac{\partial d_{n+1}}{\partial [\![\Phi]\!]_{n+1}} \\ &= -\epsilon_0\epsilon_{r,n+1}(d_{n+1}) \\ &- \epsilon_0\, [\epsilon_r^{end} - \epsilon_r^{init}]\, [\![\Phi]\!]_{n+1}\, \frac{1}{2}\, \zeta^{cbf}\, \Delta N\, \Omega^{cbf}\, C\, \exp(\check{\gamma}\, d_p)\, \delta_{a,n+1}^{\check{\beta}-1}\, \beta_\Phi^2\, [\![\Phi]\!]_{n+1} \end{aligned} \tag{3.269}$$

Because of the non-associated character of the fatigue law, $\boldsymbol{C}^{if,fer,cbf}_{alg}$ is generally non-symmetric. A

concise comprehension of the algorithmic procedure is given in Tab. 3.7.

3.9 A Penalty Formulation to Avoid Interfacial Self-Penetration

In this section a method to avoid self-penetration of the opposing interfacial bordering surfaces is introduced. In this context self-penetration is identified with negative displacement jumps in normal direction, i.e. $[\![u_n]\!] < 0$. Since self-penetration of solid interfaces is not physical, it has to be guaranteed that

$$[\![\boldsymbol{u}(\boldsymbol{x})]\!] \cdot \boldsymbol{n} \geq 0 \quad \forall \quad \boldsymbol{x} \in \Gamma \tag{3.270}$$

There are several methods to overcome this problem. Useful is the Nitsche method, see Nitsche [128] as well as Hansbo and Hansbo [60] where self-penetration is avoided in weak form, corresponding to the Dirichlet boundary and complementing conditions. For this method a so-called stability parameter has to be chosen. Normally, this parameter would be less than additional stiffnesses as used for classical penalty methods, which can lead to bad conditioned systems of equations. Another strategy is to avoid self-penetration by means of a Lagrange multiplier, see, e.g. [192]. An important disadvantage of this method is the enhancement of the global system of equations by further unknowns. Due to its simplicity, but at the same time being aware of its handicaps, a classical penalty method as described in, e.g. Bertsekas [24], is applied here. The related strategy is to enhance the free energy or,

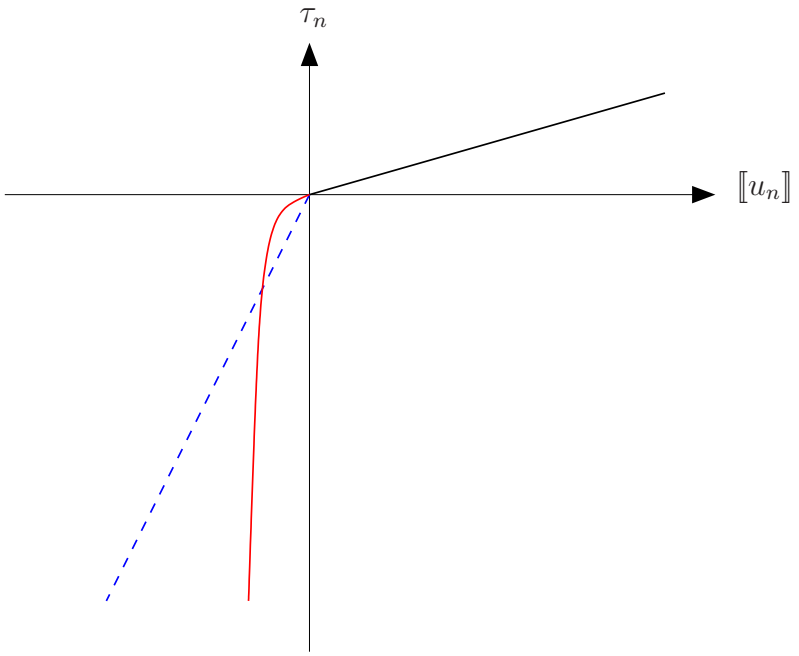

Figure 3.11: Exemplary penalty behaviour. For negative normal displacement jumps, normal stiffnesses are increased steadily (solid line). The dotted behaviour occurs if applying an unsteady, constant penalty stiffness

respectively, the electric enthalpy function by an additional term, leading towards

$$\Psi^* = \Psi + \check{\Psi}, \quad H^* = H + \check{H} \tag{3.271}$$

where

$$\check{\Psi} = \check{H} = \frac{q}{6} \langle -[\![\boldsymbol{u}]\!] \cdot \boldsymbol{n} \rangle^3 \tag{3.272}$$

For all cases discussed previously, this renders the tractions as

$$\boldsymbol{\tau}^*_{n+1} = \boldsymbol{\tau}_{n+1} + \check{\boldsymbol{\tau}}_{n+1} \tag{3.273}$$

with

$$\check{\boldsymbol{\tau}}_{n+1} = -\frac{q}{2} \langle -[\![\boldsymbol{u}]\!]_{n+1} \cdot \boldsymbol{n} \rangle^2 \boldsymbol{n} \tag{3.274}$$

Accordingly, the tangents are also extended by a further summand, reading as

$$\boldsymbol{C}^*_{alg} = \boldsymbol{C}_{alg} + \check{\boldsymbol{C}}_{alg} \tag{3.275}$$

for the purely mechanical case where

$$\check{\boldsymbol{C}}_{alg} = q \langle -[\![\boldsymbol{u}]\!]_{n+1} \cdot \boldsymbol{n} \rangle \boldsymbol{n} \otimes \boldsymbol{n} \tag{3.276}$$

As obsolete in the context of Newton's Method, this strategy renders steady tangents with respect to the relative displacements $[\![\boldsymbol{u}]\!]$, see also Fig. 3.11 for an illustration.

4 Bifurcation Analysis of Uncoupled Continuum-Interface Problems

In the mesomechanical modelling of composites, interfaces between different layers of materials play a decisive role, see e.g. Schellekens [152], Miehe and Schröder [118], Larsson and Jansson [88], Willam et al. [188], Steinmann and Häsner [170] and Utzinger et al. [180]). In particular if non-coherent interfaces are allowed for, i.e. interfacial displacement jumps can occur, the modelling of an appropriate traction-separation-law is a major challenge. It may even be reasonable to project all non-linearities and inelasticities of a problem into the interface law by this type of modelling. As a general rule, well-established constitutive laws for the bulk can be adapted for the constitutive modelling of interfaces. Apart from the constitutive modelling itself, however, an issue of interest is to investigate whether the solution of an incremental boundary value problem (IBVP) incorporating a non-coherent interface may bifurcate at a certain loading state into stationary wave-type solutions or not.

In this regard, with a view on ill-posedness, it is additionally of interest if the number of possible bifurcation modes is finite or not. From the mathematical point of view, ill-posedness is either due to the fact that the underlying boundary-value problem may exhibit an infinite number of linearly independent solutions or to the fact that the solutions of this boundary-value problem do not depend continuously on the data. There is also the possibility for the continuous problem that, in order to have a finite number of linearly independent solutions, and that these solutions depend continuously on the data, one has to enforce an infinite number of linearly independent conditions over these data. These are the general three sources for ill-posedness and necessary and sufficient conditions are known in the case of a linear boundary-value problem for this ill-posedness to occur (Benallal et al. [21], Benallal and Comi [22]). These conditions are respectively the loss of ellipticity of the governing equations, the loss of the boundary complementing condition and eventually the loss of the interfacial boundary condition when the solid is heterogeneous. The first condition is a local condition that only depends on the rate-independent constitutive equations and implies the singularity of the bulk acoustic tensor. While also local in nature, the two other conditions involve the boundary or the interfacial conditions and imply a kind of compatibility between these boundary (interfacial) conditions and the constitutive behaviour. The last two conditions may fail in the bulk elliptic regime where they retain all their importance.

The necessary and sufficient conditions for the IBVP to be well-posed are the ellipticity and the complementing condition. In what follows, the bulk material is assumed to be linearly elastic. Consequently, the constitutive operator is assumed to be positive definite and, therefore, the ellipticity condition is satisfied. Regarding the complementing condition, one has to consider both in the governing equations and in the boundary (interface) conditions the contributions with the highest order (Benallal [18]). In the field equations this is the full operator as all the terms have the same (second) order. The boundary conditions that will be adopted here include zeroth order terms (involving the

displacement field itself) and first order terms (involving the first gradient of this displacement field). Therefore, to check the complementing condition, one has to drop the zeroth order terms and consider only the terms of the highest order. In so doing, one obtains a classical linear elastic boundary value problem with classical (homogeneous) Neumann boundary conditions. For this problem the complementing condition is satisfied if the constitutive operator is positive definite. Nevertheless, bifurcation into stationary wave-type solutions is not ruled out since in this analysis all terms of arbitrary order have to be considered.

In what follows, a semi-infinite three-dimensional elastic bulk bonded via a two-dimensional non-coherent (cohesive) interface to a rigid substrate is considered in a purely mechanical, uncoupled context. Thereby, the possibility of the solution to bifurcate into stationary surface-wave-type solutions is investigated. Consequently, we consider in addition to the well-known ellipticity condition in the bulk, that checks for possible stationary bulk-wave-type solutions and also assures ellipticity of the constitutive operator, a bifurcation condition that checks for possible stationary surface-wave-type solutions incorporating traction-separation-laws at the Neumann boundary.

In the bulk, for constitutive behaviours without a lengthscale, the intimate relation between bifurcation into stationary wave-type solutions and localisation of deformation in the bulk is well-known, see for instance Hill [67], Benallal et al. [19, 20] and Benallal [17]. Fundamental further information on the topic is also provided by the monographs of, e.g. Biot [27], Ogden [130] and Šilhavỳ [185]. Both are a consequence of the failure of the ellipticity condition whereby the wavelength of the stationary wave is arbitrary and thus, in particular, can take zero values. Bifurcation into stationary wave-type solutions at surfaces, coherent interfaces (Rayleigh and Stoneley waves) and their interpretation in terms of localised deformations was discussed by Benallal et al. [21], Dowaikh and Ogden [47], Needleman and Ortiz[126]. Here, both are associated to the failure of the complementing conditions with vanishing wavelength of the stationary waves in the case of localisation. The bifurcation condition for non-coherent planar isotropic interfaces was considered by Suo et al. [173] and Bigoni et al. [26]. These studies were, however, restricted to two-dimensional investigations under the plane strain constraint. As a consequence, the interfacial plane is necessarily assumed to be isotropic. Additionally, non-planar interfaces have been considered for a cylindrical setting by Bigoni and Gei [25] based on a linear relation for the traction-separation rate.

Please note that it is well-established that for rate-independent local continua in the presence of softening and/or non-associative flow, numerical results may be highly sensitive to the space discretisation as present within a, for example, finite element context. This mesh dependency is often observed in the analysis of localisation phenomena and is generally attributed to the lack of a length scale in the continuous description of the constitutive behaviour. Established methods to overcome the problem of mesh sensitivity in a continuum are, e.g. higher gradients – see Mühlhaus and Aifantis [122], de Borst and Mühlhaus [44], Peerlings et al. [141], Steinmann [168], Menzel and Steinmann [112], Svedberg and Runesson [174], Liebe et al. [95], Benallal and Comi [22] and Askes et al. [5] – or non-local continua – see, e.g., Bažant and Pijaudier-Cabot [12] and Bažant [11]. All these formulations include a material lengthscale which renders the problem well-posed. Whether similar enhancements of a softening interface formulation are necessary has to be investigated carefully by checking if solutions with wave number $k \equiv \infty$ are possible.

The subsequent elaborations are believed to be a first step towards the prediction of the above-mentioned space discretisation sensitivities, see also Utzinger et al. [181]. Accordingly, interfacial

traction-separation-laws, as introduced in chapter 3, would play a decisive role. Incorporated in a finite element context, sensitivities would only stem from the interface, as in this context, the bulk is modelled linearly elastic.

4.1 Incremental Boundary Value Problem

Consider a semi-infinite space of bulk material being bonded via a non-coherent cohesive interface layer to a rigid substrate. In the following, a quasi-static incremental boundary value problem (IBVP) with small strain kinematics is assumed.

Accordingly, the balance of linear momentum in the semi-infinite space is here given by means of the incremental stress tensor $\delta\boldsymbol{\sigma}$

$$\operatorname{div}\delta\boldsymbol{\sigma} = \mathbf{0} \tag{4.1}$$

and the underlying kinematics are represented by relating incremental strains $\delta\boldsymbol{\varepsilon}$ to incremental displacements $\delta\boldsymbol{u}$, namely

$$\delta\boldsymbol{\varepsilon} = \nabla_{\boldsymbol{x}}^{sym}\delta\boldsymbol{u} \tag{4.2}$$

The constitutive relation, with $\mathbb{C}$ being the incremental constitutive operator, consequently takes the format

$$\delta\boldsymbol{\sigma} = \mathbb{C} : \delta\boldsymbol{\varepsilon} \tag{4.3}$$

so that combining equations (4.1), (4.2) and (4.3), for a homogeneous state, renders the quasi-static incremental balance of linear momentum, volume forces being neglected, as

$$\operatorname{div}\delta\boldsymbol{\sigma} = \operatorname{div}(\mathbb{C} : \nabla_{\boldsymbol{x}}\,\delta\boldsymbol{u}) = [\mathbb{C} : \nabla_{\boldsymbol{x}}\nabla_{\boldsymbol{x}}\,\delta\boldsymbol{u}] : \boldsymbol{I} = \mathbf{0} \tag{4.4}$$

whereby use of the minor symmetry of $\mathbb{C}$ has been made.

Next, Neumann boundary conditions for the bulk are defined: the incremental stress tensor $\delta\boldsymbol{\sigma}$ of the bulk and the incremental traction vector $\delta\boldsymbol{\tau}$ of the interface are related by

$$\delta\boldsymbol{\sigma}\cdot\boldsymbol{n} = \delta\boldsymbol{\tau} \tag{4.5}$$

The corresponding constitutive law for the interface, established as traction-separation-law, defines $\delta\boldsymbol{\tau}$ in terms of the incremental displacement jump $[\![\delta\boldsymbol{u}]\!]$. By analogy with equation (4.3), $\boldsymbol{C}^{if}$ denotes the interfacial incremental constitutive operator so that

$$\delta\boldsymbol{\tau} = \boldsymbol{C}^{if}\cdot[\![\delta\boldsymbol{u}]\!] \tag{4.6}$$

4.2 Stationary Wave-Type Ansatz for the Displacements

The correspondence between bifurcation phenomena and stationary wave-type solutions is well-established and documented in the classical mechanics literature, see the references cited before. Accordingly, an incremental stationary wave-type ansatz for $\delta\boldsymbol{u}$ is given as

$$\delta\boldsymbol{u}(\boldsymbol{x}) = \exp(i[\boldsymbol{k}\cdot\tilde{\boldsymbol{x}}])\,\boldsymbol{m} \tag{4.7}$$

wherein $\boldsymbol{m}$ is the amplitude vector and i is the imaginary unit. The two remaining vectorial contributions are $\boldsymbol{k} = \check{\boldsymbol{k}} + i\boldsymbol{k}^*$, which is the complex wave vector, composed of a real part $\check{\boldsymbol{k}}$ and an imaginary part $\boldsymbol{k}^*$. Moreover, the argument itself (on the right hand side) is denoted by $\tilde{\boldsymbol{x}}(\boldsymbol{x})$ with $\partial\tilde{\boldsymbol{x}}/\partial\boldsymbol{x} = \boldsymbol{I}$. Based on this ansatz, equation (4.7) may be rewritten more explicitly as

$$\delta\boldsymbol{u}(\boldsymbol{x}) = \exp(i[\check{\boldsymbol{k}} \cdot \tilde{\boldsymbol{x}} + i\boldsymbol{k}^* \cdot \tilde{\boldsymbol{x}}])\, \boldsymbol{m} = \exp(-\boldsymbol{k}^* \cdot \tilde{\boldsymbol{x}})\, \exp(i\, \check{\boldsymbol{k}} \cdot \tilde{\boldsymbol{x}})\, \boldsymbol{m} \tag{4.8}$$

Thus, $\boldsymbol{k}^*$ is responsible for a possible decay of $\delta\boldsymbol{u}$ whereas $\check{\boldsymbol{k}}$ controls the waviness of $\delta\boldsymbol{u}$. In view of equation (4.2), the wave-type ansatz yields

$$\nabla_{\boldsymbol{x}}\, \delta\boldsymbol{u} = i\, \exp(i[\boldsymbol{k} \cdot \tilde{\boldsymbol{x}}])\, \boldsymbol{m} \otimes \boldsymbol{k} \tag{4.9}$$

for the first gradient of the incremental displacement while the second gradient results in

$$\nabla_{\boldsymbol{x}} \nabla_{\boldsymbol{x}}\, \delta\boldsymbol{u} = -\exp(i[\boldsymbol{k} \cdot \tilde{\boldsymbol{x}}])\, \boldsymbol{m} \otimes \boldsymbol{k} \otimes \boldsymbol{k} \tag{4.10}$$

With these relations in hand, equation (4.4) is rewritten as

$$[\mathbb{C} : [\boldsymbol{m} \otimes \boldsymbol{k} \otimes \boldsymbol{k}]] : \boldsymbol{I} = \boldsymbol{Q} \cdot \boldsymbol{m} = \boldsymbol{0} \tag{4.11}$$

wherein the complex second order tensor $\boldsymbol{Q}$ is defined as (for $[\bullet]$ denoting a vectorial quantity)

$$\boldsymbol{Q} \cdot [\bullet] = [\mathbb{C} : [[\bullet] \otimes \boldsymbol{k}]] \cdot \boldsymbol{k} \tag{4.12}$$

The overall solution condition for equation (4.11) – to be specific, non-trivial solutions for $\boldsymbol{m}$ – corresponds to

$$\det \boldsymbol{Q} \doteq 0 \tag{4.13}$$

In general, equation (4.13) characterises the first condition for the occurrence of stationary wave-type solutions in the format (4.7). Please note that, to this point, boundary conditions have not yet been incorporated. In the following, we specify constitutive relations entering equation (4.3) and (4.6), respectively. The bulk is assumed to be isotropic linearly elastic while the interface is allowed to additionally account for inelastic effects. Special emphasis will be placed on interface-related stationary wave-type solutions. Since the traction-separation-law might incorporate, say, tangential stress contributions, such stationary waves are in general of anisotropic nature.

4.3 Isotropic Linear Elastic Bulk Material

Since this work focusses on interface relations, the bulk material is restricted to be isotropic and linear elastic, i.e.

$$\mathbb{C} = \lambda \boldsymbol{I} \otimes \boldsymbol{I} + 2\mu\, \mathbb{I}^{sym} = \mathbb{C}^{iso} \tag{4.14}$$

Accordingly, $\boldsymbol{Q}$ can explicitly be expressed as

$$\boldsymbol{Q} = [\lambda + \mu]\, \boldsymbol{k} \otimes \boldsymbol{k} + \mu\, [\boldsymbol{k} \cdot \boldsymbol{k}] \boldsymbol{I} \tag{4.15}$$

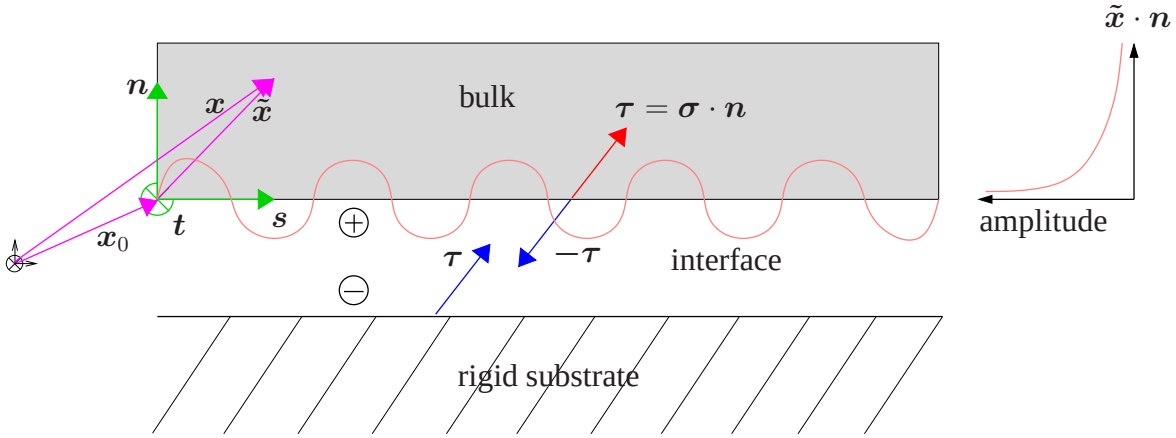

Figure 4.1: Graphical illustration of essential quantities related to the interfacial zone

Next, solutions of equation (4.13) are sought. Straightforward calculation of the underlying eigenvalue-problem of $\boldsymbol{Q}$ renders the eigenvalues (two of them being identical) as

$$\nu_0 = [2\mu + \lambda]\,[\boldsymbol{k} \cdot \boldsymbol{k}] \qquad \nu_1 = \nu_2 = \mu\,[\boldsymbol{k} \cdot \boldsymbol{k}] \tag{4.16}$$

This analysis results in

$$\det \boldsymbol{Q} = \mu^2[2\mu + \lambda][\boldsymbol{k} \cdot \boldsymbol{k}]^3 \doteq 0 \tag{4.17}$$

4.3.1 Incremental Ellipticity Condition for the Bulk Material

Focussing solely on the bulk material, let the wave vector $\boldsymbol{k}$ coincide with an arbitrary real-valued unit-vector. In this regard, equation (4.17) is reduced to

$$\det \boldsymbol{Q} = \mu^2[2\mu + \lambda] = \det \boldsymbol{Q}^{\diamond} \tag{4.18}$$

with $[2\mu + \lambda]$ being interpreted as a compression wave speed in the bulk, while μ characterises a bulk shear wave speed. The (incremental) condition of stability or rather strong Legendre-Hadamard ellipticity for the bulk material itself results in $q^{\diamond} := \text{sign}(\min(q_1^{\diamond}, q_2^{\diamond}, q_3^{\diamond}))\,|q_3^{\diamond}| > 0$ with $q_1^{\diamond} = Q_{11}^{\diamond}$, $q_2^{\diamond} = Q_{11}^{\diamond}Q_{22}^{\diamond} - Q_{12}^{\diamond}Q_{21}^{\diamond}$ and $q_3^{\diamond} = \det \boldsymbol{Q}^{\diamond}$, see also Schröder et al. [157]. This is assumed to hold in the following. Hence, stationary wave-type solutions stem exclusively from interfacial effects.

4.3.2 Specification of the Wave Vector

Let $\boldsymbol{x}_0$ denote the position vector to the origin of a local interfacial orthonormal base system $\{\boldsymbol{s}, \boldsymbol{t}, \boldsymbol{n}\}$. Furthermore, we introduce $\tilde{\boldsymbol{x}}(\boldsymbol{x}) = \boldsymbol{x} - \boldsymbol{x}_0$ as the argument entering equation (4.7), in other words, the position vector with respect to the local coordinate system. For convenience of the reader, Fig. 4.1 gives a graphical illustration of essential quantities related to the interfacial zone. As visualised, small deformation conditions are assumed with the interfacial surfaces remaining parallel. As a consequence, the bulk normal and the normal vector $\boldsymbol{n}$ of the local interfacial base system turn out to be collinear. Since the wave vector is in general not aligned with any of the base vectors $\{\boldsymbol{s}, \boldsymbol{t}, \boldsymbol{n}\}$, it turns

out to be convenient to introduce

$$\boldsymbol{k} = k_1\,\boldsymbol{e}_1 + k_2\,\boldsymbol{e}_2 + k_3\,\boldsymbol{e}_3 \quad \text{with} \quad k_j = \check{k}_j + i\,k_j^* \quad \text{and} \quad j = 1,2,3 \tag{4.19}$$

with $\{\boldsymbol{e}_1, \boldsymbol{e}_2, \boldsymbol{e}_3\}$ being the Cartesian base system. Bounded solutions require stationary waves to decay towards the bulk material. For the problem at hand, as displayed in Fig. 4.1, the decay direction must coincide with the normal direction $\boldsymbol{n}$ of the interface. Assuming the interface to be able to bifurcate and the bulk, as discussed above, to be (incrementally) elliptic, the harmonic direction – which in the classical dynamics literature is often referred to as the propagation direction – of the stationary wave lies in the plane spanned by the base vectors $\boldsymbol{s}$ and $\boldsymbol{t}$. In addition, let $\boldsymbol{e}_3 \doteq \boldsymbol{n}$ so that $\boldsymbol{e}_1$ and $\boldsymbol{e}_2$ span the same space as $\boldsymbol{s}$ and $\boldsymbol{t}$. Incorporating the essential decay characteristics renders $\boldsymbol{k} \cdot \boldsymbol{e}_3$ to be purely imaginary, i.e. $k_3 = ik_3^*$ (recall that $i\,\boldsymbol{k}$ enters equation (4.7)). Without loss of generality, we set $\check{k}_2 = 0$ as well as $k_2^* = 0$ in the progression of this work. In other words, $\boldsymbol{e}_1$ determines the tangential direction of $\boldsymbol{k}$ according to which stationary surface-wave-type solutions might occur with decay effects being excluded for this direction such that $k_1 = \check{k}_1$. Consequently, the wave vector allows representation as

$$\boldsymbol{k} = \check{k}_1 \boldsymbol{e}_1 + ik_3^* \boldsymbol{e}_3 \tag{4.20}$$

In order to abbreviate notations, and in view of subsequent considerations, the wave vector coefficients are re-named as $\check{k}_1 = k$, $k_3^* = -\nu$. Additionally, $\zeta = \boldsymbol{e}_1 \cdot \tilde{\boldsymbol{x}}$ as well as $\eta = \boldsymbol{e}_3 \cdot \tilde{\boldsymbol{x}}$ are introduced and, moreover, a decay function $\boldsymbol{w}(\eta)$ is defined via

$$\delta\boldsymbol{u}(\boldsymbol{x}) = \exp(i[\boldsymbol{k} \cdot \tilde{\boldsymbol{x}}])\,\boldsymbol{m} = \underbrace{\exp(\nu\,\eta)\,\boldsymbol{m}}_{\boldsymbol{w}(\eta)}\,\exp(ik\,\zeta) \tag{4.21}$$

For a not yet specified bulk material, equation (4.21) leads to a representation of the incremental balance of linear momentum (4.4) by means of three second order tensors $\boldsymbol{Q}_0$, $\boldsymbol{Q}_1$, and $\boldsymbol{Q}_2 = \boldsymbol{Q}^{\diamond}$, namely

$$\boldsymbol{Q}_2 \cdot \boldsymbol{w}'' + ik\;\boldsymbol{Q}_1 \cdot \boldsymbol{w}' - k^2\;\boldsymbol{Q}_0 \cdot \boldsymbol{w} = \boldsymbol{0} \tag{4.22}$$

with

$$\begin{aligned} \boldsymbol{Q}_0 \cdot [\bullet] &:= [\mathbb{C} : [[\bullet] \otimes \boldsymbol{e}_1]] \cdot \boldsymbol{e}_1 \\ \boldsymbol{Q}_1 \cdot [\bullet] &:= [\mathbb{C} : [[\bullet] \otimes \boldsymbol{e}_3]] \cdot \boldsymbol{e}_1 + [\mathbb{C} : [[\bullet] \otimes \boldsymbol{e}_1]] \cdot \boldsymbol{e}_3 \\ \boldsymbol{Q}_2 \cdot [\bullet] &:= [\mathbb{C} : [[\bullet] \otimes \boldsymbol{e}_3]] \cdot \boldsymbol{e}_3 \end{aligned} \tag{4.23}$$

Equation (4.22) is a system of ordinary differential equations of second order in η. It is treated by reformulation as an ordinary differential equation system of first order, to be solved by well-known strategies. Equation (4.22) can then be rewritten as

$$\boldsymbol{w}'' + ik\;\boldsymbol{Q}_2^{-1} \cdot \boldsymbol{Q}_1 \cdot \boldsymbol{w}' - k^2\;\boldsymbol{Q}_2^{-1} \cdot \boldsymbol{Q}_0 \cdot \boldsymbol{w} = \boldsymbol{0} \tag{4.24}$$

Having a linear elastic bulk material in mind, as reviewed in section 4.3, the (acoustic-type) tensors in equation (4.23) read as

$$\begin{aligned} \boldsymbol{Q}_0 &= [\lambda+\mu]\ \boldsymbol{e}_1 \otimes \boldsymbol{e}_1 + \mu \boldsymbol{I} \\ \boldsymbol{Q}_1 &= [\lambda+\mu]\,[\boldsymbol{e}_3 \otimes \boldsymbol{e}_1 + \boldsymbol{e}_1 \otimes \boldsymbol{e}_3] \\ \boldsymbol{Q}_2 &= [\lambda+\mu]\ \boldsymbol{e}_3 \otimes \boldsymbol{e}_3 + \mu \boldsymbol{I} \end{aligned} \tag{4.25}$$

By applying the Sherman-Morrison formula, the inverse of $\boldsymbol{Q}_2$ is thus found as

$$\boldsymbol{Q}_2^{-1} = \frac{1}{\mu}\boldsymbol{I} - \frac{[\lambda+\mu]}{\mu^2+\mu[\lambda+\mu]}\,\boldsymbol{e}_3 \otimes \boldsymbol{e}_3 \tag{4.26}$$

4.3.3 Reformulation as a First Order System

Now, we define

$$\boldsymbol{z} = \begin{bmatrix} \boldsymbol{w} \\ \boldsymbol{w}' \end{bmatrix} \tag{4.27}$$

With this in hand, equation (4.24) is rewritten as

$$\boldsymbol{z}' = \underbrace{\begin{bmatrix} \boldsymbol{0} & \boldsymbol{I} \\ k^2\,\boldsymbol{Q}_2^{-1}\cdot\boldsymbol{Q}_0 & -ik\,\boldsymbol{Q}_2^{-1}\cdot\boldsymbol{Q}_1 \end{bmatrix}}_{\boldsymbol{A}} \cdot \boldsymbol{z} \tag{4.28}$$

For the system at hand, a fundamental system of six linearly independent solutions is required. At first, the eigenproblem of $\boldsymbol{A}$ is analysed. With

$$\boldsymbol{z} = \underbrace{\begin{bmatrix} \boldsymbol{m} \\ \nu\boldsymbol{m} \end{bmatrix}}_{\boldsymbol{g}} \exp(\nu\eta) \tag{4.29}$$

equation (4.28) is equivalent to

$$[\boldsymbol{A} - \nu\,\boldsymbol{I}_6] \cdot \boldsymbol{g} = \boldsymbol{0} \tag{4.30}$$

compare appendix A. The eigenvalues ν are found by

$$\det(\boldsymbol{A} - \nu\,\boldsymbol{I}_6) = -[k^2 - \nu^2]^3 \doteq 0 \tag{4.31}$$

which is an equation of degree six in ν rendering

$$\nu_I = \nu_1 = \nu_2 = \nu_3 = -k, \quad \nu_{II} = \nu_4 = \nu_5 = \nu_6 = k \tag{4.32}$$

In the following, all eigenvectors and generalised eigenvectors are represented in terms of their coefficients with respect to a six-dimensional Cartesian base system $\{\boldsymbol{e}_1, ..., \boldsymbol{e}_6\}$. The associated eigenspaces

are given by

$$\boldsymbol{g}_I = \omega_1 \begin{bmatrix} 0 \\ -\frac{1}{k} \\ 0 \\ 0 \\ 1 \\ 0 \end{bmatrix} + \omega_2 \begin{bmatrix} \frac{i}{k} \\ 0 \\ -\frac{1}{k} \\ -i \\ 0 \\ 1 \end{bmatrix}, \qquad \boldsymbol{g}_{II} = \omega_3 \begin{bmatrix} 0 \\ \frac{1}{k} \\ 0 \\ 0 \\ 1 \\ 0 \end{bmatrix} + \omega_4 \begin{bmatrix} \frac{i}{k} \\ 0 \\ \frac{1}{k} \\ i \\ 0 \\ 1 \end{bmatrix}, \quad \omega_1, \omega_2, \omega_3, \omega_4 \in \mathcal{C} \tag{4.33}$$

Obviously, we have two eigenvalues with an algebraic multiplicity of three and two corresponding eigenspaces, each inhering a geometric multiplicity of two. This induces the necessity to compute two further generalised eigenvectors, both linearly independent with respect to the four linearly independent eigenvectors which are chosen as

$$\boldsymbol{v}_1 = \begin{bmatrix} 0 \\ -\frac{1}{k} \\ 0 \\ 0 \\ 1 \\ 0 \end{bmatrix}, \quad \boldsymbol{v}_2 = \begin{bmatrix} \frac{i}{k} \\ 0 \\ -\frac{1}{k} \\ -i \\ 0 \\ 1 \end{bmatrix}, \quad \boldsymbol{v}_3 = \begin{bmatrix} 0 \\ \frac{1}{k} \\ 0 \\ 0 \\ 1 \\ 0 \end{bmatrix}, \quad \boldsymbol{v}_4 = \begin{bmatrix} \frac{i}{k} \\ 0 \\ \frac{1}{k} \\ i \\ 0 \\ 1 \end{bmatrix} \tag{4.34}$$

After straightforward computations, the generalised eigenvectors are obtained

$$\boldsymbol{v}_1^* = \begin{bmatrix} -\dfrac{i}{k^2}\dfrac{2\mu}{\mu+\lambda} \\ 0 \\ -\dfrac{1}{k^2} \\ \dfrac{i}{k}\dfrac{3\mu+\lambda}{\mu+\lambda} \\ 0 \\ 0 \end{bmatrix}, \qquad \boldsymbol{v}_2^* = \begin{bmatrix} \dfrac{i}{k^2}\dfrac{2\mu}{\mu+\lambda} \\ 0 \\ -\dfrac{1}{k^2} \\ \dfrac{i}{k}\dfrac{3\mu+\lambda}{\mu+\lambda} \\ 0 \\ 0 \end{bmatrix} \tag{4.35}$$

4.3.4 Bounded Solution

Proceeding along equations (A.3) and (A.4), the general solution $\boldsymbol{z}$ of the first order system is derived. The linear independence of fundamental solutions is checked by computing the so-called Wronski determinant $w = \det \boldsymbol{Z}(\eta)$ of the associated fundamental matrix $\boldsymbol{Z}$. Necessarily, $w \neq 0$ has to be fulfilled, being the case for the system at hand. The first three components of the general solution vector $\boldsymbol{z}$, being expressed in coefficients with respect to the Cartesian base system $\{\boldsymbol{e}_1, \boldsymbol{e}_2, \boldsymbol{e}_3\}$, are then identical with the solution $\boldsymbol{w}(\eta)$ of the second order system from equation (4.22), reading as

$$\begin{aligned} \boldsymbol{w}(\eta) = \quad & \exp(-k\eta) \begin{bmatrix} c_2\dfrac{i}{k} - c_5\dfrac{2i\mu}{k^2[\mu+\lambda]} \\ -c_1\dfrac{1}{k} \\ -c_2\dfrac{1}{k} - c_5\dfrac{1}{k^2} \end{bmatrix} + \exp(k\eta) \begin{bmatrix} c_4\dfrac{i}{k} + c_6\dfrac{2i\mu}{k^2[\mu+\lambda]} \\ c_3\dfrac{1}{k} \\ c_4\dfrac{1}{k} - c_6\dfrac{1}{k^2} \end{bmatrix} \\ + \quad & \eta\exp(-k\eta) \begin{bmatrix} c_5\dfrac{i}{k} \\ 0 \\ -c_5\dfrac{1}{k} \end{bmatrix} + \eta\exp(k\eta) \begin{bmatrix} c_6\dfrac{i}{k} \\ 0 \\ c_6\dfrac{1}{k} \end{bmatrix} \end{aligned} \tag{4.36}$$

This solution has six constants $\boldsymbol{c} = [c_1, c_2, c_3, c_4, c_5, c_6]^t \in \mathcal{C}^6$. To achieve a bounded solution, only stationary waves decaying towards the bulk material may be considered. In this regard, k is chosen to be positive, and consequently, all non-decaying solutions are neglected. Therefore, only terms with decaying exponential factors are left. Expressed in coefficients with respect to the Cartesian base

system $\{\boldsymbol{e}_1, \boldsymbol{e}_2, \boldsymbol{e}_3\}$, this leads towards

$$\boldsymbol{w}(\eta) = \exp(-k\eta) \begin{bmatrix} c_2\frac{i}{k} - c_5\frac{2i\mu}{k^2[\mu+\lambda]} \\ -c_1\frac{1}{k} \\ -c_2\frac{1}{k} - c_5\frac{1}{k^2} \end{bmatrix} + \eta\, \exp(-k\eta) \begin{bmatrix} c_5\frac{i}{k} \\ 0 \\ -c_5\frac{1}{k} \end{bmatrix} \tag{4.37}$$

An equivalent strategy would be to choose k to be negative and, again, neglect the resulting non-decaying solution parts. Considering equations (4.21) and (4.37) and renaming the ansatz constants as $\boldsymbol{a} = [a_0, a_1, a_2]^t \in \mathcal{C}^3$ renders after some transformations the incremental displacements as

$$\delta\boldsymbol{u}(\boldsymbol{x}) = \exp(k[i\zeta - \eta]) \Big[\big[a_0 + a_1 k\eta - a_1\frac{2\mu}{[\mu+\lambda]}\big]\boldsymbol{e}_1 \,+\, a_2\boldsymbol{e}_2 \,+\, i\big[a_0 + a_1 k\eta + a_1\big]\boldsymbol{e}_3 \Big] \tag{4.38}$$

Being a linear combination of fundamental solutions, this solution trivially fulfils the PDE (4.1).

4.4 Traction Boundary Conditions at the Interface

In this section special emphasis is placed on traction-separation-laws relating the interface behaviour to the bulk response via Cauchy's theorem. Based on equations reviewed in section 4.1 and recalling that $\boldsymbol{n} = \boldsymbol{e}_3$, one obtains

$$\delta\boldsymbol{\sigma} \cdot \boldsymbol{e}_3 = \delta\boldsymbol{\tau} = \boldsymbol{C}^{if} \cdot \delta\boldsymbol{u} \quad \text{at} \quad \tilde{\boldsymbol{x}} \cdot \boldsymbol{e}_3 = \eta = 0 \tag{4.39}$$

with the rigid substrate being fixed in space. Here we associate $\boldsymbol{C}^{if}$ with the tangent of a linear comparison solid (Hill [66]), i.e. unloading is neglected. To further specify $\delta\boldsymbol{\sigma}$, as determined by equations (4.3), (4.2) and (4.14), yielding

$$\delta\boldsymbol{\sigma} = \lambda[\nabla_{\boldsymbol{x}}\, \delta\boldsymbol{u} : \boldsymbol{I}]\boldsymbol{I} + \mu[\nabla_{\boldsymbol{x}}\, \delta\boldsymbol{u} + \nabla^{\mathrm{t}}_{\boldsymbol{x}}\, \delta\boldsymbol{u}] \tag{4.40}$$

we first compute the gradient of $\delta\boldsymbol{u}$ by means of the representation highlighted in equation (4.38), and secondly, this result combined with (4.40) yields the relation sought or rather the boundary traction at the interface as

$$\begin{aligned} \delta\boldsymbol{\sigma} \cdot \boldsymbol{e}_3 \,\big|_{\eta=0} = \Bigg[&- \frac{2\mu k[-a_1\mu + a_0[\mu+\lambda]]}{\mu+\lambda}\,\boldsymbol{e}_1 - a_2\mu k\,\boldsymbol{e}_2 \\ &- i\,\frac{2\mu k[a_1\lambda + a_0[\mu+\lambda]]}{\mu+\lambda}\,\boldsymbol{e}_3 \Bigg] \exp(ik\zeta) \end{aligned} \tag{4.41}$$

Consequently, the traction-separation-laws are directly related to boundary conditions of the Neumann-type, i.e. $\delta\boldsymbol{\sigma} \cdot \boldsymbol{e}_3 = \delta\boldsymbol{\tau}$ at $\eta = 0$. In the following, interfacial constitutive relations are incorporated,

which are assumed to decouple with respect to the interface base system $\{\boldsymbol{s}, \boldsymbol{t}, \boldsymbol{n}\}$, see Fig. 4.1, and, accordingly, may reflect anisotropic constitutive response.

4.5 Interfacial Traction-Separation-Laws and Bifurcation Analysis

The second order interfacial constitutive operator $\boldsymbol{C}^{if}$ shall allow representation with respect to the orthonormal base system $\{\boldsymbol{s}, \boldsymbol{t}, \boldsymbol{n}\}$. Related interfacial constitutive parameters $\rho_s = \frac{\rho_s^*}{l_s}$, $\rho_t = \frac{\rho_t^*}{l_t}$ and $\rho_n = \frac{\rho_n^*}{l_n}$ generally inhere length parameters l_s, l_t, and l_n, which, for the sake of convenience, are again set equal to one here. The constitutive traction-separation-law for a linear-comparison-material-like interface reads

$$\begin{aligned} \delta\boldsymbol{\tau} \quad &= \boldsymbol{C}^{if} \cdot [\![\delta\boldsymbol{u}]\!] = [\rho_s\, \boldsymbol{s}\otimes\boldsymbol{s} + \rho_t\, \boldsymbol{t}\otimes\boldsymbol{t} + \rho_n\, \boldsymbol{n}\otimes\boldsymbol{n}] \cdot [\![\delta\boldsymbol{u}]\!] \\ &=: \sum_i \rho_i\, \boldsymbol{i}\otimes\boldsymbol{i} \cdot [\![\delta\boldsymbol{u}]\!] \quad \text{with} \quad i = s,t,n \quad \text{and} \quad \boldsymbol{i} = \boldsymbol{s},\boldsymbol{t},\boldsymbol{n} \end{aligned} \tag{4.42}$$

with the incremental constitutive operator being given by

$$\boldsymbol{C}^{if} = \sum_i \rho_i\, \boldsymbol{i}\otimes\boldsymbol{i} = \sum_i \boldsymbol{C}_i^{if} \tag{4.43}$$

Note that $\boldsymbol{C}^{if}$ shall be of diagonal format so that the constitutive behaviour is decoupled with respect to the local interfacial coordinate system $\{\boldsymbol{s}, \boldsymbol{t}, \boldsymbol{n}\}$. Concerning the loading branch, different constitutive relations as elasticity, elastoplasticity, damage and elastoplasticity with damage can be expressed by $\boldsymbol{C}^{if}$, see appendix B. Placing particular emphasis on the interface, i.e. $\eta = 0$, equation (4.43) renders together with equation (4.38) and $\boldsymbol{n} = \boldsymbol{e}_3$

$$\begin{aligned} \boldsymbol{C}^{if} \cdot \delta\boldsymbol{u}\,\big|_{\eta=0} = \Big[\quad & \Big[\quad a_0 - a_1 \frac{2\mu}{\mu+\lambda} \Big] [\rho_s\, \boldsymbol{s}\otimes\boldsymbol{s} + \rho_t\, \boldsymbol{t}\otimes\boldsymbol{t}] \cdot \boldsymbol{e}_1 \\ & + \quad a_2\, [\rho_s\, \boldsymbol{s}\otimes\boldsymbol{s} + \rho_t\, \boldsymbol{t}\otimes\boldsymbol{t}] \cdot \boldsymbol{e}_2 \\ & + \quad i\, [a_0 + a_1] \rho_n\, \boldsymbol{e}_3 \Big] \exp(ik\zeta) \end{aligned} \tag{4.44}$$

By inserting equations (4.44) and (4.41) into equation (4.39), we end up with

$$\begin{aligned} & \Big[-\frac{2\mu k[-a_1\mu + a_0[\mu+\lambda]]}{\mu+\lambda} \boldsymbol{I} + [a_0 - a_1 \frac{2\mu}{\mu+\lambda}][\rho_s\, \boldsymbol{s}\otimes\boldsymbol{s} + \rho_t\, \boldsymbol{t}\otimes\boldsymbol{t}] \Big] \cdot \boldsymbol{e}_1 \\ + \quad & \Big[-a_2 \mu k \boldsymbol{I} + a_2 [\rho_s\, \boldsymbol{s}\otimes\boldsymbol{s} + \rho_t\, \boldsymbol{t}\otimes\boldsymbol{t}] \Big] \cdot \boldsymbol{e}_2 \\ + \quad & i \Big[\Big[-\frac{2\mu k[a_1\lambda + a_0[\mu+\lambda]]}{\mu+\lambda} + [a_0 + a_1]\rho_n \Big]\, \boldsymbol{I} \Big] \cdot \boldsymbol{e}_3 \\ = \quad & \boldsymbol{0} \end{aligned} \tag{4.45}$$

To obtain non–trivial solutions, at least one non-vanishing ansatz constant from the set a_0, a_1 and a_2 must be at hand. For further investigations it turns out to be convenient to relate $\{\boldsymbol{s}, \boldsymbol{t}, \boldsymbol{n}\}$ and $\{\boldsymbol{e}_1, \boldsymbol{e}_2, \boldsymbol{e}_3\}$ via

$$\{\boldsymbol{s}, \boldsymbol{t}, \boldsymbol{n}\} = \boldsymbol{P} \cdot \{\boldsymbol{e}_1, \boldsymbol{e}_2, \boldsymbol{e}_3\} \quad \text{with} \quad \boldsymbol{P} \cdot \boldsymbol{P}^{\mathrm{t}} = \boldsymbol{I} \quad \text{and} \quad \det \boldsymbol{P} = 1 \tag{4.46}$$

More specificly, the rotation tensor $\boldsymbol{P}(\theta \boldsymbol{e}_3)$ can be referred to, e.g. $\{\boldsymbol{e}_1, \boldsymbol{e}_2, \boldsymbol{e}_3\}$ so that

$$\boldsymbol{P} = P_{ij}\, \boldsymbol{e}_i \otimes \boldsymbol{e}_j \quad \text{with} \quad P_{ij} = \begin{bmatrix} \cos\theta & -\sin\theta & 0 \\ \sin\theta & \cos\theta & 0 \\ 0 & 0 & 1 \end{bmatrix} \tag{4.47}$$

With this transformation in hand, straightforward computations enable to reformulate equation (4.45) in terms of a homogeneous linear system of equations with respect to the ansatz constants $\boldsymbol{a} = [a_0, a_1, a_2]^t$, reading as

$$\boldsymbol{B} \cdot \boldsymbol{a} = \boldsymbol{0} \tag{4.48}$$

with $\boldsymbol{B}$ including the entries as stated in appendix C. Non–trivial solutions of equation (4.48) with $k > 0$ according to the assumption preceding equation (4.37) reflect possible stationary surface-wave-type solutions of the IBVP as discussed above. Consequently, a bifurcation into a stationary surface-wave-type solution is possible if

$$\begin{aligned} \det \boldsymbol{B} &= [4\mu[2\mu k + \rho_n]\,[\mu k + \rho_s]\,[\mu k + \rho_t] \\ &+ [\lambda\rho_n + \mu[2k\lambda + \rho_n]] \\ &\quad [4\mu^2 k^2 + 2\rho_s\rho_t + 3\mu k[\rho_s + \rho_t] - \mu k[\rho_s - \rho_t]\cos(2\theta)] \\ &\doteq 0 \end{aligned} \tag{4.49}$$

for $k > 0$.

4.6 Results

After incorporating a general traction-separation-law for the interface, some consequences are now discussed. Special attention is given to the role of interfacial material parameters ρ_s, ρ_t, ρ_n.

4.6.1 General Considerations

Equation (4.49) is a cubic equation in k. Recall that k is real by definitions highlighted in section 4.3.2 and was chosen to be positive in section 4.3.4. In this regard, the number of bifurcation modes is one, two, three or zero. This depends, as well as the wave number k itself, on the choice of the ansatz direction θ, and on the material coefficients. Corresponding to the finite number of solutions, the given problem remains well-posed as expected. Consequently, in view of numerical applications, for instance in a finite element context, mesh-sensitivity-related problems are only expected for $k \equiv \infty$, representing vanishing wave length solutions. In view of the analytical solutions of equation (4.49),

for the general case, they would occupy too much space, so the authors abandon to list them here. On the other hand, if the problem is simplified by setting $\rho_s = \rho_t$, being the case for a transversely isotropic interface with anisotropic direction $\boldsymbol{n} = \boldsymbol{e}_3$, the solutions of equation (4.49) reduce as

$$k_I = -\frac{\rho_t}{\mu} \tag{4.50}$$

$$k_{II} = \frac{1}{8[\mu^3 + \mu^2\lambda]}\Big[- g - \sqrt{g^2 - 4[4\mu^3 + 4\mu^2\lambda][3\mu\rho_n\rho_t + \lambda\rho_n\rho_t]}\Big] \tag{4.51}$$

$$k_{III} = \frac{1}{8[\mu^3 + \mu^2\lambda]}\Big[- g + \sqrt{g^2 - 4[4\mu^3 + 4\mu^2\lambda][3\mu\rho_n\rho_t + \lambda\rho_n\rho_t]}\Big] \tag{4.52}$$

with

$$g = 4\mu^2\rho_n + 2\mu\lambda\rho_n + 4\mu^2\rho_t + 2\mu\lambda\rho_t \tag{4.53}$$

Certainly, those results do no longer depend on θ. For a linear elastic bulk it always holds that $K = \lambda + \frac{2}{3}\mu > 0$ and $\mu > 0$. Assuming that $\rho_s = \rho_t > 0$ and $\rho_n > 0$, an analysis of equations (4.50), (4.51) and (4.52) shows that no real positive wave numbers can occur for this choice and bifurcation is ruled out. If the interface is assumed to be isotropic, i.e. $\rho_s = \rho_t = \rho_n$, solutions further boil down to

$$k_1 = -\frac{\rho_n}{\mu} \tag{4.54}$$

$$k_2 = -\frac{\rho_n}{2\mu} \tag{4.55}$$

$$k_3 = -\frac{[3\mu + \lambda]\rho_n}{2\mu[\mu + \lambda]} \tag{4.56}$$

With all interfacial material parameters chosen to be positive, again, no real positive wave numbers can occur for this choice and no bifurcation will occur.

4.6.2 Examples

Now, the solutions of equation (4.49) shall be analysed for some examples of different interfacial material coefficients, reflecting an orthotropic material behaviour. In the following, the Lamé constants will be chosen as $\mu = 50000$ MPa and $\lambda = 100000$ MPa.

Orthotropic Interface with Positive Coefficients ρ_s, ρ_t, ρ_n

In this example, the planar constitutive coefficients are chosen to capture orthotropic response via $\rho_s = 20000$ MPa/m and $\rho_t = 40000$ MPa/m whereas the normal constitutive coefficient is given by

$\rho_n = 100000$ MPa/m. Equation (4.49) shows that $\det \boldsymbol{B}$ depends on the angle θ. The plot of $k_{1,2,3}(\theta)$ for $\det \boldsymbol{B} = 0$, which is displayed in Fig. 4.2, reveals that no real positive wave number exists and, accordingly, a bifurcation into stationary surface-wave-type solutions is not possible.

Another Orthotropic Interface with Positive Coefficients ρ_s, ρ_t, ρ_n

In this example, the planar constitutive coefficients are chosen as $\rho_s = 100000$ MPa/m and $\rho_t = 40000$ MPa/m whereas the normal constitutive coefficient is given by $\rho_n = 20000$ MPa/m. $\det \boldsymbol{B}$ depends on the angle θ. Plotting $k_{1,2,3}(\theta)$ for $\det \boldsymbol{B} = 0$, as displayed in Fig. 4.3, shows that, once more, no real positive wave number exists and, accordingly, a bifurcation into stationary surface-wave-type solutions is not at hand.

Orthotropic Interface with Negative ρ_s and Positive ρ_t, ρ_n

In this example, the planar constitutive coefficients are given as $\rho_s = -20000$ MPa/m, which corresponds to softening, $\rho_t = 40000$ MPa/m and $\rho_n = 100000$ MPa/m. Fig. 4.4 shows that for any angle θ exactly one stationary surface-wave-type bifurcation with an appropriate wave number k_1 is possible. Maximum wave numbers are given for $\theta \in \{\pi/2, 3\pi/2\}$, corresponding to the characteristic directions of the underlying orthotropic symmetry.

Orthotropic Interface with Negative ρ_t and Positive ρ_s, ρ_n

This example is referred to $\rho_s = 20000$ MPa/m, $\rho_t = -40000$ MPa/m, which represents softening, and $\rho_n = 100000$ MPa/m. Fig. 4.5 shows that, depending on $\theta \in [0, 2\pi]$, always one stationary surface-wave-type solution exists. The particular values $\theta \in \{0, \pi\}$ render maximum wave numbers.

Orthotropic Interface with Negative ρ_s, ρ_t and Positive ρ_n

Here, $\rho_s = -20000$ MPa/m and $\rho_t = -40000$ MPa/m, which represents orthotropic in plane softening, together with $\rho_n = 100000$ MPa/m. Fig. 4.6 shows that for all $\theta \in [0, 2\pi]$ two wave numbers exist which are related to bifurcations into stationary surface-wave-type solutions. Once more, $\theta \in \{0, \pi\}$ reflects maximum wave numbers.

Orthotropic Interface with Positive Planar Constitutive Coefficients ρ_s, ρ_t and a Negative Normal Coefficient ρ_n

In contrast to those elaborations highlighted above, we now consider a softening response with respect to the normal interface direction. The overall behaviour of the interface remains orthotropic as characterised by the coefficients $\rho_s = 20000$ MPa/m, $\rho_t = 40000$ MPa/m and $\rho_n = -100000$ MPa/m. As a result directly observable in Fig. 4.7, bifurcation into stationary surface-wave-type solutions is always possible concerning one wave number, with maximum wave numbers given at $\theta \in \{0, \pi\}$.

Orthotropic Interface with Negative ρ_s, ρ_n and Positive ρ_t

Continuing to investigate on different parameter combinations, let $\rho_s = -20000$ MPa/m, $\rho_t = 40000$ MPa/m and $\rho_n = -100000$ MPa/m. It can be clearly seen in Fig. 4.8 that for all $\theta \in [0, 2\pi]$, two wave numbers k can be related to stationary surface-wave-type solutions. Maximum wave numbers are again obtained for $\theta \in \{0, \pi\}$.

Orthotropic Interface with Negative ρ_t, ρ_n and Positive ρ_s

Furthermore, assume the parameters ρ_i to take the values $\rho_s = 20000$ MPa/m, $\rho_t = -40000$ MPa/m and $\rho_n = -100000$ MPa/m. From related results displayed in Fig. 4.9 we conclude that two stationary surface-wave-type solutions are present for all $\theta \in [0, 2\pi]$. Maximum values of k are reflected by $\theta \in \{\pi/2, 3\pi/2\}$.

Orthotropic Interface with All Negative Coefficients ρ_s, ρ_t, ρ_n

Finally, the last example deals with an orthotropic interface with all ρ_i assumed to be negative, i.e. $\rho_s = -20000$ MPa/m, $\rho_t = -40000$ MPa/m and $\rho_n = -100000$ MPa/m. Fig. 4.10 shows that for $\theta \in [0, 2\pi]$ always three stationary surface-wave-type solutions are at hand. Here, extremal values of k are obtained for angles $\theta \in \{\pi/2, 3\pi/2\}$, once more reflecting the characteristic directions of the underlying orthotropy.

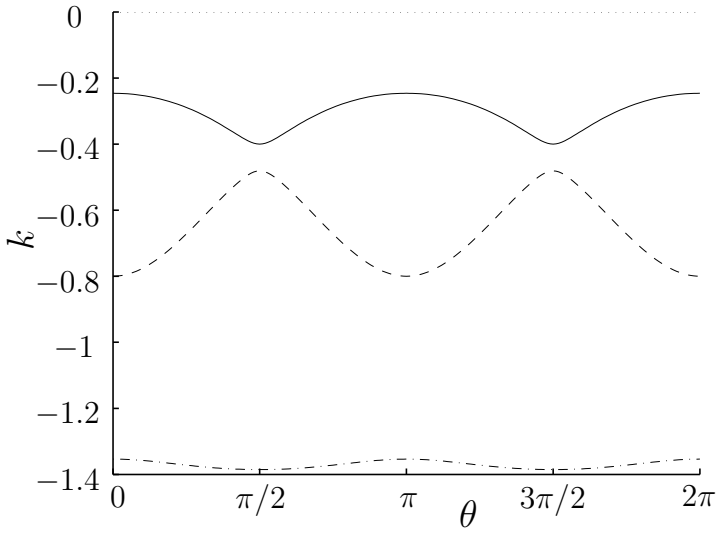

Figure 4.2: Plot of $k_{1,2,3}(\theta)$ for $\rho_s = 20000$ MPa/m, $\rho_t = 40000$ MPa/m and $\rho_n = 100000$ MPa/m

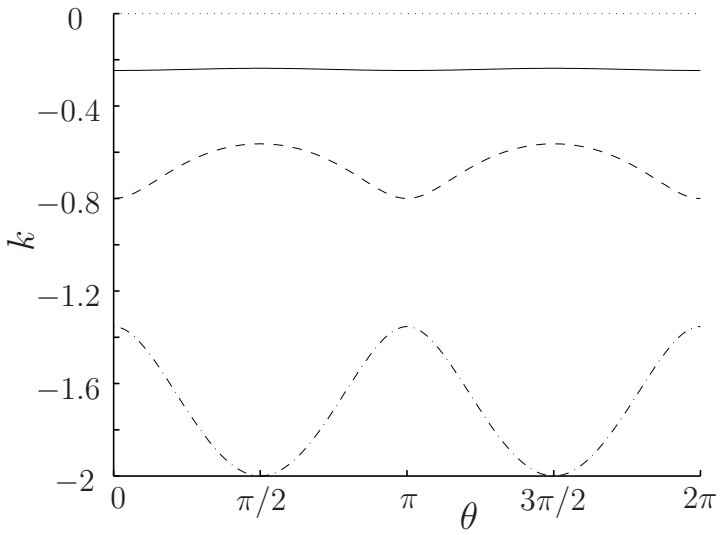

Figure 4.3: Plot of $k_{1,2,3}(\theta)$ for $\rho_s = 100000$ MPa/m, $\rho_t = 40000$ MPa/m and $\rho_n = 20000$ MPa/m

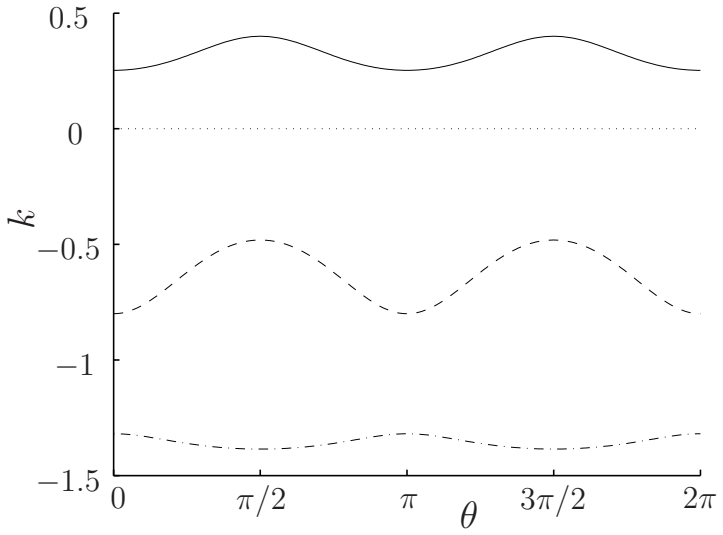

Figure 4.4: Plot of $k_{1,2,3}(\theta)$ for $\rho_s = -20000$ MPa/m, $\rho_t = 40000$ MPa/m and $\rho_n = 100000$ MPa/m

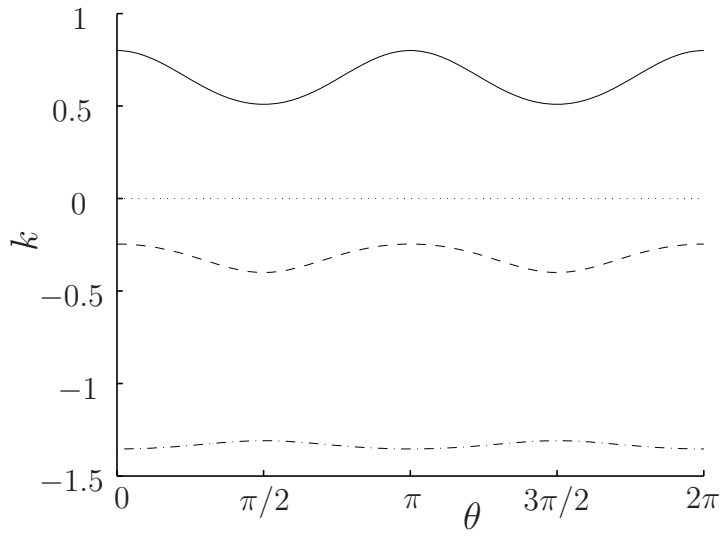

Figure 4.5: Plot of $k_{1,2,3}(\theta)$ for $\rho_s = 20000$ MPa/m, $\rho_t = -40000$ MPa/m and $\rho_n = 100000$ MPa/m

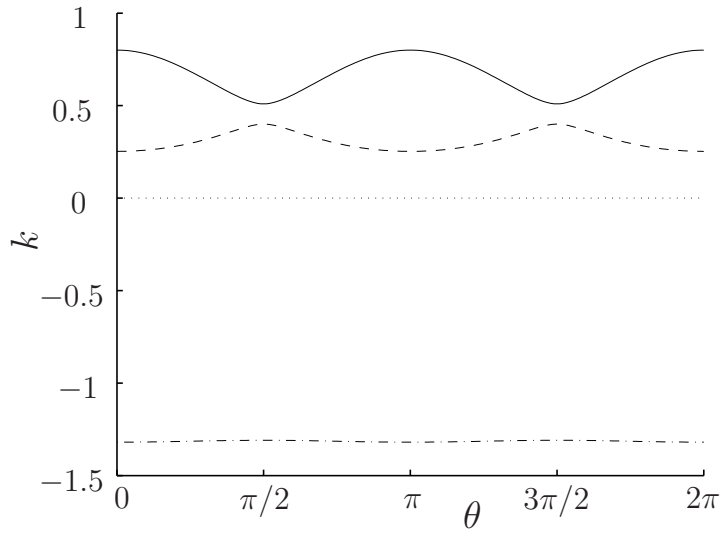

Figure 4.6: Plot of $k_{1,2,3}(\theta)$ for $\rho_s = -20000$ MPa/m, $\rho_t = -40000$ MPa/m and $\rho_n = 100000$ MPa/m

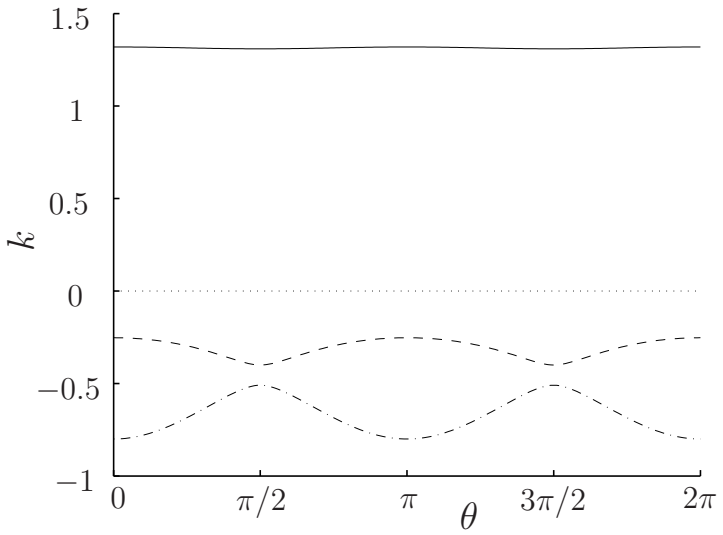

Figure 4.7: Plot of $k_{1,2,3}(\theta)$ for $\rho_s = 20000$ MPa/m, $\rho_t = 40000$ MPa/m and $\rho_n = -100000$ MPa/m

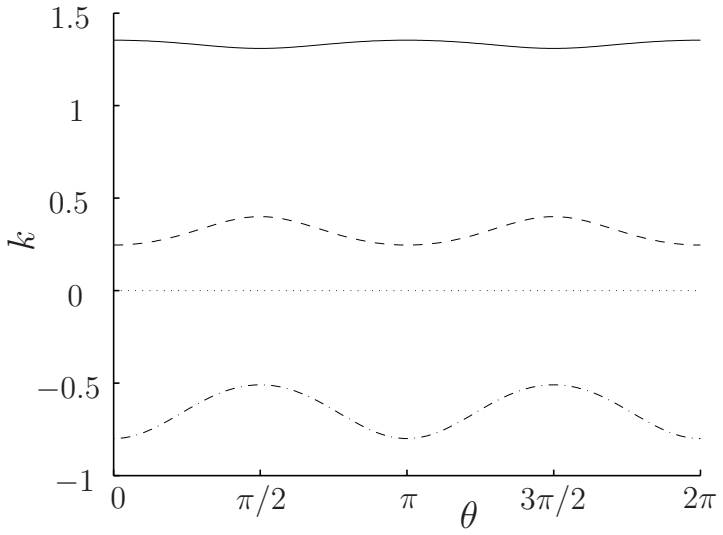

Figure 4.8: Plot of $k_{1,2,3}(\theta)$ for $\rho_s = -20000$ MPa/m, $\rho_t = 40000$ MPa/m and $\rho_n = -100000$ MPa/m

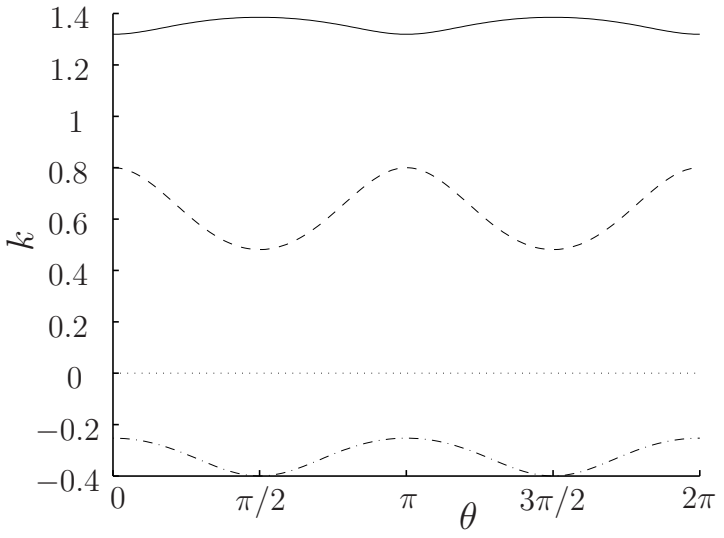

Figure 4.9: Plot of $k_{1,2,3}(\theta)$ for $\rho_s = 20000$ MPa/m, $\rho_t = -40000$ MPa/m and $\rho_n = -100000$ MPa/m

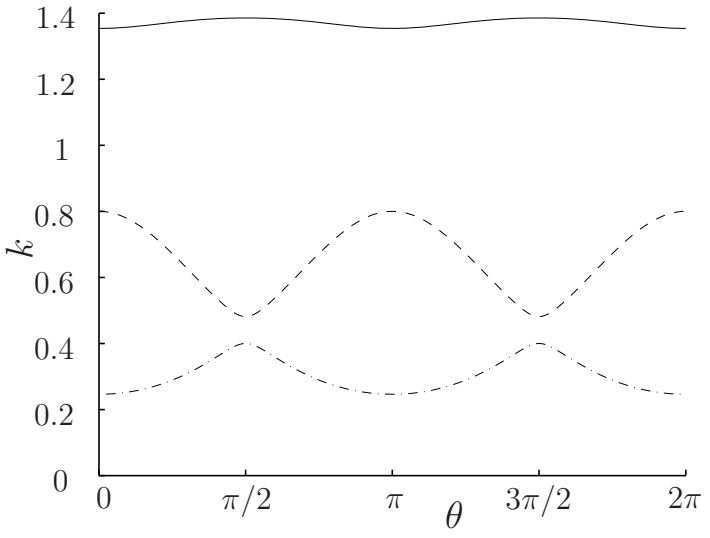

Figure 4.10: Plot of $k_{1,2,3}(\theta)$ for $\rho_s = -20000$ MPa/m, $\rho_t = -40000$ MPa/m and $\rho_n = -100000$ MPa/m

4.7 Discussion

The main goal of this chapter was to elaborate the possibility of the bifurcation of an incremental boundary value problem (IBVP) into stationary surface wave modes. The related continuum-interface problem has been formulated by means of an infinite linear elastic bulk half space which is bonded to a rigid substrate via a non-coherent cohesive interface layer. For the interface, a traction-separation-law being decoupled in its response with respect to an interfacial orthonormal base system $\{\boldsymbol{s}, \boldsymbol{t}, \boldsymbol{n}\}$ has been investigated. Thus, investigations previously reported in the literature, which in particular focussed on transversely isotropic responses, have been extended to a three-dimensional orthotropic interfacial constitutive law. Thereby, the anisotropy may be either deformation-induced, as expected from inelastic response, or already be present within the elastic regime.

The condition for the onset of bifurcation could be generalised as $\det \boldsymbol{B} \doteq 0$. Here, $\boldsymbol{B}$ is a matrix inhering various properties of interest. In the case of bifurcation stationary surface-wave-type solutions manifest in the interfacial plane as surface waves. Moreover, the specific incremental constitutive relations of the bulk and of the interface are represented via the, in general non-constant, material coefficients. As an interesting side aspect, $\boldsymbol{B}$ preserves its formal structure independent of the material parameters of the particular traction-separation-law as long as the interfacial constitutive law is decoupled with respect to some local orthonormal frame $\{\boldsymbol{s}, \boldsymbol{t}, \boldsymbol{n}\}$. In this regard, the surface ansatz used has been endowed with an angle θ which determines the harmonic direction of the wave and enters the definition of $\boldsymbol{B}$ as an additional argument.

Straightforward computations rendered $\det \boldsymbol{B} \doteq 0$ to be cubic in $k_{1,2,3}$ – additional arguments being the angle θ as well as specific values of ρ_i related to the incremental constitutive state while the elastic bulk parameters are fixed. Consequently, these coefficients ρ_i determine if stationary surface-wave-type solutions are admissible. As a result based on evaluating the derived equation of interest, up to three distinct solutions are obtained and, as expected, well-posedness is generally conserved. In this regard, various combinations of specific values for ρ_i have been studied in detail. It thereby turned out that extremal wave numbers k correspond to directions θ, which are systematically related to the interfacial axes of orthotropy. Moreover, the examples indicated that for all positive ρ_i, no stationary surface-wave-type solutions occur. The absence of stationary surface-wave-type solutions is even analytically obvious for transversal isotropy or rather planar isotropy, and full isotropy in the interface, provided that $\rho_i > 0$. Then, the present system is positive definite and the related uniqueness of the solution is in line with results of Radi et al. [145] and Gei et al. [57].

5 Bifurcation Analysis of Coupled Continuum-Interface Problems

With the elaborations for the uncoupled problem in hand, see chapter 4, the question of bifurcation into stationary wave-type solutions is now extended to the coupled problem. The basics have already been discussed at the beginning of chapter 4. Up to now, to the knowledge of the author, there are no related publications that specifically deal with electro-mechanically coupled problem in this context. Accordingly, the modus operandi is in line with chapter 4. For the bulk, a linear ferroelectric material is assumed, while the interface will be chosen as incrementally linear and ferroelectric.

5.1 Incremental Coupled Boundary Value Problem

Again, a semi-infinite space of bulk material is bonded via a non-coherent cohesive interface layer to a rigid substrate. The associated incremental boundary value problem (IBVP) is quasi-electrostatic and source-free, with body forces and external charges being neglected. It inheres small strain kinematics and is electrically-mechanically coupled.

The balance of linear momentum yields

$$\operatorname{div} \delta\boldsymbol{\sigma} = \mathbf{0} \tag{5.1}$$

whereas the second balance equation is given as a consequence of the maxwell equations:

$$\operatorname{div} \delta\boldsymbol{D} = \mathbf{0} \tag{5.2}$$

Kinematics are represented by

$$\delta\boldsymbol{\varepsilon} = \nabla_{\boldsymbol{x}}^{sym} \delta\boldsymbol{u} \tag{5.3}$$

and, respectively,

$$\delta\boldsymbol{E} = -\nabla_{\boldsymbol{x}} \delta\Phi \tag{5.4}$$

According to the coupled problem, the constitutive relations are given as

$$\delta\boldsymbol{\sigma} = \mathbb{C} : \delta\boldsymbol{\varepsilon} - \mathfrak{e}^t \cdot \delta\boldsymbol{E} \tag{5.5}$$

and

$$\delta\boldsymbol{D} = \mathfrak{e} : \delta\boldsymbol{\varepsilon} + \boldsymbol{\epsilon} \cdot \delta\boldsymbol{E} \tag{5.6}$$

where the piezoelectric tensor $\mathfrak{e}$ and the permittivity tensor $\boldsymbol{\epsilon}$ have been already introduced in chapter 2, see equations (2.97), (2.98) and (2.102). Exploiting symmetry properties, combination of equations

(5.1)–(5.6) consequently render

$$\operatorname{div}\delta\boldsymbol{\sigma} \;=\; [\mathbb{C} : \nabla_{\boldsymbol{x}}\nabla_{\boldsymbol{x}}\,\delta\boldsymbol{u}] : \boldsymbol{I} + \nabla_{\boldsymbol{x}}\nabla_{\boldsymbol{x}}\,\delta\Phi : \mathfrak{e} = \boldsymbol{0} \tag{5.7}$$

$$\operatorname{div}\delta\boldsymbol{D} \;=\; [\nabla_{\boldsymbol{x}}\nabla_{\boldsymbol{x}}\,\delta\boldsymbol{u} : \mathfrak{e}] : \boldsymbol{I} + \boldsymbol{\epsilon} : \nabla_{\boldsymbol{x}}\nabla_{\boldsymbol{x}}\,\delta\Phi = \boldsymbol{0} \tag{5.8}$$

Considering the Neumann boundary conditions, the incremental stress tensor $\delta\boldsymbol{\sigma}$ of the bulk and the incremental traction vector $\delta\boldsymbol{\tau}$ of the interface are related by

$$\delta\boldsymbol{\sigma}\cdot\boldsymbol{n} = \delta\boldsymbol{\tau} \tag{5.9}$$

Additionally, the electrical Neumann boundary condition is given as

$$\delta\boldsymbol{D}\cdot\boldsymbol{n} = \delta\Lambda \tag{5.10}$$

The related interfacial constitutive law is discussed in section 5.5.

5.2 Stationary Wave-Type Ansatz

By investigating stationary wave-type solutions, the given IBVP is checked for bifurcation possibilities, see also section 4.2. An appropriate ansatz in view of the incremental displacements and potential reads as

$$\delta\boldsymbol{u}(\boldsymbol{x}) = \exp(i[\boldsymbol{k}\cdot\tilde{\boldsymbol{x}}])\,\boldsymbol{m}_u, \qquad \delta\Phi(\boldsymbol{x}) = \exp(i[\boldsymbol{k}\cdot\tilde{\boldsymbol{x}}])\,m_\Phi \tag{5.11}$$

Please note that the wave vector is assumed to be identical for both incremental displacements and the incremental potential. To the opinion of the author, this is a reasonable first simplification. A comprehending formulation is given by

$$\delta\boldsymbol{v}(\boldsymbol{x}) = \exp(i[\boldsymbol{k}\cdot\tilde{\boldsymbol{x}}])\,\boldsymbol{m}_v, \qquad \delta\boldsymbol{v} = \begin{bmatrix} \delta\boldsymbol{u} \\ \delta\Phi \end{bmatrix}, \qquad \boldsymbol{m}_v = \begin{bmatrix} \boldsymbol{m}_u \\ m_\Phi \end{bmatrix} \tag{5.12}$$

where, compare section 4.2, the complex wave vector $\boldsymbol{k} = \check{\boldsymbol{k}} + i\boldsymbol{k}^*$ is a composition of a real part $\check{\boldsymbol{k}}$ and an imaginary part $\boldsymbol{k}^*$. Gradients follow straightforwardly as

$$\nabla_{\boldsymbol{x}}\,\delta\boldsymbol{u} = i\,\exp(i[\boldsymbol{k}\cdot\tilde{\boldsymbol{x}}])\,\boldsymbol{m}_u\otimes\boldsymbol{k}, \qquad \nabla_{\boldsymbol{x}}\,\delta\Phi = i\,\exp(i[\boldsymbol{k}\cdot\tilde{\boldsymbol{x}}])\,m_\Phi\,\boldsymbol{k} \tag{5.13}$$

and

$$\nabla_{\boldsymbol{x}}\nabla_{\boldsymbol{x}}\,\delta\boldsymbol{u} = -\exp(i[\boldsymbol{k}\cdot\tilde{\boldsymbol{x}}])\,\boldsymbol{m}_u\otimes\boldsymbol{k}\otimes\boldsymbol{k}, \qquad \nabla_{\boldsymbol{x}}\nabla_{\boldsymbol{x}}\,\delta\Phi = -\exp(i[\boldsymbol{k}\cdot\tilde{\boldsymbol{x}}])\,m_\Phi\,\boldsymbol{k}\otimes\boldsymbol{k} \tag{5.14}$$

Accordingly, equations $(5.14)_1$ and $(5.14)_2$ together with equations (5.7) and (5.8) yield

$$[\mathbb{C} : [\boldsymbol{m}\otimes\boldsymbol{k}\otimes\boldsymbol{k}]] : \boldsymbol{I} + m_\Phi\,[\boldsymbol{k}\otimes\boldsymbol{k}] : \mathfrak{e} = \boldsymbol{0} \tag{5.15}$$

as well as

$$[[\boldsymbol{m}_u \otimes \boldsymbol{k} \otimes \boldsymbol{k}] : \mathfrak{e}] : \boldsymbol{I} - \boldsymbol{\epsilon} : [\boldsymbol{k} \otimes \boldsymbol{k}]\, m_\Phi = 0 \tag{5.16}$$

This is comprehended as

$$\begin{bmatrix} \boldsymbol{Q}_{uu} & \boldsymbol{q}_{u\Phi} \\ \\ \boldsymbol{q}_{\Phi u} & q_{\Phi\Phi} \end{bmatrix} \cdot \begin{bmatrix} \boldsymbol{m}_u \\ \\ m_\Phi \end{bmatrix} = \boldsymbol{Q} \cdot \boldsymbol{m}_v = \boldsymbol{0} \tag{5.17}$$

where, $[\bullet]$ denoting an appropriate quantity, it holds

$$\begin{aligned} q_{\Phi\Phi} &= -\boldsymbol{\epsilon} : \boldsymbol{k} \otimes \boldsymbol{k} \qquad & \boldsymbol{q}_{u\Phi} &= \boldsymbol{k} \otimes \boldsymbol{k} : \mathfrak{e} \\ \boldsymbol{q}_{\Phi u} &= \boldsymbol{k} \otimes \boldsymbol{k} : \mathfrak{e} \qquad & \boldsymbol{Q}_{uu} \cdot [\bullet] &= [\mathbb{C} : [[\bullet] \otimes \boldsymbol{k}]] \cdot \boldsymbol{k} \end{aligned} \tag{5.18}$$

Equation (5.17) is equivalent to

$$[\boldsymbol{Q}_{uu} - \frac{1}{q_{\Phi\Phi}}\, \boldsymbol{q}_{u\Phi} \otimes \boldsymbol{q}_{\Phi u}] \cdot \boldsymbol{m}_u = \boldsymbol{Q}^* \cdot \boldsymbol{m}_u = 0 \tag{5.19}$$

Analogous to section 4.2, non-trivial solutions with respect to $\boldsymbol{m}_v$ exist if

$$\det \boldsymbol{Q}^* = \det \boldsymbol{Q}_{uu}\, [1 - \frac{1}{q_{\Phi\Phi}}\, \boldsymbol{q}_{\Phi u} \cdot \boldsymbol{Q}_{uu}^{-1} \cdot \boldsymbol{q}_{u\Phi}] \doteq 0 \tag{5.20}$$

Subsequently, the bulk is assumed to reflect linear ferroelectric behaviour, and both mechanical isotropy and transversal isotropy are addressed. Similar to chapter 4, stationary surface wave-type bifurcation modes are investigated with respect to the interface, which also reflects some linear and coupled behaviour.

5.3 Linear Ferroelectric Bulk Material

To account for the coupled problem discussed in this chapter, a linear ferroelectric bulk material is assumed. As an extension, both the isotropic and transversal isotropic mechanical behaviour are incorporated. The mechanical constitutive operator is thus chosen as either $\mathbb{C} = \mathbb{C}^{iso}$ in the isotropic case, see equation (2.30), or as $\mathbb{C} = \mathbb{C}^{tra}$, see equation (2.37). Independent of the choice of the purely mechanical behaviour, the piezoelectric tensor $\mathfrak{e}$ is given in equation (2.114) whereas the permittivity

tensor $\boldsymbol{\epsilon}$ has been stated in equation (2.115). Consequently, it can be specified

$$q_{\Phi\Phi} = 2\gamma_1 \boldsymbol{k}\cdot\boldsymbol{k} + 2\gamma_2[\boldsymbol{m}_0\cdot\boldsymbol{k}]^2 \tag{5.21}$$

$$\boldsymbol{q}_{u\Phi} = \boldsymbol{q}^t_{\Phi u} = -[\zeta_1\,[\boldsymbol{m}_0\cdot\boldsymbol{k}]\boldsymbol{k} + \zeta_2[\boldsymbol{m}_0\cdot\boldsymbol{k}]^2\boldsymbol{m}_0 + \frac{1}{2}[[\boldsymbol{m}_0\cdot\boldsymbol{k}]\boldsymbol{k} + [\boldsymbol{k}\cdot\boldsymbol{k}]\boldsymbol{m}_0]] \tag{5.22}$$

$$\boldsymbol{Q}^{iso}_{uu} = [\lambda+\mu]\boldsymbol{k}\otimes\boldsymbol{k} + \mu[\boldsymbol{k}\cdot\boldsymbol{k}]\boldsymbol{I} \tag{5.23}$$

$$\begin{aligned}\boldsymbol{Q}^{tra}_{uu} &= \lambda[\boldsymbol{k}\otimes\boldsymbol{k}] + \alpha[[\boldsymbol{m}_0\cdot\boldsymbol{k}]\boldsymbol{k}\otimes\boldsymbol{m}_0 + [\boldsymbol{m}_0\cdot\boldsymbol{k}]\boldsymbol{m}_0\otimes\boldsymbol{k}] + \beta[\boldsymbol{m}_0\cdot\boldsymbol{k}]^2\boldsymbol{m}_0\otimes\boldsymbol{m}_0 \\ &+ \mu_\perp[[\boldsymbol{k}\cdot\boldsymbol{k}]\boldsymbol{I} + \boldsymbol{k}\otimes\boldsymbol{k}] + [\mu_\parallel - \mu_\perp][[\boldsymbol{m}_0\cdot\boldsymbol{k}]^2\boldsymbol{I} + [\boldsymbol{m}_0\cdot\boldsymbol{k}]\boldsymbol{k}\otimes\boldsymbol{m}_0 \\ &\quad + [\boldsymbol{k}\cdot\boldsymbol{k}]\boldsymbol{m}_0\otimes\boldsymbol{m}_0 + [\boldsymbol{m}_0\cdot\boldsymbol{k}]\boldsymbol{m}_0\otimes\boldsymbol{k}]\end{aligned} \tag{5.24}$$

For the mechanically isotropic case, the determinant of $\boldsymbol{Q}^*$ is computed as

$$\begin{aligned}\det\boldsymbol{Q}^* &= \mu^2[2\mu+\lambda][\boldsymbol{k}\cdot\boldsymbol{k}]^3\Big[1 - \frac{1}{\mu[2\gamma_1\boldsymbol{k}\cdot\boldsymbol{k} + 2\gamma_2[\boldsymbol{m}_0\cdot\boldsymbol{k}]^2]} \\ &\quad \Big[[\boldsymbol{m}_0\cdot\boldsymbol{k}]^2[\zeta_1^2 + 2\zeta_1\zeta_3 + \zeta_2\zeta_3 + \frac{3}{4}\zeta_3^2 - \frac{\lambda+\mu}{2\mu+\lambda}[\zeta_1+\zeta_3]^2] \\ &\quad + \frac{[\boldsymbol{m}_0\cdot\boldsymbol{k}]^4}{\boldsymbol{k}\cdot\boldsymbol{k}}[2\zeta_1\zeta_2 + \zeta_2^2 + \zeta_2\zeta_3 - \frac{\lambda+\mu}{2\mu+\lambda}[\zeta_1+\zeta_3]2\zeta_2] \\ &\quad + \frac{1}{4}\zeta_3^2\boldsymbol{k}\cdot\boldsymbol{k} - \frac{\lambda+\mu}{2\mu+\lambda}\zeta_2^2\frac{[\boldsymbol{m}_0\cdot\boldsymbol{k}]^6}{[\boldsymbol{k}\cdot\boldsymbol{k}]^2}\Big]\Big] \doteq 0\end{aligned} \tag{5.25}$$

Please note that, despite of mechanical isotropy, the ferroelectric direction $\boldsymbol{m}_0$ is still present. The factor $\mu^2[2\mu+\lambda][\boldsymbol{k}\cdot\boldsymbol{k}]^3$ has already been discovered in section 4.3, including the ellipticity condition of the bulk, see section 4.3.1 For convenience, the determinant for the transversal isotropic case is not discussed here.

5.3.1 Specification of the Wave Vector

Following the strategy of section 4.3.2, the wave vector is again specified as $\boldsymbol{k} = k\boldsymbol{e}_1 - i\nu\boldsymbol{e}_3$. Accordingly, the wave ansatz for the incremental displacements and the incremental potential is rewritten, reading as

$$\delta\boldsymbol{u}(\boldsymbol{x}) = \underbrace{\exp(\nu\,\eta)\,\boldsymbol{m}_u}_{\boldsymbol{w}_u(\eta)}\exp(ik\,\zeta), \qquad \delta\Phi(\boldsymbol{x}) = \underbrace{\exp(\nu\,\eta)\,m_\Phi}_{w_\Phi(\eta)}\exp(ik\,\zeta) \tag{5.26}$$

With this in hand, the balance of linear momentum is expressed as

$$\boldsymbol{Q}_{2uu}\cdot\boldsymbol{w}_u''+ik\boldsymbol{Q}_{1uu}\cdot\boldsymbol{w}_u'-k^2\boldsymbol{Q}_{0uu}\cdot\boldsymbol{w}_u+\boldsymbol{q}_{2u\Phi}w_\Phi''+ik\boldsymbol{q}_{1u\Phi}w_\Phi'-k^2\boldsymbol{q}_{0u\Phi}w_\Phi=\boldsymbol{0} \tag{5.27}$$

Furthermore, the second balance equation (5.2) is rewritten as

$$\boldsymbol{q}_{2\Phi u}\cdot\boldsymbol{w}_u''+ik\boldsymbol{q}_{1\Phi u}\cdot\boldsymbol{w}_u'-k^2\boldsymbol{q}_{0\Phi u}\cdot\boldsymbol{w}_u+q_{2\Phi\Phi}\,w_\Phi''+ikq_{1\Phi\Phi}\,w_\Phi'-k^2q_{0\Phi\Phi}\,w_\Phi=0 \tag{5.28}$$

Next, equations (5.27) and (5.28) are combined as

$$\boldsymbol{Q}_2\cdot\boldsymbol{w}_v''+ik\boldsymbol{Q}_1\cdot\boldsymbol{w}_v'-k^2\boldsymbol{Q}_0\cdot\boldsymbol{w}_v=0 \tag{5.29}$$

where

$$\boldsymbol{w}_v=[\boldsymbol{w}_u;w_\Phi] \tag{5.30}$$

and

$$\boldsymbol{Q}_0=\begin{bmatrix}\boldsymbol{Q}_{0uu} & \boldsymbol{q}_{0u\Phi}\\ \boldsymbol{q}_{0\Phi u} & q_{0\Phi\Phi}\end{bmatrix},\quad \boldsymbol{Q}_1=\begin{bmatrix}\boldsymbol{Q}_{1uu} & \boldsymbol{q}_{1u\Phi}\\ \boldsymbol{q}_{1\Phi u} & q_{1\Phi\Phi}\end{bmatrix},\quad \boldsymbol{Q}_2=\begin{bmatrix}\boldsymbol{Q}_{2uu} & \boldsymbol{q}_{2u\Phi}\\ \boldsymbol{q}_{2\Phi u} & q_{2\Phi\Phi}\end{bmatrix} \tag{5.31}$$

with $\boldsymbol{q}_{0u\Phi}=\boldsymbol{q}_{0\Phi u}^t$, $\boldsymbol{q}_{1u\Phi}=\boldsymbol{q}_{1\Phi u}^t$ and $\boldsymbol{q}_{2u\Phi}=\boldsymbol{q}_{2\Phi u}^t$. For the unspecified electrically coupled problem, it is essential

$$\begin{aligned}
\boldsymbol{Q}_{0uu}\cdot[\bullet] &:= [\mathbb{C}:[[\bullet]\otimes\boldsymbol{e}_1]]\cdot\boldsymbol{e}_1\\
\boldsymbol{Q}_{1uu}\cdot[\bullet] &:= [\mathbb{C}:[[\bullet]\otimes\boldsymbol{e}_3]]\cdot\boldsymbol{e}_1+[\mathbb{C}:[[\bullet]\otimes\boldsymbol{e}_1]]\cdot\boldsymbol{e}_3\\
\boldsymbol{Q}_{2uu}\cdot[\bullet] &:= [\mathbb{C}:[[\bullet]\otimes\boldsymbol{e}_3]]\cdot\boldsymbol{e}_3\\
\boldsymbol{q}_{0u\Phi} &= [\boldsymbol{e}_1\otimes\boldsymbol{e}_1]:\mathfrak{e}\\
\boldsymbol{q}_{1u\Phi} &= [\boldsymbol{e}_3\otimes\boldsymbol{e}_1+\boldsymbol{e}_1\otimes\boldsymbol{e}_3]:\mathfrak{e}\\
\boldsymbol{q}_{2u\Phi} &= [\boldsymbol{e}_3\otimes\boldsymbol{e}_3]:\mathfrak{e}\\
q_{0\Phi\Phi} &= -\boldsymbol{\epsilon}:[\boldsymbol{e}_1\otimes\boldsymbol{e}_1]\\
q_{1\Phi\Phi} &= -\boldsymbol{\epsilon}:[\boldsymbol{e}_3\otimes\boldsymbol{e}_1+\boldsymbol{e}_1\otimes\boldsymbol{e}_3]\\
q_{2\Phi\Phi} &= -\boldsymbol{\epsilon}:[\boldsymbol{e}_3\otimes\boldsymbol{e}_3]
\end{aligned} \tag{5.32}$$

Equation (5.29) is reformulated as

$$\boldsymbol{w}_v''+ik\boldsymbol{Q}_2^{-1}\cdot\boldsymbol{Q}_1\cdot\boldsymbol{w}_v'-k^2\boldsymbol{Q}_2^{-1}\cdot\boldsymbol{Q}_0\cdot\boldsymbol{w}_v=\boldsymbol{0} \tag{5.33}$$

The inverse of $\boldsymbol{Q}_2$ is found as

$$\boldsymbol{Q}_2^{-1}=\frac{1}{\chi}\begin{bmatrix}\boldsymbol{Q}_{2uu}^{-1}+[\boldsymbol{Q}_{2uu}^{-1}\cdot\boldsymbol{q}_{2u\Phi}]\otimes[\boldsymbol{q}_{2\Phi u}\cdot\boldsymbol{Q}_{2uu}^{-1}] & -\boldsymbol{Q}_{2uu}^{-1}\cdot\boldsymbol{q}_{2u\Phi}\\ -\boldsymbol{q}_{2\Phi u}\cdot\boldsymbol{Q}_{2uu}^{-1} & 1\end{bmatrix} \tag{5.34}$$

with

$$\chi=q_{2\Phi\Phi}-\boldsymbol{q}_{2\Phi u}\cdot\boldsymbol{Q}_{2uu}^{-1}\cdot\boldsymbol{q}_{2u\Phi} \tag{5.35}$$

If the bulk is isotropic concerning its purely mechanical behaviour, with $\boldsymbol{m}_0 = \boldsymbol{e}_3$ denoting the direction of ferroelectric anisotropy, it holds

$$\begin{aligned}
\boldsymbol{Q}_{0uu} &= [\lambda+\mu]\,\boldsymbol{e}_1\otimes\boldsymbol{e}_1 + \mu\boldsymbol{I} \\
\boldsymbol{Q}_{1uu} &= [\lambda+\mu]\,[\boldsymbol{e}_3\otimes\boldsymbol{e}_1 + \boldsymbol{e}_1\otimes\boldsymbol{e}_3] \\
\boldsymbol{Q}_{2uu} &= [\lambda+\mu]\,\boldsymbol{e}_3\otimes\boldsymbol{e}_3 + \mu\boldsymbol{I} \\
\boldsymbol{q}_{0u\Phi} &= -\frac{1}{2}\,\zeta_3\,\boldsymbol{e}_3 \\
\boldsymbol{q}_{1u\Phi} &= -[\zeta_1 + \frac{1}{2}\,\zeta_3]\,\boldsymbol{e}_1 \\
\boldsymbol{q}_{2u\Phi} &= -[\zeta_1+\zeta_2+\zeta_3]\,\boldsymbol{e}_3 \\
q_{0\Phi\Phi} &= 2\gamma_1 \\
q_{1\Phi\Phi} &= 0 \\
q_{2\Phi\Phi} &= 2[\gamma_1+\gamma_2]
\end{aligned} \tag{5.36}$$

Otherwise, if transversal isotropy is at hand with respect to the purely mechanical behaviour, and the overall direction of anisotropy is identified with $\boldsymbol{m}_0 = \boldsymbol{e}_3$, it is essential

$$\begin{aligned}
\boldsymbol{Q}_{0uu} &= \mu_\perp\boldsymbol{I} + [\lambda+\mu_\perp]\,\boldsymbol{e}_1\otimes\boldsymbol{e}_1 + [\mu_\parallel+\mu_\perp]\,\boldsymbol{e}_3\otimes\boldsymbol{e}_3 \\
\boldsymbol{Q}_{1uu} &= [\lambda+\alpha+\mu_\parallel][\boldsymbol{e}_1\otimes\boldsymbol{e}_3 + \boldsymbol{e}_3\otimes\boldsymbol{e}_1] \\
\boldsymbol{Q}_{2uu} &= \mu_\parallel\boldsymbol{I} + [\lambda+2\alpha+\beta-2\mu_\perp+3\mu_\parallel]\,\boldsymbol{e}_3\otimes\boldsymbol{e}_3
\end{aligned} \tag{5.37}$$

5.3.2 Reformulation as a First Order System

Next, define

$$\boldsymbol{z} = \begin{bmatrix} \boldsymbol{w}_v \\ \boldsymbol{w}_v' \end{bmatrix} \tag{5.38}$$

Rewriting equation (5.33) as a first order system, compare section 4.3.3, renders

$$\boldsymbol{z}' = \underbrace{\begin{bmatrix} \boldsymbol{0} & \boldsymbol{I}_4 \\ k^2\,\boldsymbol{Q}_2^{-1}\cdot\boldsymbol{Q}_0 & -ik\,\boldsymbol{Q}_2^{-1}\cdot\boldsymbol{Q}_1 \end{bmatrix}}_{\boldsymbol{A}}\cdot\boldsymbol{z} \tag{5.39}$$

In this regard, the fundamental system must inhere eight linearly independent solutions. With

$$\boldsymbol{z} = \underbrace{\begin{bmatrix} \boldsymbol{m}_v \\ \nu\boldsymbol{m}_v \end{bmatrix}}_{\boldsymbol{g}}\exp(\nu\eta) \tag{5.40}$$

equation (5.39) is equivalent to

$$[\boldsymbol{A} - \nu\,\boldsymbol{I}_8]\cdot\boldsymbol{g} = \boldsymbol{0} \tag{5.41}$$

λ = 0.0630	$\times 10^{12}$ [N/m^2]	e_{31}^V = 0.0397	$\times 10^{2}$ [A s/m^2]
$\mu_\perp$ = 0.0222	$\times 10^{12}$ [N/m^2]	e_{33}^V = 0.2879	$\times 10^{2}$ [A s/m^2]
$\mu_\parallel$ = 0.0196	$\times 10^{12}$ [N/m^2]	e_{15}^V = 0.1197	$\times 10^{2}$ [A s/m^2]
ζ = 0.0007	$\times 10^{12}$ [N/m^2]	ϵ_{11} = 17152	$\times 10^{-12}$ [A^{2}s^4/[kg m^3]]
η = 0.0018	$\times 10^{12}$ [N/m^2]	ϵ_{33} = 18685	$\times 10^{-12}$ [A^{2}s^4/[kg m^3]]

Table 5.1: Material parameters in the bulk

For convenience, the solution of the eigenproblem reflected by equation (5.41) is subsequently simplified by inserting numerical values for the incorporated material parameters. The material parameters are chosen similarly to a typical ferroelectric material (PIC151, manufactured by PI Ceramic, Lederhose, Germany). For the transversal isotropic case they are specified in Tab. 5.1. The material parameters used in the present context follow as

$$\zeta_1 = -e_{31}, \quad \zeta_2 = e_{31} + 2e_{15} - e_{33}, \quad \zeta_3 = -2e_{15}, \quad \gamma_1 = -\frac{1}{2}\epsilon_{11}, \quad \gamma_2 = \frac{\epsilon_{11} - \epsilon_{33}}{2} \tag{5.42}$$

For the academic case of mechanical isotropy the Lamé constant μ is chosen as $\mu = \frac{1}{2}[\mu_\perp + \mu_\parallel]$. In order to enable numerical treatment, in the computations, the unit of time has been expressed by $[s] = 10^3[ms]$. In what follows, the bulk units are no longer given explicitly. The eigenvalues for the isotropic case are computed as

$$\begin{gathered} \nu_1 = -k, \quad \nu_2 = k, \quad \nu_3 = -0.9117k, \quad \nu_4 = 0.9117k, \\ \nu_5 = -0.9760k, \quad \nu_6 = 0.9760k, \quad \nu_7 = -1.0675k, \quad \nu_8 = 1.0675k \end{gathered} \tag{5.43}$$

For the transversal isotropic case, the eigenvalues are given by

$$\begin{gathered} \nu_1 = -1.0645k, \quad \nu_2 = 1.0645k, \quad \nu_3 = -1.2105k, \quad \nu_4 = 1.2105k, \\ \nu_5 = [-0.9024 + i0.0124]k, \quad \nu_6 = [0.9024 - i0.0124]k, \\ \nu_7 = [-0.902492 - i0.0124205]k, \quad \nu_8 = [0.902492 + i0.0124205]k \end{gathered} \tag{5.44}$$

Obviously, for both cases, eigenvalues are distinct and inhere pairwise different signs. The related eigenvectors are given in appendix D.

5.3.3 Bounded Solution

In view of the fact that all eigenvalues and eigenvectors are distinct, the general solution can be constructed without computing generalised eigenvectors. Related, for the associated Wronski-determinant, it holds $w \neq 0$. For abbreviation, the general solution is not given here. Only stationary waves which decay towards the bulk material are considered. In this respect, only terms with a negative real part exponent are relevant. For a mechanically isotropic bulk this finally renders the overall decay function

as

$$\boldsymbol{w}_v = \begin{bmatrix} \boldsymbol{w}_u \\ w_\Phi \end{bmatrix} = \exp(\nu_1\eta) \begin{bmatrix} 0 \\ -c_1/k \\ 0 \\ 0 \end{bmatrix} + \exp(\nu_3\eta) \begin{bmatrix} -i\Omega_1 c_3/k \\ 0 \\ \Omega_2 c_3/k \\ -\Omega_3 c_3/k \end{bmatrix}$$
$$+ \exp(\nu_5\eta) \begin{bmatrix} i\Omega_6 c_5/k \\ 0 \\ -\Omega_7 c_5/k \\ -\Omega_8 c_5/k \end{bmatrix} + \exp(\nu_7\eta) \begin{bmatrix} i\Omega_{11} c_7/k \\ 0 \\ -\Omega_{12} c_7/k \\ -\Omega_{13} c_7/k \end{bmatrix} \tag{5.45}$$

For full mechanically transversal isotropy the overall decay function is consequently given by

$$\boldsymbol{w}_v = \begin{bmatrix} \boldsymbol{w}_u \\ w_\Phi \end{bmatrix} = \exp(\nu_1\eta) \begin{bmatrix} 0 \\ \Omega_1 c_1/k \\ 0 \\ 0 \end{bmatrix} + \exp(\nu_3\eta) \begin{bmatrix} i\Omega_2 c_3/k \\ 0 \\ \Omega_3 c_3/k \\ \Omega_4 c_3/k \end{bmatrix}$$
$$+ \exp(\nu_5\eta) \begin{bmatrix} \Omega_7 c_5/k \\ 0 \\ \Omega_8 c_5/k \\ \Omega_9 c_5/k \end{bmatrix} + \exp(\nu_7\eta) \begin{bmatrix} \Omega_{12} c_7/k \\ 0 \\ -\Omega_{13} c_7/k \\ \Omega_{14} c_7/k \end{bmatrix} \tag{5.46}$$

In both cases, the constants c_1, c_3, c_5, c_7 are taken from the vector of complex ansatz constants given by $\boldsymbol{c} = [c_1, c_2, c_3, c_4, c_5, c_6, c_7, c_8]^t$. It is incorporated in the context of the general solution, which has not been given in detail. Please note that, because of the complex character of the eigenvalues in the fully transversal isotropic case, the decay behaviour in the normal direction is additionally characterised by some periodicity. To obtain the incremental displacements and the incremental electrical potential, results above are merged as

$$\delta\boldsymbol{u} = \boldsymbol{w}_u \exp(ik\zeta), \qquad \delta\Phi = w_\Phi \exp(ik\zeta) \tag{5.47}$$

5.4 Boundary Conditions at the Interface

Because of the numerical character of the incremental displacements and the electrical potential, only the most important steps of the computation are highlighted. At $\eta = 0$, as already discussed in section 4.4, stresses and tractions fulfil

$$\delta\boldsymbol{\sigma} \cdot \boldsymbol{e}_3 \big|_{\eta=0} = \delta\boldsymbol{\tau} \tag{5.48}$$

Furthermore, dielectric displacements of the bulk and the interface come together as

$$\delta \boldsymbol{D} \cdot \boldsymbol{e}_3 \big|_{\eta=0} = \delta\Lambda \tag{5.49}$$

Incremental stresses and dielectrical displacements are computed by inserting equation (5.47) into equations (5.5) and (5.6). The incremental interfacial quantities are computed as

$$\delta\boldsymbol{\tau} = \frac{\partial \boldsymbol{\tau}}{\partial [\![\boldsymbol{u}]\!]} \cdot [\![\delta \boldsymbol{u}]\!] + \frac{\partial \boldsymbol{\tau}}{\partial [\![\Phi]\!]} [\![\delta\Phi]\!] \tag{5.50}$$

$$\delta\Lambda = \frac{\partial \Lambda}{\partial [\![\boldsymbol{u}]\!]} \cdot [\![\delta \boldsymbol{u}]\!] + \frac{\partial \Lambda}{\partial [\![\Phi]\!]} [\![\delta\Phi]\!] \tag{5.51}$$

5.5 Interfacial Constitutive Law and Bifurcation Analysis

In what follows, a incrementally linear ferroelectric traction-separation-law is applied, yielding

$$\begin{aligned} \frac{\partial \boldsymbol{\tau}}{\partial [\![\boldsymbol{u}]\!]} &= \boldsymbol{C}^{if,el} \text{ resp. } \boldsymbol{C}^{if,tra}, & \frac{\partial \boldsymbol{\tau}}{\partial [\![\Phi]\!]} &= \boldsymbol{e}^{if}, \\ \frac{\partial \Lambda}{\partial [\![\boldsymbol{u}]\!]} &= \boldsymbol{e}^{if,t}, & \frac{\partial \Lambda}{\partial [\![\Phi]\!]} &= -\epsilon^{if} \end{aligned} \tag{5.52}$$

In view of the fact that a globally linear behaviour is chosen, the tangent operators have been denoted adequately, see section 3.7. In analogy to section 4.5, equations (5.48) and (5.49) are reiterated, yielding a homogeneous linear system of equations with respect to the ansatz constants $\boldsymbol{a} = [a_0, a_1, a_2, a_3] = [c_1, c_3, c_5, c_7]^t$, reading as

$$\boldsymbol{B} \cdot \boldsymbol{a} = \boldsymbol{0} \tag{5.53}$$

For mechanical isotropy and transversal isotropy, the matrix $\boldsymbol{B}$ is given in appendix E. The condition to have stationary surface waves, compare also section 4.5, is consequently identified with

$$\det \boldsymbol{B} \doteq 0 \tag{5.54}$$

5.6 Results

For simplification, the interfacial permittivity and coupling parameter are identified with numerical values, reading as

$$\epsilon^{if} = 5 \times 10^{-3} \, \frac{\mathrm{A}^2 \, \mathrm{s}^4}{\mathrm{kg} \, \mathrm{m}^4} \quad e^{if} = 5 \times 10^{6} \, \frac{\mathrm{A \, s}}{\mathrm{m}^3}, \tag{5.55}$$

Moreover, the interface is considered to be planar isotropic with $\mu_s = \mu_t$. Consequently, the interfacial mechanical behaviour is decoupled transversally isotropic with respect to its orthonormal base system. Thereby, the direction of anisotropy is identified with $\boldsymbol{n}$. Several choices of $\mu_s = \mu_t, \mu_n$ have been

isotropic bulk			transversal isotropic bulk		
$\mu_s = \mu_t = 5 \times 10^{15}$ kg/[m^2 s^2], $\mu_n = 10 \times 10^{15}$ kg/[m^2 s^2]					
k_I	=	$-284758 - i41156$	k_I	=	$-289597 - i21660$
k_{II}	=	$-284758 + i41156$	k_{II}	=	$-289557 + i21660$
k_{III}	=	-238903	k_{III}	=	-239364
k_{IV}	=	-140356	k_{IV}	=	-146784
$\mu_s = \mu_t = 10 \times 10^{15}$ kg/[m^2 s^2], $\mu_n = 5 \times 10^{15}$ kg/[m^2 s^2]					
k_I	=	-477806	k_I	=	-478728
k_{II}	=	$-279552 - i104524$	k_{II}	=	$-282630 + i105925$
k_{III}	=	$-279552 + i104524$	k_{III}	=	$-282630 - i105925$
k_{IV}	=	-173918	k_{IV}	=	-181131
$\mu_s = \mu_t = -5 \times 10^{15}$ kg/[m^2 s^2], $\mu_n = 10 \times 10^{15}$ kg/[m^2 s^2]					
k_I	=	$-286099 - i30043$	k_I	=	$-293127 - i16294$
k_{II}	=	$-286099 + i30043$	k_{II}	=	$-293127 + i16294$
k_{III}	=	140400	k_{III}	=	143589
k_{IV}	=	238903	k_{IV}	=	239364
$\mu_s = \mu_t = 5 \times 10^{15}$ kg/[m^2 s^2], $\mu_n = -10 \times 10^{15}$ kg/[m^2 s^2]					
k_I	=	-238903	k_I	=	-239364
k_{II}	=	$-179085 - i50559$	k_{II}	=	$-179258 + i55598$
k_{III}	=	$-179085 + i50559$	k_{III}	=	$-179258 - i55593$
k_{IV}	=	111845	k_{IV}	=	117113
$\mu_s = \mu_t = -5 \times 10^{15}$ kg/[m^2 s^2], $\mu_n = -10 \times 10^{15}$ kg/[m^2 s^2]					
k_I	=	-240916	k_I	=	-239825
k_{II}	=	86226	k_{II}	=	89531
k_{III}	=	186438	k_{III}	=	192124
k_{IV}	=	238903	k_{IV}	=	239364

Table 5.2: Wave numbers for different choices of $\mu_s = \mu_t, \mu_n$, decimal places are neglected

computed, see Tab. 5.2 for the results. In all cases, the determinant of $\boldsymbol{B}$ took the format of

$$\det \boldsymbol{B} = \frac{1}{k^4} [k_I - k][k_{II} - k][k_{III} - k][k_{IV} - k] \doteq 0 \tag{5.56}$$

with $k_I, k_{II}, k_{III}, k_{IV}$ denoting the roots of the polynomial. Please note that equation (5.56) is not fulfilled for $k \to \infty$, for which $\det \boldsymbol{B} \to 1$. As a consequence, no infinite wave number can be deduced from equation (5.56). As Tab. 5.2 reveals, for positive $\mu_s = \mu_t, \mu_n$ and both the mechanically isotropic and transversal isotropic bulk no real positive k are present. Accordingly, no stationary surface wave-type bifurcations occur in such cases. The case of a physical and linear ferroelectric interface is consequently included there. However, if some stiffness constants are chosen to be negative, real positive wave numbers occur and stationary surface wave-type solutions are possible.

5.7 Discussion

In the current chapter elaborations of chapter 4 have been extended to the coupled problem. In this context the strategies of chapter 4 have been adopted in order to investigate the possibility of stationary surface wave-type solutions for either the incremental displacements or the incremental electrical potential. For simplification, all material parameters have been substituted by numerical values. The bulk parameters have been chosen similarly to a common piezoelectric ceramic where the interfacial permittivity and coupling parameter have been chosen positive for physical reasons. Relating the bulk and the interface renders $\det \boldsymbol{B} \doteq 0$, resulting in four different wave numbers k. For positive interfacial stiffness parameters $\mu_s = \mu_t, \mu_n$, no stationary surface wave-type solutions occurred as no real positive wave numbers could be found. In contrast, if one or more of the above parameters are chosen negative, bifurcation modes are possible. Nevertheless, as well as for the uncoupled problem, the number of bifurcation modes is finite for the values of material parameters which have been incorporated here, and, additionally no wave numbers $k \to \infty$ occur.

6 Finite Element Discretisation

In the context of this work, laminar welded metal-/fibre-reinforced polymer composites as well as ferroelectric mesostructures are simulated. Thereby, the computational tool is given by the geometrically linear Finite Element Method (FEM). Typical textbooks referring to FEM are, e.g., Zienkiewicz [195], Bathe [10], Reddy [146] and Hughes [69]. Some books especially referring to nonlinear Finite Elements have been written by Wriggers [191] and Belytschko et al. [16]. For a more mathematical view on this issue, see Braess [28]. For uncoupled problems, three-dimensional simulations are conducted whereas for the coupled problem, two-dimensional examples are computed. Related, adequate three- or two-dimensional continuum finite elements are incorporated for the discretisation of the bulk. Interfaces are discretised by so-called interface elements, taking into account the fact that the interfaces considered here are a-priori-known delamination zones. Thus, interface elements combined with appropriate material models are systematically used to model zones which are expected to delaminate. Embedded between standard continuum elements, interface elements have no numerical width. They are designed to model material interfaces and do not possess typical deficiencies (as for instance ill-conditioned tangent operators) of continuum elements with a very high ratio of length and height.

The energetically conjugate quantities of the interface are tractions $\boldsymbol{\tau}$ and relative displacement jumps $[\![\boldsymbol{u}]\!]$, and, respectively, dielectric displacements Λ and electric potential jumps $[\![\Phi]\!]$. To include those jumps within a finite element context, the dependencies of $[\![\boldsymbol{u}]\!]$ and $[\![\Phi]\!]$ on absolute degrees of freedom $\boldsymbol{u}$ and Φ must be incorporated. Considering interface elements, the starting point are the displacement vectors at surrounding nodes, given at the lower and the upper side of a continuum element. First, the relative displacements between those nodes are computed, rendering displacement jump vectors at the interfacial nodes. Subsequently, it is interpolated over those jumps. The same principle is applied in view of the coupled problem where an additional degree of freedom, the electrical potential, is encountered. Accordingly, electric potential jumps would be interpolated. In Fig. 6.1, a sketch of a four-noded bilinear and a two-noded linear interface element is given. Surrounding nodes are marked by a circle whereas interfacial nodes are indexed with roman numbers in the sketch to mark the difference with respect to the surrounding nodes. For some references concerning interface elements, see, e.g., Beer [13], Needleman [125], Gens et al. [58], Schellekens [152], Schellekens and de Borst [153], Steinmann and Betsch [169], Alfano and Crisfield [1], Larsson and Jansson [88], Segurado and LLorca [159], Steinmann and Häsner [170], Utzinger et al. [180] and others. In view of localisation and mesh dependencies, some preliminary investigations have been discussed in chapters 4 and 5, see also Utzinger et al. [181]. In what follows, body forces are generally neglected.

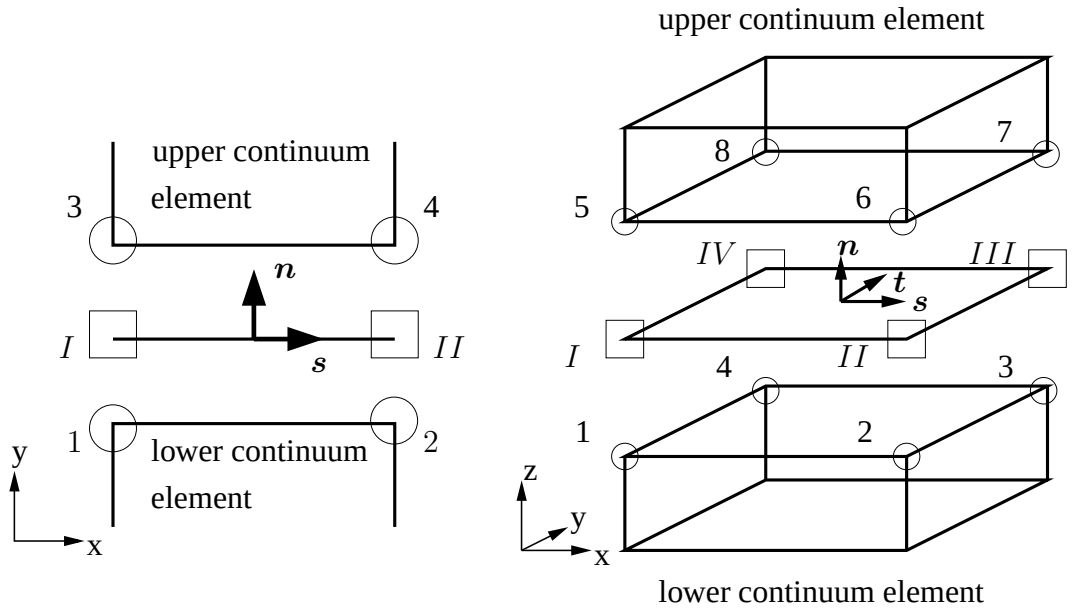

Figure 6.1: Schematic sketch of a one-dimensional (left) and two-dimensional (right) interface element

6.1 Uncoupled Problems

For the uncoupled problem the displacements $\boldsymbol{u}$ and the displacement jumps $[\![\boldsymbol{u}]\!]$ over the interface contribute to the virtual work representation by means of their virtual counterparts $\hat{\boldsymbol{u}}$ and $[\![\hat{\boldsymbol{u}}]\!]$, which are interpreted as test functions. Related to the balance of linear momentum, the principle of virtual work renders one weak equation, reading as

$$\begin{aligned} G &= \int_{\mathcal{B}\setminus\Gamma} \hat{\boldsymbol{\varepsilon}}(\hat{\boldsymbol{u}}) : \boldsymbol{\sigma}(\boldsymbol{u})\,\mathrm{d}V + \int_{\Gamma} [\![\hat{\boldsymbol{u}}]\!] \cdot \boldsymbol{\tau}([\![\boldsymbol{u}]\!])\,\mathrm{d}A \\ &- \int_{\partial\mathcal{B}_\sigma} \hat{\boldsymbol{u}} \cdot \boldsymbol{\tau}_p\,\mathrm{d}A = 0 \quad \text{and} \quad \boldsymbol{u} = \boldsymbol{u}_p \quad \text{on} \quad \partial\mathcal{B}_u \end{aligned} \tag{6.1}$$

In equation (6.1) integration areas are separated with respect to the bulk, denoted as $\mathcal{B}$, the bulk Neumann boundary $\partial\mathcal{B}_\sigma$, the bulk Dirichlet boundary $\partial\mathcal{B}_u$ and the interface, identified with Γ. Accounting for the three-dimensional problem, infinitesimal volume and surface elements are denoted as $\mathrm{d}V$ and, respectively, $\mathrm{d}A$.

6.1.1 Continuum Elements

For the discretisation of a three-dimensional bulk, trilinear eight-noded continuum elements are used, inhering the ansatz functions

$$N_N(\xi_1, \xi_2, \xi_3) = \frac{1}{8}[1 + \xi_{1N}\xi_1][1 + \xi_{2N}\xi_2][1 + \xi_{3N}\xi_3] \tag{6.2}$$

where the index $_N$ denotes the number of the node and $\xi_{1N}, \xi_{2N}, \xi_{3N}$ are the nodal coordinates. The interpolation variables are given by $\xi_1, \xi_2, \xi_3 \in [-1, 1]$. The approximated displacements and displacement test function follow straightforwardly as

$$\boldsymbol{u}^h(\xi_1, \xi_2, \xi_3) = \sum_{N=1}^{8} \boldsymbol{u}_N \, N_N(\xi_1, \xi_2, \xi_3), \quad \hat{\boldsymbol{u}}^h(\xi_1, \xi_2, \xi_3) = \sum_{N=1}^{8} \hat{\boldsymbol{u}}_N \, N_N(\xi_1, \xi_2, \xi_3) \tag{6.3}$$

Adopting standard notation, approximated quantities are endowed with an ^{h}-index. Accordingly, in Voigt notation, strains and the strain testfunction follow as

$$\boldsymbol{\varepsilon}^V = [u^h_{1,x}; u^h_{1,y}; u^h_{1,z}; u^h_{1,y} + u^h_{2,x}; u^h_{2,z} + u^h_{3,y}; u^h_{1,z} + u^h_{3,x}] = \boldsymbol{B}_{ce8} \cdot \boldsymbol{u}^N \tag{6.4}$$

$$\hat{\boldsymbol{\varepsilon}}^V = [\hat{u}^h_{1,x}; \hat{u}^h_{1,y}; \hat{u}^h_{1,z}; \hat{u}^h_{1,y} + \hat{u}^h_{2,x}; \hat{u}^h_{2,z} + \hat{u}^h_{3,y}; \hat{u}^h_{1,z} + \hat{u}^h_{3,x}] = \boldsymbol{B}_{ce8} \cdot \hat{\boldsymbol{u}}^N \tag{6.5}$$

with $\boldsymbol{u}^N = [\boldsymbol{u}_1; \boldsymbol{u}_2; \boldsymbol{u}_3; \boldsymbol{u}_4; \boldsymbol{u}_5; \boldsymbol{u}_6; \boldsymbol{u}_7; \boldsymbol{u}_8]$ and $\hat{\boldsymbol{u}}^N = [\hat{\boldsymbol{u}}_1; \hat{\boldsymbol{u}}_2; \hat{\boldsymbol{u}}_3; \hat{\boldsymbol{u}}_4; \hat{\boldsymbol{u}}_5; \hat{\boldsymbol{u}}_6; \hat{\boldsymbol{u}}_7; \hat{\boldsymbol{u}}_8]$ being the displacements at the element nodes (analogous $\hat{\boldsymbol{u}}^N$). The element operator matrix $\boldsymbol{B}_{ce8}$ is given in appendix F. Applying this discretisation with respect to equation (6.1) on the domain of a continuum element renders the associated discrete virtual work contribution and the element residuum as

$$G^{ce,h} = \int_{\mathcal{B}_{ce}} \hat{\boldsymbol{u}}^{N,t} \cdot \boldsymbol{B}^t_{ce8} \cdot \boldsymbol{\sigma}^V(\boldsymbol{u}^h) \, \mathrm{d}V_{ce}, \quad \boldsymbol{f}^{ce} = \int_{\mathcal{B}_{ce}} \boldsymbol{B}^t_{ce8} \cdot \boldsymbol{\sigma}^V(\boldsymbol{u}^h) \, \mathrm{d}V_{ce} \tag{6.6}$$

Linearisation of the virtual work contribution then renders an incremental relation on the approximated continuum element level, reading as

$$\Delta G^{ce,h} = \hat{\boldsymbol{u}}^{N,t} \cdot \underbrace{\left[\int_{\mathcal{B}_{ce}} \boldsymbol{B}^t_{ce8} \cdot \boldsymbol{C} \cdot \boldsymbol{B}_{ce8} \, \mathrm{d}V_{ce} \right]}_{\boldsymbol{K}^{ce}} \cdot \Delta \boldsymbol{u}^N \tag{6.7}$$

6.1.2 Interface Elements

Interfaces which are embedded in between two bulk material fractions are discretised by interface elements. For the uncoupled problem, a three-dimensional scenario is considered. Related, the interface elements are two-dimensional, interpolating the displacement jump of the surrounding nodes by means of a bilinear four-noded ansatz. The ansatz functions are given by

$$N_N(\xi_1, \xi_2) = \frac{1}{4}[1 + \xi_{1N}\xi_1][1 + \xi_{2N}\xi_2] \tag{6.8}$$

The interpolation variables are denoted by $\xi_1, \xi_2 \in [-1, 1]$. The approximated displacement jump and displacement jump test function are then given by

$$[\![\boldsymbol{u}]\!]^h(\xi_1, \xi_2) = \boldsymbol{B}_{ie4} \cdot \boldsymbol{u}^N, \quad [\![\hat{\boldsymbol{u}}]\!]^h(\xi_1, \xi_2) = \boldsymbol{B}_{ie4} \cdot \hat{\boldsymbol{u}}^N \tag{6.9}$$

where $\boldsymbol{u}^N = [\boldsymbol{u}_1; \boldsymbol{u}_2; \boldsymbol{u}_3; \boldsymbol{u}_4; \boldsymbol{u}_5; \boldsymbol{u}_6; \boldsymbol{u}_7; \boldsymbol{u}_8]$ and $\hat{\boldsymbol{u}}^N = [\hat{\boldsymbol{u}}_1; \hat{\boldsymbol{u}}_2; \hat{\boldsymbol{u}}_3; \hat{\boldsymbol{u}}_4; \hat{\boldsymbol{u}}_5; \hat{\boldsymbol{u}}_6; \hat{\boldsymbol{u}}_7; \hat{\boldsymbol{u}}_8]$ are the displacements at the surrounding element nodes, ditto for $\hat{\boldsymbol{u}}^N$. Again, the element operator matrix $\boldsymbol{B}_{ie4}$ is given in appendix F. To obtain the associated discrete virtual work contribution and the interface element residuum, the interfacial discretisation on the domain of an interface element, together with equation (6.1), renders

$$G^{ie,h} = \int_{\Gamma_{ie}} \hat{\boldsymbol{u}}^{N,t} \cdot \boldsymbol{B}_{ie4}^t \cdot \boldsymbol{\tau}(\llbracket \boldsymbol{u} \rrbracket^h)\, \mathrm{d}A_{ie}, \quad \boldsymbol{f}^{ie} = \int_{\Gamma_{ie}} \boldsymbol{B}_{ie4}^t \cdot \boldsymbol{\tau}(\llbracket \boldsymbol{u} \rrbracket^h)\, \mathrm{d}A_{ie} \tag{6.10}$$

Linearisation of the virtual work contribution then renders an incremental relation on the approximated interface element level, reading as

$$\Delta G^{ie,h} = \hat{\boldsymbol{u}}^{N,t} \cdot \underbrace{\left[\int_{\Gamma_{ie}} \boldsymbol{B}_{ie4}^t \cdot \boldsymbol{C}^{if} \cdot \boldsymbol{B}_{ie4}\, \mathrm{d}A_{ie} \right]}_{\boldsymbol{K}^{ie}} \cdot \Delta \boldsymbol{u}^N \tag{6.11}$$

6.2 Coupled Problems

For an electrically coupled problem, the displacements $\boldsymbol{u}$, the electric potential Φ as well as the jump quantities $\llbracket \boldsymbol{u} \rrbracket$ and $\llbracket \Phi \rrbracket$ are considered to contribute to the virtual work representation by means of their virtual counterparts. These can be interpreted as test functions $\hat{\boldsymbol{u}}$, $\hat{\Phi}$, $\llbracket \hat{\boldsymbol{u}} \rrbracket$ and $\llbracket \hat{\Phi} \rrbracket$. The principle of virtual work renders two weak equations, one related to the balance of linear momentum, the second reflecting the Gaussian law, namely

$$\begin{aligned} G_u &= \int_{B \setminus \Gamma} \hat{\boldsymbol{\varepsilon}}(\hat{\boldsymbol{u}}) : \boldsymbol{\sigma}(\boldsymbol{u}, \Phi)\, \mathrm{d}A + \int_{\Gamma} \llbracket \hat{\boldsymbol{u}} \rrbracket \cdot \boldsymbol{\tau}(\llbracket \boldsymbol{u} \rrbracket, \llbracket \Phi \rrbracket)\, \mathrm{d}S \\ &- \int_{\partial \mathcal{B}_\sigma} \hat{\boldsymbol{u}} \cdot \boldsymbol{\tau}_p\, \mathrm{d}S = 0 \quad \text{and} \quad \boldsymbol{u} = \boldsymbol{u}_p \quad \text{on} \quad \partial \mathcal{B}_u \end{aligned} \tag{6.12}$$

$$\begin{aligned} G_\Phi &= \int_{B \setminus \Gamma} \hat{\boldsymbol{E}}(\hat{\Phi}) \cdot \boldsymbol{D}(\boldsymbol{u}, \Phi)\, \mathrm{d}A + \int_{\Gamma} \hat{E}(\llbracket \hat{\Phi} \rrbracket)\, \Lambda(\llbracket \boldsymbol{u} \rrbracket, \llbracket \Phi \rrbracket)\, \mathrm{d}S \\ &+ \int_{\partial \mathcal{B}_D} \hat{\Phi}\, \Lambda_p\, \mathrm{d}S = 0 \quad \text{and} \quad \Phi = \Phi_p \quad \text{on} \quad \partial \mathcal{B}_\Phi \end{aligned} \tag{6.13}$$

Within equations (6.12) and (6.13), integration areas are separated with respect to the bulk, denoted as $\mathcal{B}$, the bulk Neumann boundaries $\partial \mathcal{B}_\sigma$ and $\partial \mathcal{B}_D$, the bulk Dirichlet boundaries $\partial \mathcal{B}_u$ and $\partial \mathcal{B}_\Phi$ and the interface Γ. In view of the two-dimensional problem, infinitesimal area and line elements are denoted as $\mathrm{d}A$ and $\mathrm{d}S$.

6.2.1 Continuum Elements

For the discretisation of a two-dimensional continuum, in this context, bilinear four-noded and linear three-noded continuum elements are considered. For the bilinear four-noded element, ansatz functions

read as

$$N_N(\xi_1,\xi_2) = \frac{1}{4}[1+\xi_{1N}\xi_1][1+\xi_{2N}\xi_2] \tag{6.14}$$

with the interpolation variables $\xi_1, \xi_2 \in [-1,1]$. Displacements and displacement test functions are approximated by

$$\boldsymbol{u}^h(\xi_1,\xi_2) = \sum_{N=1}^{4} \boldsymbol{u}_N\, N_N(\xi_1,\xi_2), \quad \hat{\boldsymbol{u}}^h(\xi_1,\xi_2) = \sum_{N=1}^{4} \hat{\boldsymbol{u}}_N\, N_N(\xi_1,\xi_2) \tag{6.15}$$

The electric potential and its testfunction are approximated by

$$\Phi^h(\xi_1,\xi_2) = \sum_{N=1}^{4} \Phi_N\, N_N(\xi_1,\xi_2), \quad \hat{\Phi}^h(\xi_1,\xi_2) = \sum_{N=1}^{4} \hat{\Phi}_N\, N_N(\xi_1,\xi_2) \tag{6.16}$$

Formulated in Voigt notation, the strains and the strain test function read as

$$\boldsymbol{\varepsilon}^V = [u^h_{1,x}; u^h_{1,y}; u^h_{1,y} + u^h_{2,x}] = \boldsymbol{B}_{ce4} \cdot \boldsymbol{u}^N \tag{6.17}$$

$$\hat{\boldsymbol{\varepsilon}}^V = [\hat{u}^h_{1,x}; \hat{u}^h_{1,y}; \hat{u}^h_{1,y} + \hat{u}^h_{2,x}] = \boldsymbol{B}_{ce4} \cdot \hat{\boldsymbol{u}}^N \tag{6.18}$$

where $\boldsymbol{u}^N = [\boldsymbol{u}_1; \boldsymbol{u}_2; \boldsymbol{u}_3; \boldsymbol{u}_4]$ and $\hat{\boldsymbol{u}}^N = [\hat{\boldsymbol{u}}_1; \hat{\boldsymbol{u}}_2; \hat{\boldsymbol{u}}_3; \hat{\boldsymbol{u}}_4]$ denote the displacements at the element nodes. The electric field vector and its testfunction, compare Schröder and Gross [155] and Schröder and Romanowski [158], follow as

$$\boldsymbol{E} = -[\Phi^h_{,x}; \Phi^h_{,y}] = -\boldsymbol{A}_{ce4} \cdot \boldsymbol{\Phi}^N \tag{6.19}$$

$$\hat{\boldsymbol{E}} = [\hat{\Phi}^h_{,x}; \hat{\Phi}^h_{,y}] = \boldsymbol{A}_{ce4} \cdot \hat{\boldsymbol{\Phi}}^N \tag{6.20}$$

where $\boldsymbol{\Phi}^N = [\Phi_1; \Phi_2; \Phi_3; \Phi_4]$ and $\hat{\boldsymbol{\Phi}}^N = [\hat{\Phi}_1; \hat{\Phi}_2; \hat{\Phi}_3; \hat{\Phi}_4]$ is the electric potential at the element nodes. For a linear material, a symmetric stiffness matrix is also achieved if signs in equations (6.20) and $(2.7)_2$ are reversed. The element operator matrices $\boldsymbol{B}_{ce4}$ and $\boldsymbol{A}_{ce4}$ are given in appendix F. Concerning three-noded linear elements, the ansatz functions are given as

$$N_1 = 1 - \xi_1 - \xi_2, \quad N_2 = \xi_1, \quad N_3 = \xi_2 \tag{6.21}$$

Again, the interpolation variables are given by $\xi_1, \xi_2 \in [-1,1]$. Displacements and displacement test functions are approximated by

$$\boldsymbol{u}^h(\xi_1,\xi_2) = \sum_{N=1}^{3} \boldsymbol{u}_N\, N_N(\xi_1,\xi_2), \quad \hat{\boldsymbol{u}}^h(\xi_1,\xi_2) = \sum_{N=1}^{3} \hat{\boldsymbol{u}}_N\, N_N(\xi_1,\xi_2) \tag{6.22}$$

Furthermore, the electric potential and its testfunction are approximated by

$$\Phi^h(\xi_1,\xi_2) = \sum_{N=1}^{3} \Phi_N \, N_N(\xi_1,\xi_2), \quad \hat{\Phi}^h(\xi_1,\xi_2) = \sum_{N=1}^{3} \hat{\Phi}_N \, N_N(\xi_1,\xi_2) \tag{6.23}$$

Accordingly, the strains and strain testfunctions are rendered as

$$\boldsymbol{\varepsilon}^V = [u^h_{1,x}; u^h_{1,y}; u^h_{1,y} + u^h_{2,x}] = \boldsymbol{B}_{ce3} \cdot \boldsymbol{u}^N \tag{6.24}$$

$$\hat{\boldsymbol{\varepsilon}}^V = [\hat{u}^h_{1,x}; \hat{u}^h_{1,y}; \hat{u}^h_{1,y} + \hat{u}^h_{2,x}] = \boldsymbol{B}_{ce3} \cdot \hat{\boldsymbol{u}}^N \tag{6.25}$$

The displacements at the element nodes are given by $\boldsymbol{u}^N = [\boldsymbol{u}_1; \boldsymbol{u}_2; \boldsymbol{u}_3]$ and $\hat{\boldsymbol{u}}^N = [\hat{\boldsymbol{u}}_1; \hat{\boldsymbol{u}}_2; \hat{\boldsymbol{u}}_3]$. The electric field vector and the related test function are given by

$$\boldsymbol{E} = -[\Phi^h_{,x}; \Phi^h_{,y}] = -\boldsymbol{A}_{ce3} \cdot \boldsymbol{\Phi}^N \tag{6.26}$$

$$\hat{\boldsymbol{E}} = [\hat{\Phi}^h_{,x}; \hat{\Phi}^h_{,y}] = \boldsymbol{A}_{ce3} \cdot \hat{\boldsymbol{\Phi}}^N \tag{6.27}$$

with $\boldsymbol{\Phi}^N = [\Phi_1; \Phi_2; \Phi_3]$ and $\hat{\boldsymbol{\Phi}}^N = [\hat{\Phi}_1; \hat{\Phi}_2; \hat{\Phi}_3]$ denoting the electric potential at the element nodes. For the element operator matrices $\boldsymbol{B}_{ce3}$ and $\boldsymbol{A}_{ce3}$, see appendix F. On the domain of a three-noded continuum element, the associated discrete virtual work contribution and the residuum are given, with respect to equation (6.12), as

$$G^{ce,h}_u = \int_{\mathcal{B}_{ce}} \hat{\boldsymbol{u}}^{N,t} \cdot \boldsymbol{B}^t_{ce3} \cdot \boldsymbol{\sigma}^V(\boldsymbol{u}^h, \Phi^h) \, \mathrm{d}A_{ce}, \quad \boldsymbol{f}^{ce}_u = \int_{\mathcal{B}_{ce}} \boldsymbol{B}^t_{ce3} \cdot \boldsymbol{\sigma}^V(\boldsymbol{u}^h, \Phi^h) \, \mathrm{d}A_{ce} \tag{6.28}$$

and, furthermore, concerning equation (6.13), it holds

$$G^{ce,h}_\Phi = \int_{\mathcal{B}_{ce}} \hat{\boldsymbol{\Phi}}^{N,t} \cdot \boldsymbol{A}^t_{ce3} \cdot \boldsymbol{D}(\boldsymbol{u}^h, \Phi^h) \, \mathrm{d}A_{ce}, \quad \boldsymbol{f}^{ce}_\Phi = \int_{\mathcal{B}_{ce}} \boldsymbol{A}^t_{ce3} \cdot \boldsymbol{D}(\boldsymbol{u}^h, \Phi^h) \, \mathrm{d}A_{ce} \tag{6.29}$$

Incremental relations on the approximated continuum element level are rendered by linearisation of the associated virtual work contribution, reading as

$$\Delta G^{ce,h}_u = \hat{\boldsymbol{u}}^{N,t} \cdot \underbrace{\left[\int_{\mathcal{B}_{ce}} \boldsymbol{B}^t_{ce3} \cdot \boldsymbol{C}_{uu} \cdot \boldsymbol{B}_{ce3} \, \mathrm{d}A_{ce} \right]}_{\boldsymbol{K}^{ce}_{uu}} \cdot \Delta \boldsymbol{u}^N + \hat{\boldsymbol{u}}^{N,t} \cdot \underbrace{\left[\int_{\mathcal{B}_{ce}} -\boldsymbol{B}^t_{ce3} \cdot \boldsymbol{C}_{u\Phi} \cdot \boldsymbol{A}_{ce3} \, \mathrm{d}A_{ce} \right]}_{\boldsymbol{K}^{ce}_{u\Phi}} \cdot \Delta \boldsymbol{\Phi}^N \tag{6.30}$$

and

$$\Delta G_{\Phi}^{ce,h} = \hat{\boldsymbol{\Phi}}^{N,t} \cdot \underbrace{\left[\int_{\mathcal{B}_{ce}} \boldsymbol{A}_{ce3}^{t} \cdot \boldsymbol{C}_{\Phi u} \cdot \boldsymbol{B}_{ce3} \, \mathrm{d}A_{ce} \right]}_{\boldsymbol{K}_{\Phi u}^{ce}} \cdot \Delta \boldsymbol{u}^{N} + \hat{\boldsymbol{\Phi}}^{N,t} \cdot \underbrace{\left[\int_{\mathcal{B}_{ce}} -\boldsymbol{A}_{ce3}^{t} \cdot \boldsymbol{C}_{\Phi\Phi} \cdot \boldsymbol{A}_{ce3} \, \mathrm{d}A_{ce} \right]}_{\boldsymbol{K}_{\Phi\Phi}^{ce}} \cdot \Delta \boldsymbol{\Phi}^{N} \tag{6.31}$$

Similar expressions are obtained for four-noded bilinear elements. The element stiffness matrix and the element residuum follow as

$$\boldsymbol{K}^{ce} = \begin{bmatrix} \boldsymbol{K}_{uu}^{ce} & \boldsymbol{K}_{u\Phi}^{ce} \\ \boldsymbol{K}_{\Phi u}^{ce} & \boldsymbol{K}_{\Phi\Phi}^{ce} \end{bmatrix}, \qquad \boldsymbol{f}^{ce} = \begin{bmatrix} \boldsymbol{f}_{u}^{ce} \\ \boldsymbol{f}_{\Phi}^{ce} \end{bmatrix} \tag{6.32}$$

6.2.2 Interface Elements

Next, emphasis is placed on the discretisation of interfaces in a two-dimensional surrounding continuum. Based on linear interfacial ansatz functions

$$N_1 = \frac{1}{2}[1 - \xi], \quad N_2 = \frac{1}{2}[1 + \xi] \tag{6.33}$$

depending on the interpolation variable $\xi \in [-1, 1]$, the approximations of the displacements and of the appropriate test functions are given as

$$[\![\boldsymbol{u}]\!]^h(\xi) = \boldsymbol{B}_{ie2} \cdot \boldsymbol{u}^N, \quad [\![\hat{\boldsymbol{u}}]\!]^h(\xi) = \boldsymbol{B}_{ie2} \cdot \hat{\boldsymbol{u}}^N \tag{6.34}$$

where $\boldsymbol{u}^N = [\boldsymbol{u}_1; \boldsymbol{u}_2; \boldsymbol{u}_3; \boldsymbol{u}_4]$ and $\hat{\boldsymbol{u}}^N = [\hat{\boldsymbol{u}}_1; \hat{\boldsymbol{u}}_2; \hat{\boldsymbol{u}}_3; \hat{\boldsymbol{u}}_4]$ are the displacements at the surrounding element nodes. The electric potential jump and its testfunction are approximated by

$$[\![\Phi]\!]^h(\xi) = \boldsymbol{a}_{ie2} \cdot \boldsymbol{\Phi}^N, \quad [\![\hat{\Phi}]\!]^h(\xi) = \boldsymbol{a}_{ie2} \cdot \hat{\boldsymbol{\Phi}}^N \tag{6.35}$$

The electric field strength over the interface and its testfunction is then given as

$$E = -[\![\Phi]\!]^h = -\boldsymbol{a}_{ie2} \cdot \boldsymbol{\Phi}^N \tag{6.36}$$

$$\hat{E} = [\![\hat{\Phi}]\!]^h = \boldsymbol{a}_{ie2} \cdot \hat{\boldsymbol{\Phi}}^N \tag{6.37}$$

with the potential at the surrounding nodes $\boldsymbol{\Phi}^N = [\Phi_1; \Phi_2; \Phi_3; \Phi_4]$ and $\hat{\boldsymbol{\Phi}}^N = [\hat{\Phi}_1; \hat{\Phi}_2; \hat{\Phi}_3; \hat{\Phi}_4]$. Once more, the element operator matrices $\boldsymbol{B}_{ie2}$ and $\boldsymbol{a}_{ie2}$ are given in appendix F. On the domain of a two-noded interface element, the associated discrete virtual work contribution and the residuum under consideration of equation (6.12) are given as

$$G_{u}^{ie,h} = \int_{\Gamma_{ie}} \hat{\boldsymbol{u}}^{N,t} \cdot \boldsymbol{B}_{ie2}^{t} \cdot \boldsymbol{\tau}([\![\boldsymbol{u}]\!]^h, [\![\Phi]\!]^h) \, \mathrm{d}S_{ie}, \quad \boldsymbol{f}_{u}^{ie} = \int_{\Gamma_{ie}} \boldsymbol{B}_{ie2}^{t} \cdot \boldsymbol{\tau}([\![\boldsymbol{u}]\!]^h, [\![\Phi]\!]^h) \, \mathrm{d}S_{ie} \tag{6.38}$$

Furthermore, with respect to equation (6.13), it holds

$$G_{\Phi}^{ie,h} = \int_{\Gamma_{ie}} \hat{\boldsymbol{\Phi}}^{N,t} \cdot \boldsymbol{a}_{ie2}^{t} \, \Lambda([\![\boldsymbol{u}]\!]^h, [\![\Phi]\!]^h) \, \mathrm{d}S_{ie}, \quad \boldsymbol{f}_{\Phi}^{ie} = \int_{\Gamma_{ie}} \boldsymbol{a}_{ie2}^{t} \, \Lambda([\![\boldsymbol{u}]\!]^h, [\![\Phi]\!]^h) \, \mathrm{d}S_{ie} \tag{6.39}$$

The incremental relations on the approximated interface element level are then rendered by linearisation of the associated virtual work contribution, yielding

$$\Delta G_{u}^{ie,h} = \hat{\boldsymbol{u}}^{N,t} \cdot \underbrace{\left[\int_{\Gamma_{ie}} \boldsymbol{B}_{ie2}^{t} \cdot \boldsymbol{C}_{uu}^{if} \cdot \boldsymbol{B}_{ie2} \, \mathrm{d}S_{ie} \right]}_{\boldsymbol{K}_{uu}^{ie}} \cdot \Delta \boldsymbol{u}^{N} + \hat{\boldsymbol{u}}^{N,t} \cdot \underbrace{\left[\int_{\Gamma_{ie}} \boldsymbol{B}_{ie2}^{t} \cdot \boldsymbol{c}_{u\Phi}^{if} \cdot \boldsymbol{a}_{ie2} \, \mathrm{d}S_{ie} \right]}_{\boldsymbol{k}_{u\Phi}^{ie}} \cdot \Delta \boldsymbol{\Phi}^{N} \tag{6.40}$$

and

$$\Delta G_{\Phi}^{ie,h} = \hat{\boldsymbol{\Phi}}^{N,t} \cdot \underbrace{\left[\int_{\Gamma_{ie}} \boldsymbol{a}_{ie2}^{t} \cdot \boldsymbol{c}_{\Phi u}^{if} \cdot \boldsymbol{B}_{ie2} \, \mathrm{d}S_{ie} \right]}_{\boldsymbol{k}_{\Phi u}^{ie}} \cdot \Delta \boldsymbol{u}^{N} + \hat{\boldsymbol{\Phi}}^{N,t} \cdot \underbrace{\left[\int_{\Gamma_{ie}} \boldsymbol{a}_{ie2}^{t} \cdot c_{\Phi\Phi}^{if} \cdot \boldsymbol{a}_{ie2} \, \mathrm{d}S_{ie} \right]}_{k_{\Phi\Phi}^{ie}} \cdot \Delta \boldsymbol{\Phi}^{N} \tag{6.41}$$

Please note that for the formulation as given in equation (6.41), the interfacial tangents $\boldsymbol{c}_{\Phi u}^{if}$ and $c_{\Phi\Phi}^{if}$ have to be computed with respect to the electric potential jump $[\![\Phi]\!]$. The element stiffness matrix and the element residuum follow as

$$\boldsymbol{K}^{ie} = \begin{bmatrix} \boldsymbol{K}_{uu}^{ie} & \boldsymbol{k}_{u\Phi}^{ie} \\ \\ \boldsymbol{k}_{\Phi u}^{ie} & k_{\Phi\Phi}^{ie} \end{bmatrix}, \qquad \boldsymbol{f}^{ie} = \begin{bmatrix} \boldsymbol{f}_{u}^{ie} \\ \\ \boldsymbol{f}_{\Phi}^{ie} \end{bmatrix} \tag{6.42}$$

6.3 Additional Remarks

All interfacial integrals are computed by transformation of the integral domain into a reference element domain. The such obtained expressions are then numerically integrated by means of the standard two-point Gauss-integration technique. Utilising an assembly algorithm, the global stiffness matrices and residua are subsequently computed to be implemented in a nonlinear finite element context. The mentioned technique of the Gauss-integration turned out to be sufficient in all cases. Oscillating constitutive responses, as described by Schellekens and de Borst [153], have not been observed.

7 Application I – Laminar Welded Metal-/Fibre-Reinforced Polymer Composites

In the course of technological progression an increasing application of lightweight structures is observed, inducing new innovative product developments in various fields of industry. Especially hybrid lightweight structures of metal-/fibre-reinforced polymer composites are of interest, e.g., in the scope of automotive and aerospace engineering. As a key technology, such composites essentially contribute to economical and ecological issues. To realise joints of metals and fibre-reinforced polymers, new joining technologies are investigated and optimised. Regarding the loading behaviour of such composites, the joining zone is of crucial importance as it is considered to be an a priori known zone of delamination. To reduce the number of experiments and in order to contribute to the improvement of the joining technologies, benchmark tests concerning such structures are computationally modelled and numerically simulated.

In section 7.1 two different methods of joining are shortly introduced, i.e. Thermal Impact Welding (TIW) and Ultrasonic Metal Welding (UMW). Furthermore, some measuring and analysis methods are concisely explained. Then, tensile tests of thermal impact welded PEEK/steel single lap tensile specimens have been simulated quasistatically by application of FEM, see section 7.2. For the steel substrates elastoplasticity with linear isotropic hardening has been applied (see section 2.3) while the very thin welding zone (including a PEEK inlay) has expediently been modelled by an interfacial traction-separation-law, i.e. elastoplasticity with damage, see section 3.4. Consequently, in the sense of chapter 6, the joining partners are discretised by 8-noded continuum elements and the welding interface is discretised by four-noded interface elements. Integral and local datasets of the experiment and the simulation are compared. Thereafter, section 7.3 includes some integral data comparison of a quasistatic test of an ultrasonic metal welded tensile specimen whereas for the substrates continuum elements are applied again, with orthotropic elasticity for CF-PA66 and elastoplasticity with linear isotropic hardening for the aluminium. The interface discretisation and modelling is adopted from the previous section. Furthermore, in section 7.4, a preliminary comparison of global and local datasets for a fatigued tensile specimen manufactured by ultrasonic metal welding is presented. Modelling and discretisation techniques concerning the substrates are adopted from the previous section, while the welding interface is modelled by the cycle-based fatigue law as discussed in section 3.6.

7.1 Manufacturing and Measuring

Since fibre-reinforced thermoplastic materials offer a great potential for lightweight design and construction, they are increasing in use. They feature high specific stiffness, strength, and impact resis-

tance as well as an excellent resistance against many chemical agents. Furthermore, many polymeric composite materials exhibit very good tribological properties, i.e. a low wear rate and low coefficients of friction, see Häger and Friedrich [59], Friedrich et al. [56], Beringer et al. [23] and Naga [124]. However, the limits of today's composites can be pushed even further by combining their advantages with the properties of traditional construction materials, e.g. thermal conductivity or strength. Moreover, the use of composite materials in more and more applications requires reliable, strong and easy-to-use methods of joining metal parts with composite structures. Thus, the development of new joining techniques for metals and thermoplastic polymeric resins is, as well as the related testing and analysis, an active field of research in the scope of the DFG Research Unit 524.

7.1.1 Thermal Impact Welding

Amongst others, Thermal Impact Welding (TIW) is a novel technique for joining thermoplastics with steel which is developed by a partner project at the Institut für Verbundwerkstoffe GmbH (IVW) in Kaiserslautern. At the IVW, manufacturing and related force-displacement testing is resident. Developing such a new joining method necessitates a thorough investigation of the stability and reproducibility of the process. At the same time, it must be ensured that the manufactured components are free of flaws. In the technical literature only few reports concerning a hot press process for joining thermoplastics with metals can be found. Two of those rare papers are Oster et al. [134] and Krüger and Meyer [87]. Oster et al. [134] describe how a hot press process (i.e. Thermal Impact Welding) can be employed to manufacture flat samples for tribological experiments.

Poly(-ether-ether)-ketone (PEEK) is a heavy-duty industrial thermoplastic resin, which is widely used in sophisticated applications. Its mechanical and thermal properties are in the upper range compared to other commercially available polymeric materials (Ehrenstein et al. [49]). It is a semi-crystalline thermoplastic with a melting temperature of 334 °C and a glass transition temperature of 143 °C. The maximum continuous utilisation temperature of PEEK is 260 °C. Furthermore, PEEK features a high specific stiffness and strength, an outstanding resistance to chemical agents, and can exhibit a maximum degree of crystallinity of 48%. The present compound is reinforced with an amount of 10 wt.% short carbon fibres. Moreover, a total of approx. 20 wt.% of various micro-particles (graphite and PTFE) are added to the formulation of the compound to improve the mechanical properties. As the metallic counterpart in the joining process, the mild steel DC01 (German standard, also referred to as DIN EN 10131 or material number 1.0330) exhibits a Young's modulus E of approximately 165 GPa, a yield strength $R_{p\,0,2}$ of 145 MPa and a tensile strength R_m of approximately 290 MPa. The steel substrates were grit-blasted before having been thermally welded. It is believed that the enhanced surface roughness after grit-blasting facilitates the bonding of the polymeric compound to the metal substrate due to mechanical hooking of the polymer. Furthermore, blasting leads to a chemical activation of the surface layer, thus ameliorating the adhesion between the two materials to be joined. In the TIW process the metallic substrates together with a PEEK-layer are inserted into a hot press, see Fig. 7.1. The parts to be joined are then heated to 380 °C, a temperature above the melting temperature of the PEEK-compound. Once the PEEK has melted, a pressure is applied to the setup and the heating of the hot press is switched off. As the temperature drops, the PEEK becomes more and more viscous. During this process the pressure on the parts to be joined needs to be maintained because a decrease in joining pressure could result in cavities or shrink holes in the polymer, thus

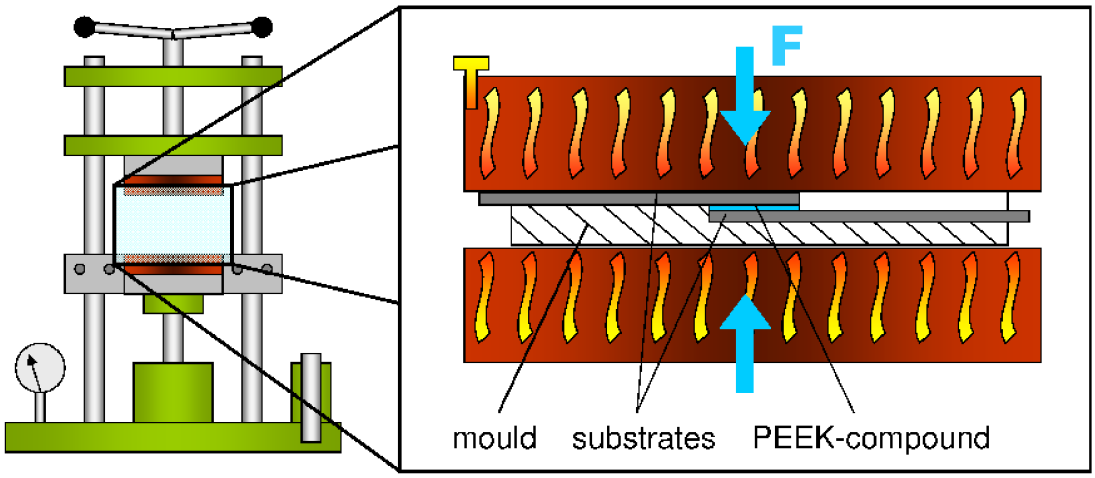

Figure 7.1: Schematic representation of the hot press process

leading to a reduced strength of the PEEK-layer and weak bonding to the metal substrates. Shortly before the PEEK eventually solidifies, the pressure needs to be increased in order to compensate the shrinkage due to crystallisation of the polymer. The specimens remain in the hot press until the temperature of the setup drops below 300 °C to make sure that the polymeric compound solidifies and the removal of the still hot specimens does not influence the strength of the weld. The geometry of such a specimen is given in Fig. 7.2.

7.1.2 Ultrasonic Metal Welding

Ultrasonic Metal Welding (UMW) is, according to Balle et al. [6], already established in industrial manufacturing (Ehrenstein [49], Wodara [190], Potente [144]). However, up to now, mainly similar materials have been joined by UMW. The method of UMW is substantially different to the method of TIW, inhering low temperatures and energy inputs as well as a short welding time.

Here, joining partners are given by $AlMg_3$ and the thermoplastic composite material CF-PA66. Manufacturing and related force-displacement testing is resident at the Institute of Materials Science and Engineering (WKK) at the University of Kaiserslautern. The aluminium exhibits a Young's modulus E of approximately 70 GPa, a yield strength $R_{p\,0,2}$ of 175 MPa and a tensile strength R_m of approximately 250 MPa. The PA66 is reinforced with carbon fibres, inhering a volume of approx. 48 %. The compound is manufactured in an autoclave process where an Atlas 1/4-fabric is created. CF-PA66 generally shows a orthotropic elastic behaviour. The material constants have been passed by a partner project manufacturing the CF-PA66. Expressed in the parameters as discussed in section 2.2.3, the orthotropic behaviour is specified by $\lambda = 4555$ MPa, $\alpha_1 = -3263$ MPa, $\alpha_2 = -3263$ MPa, $\beta_1 = 51466$ MPa, $\beta_2 = 51466$ MPa, $\beta_3 = 7524$ MPa, $\mu = -1000$ MPa, $\mu_1 = 1900$ MPa, $\mu_2 = 1900$ MPa. The main components of an UMW system are given in Fig. 7.3 (Balle et al. [6]). It consists of an ultrasonic generator (1), a converter (2), a booster (3) and the welding tool which is called sonotrode (4). A 50 Hz main voltage is converted into a high frequency alternating voltage output of 20 kHz

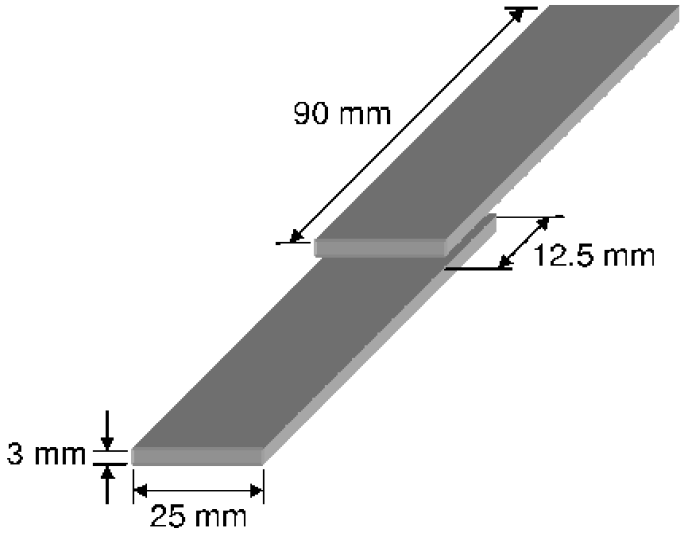

Figure 7.2: Single lap tensile specimen as manufactured by TIW

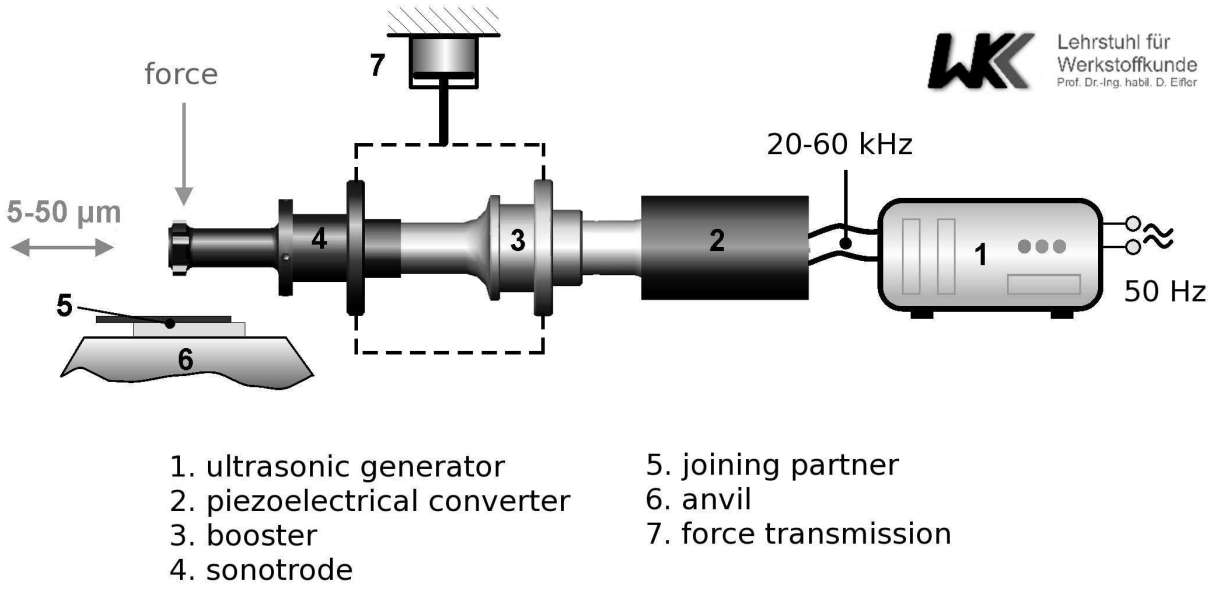

Figure 7.3: The process machinery of Ultrasonic Metal Welding (Balle [6])

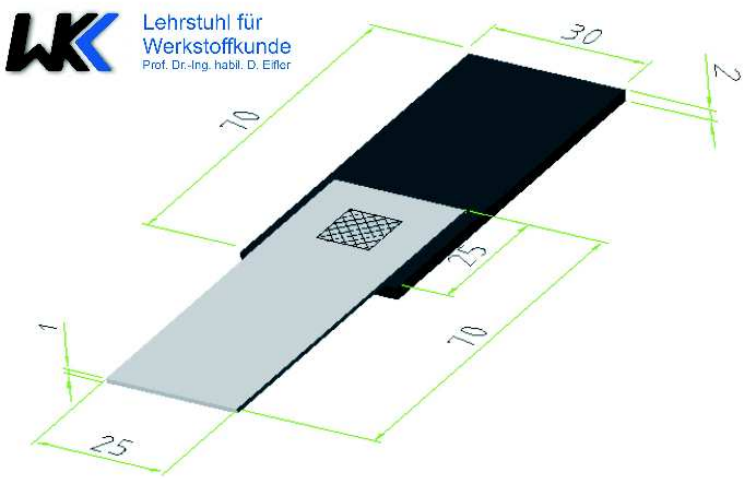

Figure 7.4: Single lap tensile specimen as manufactured by UMW

by an ultrasonic generator. This converter uses the reversed piezoelectrical effect, transforming the high frequency voltage into mechanical oscillations. The necessary oscillation amplitude in the welding zone which is between 5 to 50 μm is achieved by an appropriate booster and sonotrode design. A static pressure (7) and the welding energy by means of ultrasonic shear waves are simultaneously applied to the joining partners (5) which are fixed to an anvil (6). In the course of this process, the PA66 matrix is forced out of the welding zone. Related, the aluminium gets very close to the carbon fibres. It could be proved that both an intermolecular contact as well as a mechanical interlocking are accomplished by UMW (Balle et al. [6]). The typical geometry of a such manufactured specimen is displayed in Fig. 7.4

7.1.3 Displacement and Strain Analysis

In order to produce integral force-displacement-curves, tensile test specimens manufactured by TIW and UMW are tested with a tensile testing machine by the project partners in the context of the DFG Research Unit 524. The test setup is displayed in Fig. 7.5. The single lap tensile specimens are mounted into the chuck jaw of the testing machine. The tests are conducted at a constant cross head speed. During the tests a data acquisition programme continously records the tensile forces and the elongation.

To specify the theoretical model, it is necessary to compare not only force-displacement-curves. For a more detailed verification of the simulation, a locally resolved optical measurement method is applied to obtain local displacement and strain fields. Therefore, the in-plane and out-of-plane deformation is recorded, using modern optical measurement techniques based on Electronic Speckle Pattern Interferometry (ESPI) (Cloud [37], Busse et al. [29]). By ESPI, such data fields are achieved for all three dimensions and for different loadings at any point of the specimen surface. ESPI (Fig. 7.6) uses a laser which is split into a reference beam and a beam for the purpose of object illumination.

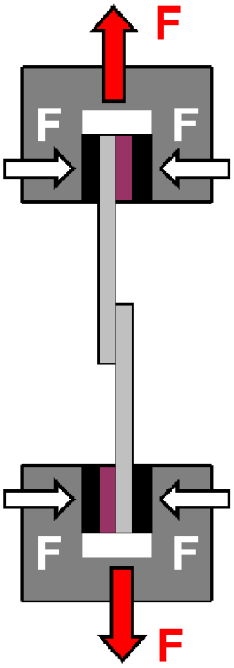

Figure 7.5: Tensile test setup

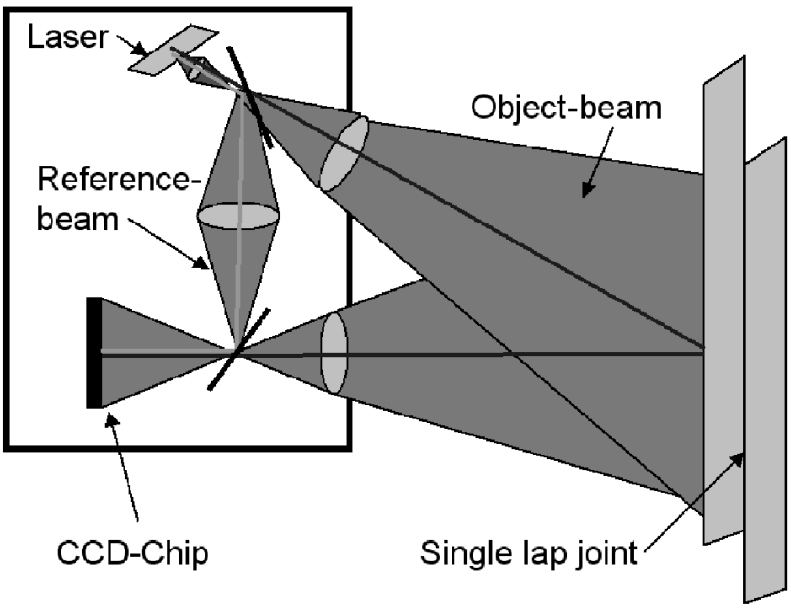

Figure 7.6: Principle of ESPI

After the recombination of the two beams, the SPECKLE pattern (Fig. 7.7) is obtained that correlates with the roughness of the observed object. The phase Φ between the two laser beams depends on the optical path lengths. The deformation of the object changes this length, and correlating pictures before and after loading enables the elimination of the unknown phase Φ. The result is the phase angle Δ which directly corresponds to the deformation of the object. The accuracy of the measured phase angle depends only on the geometrical setup and the wavelength of the laser used. The achieved sensitivity based on a Q300 ESPI system by Dantec Ettemeyer (see Yang and Ettemeyer [194]) is better then 0.1 μm in all directions. Computing the gradient in space of the displacement field determines the strain contribution in every point of the object surface. Additionally to ESPI, the so-called Digital Image Correlation (DIC) is applied to obtain local displacement and strain fields. For detailed remarks concerning the method of DIC, it is referred to, e.g., Friebe and Winter [55], Winter [189] as well as Kornmann and Kröplin [82].

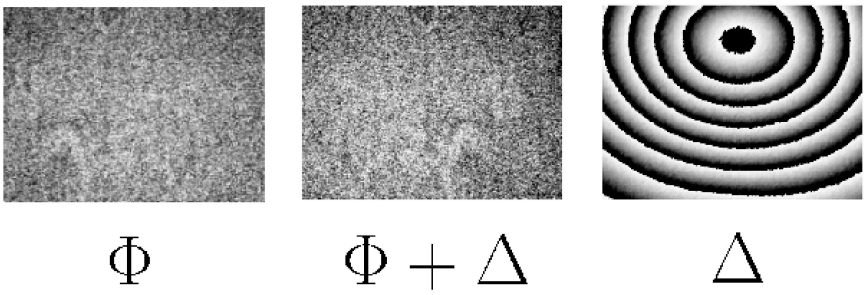

Figure 7.7: SPECKLE pattern of a circular loaded plate

7.2 Simulation of Tensile Tests of Thermal Impact Welded PEEK/Steel Single Lap Tensile Specimens

In order to predict the mechanical properties of more complex PEEK-steel components to be manufactured by the method of TIW in the future, for now, simulation techniques focus on single lap tensile tests. As such, the developed models shall permit the determination of the strength as well as inelastic properties of the joint in order to reduce the number of experiments. Using the Finite Element Method (FEM) for simulation, the importance of so-called interface elements must be emphasised. The representation of the loading behaviour of the weld interface is essentially based on appropriate material models for the interface elements which is chosen to be elastoplastic with damaging effects, see section 3.4. The steel substrate is modelled by elastoplasticity with linear isotropic hardening. The local and integral empirical data resulting from testing and analysis is consequently used to verify the FEM-based numerical modelling.

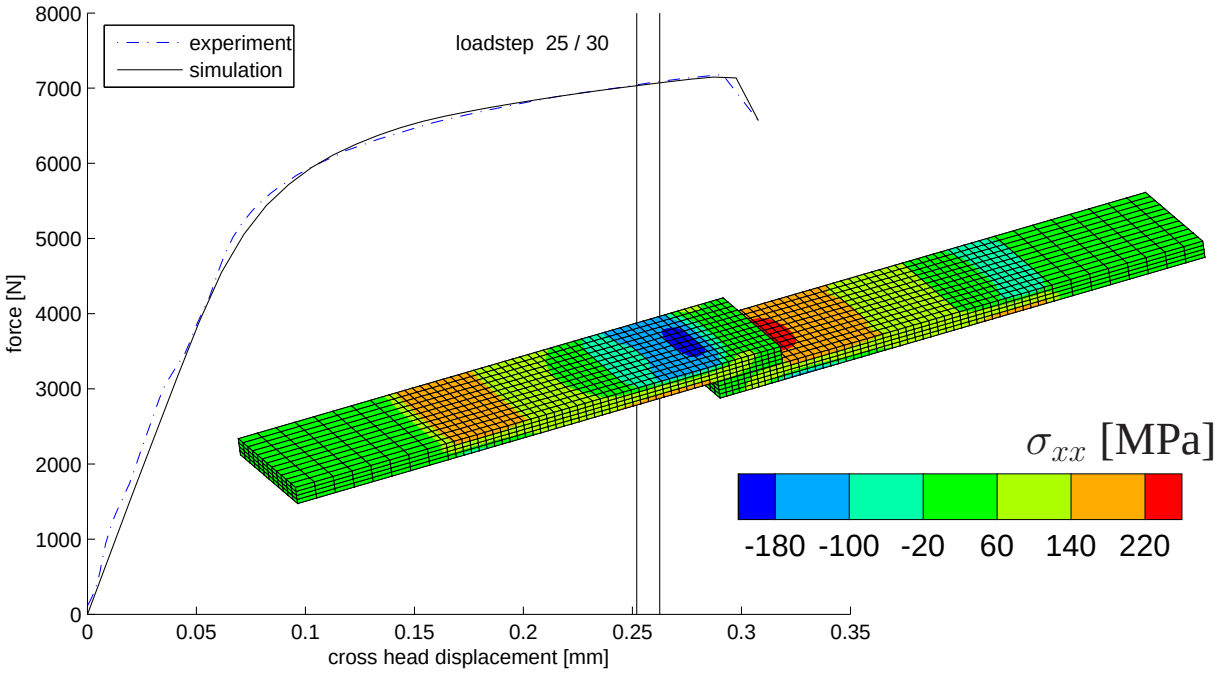

Figure 7.8: Force-displacement-curve of a thermal impact welded single lap tensile specimen (left), normal stress in loading direction σ_{xx}, loadstep 25/30 (right)

7.2.1 Results

As can be seen in Fig. 7.8, the experimentally obtained macroscopic force-displacement-curve is nicely reproduced by the simulation whereby a model with 5208 elements has been applied, with 120 interface elements for the discretisation of the welding zone. The chosen material parameters for the steel substrate are: Young's Modulus 166900 MPa, Poisson Ratio 0.3, yield stress 140.3 MPa and hardening modulus 95 MPa while suitable material parameters for the interface are: c_s = c_t = 35211 MPa/m, c_n = 100000 MPa/m, Y_{0s} = Y_{0t} = Y_{0n} = 21.5 MPa/m, H_s = H_t = H_n = 150 MPa/m, μ_{0s} = μ_{0t} = μ_{0n} = 0.059 MPa m, and j_s = j_t = j_n = 130 (MPa m)$^{-1}$. Three zones can be identified from Fig. 7.8: an elastic zone, an elastoplastic zone and a damaged zone. According to the appropriate model and set of material parameters, the simulated force-displacement-curve fits to the experimental data. The first zone is given by an elastic straight line. In the second zone, beginning at a force of approximately 4500 N, elastoplastic hardening effects in both the bulk and the interface occur. Identifying the third zone which begins at approximately 7000 N, a softening behaviour of the specimen can be seen due to interfacial damage activity, followed by complete failure. Since integral-type-data is essentially one-dimensional, local analyses using Electronic Speckle Pattern Interferometry (ESPI) are additionally performed. Based on two-dimensional data fields, comparisons between ESPI and numerical simulations constitute an important part of the validation procedure so that the set of material parameters is not determined from purely one-dimensional measurements. To be specific, using different material parameters, similar one-dimensional force-displacement curves can be generated. The optical analyses with ESPI shown here are applied to the narrow side of the specimen and are supported during the entire loading history. Here, Figs. 7.9-7.11 are referred to loadstep 25/30. Concerning simulation

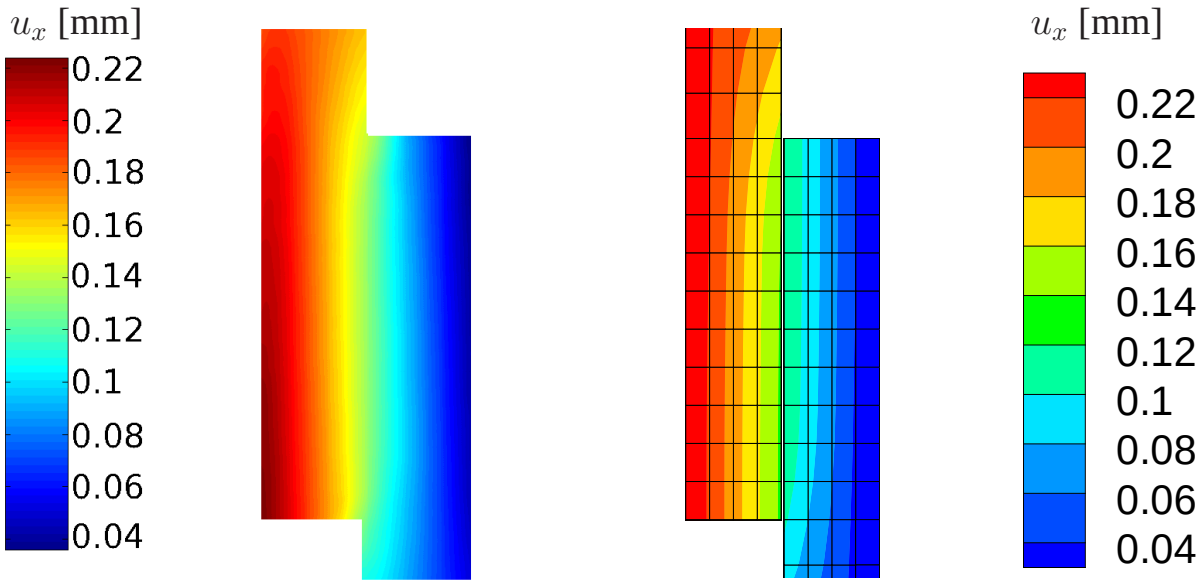

Figure 7.9: ESPI image of a displacement offset in loading direction (left), corresponding simulation loadstep 25/30 (right)

details, the discretisation of the mesh is throughout shown in the undeformed configuration. Note that the interface itself is not displayed in the results because of its dimensional deficiency. Placing emphasis on Fig. 7.9, one observes quantitative agreements between experimental and simulation results concerning deformations in loading direction. In Fig. 7.10, the so-called out-of-plane deformation (bending displacement) is shown. By analogy with Fig. 7.9 good quantitative similarities are observed. Finally, strain distributions in loading direction are compared in Fig. 7.11. Apart from the distinct qualitative similarity of the ESPI image and the simulation quantities are in good agreement.

7.2.2 Discussion

First, it has to be mentioned that the quality of the ESPI result is influenced by smoothing data, and by the fact that the specimen turns out of the fixed observation frame which is shown here, due to the torque induced by the geometry. Besides this, a possible reason for differences may be that in the process of TIW, PEEK leaks out of the interfacial zone and accumulates at the corners, which is not accounted for in the simulation. This possibly causes that in the simulation result, maximum strains occur slightly shifted compared to the ESPI image. Consequently, by using interfacial elastoplasticity with Lemaitre-type-damage, the phenomenological simulation of global force-displacement-curves is successfully recaptured. One-dimensional integral-type data as well as two-dimensional data, especially local displacements, have quantitatively been captured. Good qualitative and, up to some degree, also quantitative similarities occur when comparing local strains in loading direction.

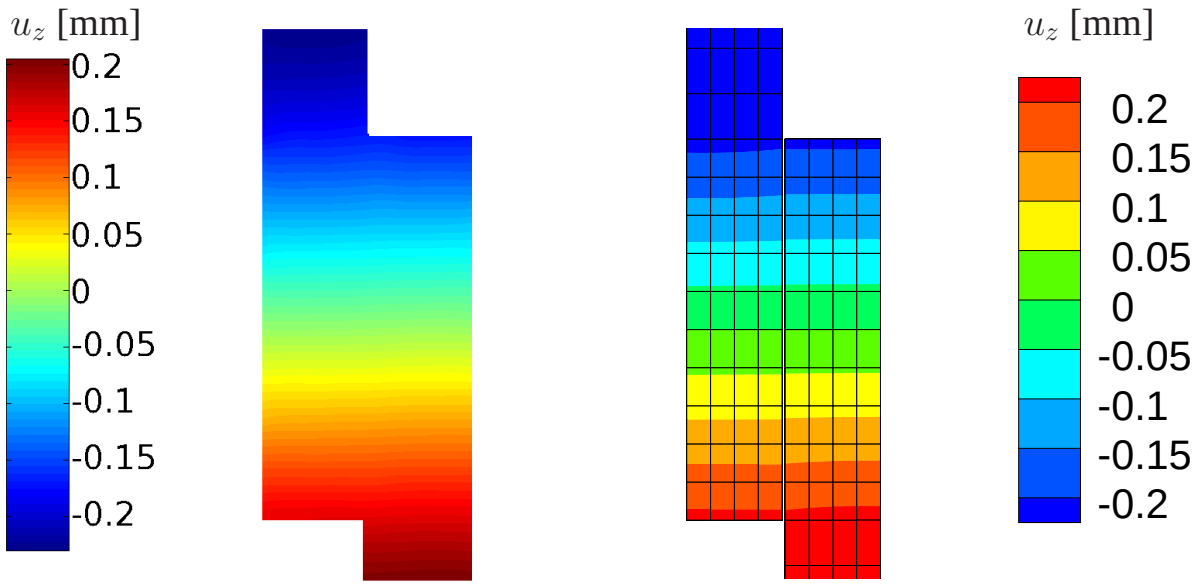

Figure 7.10: ESPI image of a displacement offset in out-of-plane direction (left), corresponding simulation loadstep 25/30 (right)

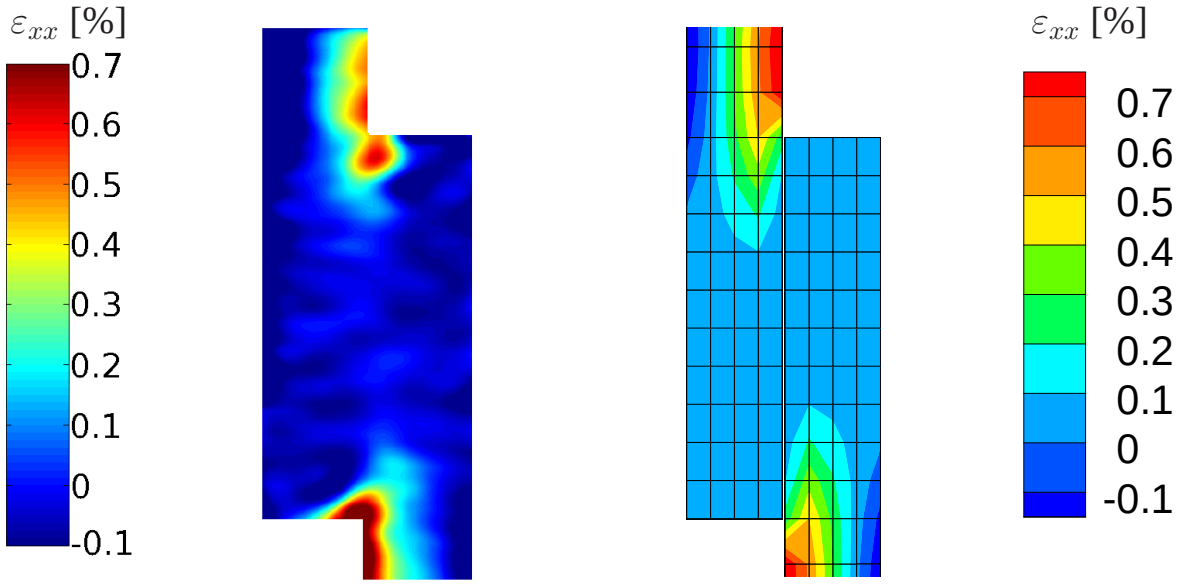

Figure 7.11: ESPI image based strains in loading direction (left), corresponding simulation loadstep 25/30 (right)

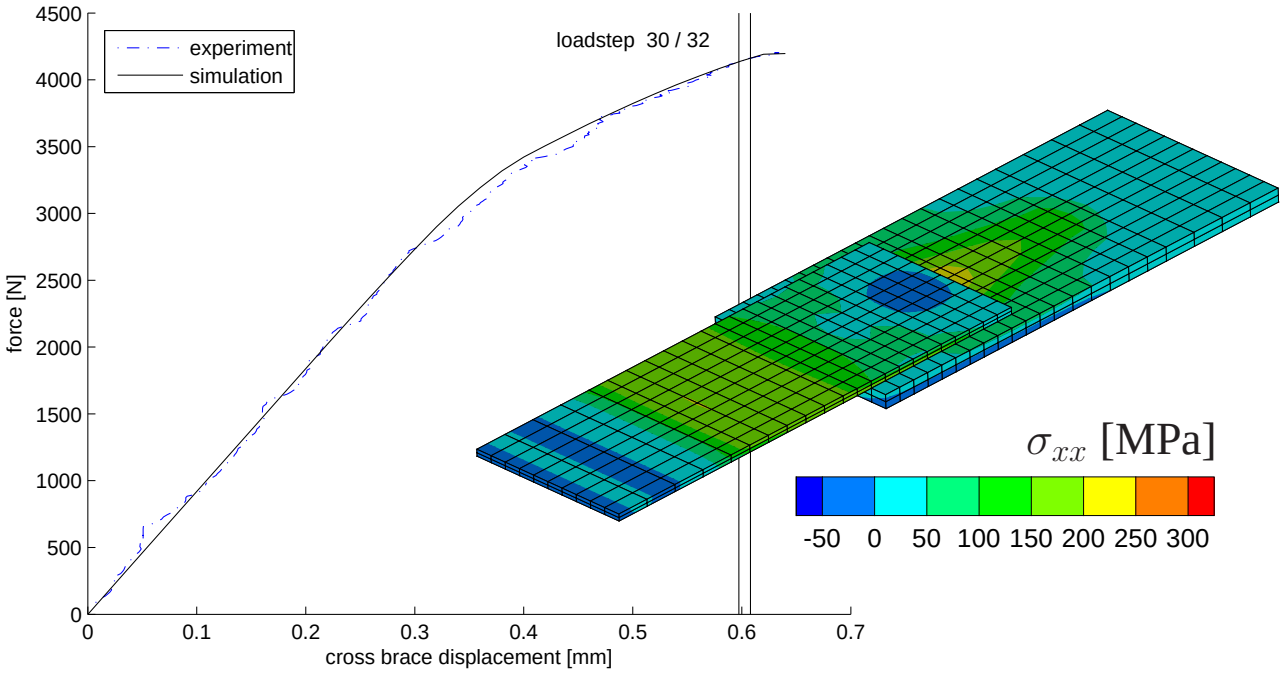

Figure 7.12: Force-displacement-curve of a ultrasonic metal welded single lap tensile specimen (left); normal stress in loading direction σ_{xx}, loadstep 25/30 (right)

7.3 Simulation of Tensile Tests of Ultrasonic Metal Welded CF-PA66/AlMg$_3$ Single Lap Tensile Specimens

For the same motivation as for TIW, investigations for now concentrate on single lap tensile tests. The interface has again been modelled by elastoplasticity with damage, while the aluminium is modelled by elastoplasticity with linear isotropic hardening. For CF-PA66, orthotropic elasticity is assumed.

7.3.1 Results

Fig. 7.12 shows that the macroscopic force-displacement-curve of the experiment is reproduced by the simulation. Here, a model with 984 elements has been applied, with 16 interface elements for the discretisation of the sonotrode contact area. The aluminium substrate is modelled by means of the following material parameters: A Young's Modulus of 70580 MPa, a Poisson Ratio of 0.33, a yield stress of 175.3 MPa and a hardening modulus of 3500 MPa. Interfacial material parameters are given as c_s = c_t = 190 MPa/m, c_n = 540 MPa/m, Y_{0s} = Y_{0t} = Y_{0n} = 33 MPa/m, H_s = H_t = H_n = 115 MPa/m, μ_{0s} = μ_{0t} = μ_{0n} = 5.9 MPa m and j_s = j_t = j_n = 50 (MPa m)$^{-1}$. According to Fig. 7.8, an elastic zone, an elastoplastic zone and a damaged zone are identified. The elastoplastic zone begins at approx. 3000 N, where elastoplastic hardening effects in both the bulk and the interface occur. The damaged zone is relatively narrow and begins at approx. 4100 N. At the end of the loading history, a very a brittle behaviour is present.

7.3.2 Discussion

Integral data of a statistically confirmed force-displacement plot has been captured by the simulation very nicely. Nevertheless, unlike in section 7.2, a local comparison could not yet be conducted. Therefore, the recording of two-dimensional data fields by optical analysis methods as, e.g., ESPI is needed. This is of primary interest in order to verify the parameters of the simulation.

7.4 Simulation of Tensile Fatigue Tests of Ultrasonic Metal Welded CF-PA66/AlMg$_3$ Single Lap Tensile Specimens

Subsequently, two experimental results of tensile fatigue tests of Ultrasonic Welded CFK-PA66/AlMg$_3$ single lap tensile specimens are compared to simulations. The aluminium substrate is modelled by elastoplasticity with linear isotropic hardening while for CF-PA66, orthotropic elasticity is assumed. The welding interface is modelled by cycle-based fatigue as discussed in section 3.6. Here, only preliminary experimental results achieved by the Lehrstuhl für Ressourcengerechte ProduktEntwicklung (RPE) at the University of Kaiserslautern could be incorporated. In view of the fact that the experimental setup is quite difficult to handle, for this time, simulation shall not remodel reality but rather is interpreted as a tool to evaluate the experimental results. Certainly, the simulation will not display reality until it is verified with statistically proven data.

7.4.1 Results

The material parameters of the substrates have been adopted from section 7.3. Keeping in mind that high-cycle-fatigue behaviour is at hand, the aforementioned cycle-based fatigue formulation, including a penalty formalism as discussed in section 3.11, is incorporated for the interface. The basic interfacial material parameters are given by $\beta_s = \beta_t = 0.2$, $\beta_n = 1$, $\alpha = 10$, $\beta = 1$, $\kappa = 0$. For experiment 1, the

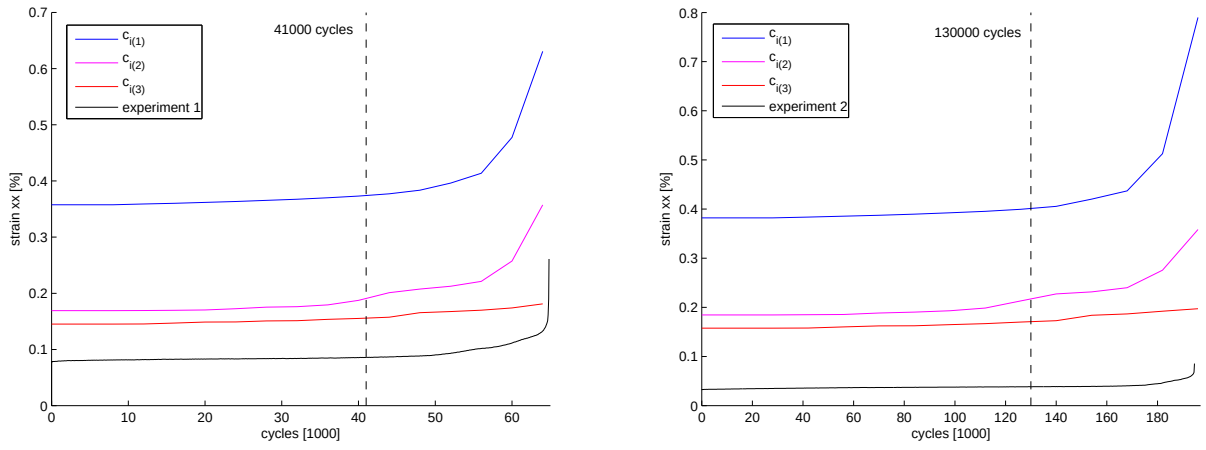

Figure 7.13: Strains over cycle number, experiment 1 and simulation (left), experiment 2 and simulation (right)

	Experiment 1 ($\Delta N = 4000$, 16 load steps)			
stiffness 1	$c_{s(1)} = c_{t(1)} = 190$ MPa/m	$c_{n(1)} = 540$ MPa/m	$q = 5400$ MPa/m	$C = 0.0027$
stiffness 2	$c_{s(2)} = c_{t(2)} = 10\, c_{s(1)}$	$c_{n(2)} = 10\, c_{n(1)}$	$q = 54000$ MPa/m	$C = 0.175$
stiffness 3	$c_{s(3)} = c_{t(3)} = 100\, c_{s(1)}$	$c_{n(3)} = 100\, c_{n(1)}$	$q = 540000$ MPa/m	$C = 6.06$
	Experiment 2 ($\Delta N = 14000$, 14 load steps)			
stiffness 1	$c_{s(1)} = c_{t(1)} = 190$ MPa/m	$c_{n(1)} = 540$ MPa/m	$q = 5400$ MPa/m	$C = 0.0009$
stiffness 2	$c_{s(2)} = c_{t(2)} = 10\, c_{s(1)}$	$c_{n(2)} = 10\, c_{n(1)}$	$q = 54000$ MPa/m	$C = 0.0582$
stiffness 3	$c_{s(3)} = c_{t(3)} = 100\, c_{s(1)}$	$c_{n(3)} = 100\, c_{n(1)}$	$q = 540000$ MPa/m	$C = 2.0$

Table 7.1: Interfacial stiffnesses, penalty and fatigue parameters for experiments 1 and 2

strain in loading direction is plotted over the cycle number in Fig. 7.13 on the left hand side, while the right hand side features experiment 2. In order to approach the experimental results, three simulations with different interfacial stiffnesses have been conducted for each experiment. The results are also displayed in Fig. 7.13. Related material parameters are given in Tab. 7.1. Obviously, the (lowest) stiffnesses 1 as adopted from the tensile test simulation of section 7.3 do not fit the experimental strain-cycle curves of Fig. 7.13. For both experiments, the global data, given as strain-cycle curves, is the better approximated the higher the stiffnesses are chosen. Nevertheless, for even very high interfacial stiffnesses, the experimental curves cannot be reached. Additional local data recorded by the Digital Image Correlation (DIC) is compared with the simulation in Fig. 7.14. All pictures are valid for (the lowest) stiffnesses 1 at 2/3 of the cyclic loading history, what is also denoted in Fig. 7.13. On the left hand side of Fig. 7.14, the strains in loading direction ε_{xx} for experiment 1 and, below, the simulation result are shown, while the right hand side features the strains in loading direction ε_{xx} for experiment 2 (above) and the simulation result (below). The simulation results are qualitatively similar for both experiments. Concerning experiment 2 on the right hand side of Fig. 7.14, experimental and simulation results clearly diverge. In contrast, for experiment 1 which is depicted on the left hand side of Fig. 7.14, at least a qualitative tendency is observable. The strain field on the aluminium substrate resulting from DIC measurements is minimal at the upper side, while it is maximal at the lower side. This is roughly reflected by the simulation.

7.4.2 Discussion

First, it has to be noted that experiments 1 and 2 show very different results. Both specimens have been cycled with a loading amplitude of 2 kN. Concerning the strain-cycle curves of Fig. 7.13, this is partially due to the clip-on strain gauge that has been applied over different distances for experiments 1 and 2, which certainly has been considered in the simulation. Nevertheless, especially the locally resolved experimental data is differing. The specimen used for experiment 1, as a preliminary test, has been cycled before with low amplitudes and very high cycle numbers without revealing any inelastic behaviour. It is questionable how this has to be interpreted in light of the comparison of experiment 1 and 2.

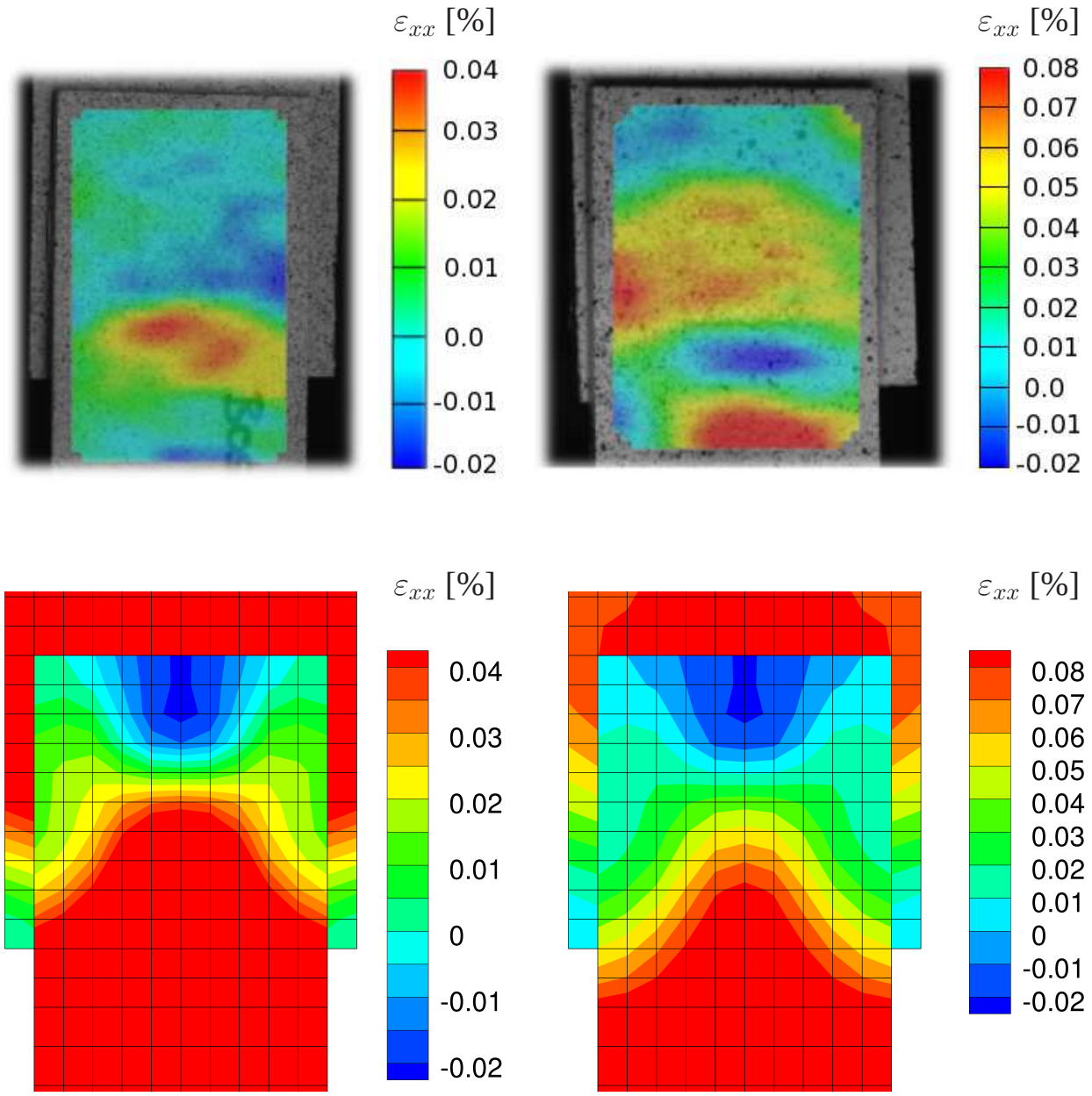

Figure 7.14: Above: DIC image of strains in loading direction at 2/3 of the cyclic loading history, experiment 1 (left), experiment 2 (right). Below: strains in loading direction, simulation of experiment 1 with stiffness $c_{i(1)}$ (left), and strains in loading direction, simulation of experiment 2 also with stiffness $c_{i(1)}$ (right)

In view of the simulation, only the sonotrode contact area has been discretised by means of interface elements. Normally, during the process of UMW, the polyamide melts and induces an extended contact area, which is not accounted for in the simulation. Furthermore, for numerical reasons, a very steep rise of the strains as observed in Fig. 7.13 for both experiments at the end of the cyclic loading history, could not yet be generated.

From Fig. 7.13, it can be concluded that either the substrates are modelled too soft or that the clip-on strain gauge data is in need of improvement. A rise of interfacial stiffnesses does not seem to solve this problem completely. Moreover, the results of section 7.3 would suggest the lowest interfacial stiffnesses. The divergence of experimental data as indicated by Figs. 7.13 and 7.14 means that the experimental setup is not yet reproducible. Despite the fact that for experiment 1 a cyclic prehistory has been at hand, the differences are quite immense. Nevertheless, the local data of the first experiment given by the strain field in loading direction is roughly reproduced in the simulation.

In order to improve the experiments and to reduce the variation of the results, a new clamping tool is currently developed at the Institute of Materials Science and Engineering (WKK) at the University of Kaiserslautern. This, as well as a comparison of specimens with the same prehistory and an identical application of the clip-on strain gauge is needed. To sum up, the setup of experiment 1 seems to approach the numerical simulation more than experiment 2, and the cycle-based fatigue law which is applied to the interface is principally applicable for the simulation of such fatigue experiments as given here.

8 Application II – Piezoelectric Mesostructures

In recent years, smart materials have occupied a decisive role in many fields of engineering science. They can be subdivided into several subclasses, e.g., piezoelectric solids, shape memory alloys, electro-rheostatic and magneto-rheostatic fluids, to name but a few. By means of their revolutionary properties, smart materials expand technical possibilities, in turn giving new inspiration to their own evolution. An obvious example is the continuing downsizing of the application scales, being documented by developments related to nanotechnology. Depending on the type of application, use can be made of both the direct as well as the inverse piezoelectric effect. Furthermore, so-called ferroelectric materials are a subcategory of piezoelectric materials. They inhere the ability that domain states can be modified by loadings of sufficient magnitude. In any case, cyclic loading conditions are common, resulting in fatigue-related degradation of the various material properties.

In this respect and in addition to laminar welded lightweight structures, piezoelectric ceramics are another class of modern engineering materials occurring in this work. In the following, a polycrystalline mesostructure of PZT is discretised by triangular continuum elements for the grains and by interface elements for the grain boundaries. The continuum material law is linear ferroelectric, see section 2.4, while the interfacial material law is basically linear and decoupled but endowed with a penalty formalism and two different fatigue damage evolutions. The first type is suitable for low-cycle-fatigue, while the second type captures high-cycle-fatigue. These material laws have been discussed in section 3.8. The constitutive model of the interface is artificial in nature, due to missing reliable information on the exact grain boundary behaviour for fatigue-type loading (Utzinger et al. [183, 182]). It is designed to place emphasis on grain boundary effects and is believed to be a first step towards a sound physics-based model of real fatigue processes as, e.g., observed near the electrodes for electric loading. First, section 8.1 includes the results of a literature survey on the issues of piezoelectric fatigue, grain boundaries and material modelling. This is followed in section 8.2 by some remarks concerning the interfacial modelling in the present elaboration. A discretisation of a rectangular PZT mesostructure which is adopted from a micrograph is introduced in section 8.3, serving as a framework for the implementation of the cohesive models examined before. Representative numerical results are presented in section 8.4. Thereby, different low- and high-cycle-fatigue motivated boundary conditions are applied considering both mechanical and electrical cycling. Finally, the results are discussed in section 8.5. Please note that all considerations in this chapter are reviewed for a two-dimensional problem.

8.1 Literature Survey

Concerning fatigue life, many physical processes, occurring on different scales, are of interest. According to the literature, there are two types of fatigue, the first being due to embrittlement and the second resulting from fatigue crack growth (Lupascu [99]). In Daining et al. [43] it was found for PZT that for cyclic electric loading with an amplitude far below the coercitive field strength E_c, the evolution and propagation of parallel microcracks is observed. With the amplitude getting closer to E_c, macrocracks are emerging. Due to diffusion processes, the behaviour of piezoelectric materials is rate dependent (Lohkämper et al. [97]) and, consequently, fatigue effects are in general subject to cyclic frequency loading (Schorn et al. [154]). Depending on the particular application being considered, either low-cycle-fatigue or high-cycle-fatigue effects are observed. In this regard, geometrical influences as, e.g., notches (Westram et al. [187]), can lead to a very limited fatigue life. For electric loading, fatigue related influences are highly concentrated at the electrodes. Certainly, in view of oscillating loading conditions close to some operating point near to the polarisation saturation, the high-cycle-loading type is most common. However, on the micro scale, domain switching within the grains, grain boundary effects and their interactions all together cause the fatigue properties of a ferroelectric material on the meso scale.

In the current chapter, focus is placed on grain boundaries, amongst others being relevant when considering electrical properties of a ferroelectric ceramic (Knauer [81]) and playing a crucial role in the fatigue behaviour (Lupascu [99]). The smaller the grains are, the larger the influence of the grain boundaries on the global behaviour of the material becomes (Schaumburg [151]). Consequently, grain boundaries are of crucial importance on the nano scale (Rühle [150]). They are mechanically weak (Lupascu [99]) and reveal a lower permittivity than the grain bulk (Bast [9]). Additionally, amorphous structures in the grain boundaries emerging under fatigue loading conditions (Lupascu [99]) suggest very reduced coupling effects. According to Schaumburg [151], driving forces for the defect structure of grain boundaries are the electrostatical potential, the degradation of elastic strain energy and the formation of associated defects with dipole character.

To reduce the number of experiments, various simulation tools can be applied. Furthermore, by relating simulations and experimental results further insight can be gained. In this context, the Finite Element Method makes a model of the mesostructure accessible to simulation. There are several suggestions for thermodynamically motivated constitutive models for the bulk, see e.g. Kamlah [76], Kamlah and Böhle [77], Schröder and Gross [155], Schröder and Romanowski [158], Klinkel [78, 79] and Mehling et al. [108], mostly incorporating switching phenomena, see also Arockiarajan et al. [4], Arockiarajan and Menzel [3], Menzel et al. [110] and references cited therein. In view of Finite-Element discretisations of polycrystalline mesostructures, it is well-established to generate appropriate meshes by utilisation of the Voronoi-tessellation (Espinosa and Zavattieri [53], Sfantos and Aliabadi [161]). Additionally, though restricted in its applications, the Boundary-Element-Method can be applied to discretise grain boundaries (Sfantos and Aliabadi [161]), thereby omitting the computational costs induced by discretised grains.

Grain boundaries are very narrow zones, being located in between surrounding grains. In this work they are identified as a priori known zones of delamination. Hence, combined with appropriate constitutive models, it is obvious that interface elements should be used systematically to model the intergranular weak zones, see also Cannmo et al. [33, 32]. Interface elements are one dimension

smaller than surrounding continuum elements, thereby avoiding bad-conditioned stiffness matrices as obtained for too narrow continuum elements (Schellekens and de Borst [153], Utzinger et al. [180]). In this context, concerning the numerical modelling of interfaces, see also the approach based on regularised discontinuities by Jansson and Larsson [72] and Larsson and Jansson [88]. To simulate grain boundaries in ceramics, Espinosa and Zavattieri [53] incorporated a bilinear, irreversible cohesive law in an interfacial Finite-Element context. Concerning fatigue damage, the reader is referred to the investigations by, e.g., Paas et al. [135] and Peerlings et al. [140]. In these works evolution criteria for non-piezoelectric bulk materials under cyclic loading are developed, especially suited for high-cycle-fatigue. Similar formulations have been proposed by Robinson et al. [149], Munoz et al. [123] and Erinc et al. [50] for non-piezoelectric interfaces. A cohesive low-cycle-fatigue formalism was developed by Nguyen et al. [127], and further extended by Arias et al. [2] for coupled problems, however, without placing emphasis on its numerical implementation. For a detailed discussion concerning these issues see chapter 3.

8.2 Modelling Aspects

In order to concentrate on grain boundary effects, a linear coupled material law is incorporated for the grains. Accordingly, an operating point close to a saturated polarisation is assumed and switching effects are neglected. Furthermore, any rate dependencies are excluded. In view of the grain boundaries or rather interfaces, the quantities of displacements and electric potential are replaced by jump-quantities over the interface, i.e. the displacement jump and the electric potential jump, due to reasons discussed in the introduction of chapter 3. The starting point for the subsequent elaborations is a linear and coupled interfacial material behaviour. As a penetration of the opposite surface lines should be avoided for obvious physical reasons, an adequate penalty formalism as introduced in section 3.11 is additionally considered. Furthermore, to account for fatigue effects, a change of constitutive tensors is incorporated in the subsequent elaborations. This is accomplished by incorporating fatigue-dependent Lemaitre-type damage as discussed in section 3.8.

In grain boundaries, foreign atoms and impurities are deposited, not fitting into the stable crystal configuration of the grains. Additionally, secondary phases can occur (Schaumburg [151]), resulting in a more or less heterogeneous consistency. As already mentioned, amorphous structures in the grain boundaries emerge under fatigue loading conditions. Based on these informations, a piezoelectric coupling mechanism is considered to be of a very reduced intensity. Consequently, the interfacial coupling factor will be set to zero. Depending on certain doping conditions, grain boundaries might become highly charged interface layers (Lupascu [99]). In that event, capacitor-type interfacial material laws could be applied, which is of interest concerning future research.

From the experimental point of view it could not yet been clarified how the grain boundary permittivity changes under fatigue loading conditions. The permittivity is defined as the polarisation capability of a medium. An argument for a decreasing permittivity could be that given dipolar structures are destroyed by some kind of fatigue-related erosion, or that the intergranular medium is endowed with e.g. oxygen vacancies, eventually diffusing out of the bulk under fatigue loading (Lupascu [99]). In view of the permittivity-decreasing influence of cracks, the present model only accounts for a very reduced broadening of grain boundaries. The phenomenon of microcracking is not yet fully understood and is still subject of intense discussion, see Lupascu [99] and references cited therein. Moreover,

shaking and aligning of ions due to fatigue loading conditions as well as some hypothetical increase of the ion concentration in the grain boundaries due to cyclic loading would suggest an increasing permittivity. For the present work, a simplified electrical enthalpy approach as given in section 3.8 has been made. Chemical potentials as well as any fluxes, diffusion phenomena or dipolar charges are neglected, but certainly play a role and consequently motivate further research and enhanced modelling approaches. Due to the unclear physical circumstances for the grain boundary permittivity, an artificial but simple linear relation dependent to the damage parameter is applied as given in equation (3.254).

8.3 Discretisation

To enlighten the functionality of the fatigue-related material laws of section 3.8, a piezoelectric mesostructure, imported from Nuffer et al. [129], is discretised with finite elements. In a nonlinear finite element algorithm, low- and high-cycle-fatigue related constitutive relations are reflected by means of algorithmic tangent moduli. Then, the discretisation can be subjected to different low- and high-cycle-fatigue-motivated boundary conditions. The present mesostructure, shown in Fig. 8.1 on the left hand side, is a micrograph of PIC 151, manufactured by PI Ceramic, Lederhose, Germany. It has been generated by a scanning electron microscope (SEM). PIC 151 is a standard material for actuators and suitable for low-power ultrasonic transducers and low-frequency sound transducers. On the right hand side of Fig. 8.1 an adequate discretisation of this mesostructure is highlighted. Grains are represented by continuum elements and are red-coloured. A pragmatic choice are linear triangular elements, geometrically defined by some point inside the grain and the grain polygon. The dark-blue-coloured interface elements are given at every grain boundary as one side of the related grain polygons, whereby each interface element is surrounded by two triangular elements. Please note that a discretisation of polycrystalline grain boundaries by means of interface elements has also been introduced by Cannmo et al. [33, 32]. In this two-dimensional approximation of a real mesostructure, concerning the micrograph on the left hand side of Fig. 8.1, surfaces of underlying grains, apparent as black areas, are treated as voids in the related discretisation. See the right hand side of Fig. 8.1. In the following, different low- and high-cycle-fatigue-motivated boundary conditions are applied to the discretisation shown on the right hand side of Fig. 8.1, considering mechanical and electrical cycle loading. Both the time-based and the cycle-based model are incorporated, and, consequently, compared. As a starting point, the material parameters of the grains, or respectively, the bulk material, have already been highlighted in Tab. 5.1. All material parameters of the bulk are related to PIC 151. Concerning the material parameters of the interface, no specific stiffness or permittivity values could be retrieved from the literature. Based on Lupascu [99] and Bast [9], grain boundaries are supposed to be mechanically weaker than grains and, moreover, seem to inhere a lower permittivity. In this chapter, the internal length of the interface is a default value and set as $l = 0.3 \times 10^{-6}$ [m], related to the width of a grain boundary. Consequently, stiffnesses and permittivities have been academically chosen as

$$c_s = c_n = \frac{[\boldsymbol{C}^{tra}]_{33}}{10\,l}, \quad q = \frac{[\boldsymbol{C}^{tra}]_{33}}{l}, \quad \epsilon_r^{init} = \alpha^{init}\,\frac{[\boldsymbol{\epsilon}]_{33}}{\epsilon_0\,l}, \quad \epsilon_r^{end} = \alpha^{end}\,\frac{[\boldsymbol{\epsilon}]_{33}}{\epsilon_0\,l} \tag{8.1}$$

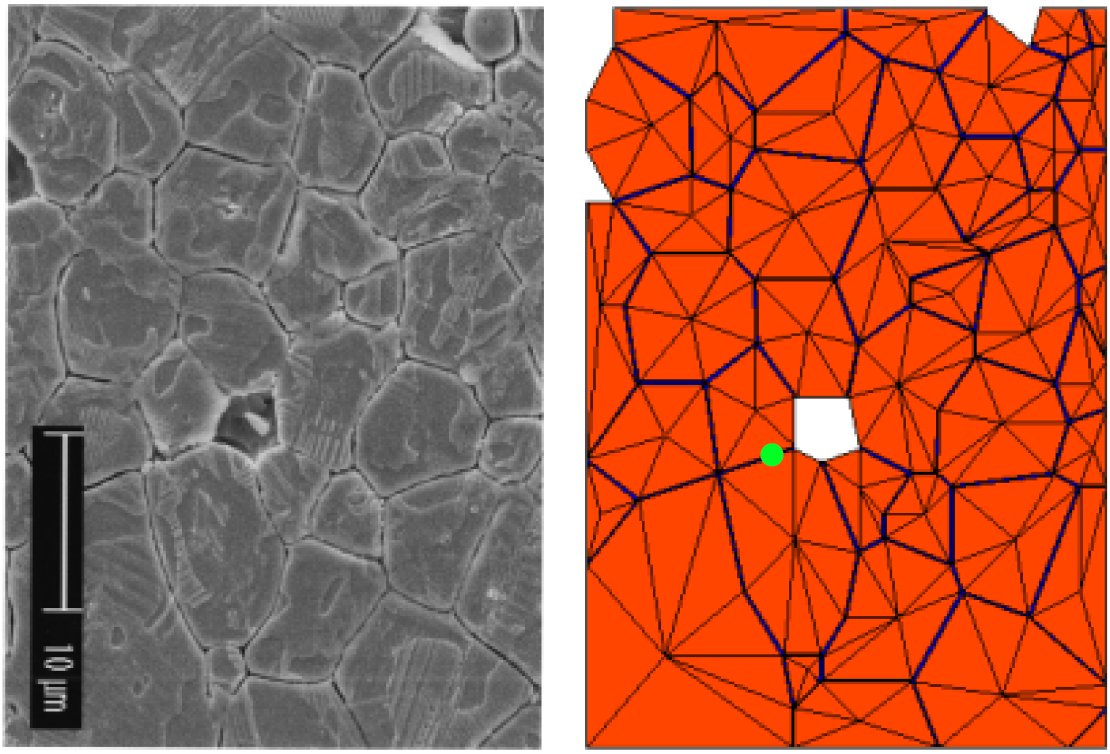

Figure 8.1: Micrograph of PIC 151 (left, courtesy by Prof. D.C. Lupascu, see Nuffer et al. [129]) and finite element discretisation (right). Continuum elements are coloured red, interface elements are dark blue. The green spot marks the Gauss point where the damage variables for Fig. 8.20 and 8.21 are saved

with coupling effects in the interface being neglected. In the examples to be shown, an interfacial permittivity varying with the damage has been assumed, in accordance with equations (3.250)–(3.253) and $\alpha^{init} = 1/10$. The material parameters incorporated in the effective quantity δ are chosen as β_s = 1 [m^{-1}], β_n = 1 [m^{-1}], and β_Φ = 0.01 [A s^3/[kg m^2]]. The comparatively low influence of the electric potential jump is considered to reflect the underlying physical behaviour, as the mechanical and electrical disruption of the grain boundary is considered to be dominant due to mechanical effects. Please note that, to improve numerical accuracy, it is necessary to express the unit of time as [s] = 10^3 [ms] for all computational input parameters. Furthermore, it shall be noted that due to the non-associated character of the incorporated fatigue law, the interface element stiffness matrix $\boldsymbol{K}^{ie}$ turns out to be in general non-symmetric.

8.4 Results

In the following, some representative numerical results are illustrated and described. For the grain boundaries, time- and cycle-based models are applied as well as increasing and decreasing permittivities. Concerning the boundary conditions, both mechanical and electrical cycling are incorporated.

8.4.1 Time-Based Fatigue Computations

In the examples of this section the time-based material law is applied, see section 3.8. The FE-discretisation introduced in the above serves as input for a nonlinear FE-programme, together with appropriate boundary conditions. The material parameter has been chosen as $\alpha = 4 \times 10^{-7}$.

Displacement Loading

The boundary conditions of the first example are schematically shown in Fig. 8.2. On the right hand side, it can be seen that on the upper boundary of the rectangular model cyclic displacements are applied. On the left hand side of Fig. 8.2, the same cyclic displacements are plotted over the number of loading steps. The cyclic load is applied such that it is always in the global range of tensile loading, with 14 loading steps for each cycle, and 288 steps in total to simulate 20 cycles including one additional loading step for the first loading sequence. The resulting stresses in vertical direction in the bulk, denoted as σ_{yy}, are displayed in Fig. 8.3 while the electric field in vertical direction in the bulk, E_y, is shown in Fig. 8.4. In both figures, snapshots are taken after the first loading amplitude ($\doteq$ 0 cycles), 5 and 20 cycles, all of them being marked in Fig. 8.2 by red circles. Fig. 8.3 shows that the stresses σ_{yy} decrease under continued cycling. This clearly accompanies a damage-related stiffness decrease. With a damage-induced increasing permittivity in mind ($\alpha^{end} = 3/10$) and only considering electric effects, the electric potential jump over the interface would tend to decrease, and in consequence, a related fraction of the electric field in the bulk would increase to compensate this. Hence, the fraction of strains in the bulk related to this is raised by some amount. In turn, this raises the displacement jumps in the interface, supporting damage evolution. For the current $\beta_\Phi \ll \beta_s = \beta_n$, mostly the displacement jump contributes to the damage. Considering the overall constitutive answer, the decreasing absolute value of the electric field component E_y as shown in Fig. 8.4 seems to be due to the dominant influence of decreasing interfacial stiffnesses. For a lower stiffness in the interface, strains in the bulk decrease. Simultaneously, also a large reduction of the absolute value of the electric field E_y will occur. The prevailing role of stiffnesses seems to be induced by the mechanical boundary conditions of cyclic displacement loading, while at the same time, at the upper boundary of the specimen, the electric potential boundary condition is free. Therefore, the electrical field behaviour in the bulk is dominated by the mechanical response, leading to decreasing values of E_y due to decreasing stiffnesses.

For similar boundary conditions (see Fig. 8.5) and a decreasing permittivity ($\alpha^{end} = 1/100$), the electric potential jump would tend to increase. Consequently, this effect does not assist the bulk strains to increase, and therefore, in the sense of the correlations described in the above, this effect does not support the damage evolution. With Fig. 8.6 revealing solely a slight influence of this effect for the stresses σ_{yy}, the electric field E_y given in Fig. 8.7 shows a smaller decrease as compared to Fig. 8.4.

Electric Potential Loading

In contrast, for a cyclic electric potential, adequate boundary conditions are found in Fig. 8.8. Again, 7 loading steps are chosen for loading and unloading within one cycle, resulting in 288 loading steps for 20 cycles including one more loading step in the first loading sequence. Moreover, Fig. 8.9 and 8.10 display snapshots after the first loading amplitude ($\doteq$ 0 cycles), 5 and 20 cycles. The interfacial

permittivity is considered to increase, i.e. $\alpha^{end} = 3/10$. Concerning the electric field component in vertical direction E_y, Fig. 8.10 shows that the absolute value of E_y increases with continued cycling. This can be related to increasing permittivities in the interfaces. With a cyclic electric potential given as a boundary condition, no displacements are prescribed for the upper boundary. Therefore, it is considered that electric fatigue effects superpose mechanical-related effects concerning the absolute value of the electric field component E_y. This is not the case for the stresses σ_{yy}, displayed in Fig. 8.9. There, mechanical influences still prevail and stresses are reduced with continued cycling.

8.4.2 Cycle-Based Fatigue Computations

Concerning cycle-based fatigue, the boundary conditions are essentially similar to the boundary conditions of section 8.4.1, with a difference concerning the number of cycles and the numerical implementation. The appropriate material law is discussed in section 3.8. Material parameters have been chosen as C = 1.5 $\times$ 10^9, β = 1 and γ = 0.

Displacement Loading

For the case of cyclic displacement loading, boundary conditions are given in Fig. 8.11. In view of the numerical implementation, displacements are applied in the first loading step. In subsequent loading steps, the displacements, given at the upper boundary, are fixed. For each loading step, $\Delta N = 10^5$ cycles are assumed to take place, resulting in 4.1 $\times$ 10^6 cycles distributed on 41 loading steps. This is illustrated on the left hand side of Fig. 8.11. Snapshots are taken after 10^5, 3.1 $\times$ 10^6 and 4.1 $\times$ 10^6 cycles. At first, increasing interfacial permittivities are assumed ($\alpha^{end} = 3/10$). Stresses in vertical direction σ_{yy} are given in Fig. 8.12 while the electric field component in vertical direction E_y is displayed in Fig. 8.13. As Fig. 8.12 reveals, stresses σ_{yy} decrease due to decreasing stiffnesses induced by cycle-based fatigue. Simultaneously, the absolute values of the vertical electric field component E_y also decrease. This seems to be due to the superposition of electric effects by mechanical effects as described before, caused by dominant mechanical boundary conditions.

For identical boundary conditions (Fig. 8.14) and a decreasing permittivity with $\alpha^{end} = 1/100$, the damage evolution is, again, less pronounced. This is understood by comparing the stresses σ_{yy} of Fig. 8.12 and Fig. 8.15 and the electric field component E_y of Fig. 8.13 and Fig. 8.16. As observed from Fig. 8.15 and Fig. 8.16, this effect is even more significant for the cycle-based fatigue than for the time-based fatigue.

Electric Potential Loading

In view of electric potential loading, boundary conditions are illustrated in Fig. 8.17. Again, each loading step represents $\Delta N = 10^5$ cycles as explained in section 8.4.2. In this context, snapshots are once more taken after 10^5, 3.1 $\times$ 10^6 and 4.1 $\times$ 10^6 cycles. Interfacial permittivities are considered to increase, i.e. $\alpha^{end} = 3/10$. The corresponding plots of the stresses in vertical direction σ_{yy} are given in Fig. 8.18 while the vertical component of the electric field E_y is displayed in Fig. 8.19, revealing increasing absolute values of E_y corresponding to increasing interfacial permittivities. According to the precedent examples, electrical effects seem to match the intensity of mechanical effects concerning the absolute value of the electric field component E_y. Moreover, it emerges that concerning the stresses σ_{yy}, mechanical influences still prevail and stresses are reduced with continued cycling.

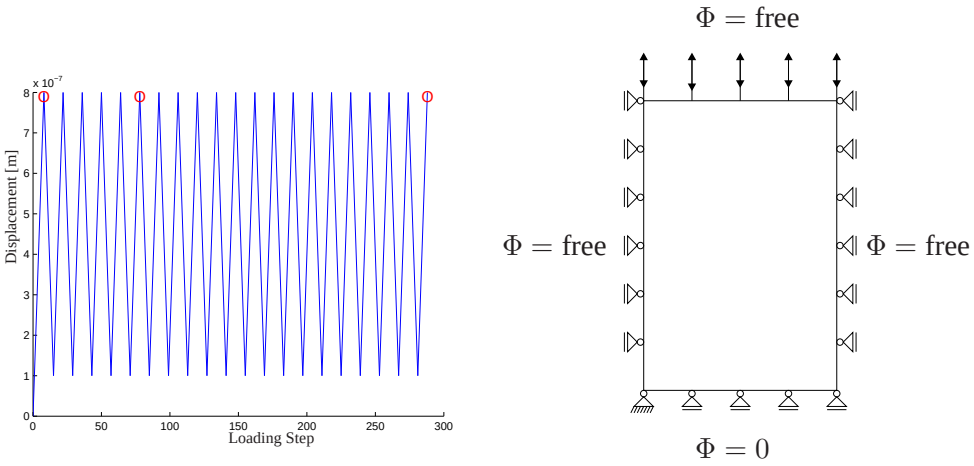

Figure 8.2: Loading history (left) and boundary conditions (right, cyclic displacements): increasing interfacial permittivity

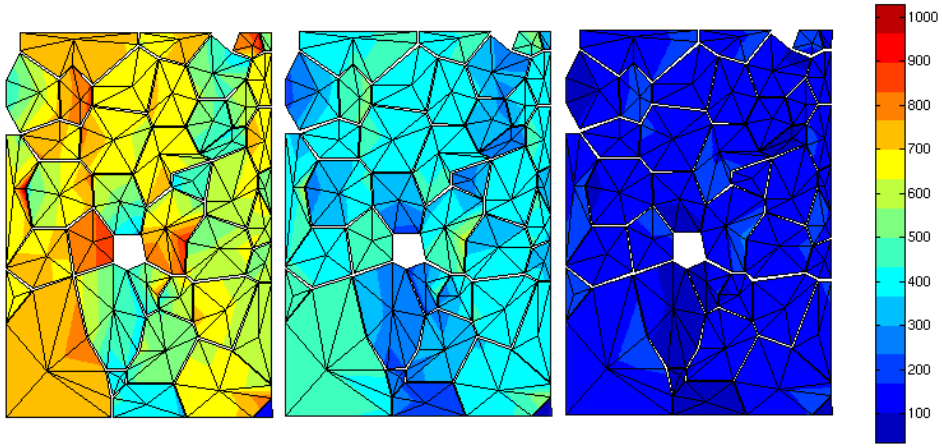

Figure 8.3: σ_{yy} [MPa] after 0 (left), 5 (middle) and 20 (right) cycles

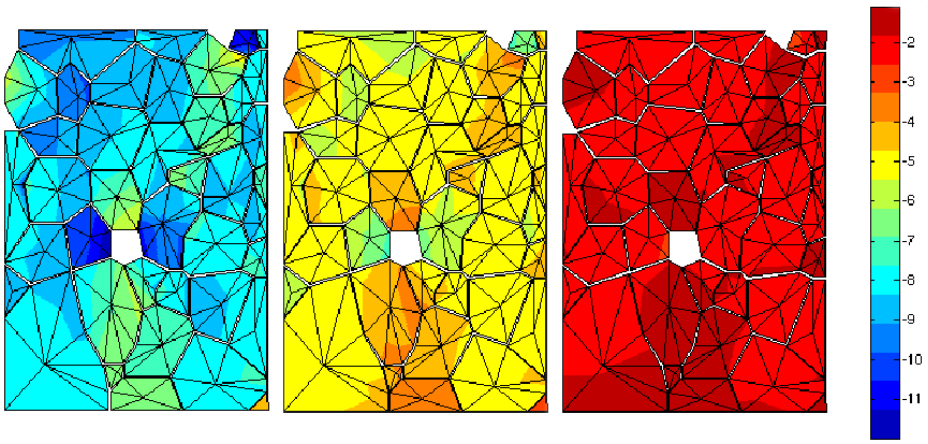

Figure 8.4: E_y [MV/m] after 0 (left), 5 (middle) and 20 (right) cycles

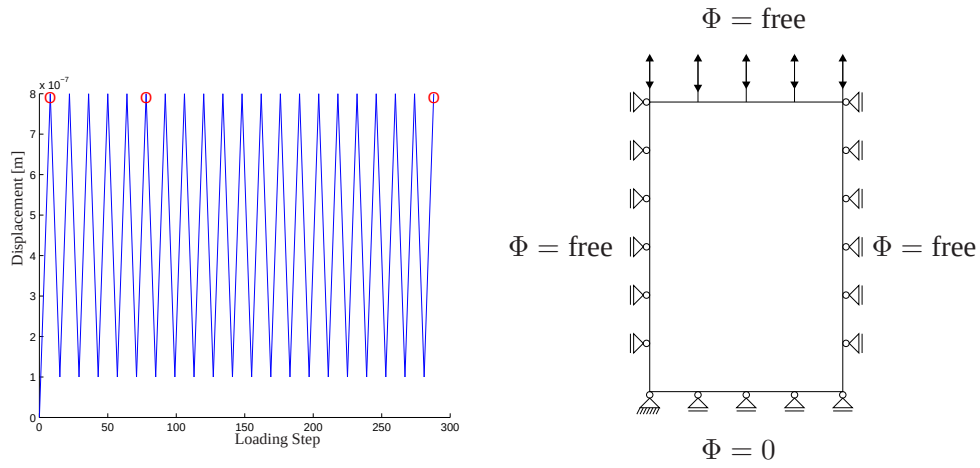

Figure 8.5: Loading history (left) and boundary conditions (right, cyclic displacements): decreasing interfacial permittivity

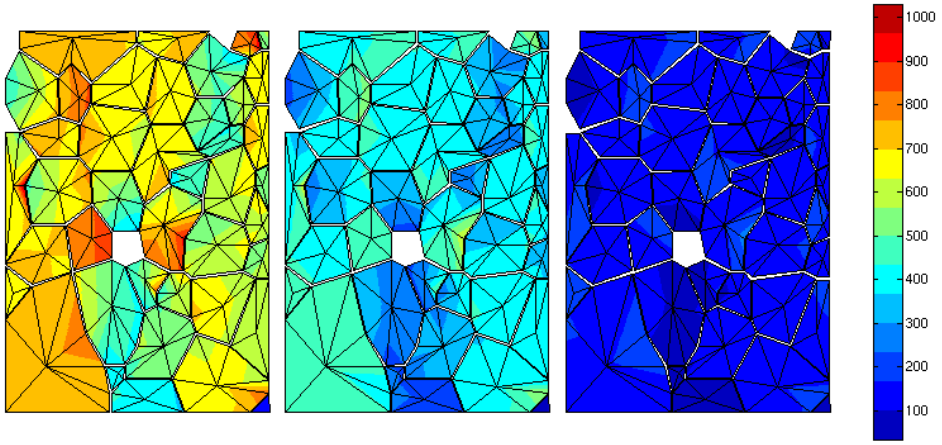

Figure 8.6: σ_{yy} [MPa] after 0 (left), 5 (middle) and 20 (right) cycles

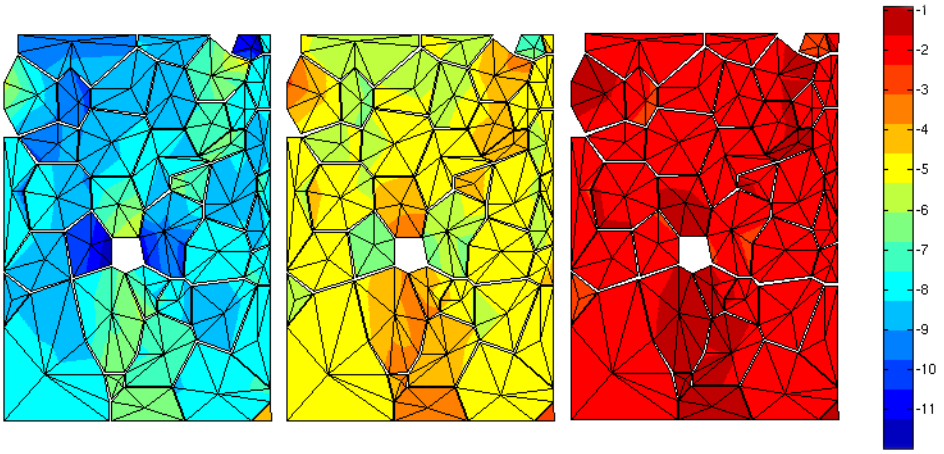

Figure 8.7: E_y [MV/m] after 0 (left), 5 (middle) and 20 (right) cycles

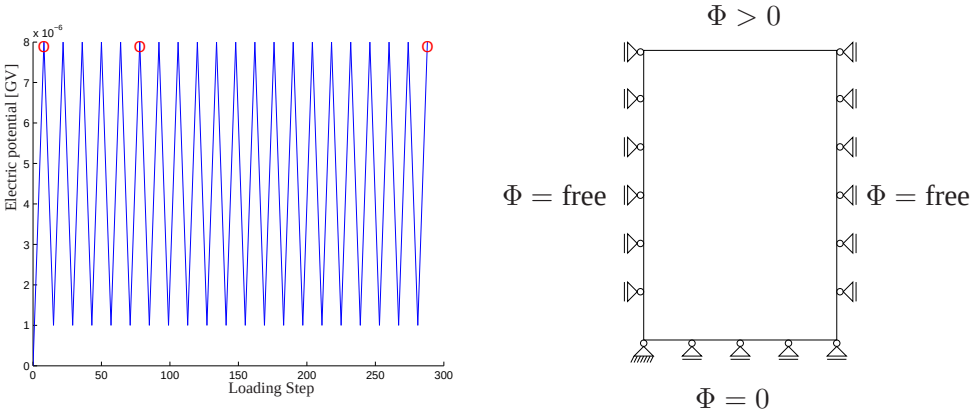

Figure 8.8: Loading history (left) and boundary conditions (right, cyclic electric potential): increasing interfacial permittivity

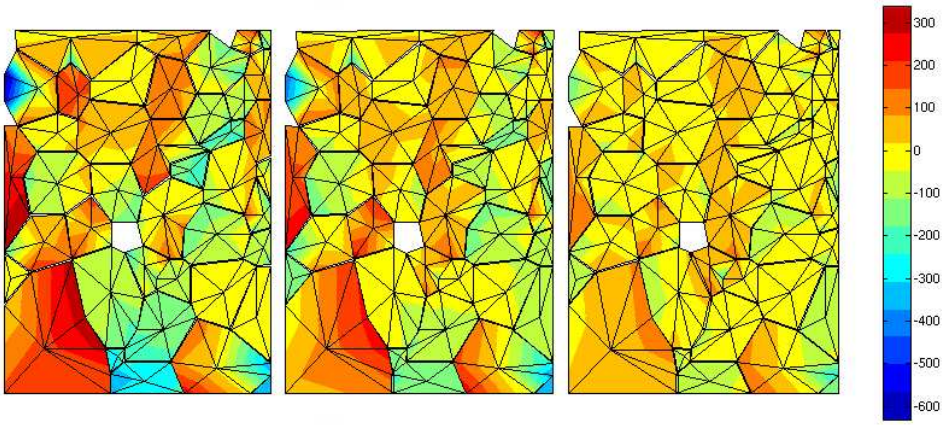

Figure 8.9: σ_{yy} [MPa] after 0 (left), 5 (middle) and 20 (right) cycles

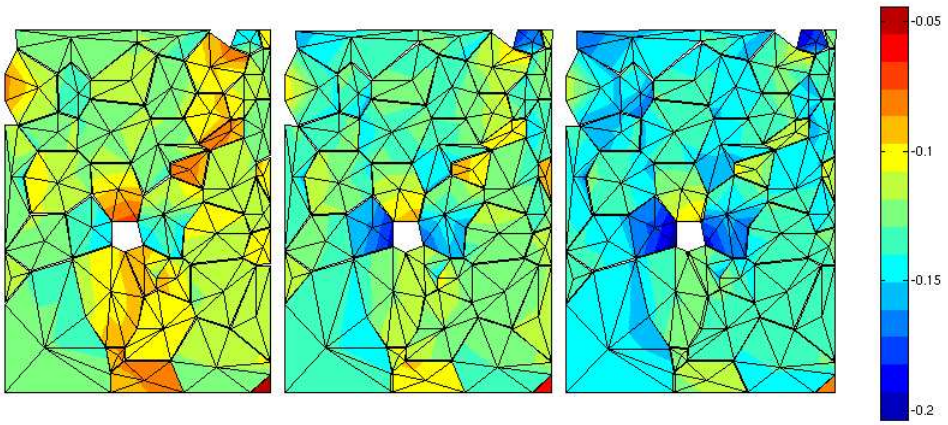

Figure 8.10: E_y [GV/m] after 0 (left), 5 (middle) and 20 (right) cycles

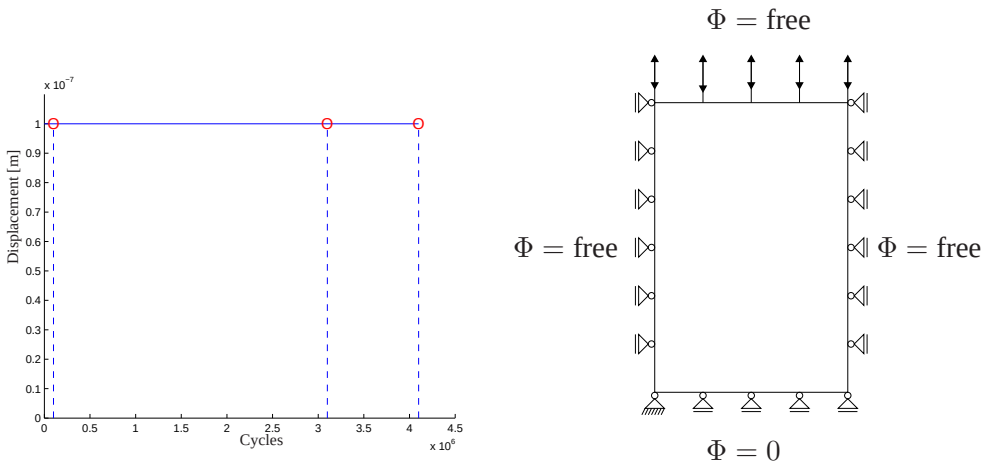

Figure 8.11: Loading history (left) and boundary conditions (right, cyclic displacements): increasing interfacial permittivity

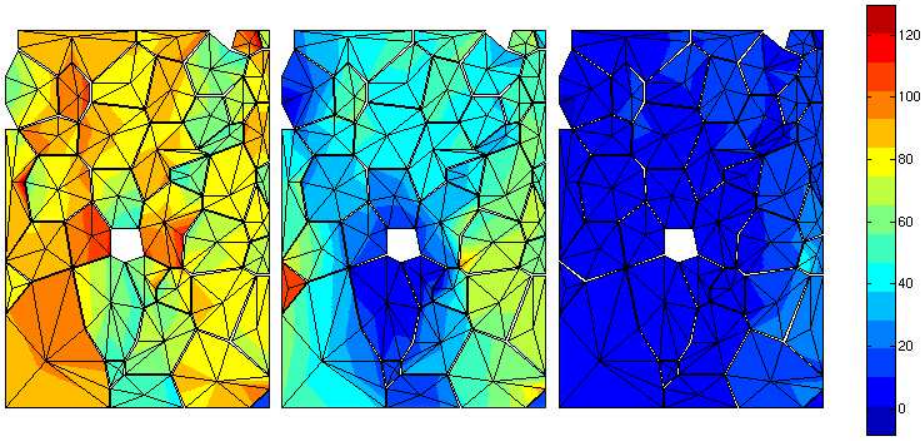

Figure 8.12: σ_{yy} [MPa] after 10^5 (left), 3.1×10^6 (middle) and 4.1×10^6 (right) cycles

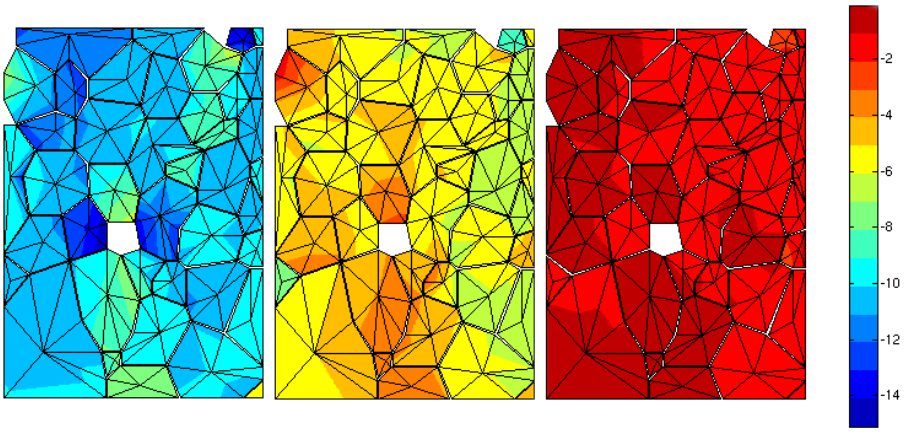

Figure 8.13: E_y [10^2 kV/m] after 10^5 (left), 3.1×10^6 (middle) and 4.1×10^6 (right) cycles

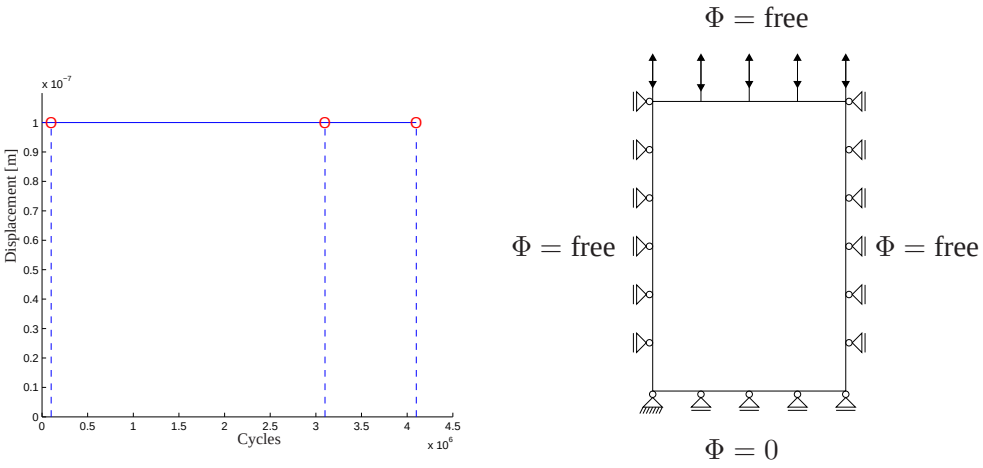

Figure 8.14: Loading history (left) and boundary conditions (right, cyclic displacements): decreasing interfacial permittivity

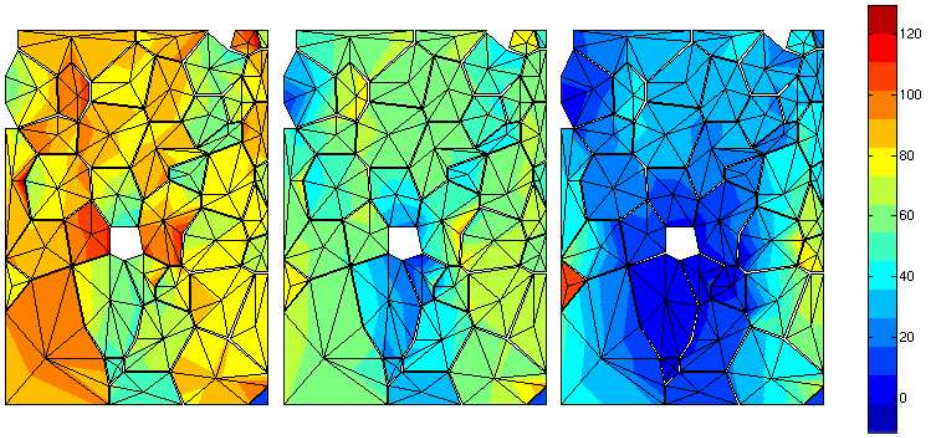

Figure 8.15: σ_{yy} [MPa] after 10^5 (left), 3.1×10^6 (middle) and 4.1×10^6 (right) cycles

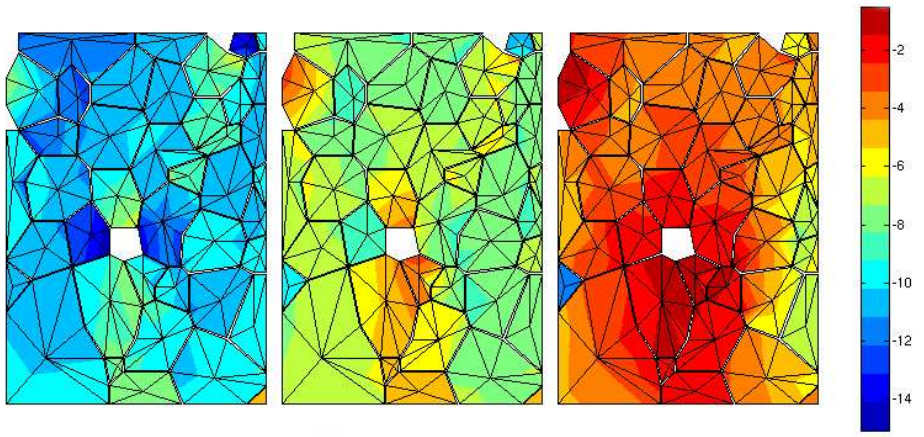

Figure 8.16: E_y [10^2 kV/m] after 10^5 (left), 3.1×10^6 (middle) and 4.1×10^6 (right) cycles

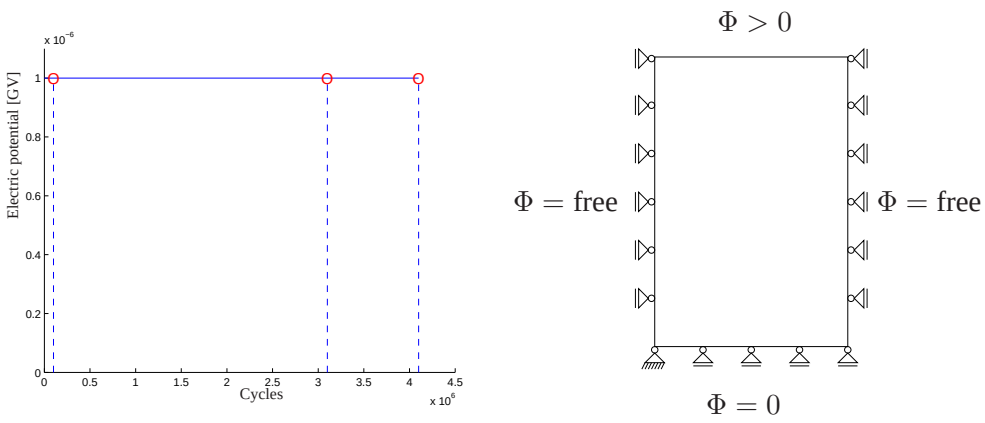

Figure 8.17: Loading history (left) and boundary conditions (right, cyclic electric potential): increasing interfacial permittivity

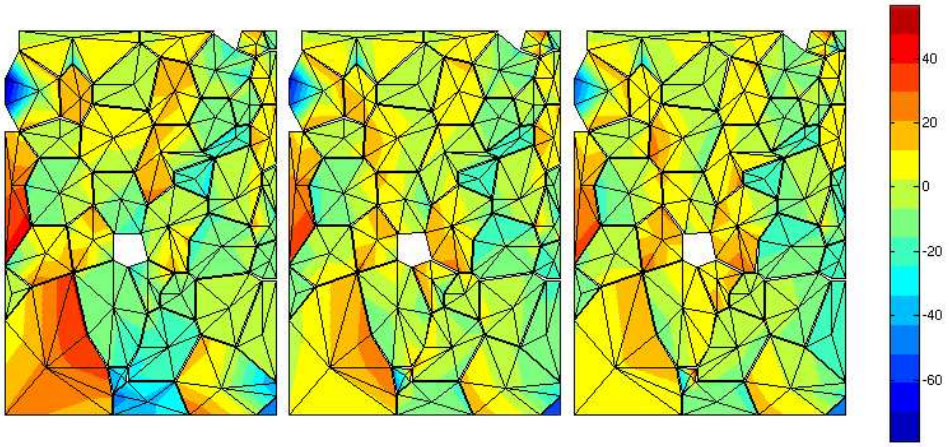

Figure 8.18: σ_{yy} [MPa] after 10^5 (left), 3.1×10^6 (middle) and 4.1×10^6 (right) cycles

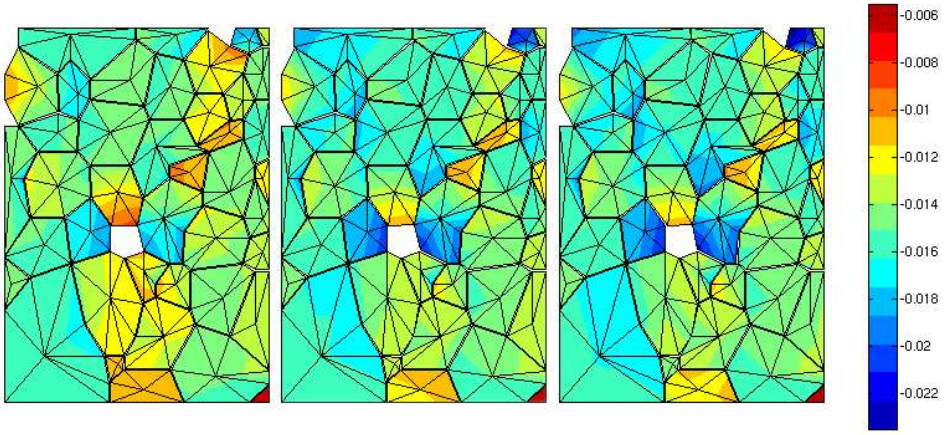

Figure 8.19: E_y [GV/m] after 10^5 (left), 3.1×10^6 (middle) and 4.1×10^6 (right) cycles

8.5 Discussion

Subsequently, some important aspects concerning the above results are discussed. Specifically, the time- and the cycle-based fatigue evolution are compared, the role of the interfacial weighting factors is discussed, the influence of increasing and decreasing interfacial permittivities is compared and finally, some notes on the grain structure and the discretisation influence are given.

8.5.1 Comparison of the Time-Based and the Cycle-Based Fatigue Evolution

First of all, it is noteworthy that for the two fatigue-damage evolutions described in section 3.8 different functional dependencies are incorporated. This must clearly result in different types of the damage evolution. In Fig. 8.20 the damage parameter is plotted over the number of load steps for the time-based fatigue examples of section 8.4.1 for increasing permittivities. The damage parameter d is displayed for the Gauss point marked in Fig. 8.1. The step patterns result from the fact that only for loading, the damage parameter is updated. Moreover, it is recognised that the damage evolution for cyclic electric potential loading is more progressive than for cyclic displacement loading. The dependencies for cycle-based fatigue are shown in Fig. 8.21. Please note that, for the Gauss point considered, the damage cut-off is reached after 30×10^5 cycles for displacement loading. However, different evolution techniques for time-based and cycle-based fatigue damage lead to different evolutions concerning, e.g., stresses or the electric field components. Furthermore, the cycle-based fatigue evolutions seem to provide more freedom to be fitted to experimental data due to a larger number of material parameters. In this context, only academic simulations are accomplished. Comparisons with experiments would give further information on the practicability of the models. Indeed, before considering comparisons with measurements, further significant attributes of ferroelectric material behaviour, for example switching effects, should additionally be included in the computational formulation. The results are further supported by plots of the forces at the upper nodes, where the cyclic boundary conditions are applied. In Fig. 8.22 the sum of all upper nodal forces is plotted over the loading steps for the time-based simulation with increasing permittivities and displacement loading. In accordance to the degressive damage evolution shown in Fig. 8.20, the forces also decrease degressively. In contrast, for the cycle-based simulation with increasing permittivities and displacement loading, the forces progressively decrease, as Fig. 8.23 reveals. This is in line with the progressive damage increase for displacement loading shown in Fig. 8.21.

8.5.2 Neglected Coupling Effects in the Interface and the Role of β_s, β_n and β_Φ

With the numerical examples discussed above, interfacial coupling effects have been neglected in order to model the very reduced coupling abilities occurring along the amorphous grain boundaries. Direct consequences thereof are as follows: If cyclic displacement boundary conditions are applied to an interface and, at the same time, electric potential boundary conditions at the top of the specimen are free, mostly the interfacial displacement jumps are cycled, whereas the electric potential jumps are affected in a smaller amount, not being coupled to the displacement jumps. From this it can be

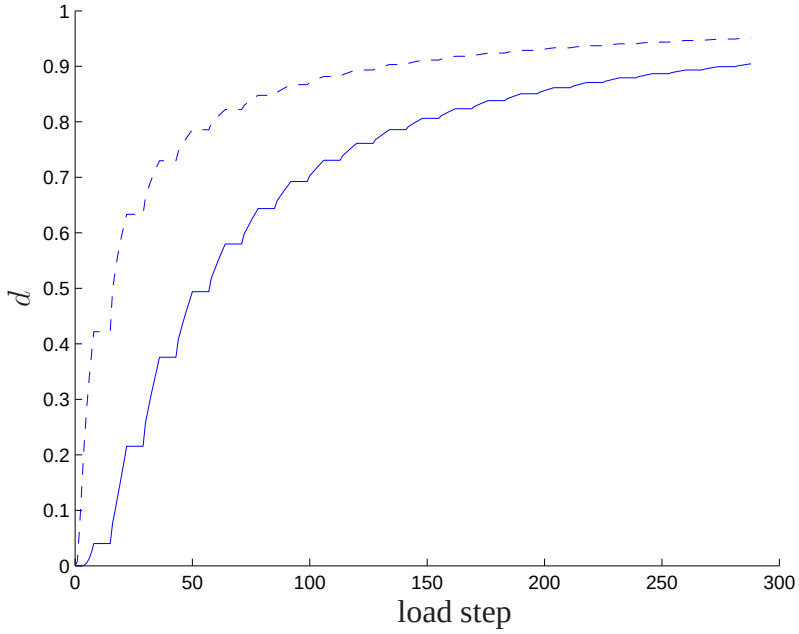

Figure 8.20: Time-based fatigue: damage parameter d over number of load steps. Solid line: displacement loading, dotted line: electric potential loading

concluded that displacement jumps and stiffnesses in the interface will dominate the stresses and the electric field in the bulk, triggered by interfacial effects. The interfacial electric potential jumps are then influenced by the damage variable and the related change of permittivity and, as inherent to the overall solution of the coupled BVP, the bulk itself. Here, however, the electric potential jump influences the bulk only in a small amount. Moreover, mainly displacement jumps would contribute to the damage evolution. Analogous effects occur when the mechanical boundary conditions at the top of the specimen are free and a cyclic electric potential is applied. Then, mainly electric potential jumps would contribute to the damage evolution and bulk actions are dominated by interfacial electric potential jumps and permittivities. Nevertheless, no matter which degrees of freedom are cycled, the associated damage variable will always be applied to both the interfacial stiffnesses and permittivities. What clearly influences the weighting of displacement or electric potential jumps concerning damage evolution are the parameters β_s, β_n and β_Φ, see also equation (3.255). In the current work, β_Φ has been chosen much smaller than β_s, β_n which is considered to reflect some physics of piezoceramic grain boundaries. Consequently, the role of the electric potential jump and of varying permittivities is reduced as compared to the influence of the displacement jump and reduced stiffnesses.

These correlations are generally reflected by the simulation results. For cyclic displacements combined with the time-based or the cycle-based fatigue model, stresses σ_{yy} are decreasing due to decreasing stiffnesses. Simultaneously, the absolute value of the electric field component E_y is also decreasing due to the dominant role of interfacial displacement jumps – the electric potential at the upper boundary is free. For cyclic electric potentials and both fatigue models, the absolute values of

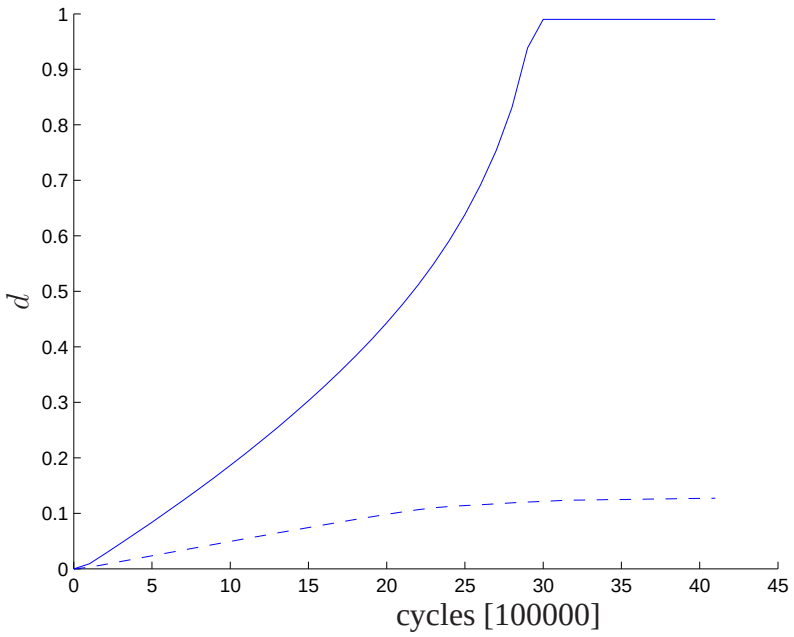

Figure 8.21: Cycle-based fatigue: damage parameter d over number of cycles. Solid line: displacement loading, dotted line: electric potential loading

the electric field components E_y rise with continued cycling, which can be correlated to the dominant role of the interfacial electric potential jumps and the related increase of permittivities which has been assumed in those examples. In view of the stresses σ_{yy}, mechanical influences still prevail, and a decrease is observed, due to the small value of β_Φ and the electric-field-induced increase of the bulk strains, promoting increasing interfacial displacement jumps.

8.5.3 Influence of Increasing and Decreasing Interfacial Permittivities

For both the time-based and the cycle-based fatigue computations, increasing and decreasing interfacial permittivities have been investigated for cyclic displacement boundary conditions. Concerning the overall constitutive behaviour, the cyclic displacement boundary conditions induce that the overall electric field is triggered by the strains, both decreasing with increasing damage with respect to the cycling history. The damage is directly influenced by the interfacial jump quantities. Due to the small weighting factor β_Φ, the direct influence of the potential jump and the permittivities is of minor significance; nevertheless, they still indirectly influence the overall damage, though being strongly superposed by mechanical effects.

For increasing permittivities, the electric potential jump over the interface would tend to decrease. Hence, a related fraction of the electric field in the bulk would increase to compensate this and the related fraction of bulk strains would then be raised by some amount due to piezoelectric coupling. As a consequence, this raises the displacement jumps in the interface, which supports the damage

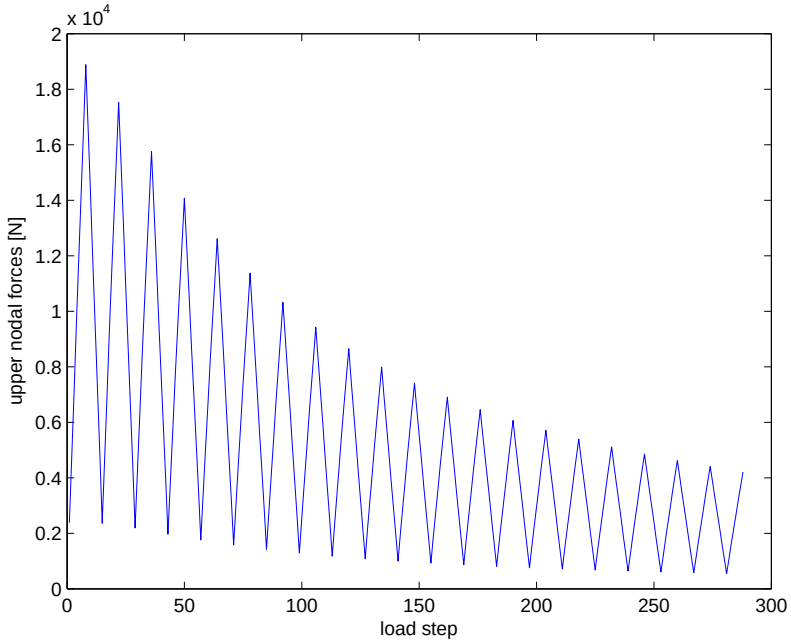

Figure 8.22: Time-based fatigue: upper nodal forces over load steps

evolution. In contrast, for decreasing permittivities, the electric potential jump over the interface would tend to increase, causing a certain fraction of the bulk strains to decrease. Such behaviour would decrease the displacement jumps in the interface, restraining the damage evolution to some amount. Consequently, such effects are indicated in the results. Due to the circumstances discussed in the above, for decreasing permittivities, stresses σ_{yy} and the electric field component E_y decrease less than for increasing permittivities, which stems from the restrained damage evolution.

8.5.4 Influence of Grain Structure and Discretisation

For the micrograph considered, compare Fig. 8.1, a void is present in the middle of the discretisation. For cyclic displacements and both fatigue models, but especially for the cycle-based fatigue evolution, fatigue-motivated damage starts in an area around the mentioned void, compare Figs. 8.12, 8.13, 8.15 and 8.16. Concerning the discretisation of the continuum, linear triangular elements have been applied, inhering rather poor approximation abilities compared to the application of higher order ansatz functions or finer meshes. Nevertheless, the discretisation used turns out to reflect all important properties of the academic example investigated.

8.5.5 Additional Remarks

In this chapter, a SEM-obtained mesostructure (Nuffer et al. [129]) of the piezoelectric material PIC 151 has been discretised by applying linear triangular finite elements for the grains and linear in-

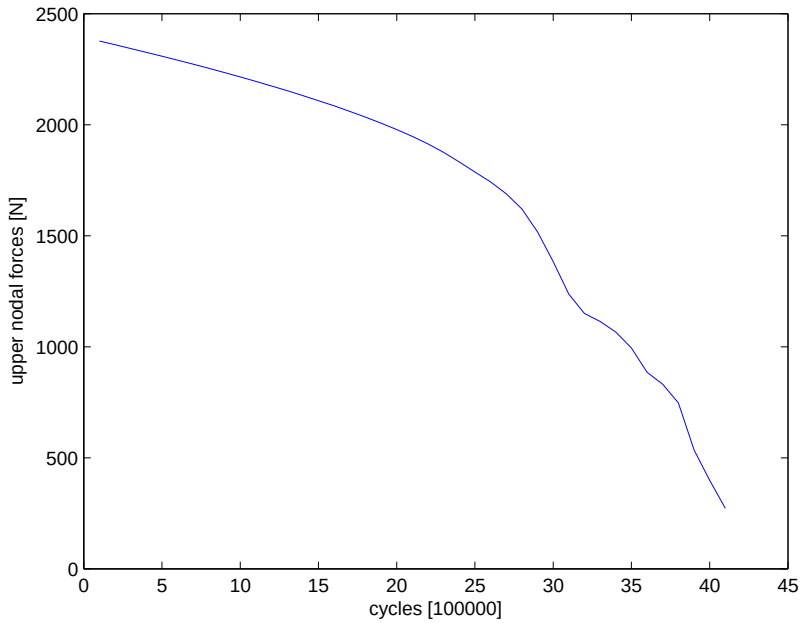

Figure 8.23: Cycle-based fatigue: upper nodal forces over cycles

terface elements for the grain boundaries. Different fatigue-loading-motivated boundary conditions have been applied to the discretisation. In this context, a first attempt has been made to model such a structure, emphasising the grain boundary behaviour (Utzinger et al. [183, 182]). For the grains, or rather the bulk material, a linearly coupled material law has been implemented. Concerning the grain boundaries, discretised by interface or, respectively, cohesive-type elements, two different material models have been considered: the first appropriate by capturing low-cycle-fatigue and the second material model being able to reflect high-cycle-fatigue behaviour. For the bulk, PIC 151-like material parameters have been incorporated. In view of the interface, an effective parameter δ has been incorporated into the fatigue-motivated damage evolution, being academic in nature due to missing reliable information on the exact physical processes in grain boundaries under fatigue loading. Electrical and mechanical effects have been decoupled concerning the linear response. The first interfacial material model, reflecting low-cycle-fatigue behaviour, is of an exponential format. It has been entitled “time-based fatigue formulation” and explicitly tracks the loading history of single cycles. In contrast, a second interfacial material model, also being of an exponential though of different format, captures high-cycle-fatigue behaviour by directly incorporating a certain number of cycles. It has been entitled as “cycle-based fatigue formulation”. For an accurate description of those interfacial fatigue laws, see section 3.8. The related damage parameter d is constrained by the driving force in a thermodynamical consistent framework. For the chosen academic examples it turned out that the proposed assumptions of a fatigue-related decrease of interfacial mechanical tractions and varying permittivities are reflected in the results. So far, the literature does not clearly reveal experimental results concerning the permittivity behaviour under fatigue-related loading boundary conditions. Anyhow, literature reveals that

grain boundary permittivity is generally lower than the permittivity of the grains.

In view of the fact that only permittivities and stiffnesses are accounted for in this work, it is clear that realistic grain boundaries must inhere further and more complex phenomena under fatigue loading than those incorporated here. In this context, it is necessary to prospect for new experimental results and to improve knowledge concerning the fatigue-related grain boundary behaviour. As this is just a first step towards an integral modelling of a fatigued piezoelectric mesostructure, nonlinear effects as phase transformations have to be included in the bulk constitutive response in the future to account for ferroelectric effects. To model polarisation switching of domain structures, e.g., internal variable methods can be applied (e.g., Lynch and McMeeking [101], Lynch [100], Arockiarajan et al. [4], Arockiarajan and Menzel [3] as well as Menzel et al. [110]). Finally, when the mesomechanical material models are accurate enough, an incorporation into multiscale computations could be accomplished.

9 Conclusions

The goals of the present work have been structured in three parts.

According to the introduction, the first part was concerned with the modelling, the numerics and the simulation of welded lightweight structures of metal/fibre-reinforced polymer composites. In chapter 2, material laws for the substrates have been discussed including isotropic, transversal isotropic and orthotropic elasticity as well as linear elastoplasticity with linear isotropic hardening. Concerning the welding interface, elastoplasticity with Lemaitre-type damage as well as a high-cycle-fatigue related traction-separation-law have been introduced in chapter 3 in order to be incorporated into current simulations. Furthermore, a low-cycle-fatigue related traction-separation-law as well as viscoelasticity with Lemaitre-type damage and viscoplasticity with Lemaitre-type damage have been discussed in view of future applications. For all the mentioned cohesive laws, prototype examples have been accomplished, showing the functionality of the models. Moreover, a penalty method has been introduced in order to avoid an unphysical self-penetration of the interface. Adequate finite element procedures have been discussed in chapter 6. For both the interface and the bulk, element stiffness matrices and residua have been deduced. After an excursion with respect to manufacturing and measuring methods, chapter 7 deals with the comparison of experimental data and numerical simulations which are accomplished by means of the above models in the context of a nonlinear FEM-programme. Concerning thermal impact welded tensile specimens, a very good agreement of local and integral data sets was demonstrated. For ultrasonic metal welded tensile specimens a comparison based on integral data has successfully been accomplished. Furthermore, local and integral data was compared with simulations for a preliminary tensile fatigue test with a ultrasonic metal welded tensile specimen. The simulations partially corresponded to the experimental data, but further statistically confirmed experiments have to be conducted.

The goal of the second part has been the academic simulation of piezoelectric mesostructures under fatigue-motivated boundary conditions. For the grain bulk, a linear ferroelectric material law has been introduced in chapter 2. In chapter 3, low- and high-cycle-fatigue motivated ferroelectric cohesive laws have been discussed. These, together with the discretisation of the coupled weak forms and the deduction of element stiffness matrices and residua in chapter 6, have been incorporated in the simulations presented in chapter 8. A piezoelectric mesostructure obtained by scanning electron microscopy has there been subjected to mechanical and electrical low- and high-cycle fatigue boundary conditions. The results have been discussed, revealing a sound impression concerning the computed boundary value problems. Additionally, a literature survey concerning the issues of piezoelectric fatigue, grain boundaries and piezoelectric modelling has been conducted in the beginning of chapter 8.

The goals of the third part concerned investigations on surface-wave type bifurcation modes in a two-dimensional non-coherent (cohesive) interface, connecting a semi-infinite three-dimensional linear bulk with a rigid substrate. For the uncoupled problem this has been discussed in chapter 4.

Therein, the bulk material has been chosen to be linear isotropic elastic, while for the interface, inelastic behaviour in an incrementally linear context has been assumed. For the case of positive interfacial material constants no bifurcations occurred, while for negative constants, a maximum of three bifurcation possibilities is present. For the coupled problem as discussed in chapter 5, a linear ferroelectric bulk material has been assumed. For simplification, and in addition to the transversal isotropic elastic part of the bulk material behaviour, the latter has been complemented by isotropic elasticity. The interface constitutive behaviour has been chosen to be incrementally linear ferroelectric. In contrast to chapter 4, for all material parameters, numerical values have been inserted. Generally, for the parameters chosen, a maximal number of four surface wave-type bifurcation modes is possible. Though, if the interfacial stiffness parameters are chosen positive, no such bifurcations occur. Consequently, for both the uncoupled and the coupled problem, the number of surface-wave type bifurcation modes is finite, with respect to the incorporated simplifications and chosen parameters. Accordingly, related numerical solutions of the boundary value problem are not considered to be mesh-dependent.

The execution of the tasks related to this work is additionally documented in several refereed journal publications (Utzinger et al. [180], Utzinger et al. [181], and Utzinger et al. [183]).

Outlook

During the thorough elaborations in view of the goals of this work, new questions and inspirations for future works emerged. These are subsequently listed.

- For a more accurate simulation of the metallic substrates, geometrically nonlinear formulations are supposable. Especially multiplicative elastoplasticity is of interest (e.g. Schröder et al. [156], Menzel et al. [111] and Steinmann et al. [171]).
- In order to improve simulation parameters, advanced elaborations on the identification of material parameters are contemplated (Mahnken and Stein [102, 103]).
- For further verification of the applied cohesive laws, also mode-I and mode-III tests as well as mixed-mode tests are imperative.
- The constitutive response of some of the proposed interfacial models is decoupled with respect to projections onto $\boldsymbol{s}$, $\boldsymbol{t}$ and $\boldsymbol{n}$. Otherwise, e.g. in the case of elastoplasticity with Lemaitre-type damage, coupled formulations would entail local iterations in order to solve for the Lagrange multipliers from the set of nonlinear equations. From the algorithmic point of view, then it would not be significantly more expensive to additionally account for nonlinear hardening effects.
- The viscous models introduced in chapter 3 could not yet be verified by comparisons with experiments. Comparative creep and relaxation tests would therefore be of interest.
- In view of the preliminary fatigue tests and the related simulations, statistically proven experimental data is required. Then, further simulations have to be conducted.
- In the scope of the DFG Research Unit 524, the manufacturing of component parts including the mentioned welding methods is planned. In this respect, geometrically nonlinear cohesive

laws have to be considered to simulate the large deformations of semi-finished parts (see e.g. Steinmann and Betsch [169], Larsson and Jansson [88]).

- Taking a complete interfacial decohesion into account, fragmentation methods are supposed, see e.g. Pandolfi and Ortiz [138].
- Another interesting point concerning the DFG Research Unit 524 is the thermal coupling of both the bulk and the interface (Steinmann and Häsner [170], Krol [85], Miehe [117], Ibrahimbegovic et al. [70]). With this in hand, heat conduction processes and residual stresses could be simulated.
- The welding zone could also be regarded on the micro scale. Then, microscopic material behaviour could be projected onto the meso scale by means of multiscale methods.

- In order to model polarisation switching of domain structures, for example, internal variable methods can be applied (e.g., Lynch and McMeeking [101], Lynch [100], Arockiarajan et al. [4], Arockiarajan and Menzel [3], Menzel et al. [110]).
- In the context of ferroelectric fatigue, it is a matter of ongoing research to implement cohesive laws possibly substantially different to the ones presented in this work. In this regard, a capacitor-like behaviour of the interface is investigated. Additionally, fracture energy related models are possible.
- When the mesomechanical material models which are applied to the mesostructure are accurate enough, an incorporation into multiscale computations can be considered.
- The evolution of the interfacial permittivity could also be directly motivated from the dissipation inequality.
- The discretisation methods concerning polycrystalline mesostructures could also be applied to other materials, e.g. metals, maybe also in the context of multiscale applications.

- Concerning future research on the issue of bifurcation, the connection of two deformable bodies by a non-coherent interface is of interest.
- In view of the uncoupled problem, inelastic and also further anisotropic bulk responses could be investigated as well.
- Concerning the coupled problem, different wave vectors with respect to the incremental displacement and electrical potential ansatz are supposable.
- Moreover, the comparison of the bifurcation-related theoretical elaborations as given in chapters 4 and 5 with numerical, for instance finite element based simulations is both promising and relevant in view of engineering applications.

A Solving 2nd Order Differential Equations

The general and complete solution of some p-dimensional ordinary differential equation system of first order of the form $\boldsymbol{y}'(\eta) = \boldsymbol{M} \cdot \boldsymbol{y}(\eta)$ is defined as

$$\boldsymbol{y}(\eta) = \boldsymbol{Y}(\eta) \cdot \boldsymbol{c} \quad \text{with} \quad \boldsymbol{Y}(\eta) = [\boldsymbol{y}_1(\eta), \boldsymbol{y}_2(\eta), ...\boldsymbol{y}_p(\eta)] \quad \text{and} \quad \boldsymbol{c} \in \mathcal{C}^p \tag{A.1}$$

where fundamental solutions $\boldsymbol{y}_i(\eta)$, constituting the fundamental matrix $\boldsymbol{Y}(\eta)$, are constructed by means of a base system of eigenvectors $\boldsymbol{v}$, and, if needed, generalised eigenvectors $\boldsymbol{v}^*$. Generalised eigenvectors $\boldsymbol{v}^*$ of level l related to an eigenvalue υ of $\boldsymbol{M}$ can be computed by solving

$$[\boldsymbol{M} - \upsilon \boldsymbol{I}_n]^l \cdot \boldsymbol{v}^* = \boldsymbol{0} \tag{A.2}$$

with $\boldsymbol{I}_n$ being a $n \times n$ second-order identity-tensor. Fundamental solutions based on eigenvectors $\boldsymbol{v}$ related to the eigenvalue υ of $\boldsymbol{M}$ are constructed as

$$\boldsymbol{y}(\eta) = \exp(\upsilon\eta)\boldsymbol{v} \tag{A.3}$$

while fundamental solutions based on generalised eigenvectors $\boldsymbol{v}^*$ of level l related to the eigenvalue υ of $\boldsymbol{M}$ are constructed as

$$\boldsymbol{y}(\eta) = \exp(\upsilon\eta)\left[\boldsymbol{v}^* + \eta[\boldsymbol{M} - \upsilon\boldsymbol{I}_n] \cdot \boldsymbol{v}^* \; + \; ... \; + \; \frac{\eta^{l-1}}{[l-1]!}[\boldsymbol{M} - \upsilon\boldsymbol{I}_n]^{l-1} \cdot \boldsymbol{v}^*\right] \tag{A.4}$$

This strategy can be found in, e.g., the book of Meyberg and Vachenauer [116] and is required for the efforts undertaken.

B Examples for the Bifurcation-Related Interfacial Constitutive Operator

The incremental interfacial constitutive operator $\boldsymbol{C}^{if}$ can be motivated by the loading branches of elastic and inelastic traction-separation-laws. It relates the incremental quantities or rates of tractions and displacement jumps by

$$\delta\boldsymbol{\tau} = \boldsymbol{C}^{if} \cdot [\![\delta\boldsymbol{u}]\!] \tag{B.1}$$

For elastoplasticity with damage, the interfacial tangent modulus has been computed in section 3.4, reading as

$$\boldsymbol{C}^{if,epd} = \sum_i \underbrace{\left[[1-d_i]c_i\left[1-\frac{1}{1+H_i^p/c_i}\right] - d_i'\left[\bar{\tau}_i^2\left[1-\frac{1}{1+H_i^p/c_i}\right] - \frac{\bar{R}_i\,|\bar{\tau}_i|}{1+H_i^p/c_i}\right]\right]}_{\rho_i^{epd}} \boldsymbol{i}\otimes\boldsymbol{i} \tag{B.2}$$

see section 3.4 for further explanation. If damage evolution is not active ($d_i = 0$, $\dot{d}_i = 0$), this reduces to

$$\boldsymbol{C}^{if,ep} = \sum_i \underbrace{c_i\left[1-\frac{1}{1+H_i^p/c_i}\right]}_{\rho_i^{ep}} \boldsymbol{i}\otimes\boldsymbol{i} \tag{B.3}$$

Otherwise, if damage is active and plasticity is switched off ($H_i^p \to \infty$, $\alpha_i^p = 0$), the interfacial tangent modulus is given by

$$\boldsymbol{C}^{if,ed} = \sum_i \underbrace{\left[[1-d_i]c_i - d_i'\,\bar{\tau}_i^2\right]}_{\rho_i^{ed}} \boldsymbol{i}\otimes\boldsymbol{i} \tag{B.4}$$

Accordingly, if all inelastic effects are excluded, the elastic tangent is rendered as

$$\boldsymbol{C}^{if,el} = \sum_i c_i\,\boldsymbol{i}\otimes\boldsymbol{i} \tag{B.5}$$

Please note that for active damage, the parameters ρ_s^{ed}, ρ_t^{ed}, and ρ_n^{ed} depend on the deformation history. Recapitulating, the interfacial material parameters ρ_i depend on the specific interfacial material law:

$$\rho_i = \begin{cases} c_i & \text{elasticity} \\ \rho_i^{ep} & \text{elastoplasticity} \\ \rho_i^{ed} & \text{elasticity with damage} \\ \rho_i^{epd} & \text{elastoplasticity with damage} \end{cases} \tag{B.6}$$

C Linear Homogeneous Equation System Matrix B, Uncoupled Problem

Here, the entries of $\mathbf{B}$ are given as

$$\mathrm{B}_{11} = -2\mu k - [\rho_s \cos^2\theta + \rho_t \sin^2\theta] \tag{C.1}$$

$$\mathrm{B}_{12} = \frac{2\mu^2 k}{\mu+\lambda} + \frac{2\mu}{\mu+\lambda}[\rho_s \cos^2\theta + \rho_t \sin^2\theta] \tag{C.2}$$

$$\mathrm{B}_{13} = -[\rho_s - \rho_t]\cos\theta \sin\theta \tag{C.3}$$

$$\mathrm{B}_{21} = -[\rho_s - \rho_t]\cos\theta \sin\theta \tag{C.4}$$

$$\mathrm{B}_{22} = \frac{2\mu}{\mu+\lambda}[\rho_s - \rho_t]\cos\theta \sin\theta \tag{C.5}$$

$$\mathrm{B}_{23} = -\mu k - [\rho_t \cos^2\theta + \rho_s \sin^2\theta] \tag{C.6}$$

$$\mathrm{B}_{31} = -[2\mu k + \rho_n] \tag{C.7}$$

$$\mathrm{B}_{32} = -\frac{1}{\mu+\lambda}[\lambda\rho_n + \mu[2k\lambda + \rho_n]] \tag{C.8}$$

$$\mathrm{B}_{33} = 0 \tag{C.9}$$

D Eigenvectors of the Ferroelectric System Matrix A

For some mechanically isotropic material, the eigenvectors are given as

$$\boldsymbol{v}_1 = \begin{bmatrix} 0 \\ -1/k \\ 0 \\ 0 \\ 0 \\ 1 \\ 0 \\ 0 \end{bmatrix}, \quad \boldsymbol{v}_2 = \begin{bmatrix} 0 \\ 1/k \\ 0 \\ 0 \\ 0 \\ 1 \\ 0 \\ 0 \end{bmatrix}, \quad \boldsymbol{v}_3 = \begin{bmatrix} -i\Omega_1/k \\ 0 \\ \Omega_2/k \\ -\Omega_3/k \\ i\Omega_4 \\ 0 \\ -\Omega_5 \\ 1 \end{bmatrix}, \quad \boldsymbol{v}_4 = \begin{bmatrix} -i\Omega_1/k \\ 0 \\ -\Omega_2/k \\ \Omega_3/k \\ -i\Omega_4 \\ 0 \\ -\Omega_5 \\ 1 \end{bmatrix},$$

$$\boldsymbol{v}_5 = \begin{bmatrix} i\Omega_6/k \\ 0 \\ -\Omega_7/k \\ -\Omega_8/k \\ -i\Omega_9 \\ 0 \\ \Omega_{10} \\ 1 \end{bmatrix}, \quad \boldsymbol{v}_6 = \begin{bmatrix} i\Omega_6/k \\ 0 \\ \Omega_7/k \\ \Omega_8/k \\ i\Omega_9 \\ 0 \\ \Omega_{10} \\ 1 \end{bmatrix}, \quad \boldsymbol{v}_7 = \begin{bmatrix} i\Omega_{11}/k \\ 0 \\ -\Omega_{12}/k \\ -\Omega_{13}/k \\ -i\Omega_{14} \\ 0 \\ \Omega_{15} \\ 1 \end{bmatrix}, \quad \boldsymbol{v}_8 = \begin{bmatrix} i\Omega_{11}/k \\ 0 \\ \Omega_{12}/k \\ \Omega_{13}/k \\ i\Omega_{14} \\ 0 \\ \Omega_{15} \\ 1 \end{bmatrix} \tag{D.1}$$

where

$$\begin{aligned} &\Omega_1 = 0.8300, \quad \Omega_2 = 1.1568, \quad \Omega_3 = 1.0967, \quad \Omega_4 = 0.7568, \quad \Omega_5 = 1.0547, \\ &\Omega_6 = 7.8819, \quad \Omega_7 = 7.9757, \quad \Omega_8 = 1.0245, \quad \Omega_9 = 7.6934, \quad \Omega_{10} = 7.7850, \\ &\Omega_{11} = 4.1545, \quad \Omega_{12} = 3.5782, \quad \Omega_{13} = 0.9367, \quad \Omega_{14} = 4.4353, \quad \Omega_{15} = 3.8200 \end{aligned} \tag{D.2}$$

Otherwise, if the bulk inheres fully transversal isotropy, eigenvectors read as

$$\boldsymbol{v}_1 = \begin{bmatrix} 0 \\ \Omega_1/k \\ 0 \\ 0 \\ 0 \\ 1 \\ 0 \\ 0 \end{bmatrix}, \quad \boldsymbol{v}_2 = \begin{bmatrix} 0 \\ -\Omega_1/k \\ 0 \\ 0 \\ 0 \\ 1 \\ 0 \\ 0 \end{bmatrix}, \quad \boldsymbol{v}_3 = \begin{bmatrix} i\Omega_2/k \\ 0 \\ \Omega_3/k \\ \Omega_4/k \\ i\Omega_5 \\ 0 \\ \Omega_6 \\ 1 \end{bmatrix}, \quad \boldsymbol{v}_4 = \begin{bmatrix} i\Omega_2/k \\ 0 \\ -\Omega_3/k \\ -\Omega_4/k \\ -i\Omega_5 \\ 0 \\ \Omega_6 \\ 1 \end{bmatrix},$$

$$\boldsymbol{v}_5 = \begin{bmatrix} \Omega_7/k \\ 0 \\ \Omega_8/k \\ \Omega_9/k \\ \Omega_{10} \\ 0 \\ \Omega_{11} \\ 1 \end{bmatrix}, \quad \boldsymbol{v}_6 = \begin{bmatrix} \Omega_7/k \\ 0 \\ -\Omega_8/k \\ -\Omega_9/k \\ -\Omega_{10} \\ 0 \\ \Omega_{11} \\ 1 \end{bmatrix}, \quad \boldsymbol{v}_7 = \begin{bmatrix} \Omega_{12}/k \\ 0 \\ \Omega_{13}/k \\ \Omega_{14}/k \\ \Omega_{15} \\ 0 \\ \Omega_{16} \\ 1 \end{bmatrix}, \quad \boldsymbol{v}_8 = \begin{bmatrix} \Omega_{12}/k \\ 0 \\ -\Omega_{13}/k \\ -\Omega_{14}/k \\ -\Omega_{15} \\ 0 \\ \Omega_{16} \\ 1 \end{bmatrix} \tag{D.3}$$

with

$$\begin{aligned} &\Omega_1 = -0.9394, \quad \Omega_2 = 3.0904, \quad \Omega_3 = -2.2530, \quad \Omega_4 = -0.8261, \quad \Omega_5 = -3.7409, \\ &\Omega_6 = 2.7273, \quad \Omega_7 = -1.2209 + i0.2551, \quad \Omega_8 = -0.0709 - i1.4872, \\ &\Omega_9 = -1.1078 - i0.0152, \quad \Omega_{10} = 1.0986 - i0.2454, \quad \Omega_{11} = 0.0824 + i1.3413, \\ &\Omega_{12} = 1.2209 + i0.2551, \quad \Omega_{13} = -0.0709 + i1.4872, \quad \Omega_{14} = -1.1078 + i0.0152, \\ &\Omega_{15} = -1.0986 - i0.2454, \quad \Omega_{16} = 0.0824 - i1.3413 \end{aligned} \tag{D.4}$$

E Linear Homogeneous Equation System Matrix B, Coupled Problem

For mechanical isotropy, the entries of $\mathbf{B}$ are given as

$$\mathrm{B}_{11} = [\mu_s - \mu_t]\,\cos\theta\,\sin\theta/k \tag{E.1}$$

$$\mathrm{B}_{12} = -i\,[\mu\nu_3\Omega_1 - \mu k\Omega_2 + e_{15}k\Omega_3 - \Omega_1[\mu_s\cos^2\theta + \mu_t\sin^2\theta]]/k \tag{E.2}$$

$$\mathrm{B}_{13} = -i\,[-\mu\nu_5\Omega_6 + \mu k\Omega_7 + e_{15}k\Omega_8 + \Omega_6[\mu_s\cos^2\theta + \mu_t\sin^2\theta]]/k \tag{E.3}$$

$$\mathrm{B}_{14} = -i\,[-\mu\nu_7\Omega_{11} + \mu k\Omega_{12} + e_{15}k\Omega_{13} + \Omega_{11}[\mu_s\cos^2\theta + \mu_t\sin^2\theta]]/k \tag{E.4}$$

$$\mathrm{B}_{21} = [\mu_s\sin^2\theta + \mu_t\cos^2\theta - \mu\nu_1]/k \tag{E.5}$$

$$\mathrm{B}_{22} = i\,[\mu_s - \mu_t]\Omega_1\,\sin\theta\,\cos\theta/k \tag{E.6}$$

$$\mathrm{B}_{23} = -i\,[\mu_s - \mu_t]\Omega_6\,\sin\theta\,\cos\theta/k \tag{E.7}$$

$$\mathrm{B}_{24} = -i\,[\mu_s - \mu_t]\Omega_{11}\,\sin\theta\,\cos\theta/k \tag{E.8}$$

$$\mathrm{B}_{31} = 0 \tag{E.9}$$

$$\mathrm{B}_{32} = \lambda\Omega_1 + [2\mu\nu_3\Omega_2 + \lambda\nu_3\Omega_2 - \mu_n\Omega_2 + e^{if}\Omega_3 - e_{33}\nu_3\Omega_3]/k \tag{E.10}$$

$$\mathrm{B}_{33} = -[k\lambda\Omega_6 + 2\mu\nu_5\Omega_7 + \lambda\nu_5\Omega_7 - \mu_n\Omega_7 - e^{if}\Omega_8 + e_{33}\nu_5\Omega_8]/k \tag{E.11}$$

$$\mathrm{B}_{34} = -[k\lambda\Omega_{11} + 2\mu\nu_7\Omega_{12} + \lambda\nu_7\Omega_{12} - \mu_n\Omega_{12} - e^{if}\Omega_{13} + e_{33}\nu_7\Omega_{13}]/k \tag{E.12}$$

$$\mathrm{B}_{41} = 0 \tag{E.13}$$

$$\mathrm{B}_{42} = e_{31}\Omega_1 + [-e^{if}\Omega_2 + e_{33}\nu_3\Omega_2 - \epsilon^{if}\Omega_3 + \epsilon_{33}\nu_3\Omega_3]/k \tag{E.14}$$

$$\mathrm{B}_{43} = -[e_{31}k\Omega_6 - e^{if}\Omega_7 + e_{33}\nu_5\Omega_7 + \epsilon^{if}\Omega_8 - \epsilon_{33}\nu_5\Omega_8]/k \tag{E.15}$$

$$\mathrm{B}_{44} = -[e_{31}k\Omega_{11} - e^{if}\Omega_{12} + e_{33}\nu_7\Omega_{12} + \epsilon^{if}\Omega_{13} - \epsilon_{33}\nu_7\Omega_{13}]/k \tag{E.16}$$

Otherwise, if the bulk inheres fully transversal isotropy, the entries of $\mathbf{B}$ read as

$$\mathrm{B}_{11} = -[\mu_s - \mu_t]\Omega_1 \cos\theta \sin\theta/k \tag{E.17}$$

$$\mathrm{B}_{12} = i\left[\nu_3\mu_\parallel\Omega_2 + k[\mu_\parallel\Omega_3 + e_{15}\Omega_4] - \mu_s\Omega_2\cos^2\theta - \mu_t\Omega_2\sin^2\theta\right]/k \tag{E.18}$$

$$\mathrm{B}_{13} = [\nu_5\mu_\parallel\Omega_7 + ik[\mu_\parallel\Omega_8 + e_{15}\Omega_9] - \mu_s\Omega_7\cos^2\theta - \mu_t\Omega_7\sin^2\theta]/k \tag{E.19}$$

$$\mathrm{B}_{14} = [\nu_7\mu_\parallel\Omega_{12} + ik[\mu_\parallel\Omega_{13} + e_{15}\Omega_{14}] - \mu_s\Omega_{12}\cos^2\theta - \mu_t\Omega_{12}\sin^2\theta]/k \tag{E.20}$$

$$\mathrm{B}_{21} = [-\mu_t\Omega_1\cos^2\theta - \mu_s\Omega_1\sin^2\theta + \Omega_1\nu_1\mu_\parallel]/k \tag{E.21}$$

$$\mathrm{B}_{22} = -i[\mu_s - \mu_t]\Omega_2\cos\theta\sin\theta/k \tag{E.22}$$

$$\mathrm{B}_{23} = -[\mu_s - \mu_t]\Omega_7\cos\theta\sin\theta/k \tag{E.23}$$

$$\mathrm{B}_{24} = -[\mu_s - \mu_t]\Omega_{12}\cos\theta\sin\theta/k \tag{E.24}$$

$$\mathrm{B}_{31} = 0 \tag{E.25}$$

$$\mathrm{B}_{32} = -[\alpha + \lambda]\Omega_2 + [2\alpha + \beta + \lambda + 4\mu_\parallel - 2\mu_\perp]\nu_3\Omega_3/k \tag{E.26}$$

$$- [\mu_n\Omega_3 + e^{if}\Omega_4]/k + e_{33}\nu_3\Omega_4/k \tag{E.27}$$

$$\mathrm{B}_{33} = i[\alpha + \lambda]\Omega_7 + [2\alpha + \beta + \lambda + 4\mu_\parallel - 2\mu_\perp]\nu_5\Omega_8/k \tag{E.28}$$

$$- [\mu_n\Omega_8 + e^{if}\Omega_9]/k + e_{33}\nu_5\Omega_9/k \tag{E.29}$$

$$\mathrm{B}_{34} = i[\alpha + \lambda]\Omega_{12} + [2\alpha + \beta + \lambda + 4\mu_\parallel - 2\mu_\perp]\nu_7\Omega_{13}/k \tag{E.30}$$

$$- [\mu_n\Omega_{13} + e^{if}\Omega_{14}]/k + e_{33}\nu_7\Omega_{14}/k \tag{E.31}$$

$$\mathrm{B}_{41} = 0 \tag{E.32}$$

$$\mathrm{B}_{42} = -[e_{31}k\Omega_2 + e^{if}\Omega_3 - e_{33}\nu_3\Omega_3 - \epsilon^{if}\Omega_4 + \epsilon_{33}\nu_3\Omega_4]/k \tag{E.33}$$

$$\mathrm{B}_{43} = [ie_{31}k\Omega_7 - e^{if}\Omega_8 + e_{33}\nu_5\Omega_8 + \epsilon^{if}\Omega_9 - \epsilon_{33}\nu_5\Omega_9]/k \tag{E.34}$$

$$\mathrm{B}_{44} = [ie_{31}k\Omega_{12} - e^{if}\Omega_{13} + e_{33}\nu_7\Omega_{13} + \epsilon^{if}\Omega_{14} - \epsilon_{33}\nu_7\Omega_{14}]/k \tag{E.35}$$

F Element Operator Matrices

In what follows, the element operator matrices as introduced in chapter 6 are given.

$$\boldsymbol{B}_{ce8} = [\boldsymbol{N}_1, \boldsymbol{N}_2, \boldsymbol{N}_3, \boldsymbol{N}_4, \boldsymbol{N}_5, \boldsymbol{N}_6, \boldsymbol{N}_7, \boldsymbol{N}_8], \quad \text{with} \quad \boldsymbol{N}_i = \begin{bmatrix} N_{i,x} & 0 & 0 \\ 0 & N_{i,y} & 0 \\ 0 & 0 & N_{i,z} \\ N_{i,y} & N_{i,x} & 0 \\ 0 & N_{i,z} & N_{i,y} \\ N_{i,z} & 0 & N_{i,x} \end{bmatrix} \tag{F.1}$$

$$\boldsymbol{B}_{ce4} = [\boldsymbol{N}_1, \boldsymbol{N}_2, \boldsymbol{N}_3, \boldsymbol{N}_4], \quad \text{with} \quad \boldsymbol{N}_i = \begin{bmatrix} N_{i,x} & 0 \\ 0 & N_{i,y} \\ N_{i,y} & N_{i,x} \end{bmatrix} \tag{F.2}$$

$$\boldsymbol{B}_{ce3} = [\boldsymbol{N}_1, \boldsymbol{N}_2, \boldsymbol{N}_3], \quad \text{with} \quad \boldsymbol{N}_i = \begin{bmatrix} N_{i,x} & 0 \\ 0 & N_{i,y} \\ N_{i,y} & N_{i,x} \end{bmatrix} \tag{F.3}$$

$$\boldsymbol{B}_{ie4} = [-\boldsymbol{N}_1, -\boldsymbol{N}_2, -\boldsymbol{N}_3, -\boldsymbol{N}_4, \boldsymbol{N}_1, \boldsymbol{N}_2, \boldsymbol{N}_3, \boldsymbol{N}_4], \quad \text{with} \quad \boldsymbol{N}_i = \begin{bmatrix} N_i & 0 & 0 \\ 0 & N_i & 0 \\ 0 & 0 & N_i \end{bmatrix} \tag{F.4}$$

$$\boldsymbol{B}_{ie2} = [-\boldsymbol{N}_1, -\boldsymbol{N}_2, \boldsymbol{N}_2, \boldsymbol{N}_1], \quad \text{with} \quad \boldsymbol{N}_i = \begin{bmatrix} N_i & 0 \\ 0 & N_i \end{bmatrix} \tag{F.5}$$

$$\boldsymbol{A}_{ce4} = [\boldsymbol{N}_1, \boldsymbol{N}_2, \boldsymbol{N}_3, \boldsymbol{N}_4], \quad \text{with} \quad \boldsymbol{N}_i = \begin{bmatrix} N_{i,x} \\ N_{i,y} \end{bmatrix} \tag{F.6}$$

$$\boldsymbol{A}_{ce3} = [\boldsymbol{N}_1, \boldsymbol{N}_2, \boldsymbol{N}_3], \quad \text{with} \quad \boldsymbol{N}_i = \begin{bmatrix} N_{i,x} \\ N_{i,y} \end{bmatrix} \tag{F.7}$$

$$\boldsymbol{a}_{ie2} = [-N_1, -N_2, N_2, N_1] \tag{F.8}$$

G Nomenclature

Let a Cartesian base system resident in an Euclidian space be introduced as $\{\boldsymbol{e}_1, \boldsymbol{e}_2, \boldsymbol{e}_3\}$, and furthermore, it holds Einstein's summation convention while δ_{ij} denotes the Kronecker Delta. In this work, scalars or zeroth order quantities are denoted by non-bold symbols as e.g., a, α, or A. Furthermore, vectors or, respectively, first order quantities are indicated by small bold symbols $\boldsymbol{a} = a_i \boldsymbol{e}_i$. Second order tensors are given as capital bold symbols $\boldsymbol{A} = A_{ij} \boldsymbol{e}_i \otimes \boldsymbol{e}_j$ with exception of $\boldsymbol{\varepsilon}$, $\boldsymbol{\sigma}$ and $\boldsymbol{e}$, being second order tensors, and $\boldsymbol{E}$ and $\boldsymbol{D}$, being vectors, due to common notation. Third order tensors are specified in the Schwabach style in small letters as $\mathfrak{a} = [\mathfrak{a}]_{kij} \boldsymbol{e}_k \otimes \boldsymbol{e}_i \otimes \boldsymbol{e}_j$ while fourth order tensors are denoted by blackboard-style bold symbols $\mathbb{A} = [\mathbb{A}]_{ijkl} \boldsymbol{e}_i \otimes \boldsymbol{e}_j \otimes \boldsymbol{e}_k \otimes \boldsymbol{e}_l$. First, some related calculation rules are introduced as

contraction	c	$=$	$\boldsymbol{a} \cdot \boldsymbol{b}$	c	$=$	$a_i b_i$
	$\boldsymbol{c}$	$=$	$\boldsymbol{A} \cdot \boldsymbol{b}$	c_i	$=$	$A_{ij} b_j$
	$\boldsymbol{C}$	$=$	$\boldsymbol{A} \cdot \boldsymbol{B}$	C_{ij}	$=$	$A_{ik} B_{kj}$
	$\mathfrak{c}$	$=$	$\mathbb{A} \cdot \boldsymbol{b}$	c_{ijk}	$=$	$[\mathbb{A}]_{ijkl} b_l$
double contraction	c	$=$	$\boldsymbol{A} : \boldsymbol{B}$	c	$=$	$A_{ij} B_{ij}$
	$\boldsymbol{C}$	$=$	$\mathbb{A} : \boldsymbol{B}$	C_{ij}	$=$	$[\mathbb{A}]_{ijkl} B_{kl}$
dyadic product	$\boldsymbol{C}$	$=$	$\boldsymbol{a} \otimes \boldsymbol{b}$	C_{ij}	$=$	$a_i b_j$
	$\mathfrak{c}$	$=$	$\boldsymbol{A} \otimes \boldsymbol{b}$	$[\mathfrak{c}]_{ijk}$	$=$	$A_{ij} b_k$
	$\mathbb{C}$	$=$	$\boldsymbol{A} \otimes \boldsymbol{B}$	$[\mathbb{C}]_{ijkl}$	$=$	$A_{ij} B_{kl}$

transpose

$$\boldsymbol{A}^t = A_{ij} \boldsymbol{e}_j \otimes \boldsymbol{e}_i = A_{ji} \boldsymbol{e}_i \otimes \boldsymbol{e}_j$$

$$\mathfrak{a}^t = [\mathfrak{a}]_{kij} \boldsymbol{e}_i \otimes \boldsymbol{e}_j \otimes \boldsymbol{e}_k = [\mathfrak{a}]_{ijk} \boldsymbol{e}_k \otimes \boldsymbol{e}_i \otimes \boldsymbol{e}_j$$

In the following, identity tensors are defined.

$$
\begin{aligned}
\boldsymbol{I} &= \delta_{ij}\,\boldsymbol{e}_i \otimes \boldsymbol{e}_j \\
\boldsymbol{I} \otimes \boldsymbol{I} &= \delta_{ij}\delta_{kl}\,\boldsymbol{e}_i \otimes \boldsymbol{e}_j \otimes \boldsymbol{e}_k \otimes \boldsymbol{e}_l \\
\mathbb{I}^{sym} &= \frac{1}{2}[\delta_{ik}\delta_{jl} + \delta_{il}\delta_{jk}]\,\boldsymbol{e}_i \otimes \boldsymbol{e}_j \otimes \boldsymbol{e}_k \otimes \boldsymbol{e}_l \\
\mathbb{I}^{skw} &= \frac{1}{2}[\delta_{ik}\delta_{jl} - \delta_{il}\delta_{jk}]\,\boldsymbol{e}_i \otimes \boldsymbol{e}_j \otimes \boldsymbol{e}_k \otimes \boldsymbol{e}_l \\
\mathbb{I}^{sph} &= \frac{1}{n}\boldsymbol{I} \otimes \boldsymbol{I} = \frac{1}{n}\delta_{ij}\delta_{kl}\,\boldsymbol{e}_i \otimes \boldsymbol{e}_j \otimes \boldsymbol{e}_k \otimes \boldsymbol{e}_l \\
\mathbb{I}^{dev} &= \mathbb{I}^{sym} - \mathbb{I}^{sph}
\end{aligned}
$$

With $\bullet$ being some relevant quantity, brackets $[\bullet]$ denote mathematical groupings, intervals and the so-called index notation, parentheses $(\bullet)$ denote functional dependencies and curly brackets $\{\bullet\}$ are used in the context of sets and to indicate some index notation. Double brackets $[\![\bullet]\!]$ denote a jump of some relevant argument, while the so-called Macaulay-brackets are defined as

$$
\text{Macaulay-brackets} \qquad \langle\bullet\rangle = \begin{cases} \bullet & \text{if} \quad \bullet > 0 \\ 0 & \text{if} \quad \bullet \leq 0 \end{cases}
$$

Furthermore, some frequently used indices and notation is listed below.

$\bullet^{-1}$	inverse
$\bullet^{dev}$	deviatoric part
$\bullet^{h}$	approximated quantity
$\bullet_{ijkl}$	tensorial indices
$\bullet_n, \bullet_{(n)}$	point of time $n < n+1$
$\bullet_{n+1}, \bullet_{(n+1)}$	point of time $n+1 > n$
$\bullet_N$	quantity after N cycles
$\bullet_{N+\Delta N}$	quantity after $N + \Delta N$ cycles
$\bullet_t$	quantity at time t
$\bullet_{t+\Delta t}$	quantity at time $t + \Delta t$
$\bullet_p$	prescribed quantity
$\bullet^{sph}$	spherical part
$\bullet^{sym}$	symmetric part
$\bullet^{t}$	transposed
$\bullet_{trial}$	trial quantity
$\bullet^{V}$	Voigt notation
$\dot{\bullet}$	derivation with respect to time
$\Delta\bullet$	finite increment with respect to time
$\delta\bullet$	increment with respect to time
$\hat{\bullet}$	test quantity

The symbols being used in this work are given below, sorted by zeroth, first, second, third and fourth order quantities, and miscellaneous quantities.

Zeroth Order Quantities

a_0, a_1, a_2	complex ansatz constants
C	material constant, cycle-based fatigue
$c_1, c_2, c_3, c_4, c_5, c_6, c_7, c_8$	complex ansatz constants
c_I	shortcut, Prandtl-Reuss Tensor
c_{II}	shortcut, Prandtl-Reuss Tensor
c_s, c_t, c_n	interfacial stiffness parameters
c_s^*, c_t^*, c_n^*	interfacial elastic stiffnesses
c_s^m, c_t^m, c_n^m	interfacial elastic stiffnesses, damper-serial spring $\Rightarrow$ viscoelasticity
$c_s^\infty, c_t^\infty, c_n^\infty$	interfacial elastic stiffnesses, parallel spring $\Rightarrow$ viscoelasticity
$c_{\Phi\Phi}^{cbf}$	electrical-electrical component of $\boldsymbol{C}_{alg}^{if,fer,cbf}$
$c_{\Phi\Phi}^{tbf}$	electrical-electrical component of $\boldsymbol{C}_{alg}^{if,fer,tbf}$
d	damage parameter, synchronous conc. the interf. orthon. base system
d_k	damage parameter during cycle k
d_p	damage predictor value $\Rightarrow$ cycle-based fatigue
d_s, d_t, d_n	damage parameters, decoupled conc. the interf. orthon. base system
$\mathcal{D}$	dissipation power
$\mathcal{D}_{loc}$	local part of dissipation power
$\mathcal{D}_{red}$	reduced dissipation power
E	electric field strength over the interface
f	damage loading function, cycle-based fatigue
g	shortcut
G	virtual work of the uncoupled problem
G_u	virtual work resulting from the balance of linear momentum
G_Φ	virtual work resulting from the Gaussian law
$G^{ce,h}$	virtual work of the uncoupled problem for one continuum element
$G^{ie,h}$	virtual work of the uncoupled problem for one interface element
$G_u^{ce,h}$	virtual work res. from the balance of lin. mom. for one cont. element
$G_u^{ie,h}$	virtual work res. from the balance of lin. mom. for one interface element
$G_\Phi^{ce,h}$	virtual work resulting from the Gaussian law for one continuum element
$G_\Phi^{ie,h}$	virtual work resulting from the Gaussian law for one interface element
$\Delta G^{ce,h}$	linearisation of $G^{ce,h}$
$\Delta G^{ie,h}$	linearisation of $G^{ie,h}$
$\Delta G_u^{ce,h}$	linearisation of $G_u^{ce,h}$

$\Delta G_u^{ie,h}$	linearisation of $G_u^{ie,h}$
$\Delta G_\Phi^{ce,h}$	linearisation of $G_\Phi^{ce,h}$
$\Delta G_\Phi^{ie,h}$	linearisation of $G_\Phi^{ie,h}$
h	evolution function, cycle-based fatigue
H	electric enthalpy function
H_1	electric enthalpy function in mechanical basic invariants
H_2	electric enthalpy function in electric basic invariants
H_3	electric enthalpy function in coupled basic invariants
H^p	plastic hardening modulus
H_s^p, H_t^p, H_n^p	plastic hardening moduli of the interface
$H_s^{vp}, H_t^{vp}, H_n^{vp}$	viscoplastic hardening moduli of the interface
$\check{H}$	penalty part of the electric enthalpy function
H^*	penalty-extended electric enthalpy function
i	imaginary unit
$I_\bullet$	basic invariants, elasticity
$I_\bullet^*$	principal invariants, elasticity
$I_s^{if}, I_t^{if}, I_n^{if}$	coefficients, interfacial elasticity
J^{if}	coefficients, interfacial ferroelectricity
$J_\bullet$	electric basic invariants, ferroelectricity
j_s, j_t, j_n	intensities of damage evolution
k	real part of the first cartesian coefficient of the wave vector/wave number
k_1, k_2, k_3	some cartesian coefficient of the wave vector
$k_I, k_{II}, k_{III}, k_{IV}$	wave numbers (roots of $\det(\boldsymbol{B})$)
$\check{k}_j$	real part of some cartesian coefficient of the wave vector
k_j^*	imaginary part of some cartesian coefficient of the wave vector
$k_{\Phi\Phi}^{ie}$	electrical-electrical part of $\boldsymbol{K}^{ie}$
K^{if}	coefficients, interfacial ferroelectricity
$K_\bullet$	coupled basic invariants, ferroelectricity
l_s, l_t, l_n	interfacial inherent lengths
l_ϵ	interfacial inherent length
m_Φ	amplitude of the incremental electrical potential
N	cycle number, cycle-based fatigue
N_N	ansatz function
ΔN	cycle increment, cycle-based fatigue
q	penalty-stiffness parameter
$q_{0\Phi\Phi}$	electrical-electrical part of $\boldsymbol{Q}_0$
$q_{1\Phi\Phi}$	electrical-electrical part of $\boldsymbol{Q}_1$
$q_{2\Phi\Phi}$	electrical-electrical part of $\boldsymbol{Q}_2$
$q_{\Phi\Phi}$	electrical-electrical part of the complex acoustic-type tensor

R	internal stress = hardening stress
R_s, R_t, R_n	nominal internal tractions = nominal hardening tractions
$\bar{R}_s, \bar{R}_t, \bar{R}_n$	effective internal tractions = effective hardening tractions
$\bar{R}_{s,trial}, \bar{R}_{t,trial}, \bar{R}_{n,trial}$	effective internal tractions = effective hardening tractions, trial values
T_s, T_t, T_n	relaxation times
$\Delta t = t_{n+1} - t_n$	time increment
t_n	$< t_{n+1}$, point of time
t_{n+1}	$> t_n$, point of time
w	Wronski-determinant
w_Φ	electrical potential decay function
W, W_{mech}	strain/displacement jump energy function
W^*_{elec}	complementary electric field energy function
$\mathcal{W}, \mathcal{W}_{mech}$	stress/traction power
$\mathcal{W}^*_{elec}$	complementary dielectric displacement power
Y	driving force, ferroelectric interfacial fatigue
Y_0	yield stress
$Y_{s(0)}, Y_{t(0)}, Y_{n(0)}$	interfacial yield tractions
Z	antiderivative of the cycle-based fatigue evolution function
α,α_1,α_2	elastic material constants
α^p	plastic parameter
$\alpha^p_s, \alpha^p_t, \alpha^p_n$	plastic parameters of the interface
$\alpha^{vp}_s, \alpha^{vp}_t, \alpha^{vp}_n$	viscoplastic parameters of the interface
$\check{\alpha}$	time-based fatigue material parameter
β,β_1,β_2,β_3	elastic material constants
$\beta_s, \beta_t, \beta_n$	fatigue material parameters: displacement jump weighting factors
β_Φ	fatigue material parameter: electric potential jump weighting factor
$\check{\beta}$	cycle-based fatigue material parameter
$\check{\gamma}$	cycle-based fatigue material parameter
$\dot{\gamma}$	Lagrange multiplier, elastoplastic bulk
$\dot{\gamma}^p_s, \dot{\gamma}^p_t, \dot{\gamma}^p_n$	Lagrange multipliers, elastoplastic interface
$\dot{\gamma}^{vp}_s, \dot{\gamma}^{vp}_t, \dot{\gamma}^{vp}_n$	penalty parameters, viscoplastic interface
γ_1	ferroelectric material constant
γ_2	ferroelectric material constant
δ	effective quantity
$\tilde{\delta}$	history-dependent effective quantity
δ_a	effective quantity amplitude
δ_k	effective quantity during cycle k
$\delta_{a,k}$	effective quantity amplitude for cycle k

ϵ^{if}	Ferroelectric Interfacial Electrical-Electrical Tangent
ϵ_0	permittivity of the vacuum
ϵ_r	relative permittivity
ϵ_r^{init}	relative permittivity at the beginning of the fatigue history
ϵ_r^{end}	relative permittivity at the end of the fatigue history
$\varepsilon_\bullet$	eigenvalues of $\boldsymbol{\varepsilon}$
ζ	shortcut for $\boldsymbol{e}_1 \cdot \tilde{\boldsymbol{x}}$
ζ_1	ferroelectric material constant
ζ_2	ferroelectric material constant
ζ_3	ferroelectric material constant
ζ^{tbf}	interfacial time-based fatigue evolution switch
ζ^{cbf}	interfacial cycle-based fatigue evolution switch
ζ_i^{ep}	interfacial plastic evolution switch
ζ_i^{vp}	interfacial viscoplastic evolution switch
η	shortcut for $\boldsymbol{e}_3 \cdot \tilde{\boldsymbol{x}}$
η_s, η_t, η_n	viscosities
θ	angle in the interfacial plane (spanned by $\boldsymbol{s}$ and $\boldsymbol{t}$)
κ	threshold, cycle-based fatigue
λ	Lamé-parameter, elastic material constant
Λ	dielectric displacement in the interface
Λ_{Γ^-}	dielectric displacement at Γ^-
Λ_{Γ^+}	dielectric displacement at Γ^+
μ	Lamé-parameter, elastic material constant
μ_1	elastic material constant
μ_2	elastic material constant
μ_s, μ_t, μ_n	damage progression parameters
$\mu_{s(0)}, \mu_{t(0)}, \mu_{n(0)}$	damage thresholds
$\bar{\mu}_s, \bar{\mu}_t, \bar{\mu}_n$	damage driving forces
$\mu_\parallel$	elastic material constant
$\mu_\perp$	elastic material constant
ν	eigenvalue/negative imag. part of the first cart. coeff. of the wave vector
$\nu_0, \nu_1, \nu_2, \nu_3, \nu_4, \nu_5, \nu_6$	eigenvalues
ν_I, ν_{II}	multiple eigenvalues
ξ	interpolation variable
ξ_1, ξ_2, ξ_3	interpolation variables
$\xi_{1N}, \xi_{2N}, \xi_{3N}$	nodal coordinates

$\rho_s^{ed}, \rho_t^{ed}, \rho_n^{ed}$	interfacial constitutive parameters, elasticity with damage
$\rho_s^{ep}, \rho_t^{ep}, \rho_n^{ep}$	interfacial constitutive parameters, elastoplasticity
$\rho_s^{epd}, \rho_t^{epd}, \rho_n^{epd}$	interfacial constitutive parameters, elastoplasticity with damage
$\rho_s^*, \rho_t^*, \rho_n^*$	interfacial constitutive quantities
ρ_s, ρ_t, ρ_n	interfacial constitutive parameters
τ	time variable
φ	part of the yield function Φ^p
Φ	electrical potential
Φ_{Γ^-}	electrical potential at Γ^-
Φ_{Γ^+}	electrical potential at Γ^+
$\Phi_1, \Phi_2, ...$	combinations of material parameters
Φ_s, Φ_t, Φ_n	expressing interfacial material parameters, elasticity
Φ_{En}	expressing an interfacial material parameter, ferroelectricity
Φ_N	electric potential at element node N
$\Phi_{[\![u]\!]En}$	expressing an interfacial material parameter, ferroelectricity
Φ^p	plastic yield function and potential, associative
$\Phi^{p,\star}$	plastic potential, non-associative
$\Phi_s^p, \Phi_t^p, \Phi_n^p$	interfacial plastic yield functions
$\Phi_{s,trial}^p, \Phi_{t,trial}^p, \Phi_{n,trial}^p$	interfacial plastic trial yield functions
$\Phi_s^{vp}, \Phi_t^{vp}, \Phi_n^{vp}$	interfacial viscoplastic yield functions
$\Phi_{s,trial}^{vp}, \Phi_{t,trial}^{vp}, \Phi_{n,trial}^{vp}$	interfacial viscoplastic trial yield functions
$[\![\Phi]\!]$	electric potential jump over the interface
χ	shortcut in the context of coupled bifurcation
Ψ	free energy function
Ψ^{el}	elastic part of the free energy function
Ψ^{eld}	elastic-damaging part of the free energy function
Ψ^{ep}	elastoplastic part of the free energy function
Ψ^{epd}	plastic-damaging part of the free energy function
Ψ^m	damper-serial part of the free energy function $\Rightarrow$ viscoelasticity
Ψ^{vpd}	viscoplastic-damaging part of the free energy function
$\check{\Psi}$	penalty part of the free energy function
Ψ^*	penalty-extended free energy function
Ψ^∞	parallel part of the free energy function $\Rightarrow$ viscoelasticity
$\omega_1, \omega_2, \omega_3, \omega_4$	complex parameters
Ω^{cbf}	interfacial cycle-based fatigue loading switch
$\Omega_1, \Omega_2, \Omega_3, ...$	auxiliary quantity in the context of coupled bifurcation
$\aleph$	shortcut in the context of plasticity

First Order Quantities

$\boldsymbol{a}$	vector of complex constants
$\boldsymbol{a}_{ie2}$	element operator matrix for a linear two-noded interface element
$\boldsymbol{c}$	vector of complex constants
$\boldsymbol{c}_{\Phi u}^{cbf}$	electrical-mechanical component of $\boldsymbol{C}_{alg}^{if,fer,cbf}$
$\boldsymbol{c}_{u\Phi}^{cbf}$	mechanical-electrical component of $\boldsymbol{C}_{alg}^{if,fer,cbf}$
$\boldsymbol{c}_{\Phi u}^{tbf}$	electrical-mechanical component of $\boldsymbol{C}_{alg}^{if,fer,tbf}$
$\boldsymbol{c}_{u\Phi}^{tbf}$	mechanical-electrical component of $\boldsymbol{C}_{alg}^{if,fer,tbf}$
$\boldsymbol{D}$	dielectric displacement vector
$\boldsymbol{e}_1, \boldsymbol{e}_2, \boldsymbol{e}_3$	vectors of the three-dimensional cartesian base system
$\boldsymbol{e}_1, \boldsymbol{e}_2, \boldsymbol{e}_3, \boldsymbol{e}_4, \boldsymbol{e}_5, \boldsymbol{e}_6$	vectors of the six-dimensional cartesian base system
$\boldsymbol{e}_i, \boldsymbol{e}_j, \boldsymbol{e}_k, \boldsymbol{e}_l$	vectors of the cartesian base system
$\boldsymbol{e}^{if}$	Ferroelectric Interfacial Electromechanical Tangent Vector
$\boldsymbol{e}^{if,\Delta}$	Ferroelectric Interfacial Auxiliary Tensor
$\boldsymbol{E}$	electric field vector
$\boldsymbol{f}^{ce}$	continuum element residuum
$\boldsymbol{f}_u^{ce}$	mechanical part of the continuum element residuum
$\boldsymbol{f}_\Phi^{ce}$	electrical part of the continuum element residuum
$\boldsymbol{f}^{ie}$	interface element residuum
$\boldsymbol{f}_u^{ie}$	mechanical part of the interface element residuum
$\boldsymbol{f}_\Phi^{ie}$	electrical part of the interface element residuum
$\boldsymbol{g}$	eigenvector
$\boldsymbol{g}_I, \boldsymbol{g}_{II}$	eigenspaces
$\boldsymbol{k}$	complex wave vector
$\check{\boldsymbol{k}}$	real part of the complex wave vector
$\boldsymbol{k}^*$	imaginary part of the complex wave vector
$\boldsymbol{k}_{u\Phi}^{ie}$	mechanical-electrical part of $\boldsymbol{K}^{ie}$
$\boldsymbol{k}_{\Phi u}^{ie}$	electrical-mechanical part of $\boldsymbol{K}^{ie}$
$\boldsymbol{m}$	amplitude vector
$\boldsymbol{m}_u$	amplitude vector of the incremental displacements
$\boldsymbol{m}_v$	overall amplitude vector, including $\boldsymbol{m}_u$ and m_Φ
$\boldsymbol{m}_0$, $\boldsymbol{m}_1$, $\boldsymbol{m}_2$	directions of anisotropy
$\boldsymbol{n}_D$	outward normal vector of $\partial\mathcal{B}_D$
$\boldsymbol{n}_\sigma$	outward normal vector of $\partial\mathcal{B}_\sigma$
$\boldsymbol{n}_{\Gamma^-} \equiv \boldsymbol{n}$	outward normal vector of $\mathcal{B}^-$ at the interface
$\boldsymbol{n}_{\Gamma^+}$	outward normal vector of $\mathcal{B}^+$ at the interface
$\boldsymbol{n}$	normal vector in the interfacial orthonormal base system
$\boldsymbol{n}_{trial}$	interfacial trial direction

$\boldsymbol{q}_{0u\Phi}$	mechanical-electrical part of $\boldsymbol{Q}_0$
$\boldsymbol{q}_{1u\Phi}$	mechanical-electrical part of $\boldsymbol{Q}_1$
$\boldsymbol{q}_{2u\Phi}$	mechanical-electrical part of $\boldsymbol{Q}_2$
$\boldsymbol{q}_{0\Phi u}$	electrical-mechanical part of $\boldsymbol{Q}_0$
$\boldsymbol{q}_{1\Phi u}$	electrical-mechanical part of $\boldsymbol{Q}_1$
$\boldsymbol{q}_{2\Phi u}$	electrical-mechanical part of $\boldsymbol{Q}_2$
$\boldsymbol{q}_{u\Phi}$	mechanical-electrical part of the complex acoustic-type tensor
$\boldsymbol{q}_{\Phi u}$	electrical-mechanical part of the complex acoustic-type tensor
$\boldsymbol{s}$	tangential vector in the interfacial orthonormal base system
$\boldsymbol{s}_{trial}$	interfacial trial direction
$\boldsymbol{t}$	tangential vector in the interfacial orthonormal base system
$\boldsymbol{t}_{trial}$	interfacial trial direction
$\boldsymbol{u}$	displacement vector
$\boldsymbol{u}_{\Gamma^-}$	displacement vector at Γ^-
$\boldsymbol{u}_{\Gamma^+}$	displacement vector at Γ^+
$\boldsymbol{u}_N$	displacement vector at element node N
$\boldsymbol{u}^N$	displacement vector containing all $\boldsymbol{u}_N$
$\Delta\boldsymbol{u}^N$	linearisation increment of $\boldsymbol{u}^N$
$[\![\boldsymbol{u}]\!]$	displacement jump over the interface
$[\![\boldsymbol{u}]\!]^e$	elastic part of the displacement jump
$[\![\boldsymbol{u}]\!]^p$	plastic part of the displacement jump
$[\![\boldsymbol{u}]\!]^{ve}$	viscous (elastic) part of the displacement jump
$[\![\boldsymbol{u}]\!]^{vp}$	viscous (plastic) part of the displacement jump
$\boldsymbol{v}_1, \boldsymbol{v}_2, \boldsymbol{v}_3, \boldsymbol{v}_4, \boldsymbol{v}_5, \boldsymbol{v}_6, \boldsymbol{v}_7, \boldsymbol{v}_8$	eigenvectors
$\boldsymbol{v}_1^*, \boldsymbol{v}_2^*$	generalised eigenvectors
$\boldsymbol{w}$	decay function, solution of the first order diff. equation system
$\boldsymbol{w}_u$	decay function of displacements
$\boldsymbol{w}_v$	overall decay function
$\boldsymbol{x}$	position vector to some point of interest
$\boldsymbol{x}_0$	position vector to the interfacial orthonormal system
$\tilde{\boldsymbol{x}}$	argument of the wave-type ansatz
$\boldsymbol{z}$	solution of some first order differential equation system

$\boldsymbol{\tau}$	(nominal) traction vector
$\bar{\boldsymbol{\tau}}$	effective traction vector
$\boldsymbol{\tau}^m$	traction of damper-serial spring $\Rightarrow$ viscoelasticity
$\boldsymbol{\tau}_{\Gamma^-}$	outward traction at Γ^-
$\boldsymbol{\tau}_{\Gamma^+}$	outward traction at Γ^+
$\check{\boldsymbol{\tau}}$	penalty part of traction
$\boldsymbol{\tau}^*$	penalty-extended traction
$\boldsymbol{\tau}^\infty$	traction of parallel spring $\Rightarrow$ viscoelasticity
$\bar{\boldsymbol{\tau}}_{trial}$	effective trial tractions
$\bar{\boldsymbol{\tau}}^{ex}$	excess traction $\Rightarrow$ viscoplasticity
$\boldsymbol{\Phi}^N$	displacement vector containing all Φ_N
$\Delta\boldsymbol{\Phi}^N$	linearisation increment of $\boldsymbol{\Phi}^N$

Second Order Quantities

$\boldsymbol{A}$	system matrix of some first order differential equation system
$\boldsymbol{A}_{ce4}$	element operator matrix for a bilinear four-noded continuum element
$\boldsymbol{A}_{ce3}$	element operator matrix for a linear three-noded continuum element
$\boldsymbol{B}$	system matrix of some homogeneous linear equation system
$\boldsymbol{B}_{ce8}$	element operator matrix for a trilinear eight-noded continuum element
$\boldsymbol{B}_{ce4}$	element operator matrix for a bilinear four-noded continuum element
$\boldsymbol{B}_{ce3}$	element operator matrix for a linear three-noded continuum element
$\boldsymbol{B}_{ie4}$	element operator matrix for a bilinear four-noded interface element
$\boldsymbol{B}_{ie2}$	element operator matrix for a linear two-noded interface element
$\boldsymbol{C}$	Voigt-notated Continuum Tangent Stiffness Tensor
$\boldsymbol{C}^{el}$	Voigt-notated Elastic Continuum Tangent Stiffness Tensor
$\boldsymbol{C}^{if}$	interfacial incremental constitutive operator/tangent stiffness tensor
$\boldsymbol{C}^{if}_{uu}$	mechanical-mechanical interfacial tangent tensor
$\boldsymbol{C}^{if}_{u\Phi}$	mechanical-electrical interfacial tangent tensor
$\boldsymbol{C}^{if}_{\Phi u}$	electrical-mechanical interfacial tangent tensor
$\boldsymbol{C}^{if}_{\Phi\Phi}$	electrical-electrical interfacial tangent tensor
$\boldsymbol{C}^{if,cbf}_{alg}$	algorithmic tangent modulus of the interfacial cycle-based fatigue formalism
$\boldsymbol{C}^{if,ed}$	interfacial tangent modulus for elasticity with damage
$\boldsymbol{C}^{if,el}$	Elastic Interfacial Tangent Stiffness Tensor
$\boldsymbol{C}^{if,el,m}$	Elastic Interfacial Tangent Stiffness Tensor, damper-serial spring $\Rightarrow$ viscoelasticity
$\boldsymbol{C}^{if,el,\infty}$	Elastic Interfacial Tangent Stiffness Tensor, parallel spring $\Rightarrow$ viscoelasticity
$\boldsymbol{C}^{if,ep}$	interfacial tangent modulus for elastoplasticity
$\boldsymbol{C}^{if,epd}$	interfacial tangent modulus for elastoplasticity with damage
$\boldsymbol{C}^{if,epd}_{alg}$	algorithmic tangent modulus of interfacial elastoplasticity with damage
$\boldsymbol{C}^{if,fer}$	Linear Ferroelectric Interfacial Tangent Tensor
$\boldsymbol{C}^{if,fer,el}$	mechanical-mechanical part of the Linear Ferroel. Interfacial Tangent Tensor
$\boldsymbol{C}^{if,fer,tbf}_{alg}$	algorithmic tangent modulus of the interf. ferroelectric time-based fatigue formalism
$\boldsymbol{C}^{if,fer,cbf}_{alg}$	algorithmic tangent modulus of the interf. ferroelectric cycle-based fatigue formalism
$\boldsymbol{C}^{if,tbf}_{alg}$	algorithmic tangent modulus of the interf. time-based fatigue formalism
$\boldsymbol{C}^{if,ved}_{alg}$	algorithmic tangent modulus of interf. viscoelasticity with damage
$\boldsymbol{C}^{if,vpd}_{alg}$	algorithmic tangent modulus of interf. viscoplasticity with damage
$\boldsymbol{C}^{fer}$	Voigt-notated Ferroelectric Continuum Tangent Tensor: mech. part, stiffness tensor
$\boldsymbol{C}^{iso}$	Voigt-notated isotropic Elastic Continuum Tangent Stiffness Tensor
$\boldsymbol{C}^{ort}$	Voigt-notated orthotropic Elastic Continuum Tangent Stiffness Tensor
$\boldsymbol{C}^{cbf}_{uu}$	mechanical-mechanical component of $\boldsymbol{C}^{if,fer,cbf}_{alg}$
$\boldsymbol{C}^{tbf}_{uu}$	mechanical-mechanical component of $\boldsymbol{C}^{if,fer,tbf}_{alg}$

$\boldsymbol{C}^{tra}$	Voigt-notated transversal isotropic Elastic Continuum Tangent Stiffness Tensor
$\boldsymbol{C}_{uu}$	Voigt-notated mechanical-mechanical continuum tangent tensor
$\boldsymbol{C}_{u\Phi}$	Voigt-notated mechanical-electrical continuum tangent tensor
$\boldsymbol{C}_{\Phi u}$	Voigt-notated electrical-mechanical continuum tangent tensor
$\boldsymbol{C}_{\Phi\Phi}$	Voigt-notated electrical-electrical continuum tangent tensor
$\check{\boldsymbol{C}}_{alg}$	penalty part of algorithmic tangent modulus
$\boldsymbol{C}^{*}_{alg}$	penalty-extended algorithmic tangent modulus
$\boldsymbol{e}$	Voigt-notated Ferroelectric Continuum Tangent Tensor: coupling part, perm. tensor
$\boldsymbol{I}$	second order identity tensor
$\boldsymbol{I}_n$	$n \times n$ second order identity tensor
$\boldsymbol{K}^{ce}$	stiffness matrix of a continuum element
$\boldsymbol{K}^{ce}_{uu}$	mechanical-mechanical part of $\boldsymbol{K}^{ce}$
$\boldsymbol{K}^{ce}_{u\Phi}$	mechanical-electrical part of $\boldsymbol{K}^{ce}$
$\boldsymbol{K}^{ce}_{\Phi u}$	electrical-mechanical part of $\boldsymbol{K}^{ce}$
$\boldsymbol{K}^{ce}_{\Phi\Phi}$	electrical-electrical part of $\boldsymbol{K}^{ce}$
$\boldsymbol{K}^{ie}$	stiffness matrix of an interface element
$\boldsymbol{K}^{ie}_{uu}$	mechanical-mechanical part of $\boldsymbol{K}^{ie}$
$\boldsymbol{M}$, $\boldsymbol{M}_1$, $\boldsymbol{M}_2$	structure tensors
$\boldsymbol{N}$	direction of plasticity
$\boldsymbol{P} = \boldsymbol{P}(\theta \boldsymbol{e}_3)$	rotation tensor
$\boldsymbol{Q}$	complex acoustic-type tensor
$\boldsymbol{Q}^{*}$	auxiliary tensor
$\boldsymbol{Q}_{uu}$	mechanical-mechanical part of the complex acoustic-type tensor
$\boldsymbol{Q}^{iso}_{uu}$	mechanical-mechanical part of the complex acoustic-type tensor, isotropy
$\boldsymbol{Q}^{tra}_{uu}$	mechanical-mechanical part of the complex acoustic-type tensor, transv. isotropy
$\boldsymbol{Q}_0, \boldsymbol{Q}_1, \boldsymbol{Q}_2$	complex acoustic-type tensors
$\boldsymbol{Q}_{0uu}$	mechanical-mechanical part of $\boldsymbol{Q}_0$
$\boldsymbol{Q}_{1uu}$	mechanical-mechanical part of $\boldsymbol{Q}_1$
$\boldsymbol{Q}_{2uu}$	mechanical-mechanical part of $\boldsymbol{Q}_2$
$\boldsymbol{Q}^{\diamond} = \boldsymbol{Q}_2$	acoustic tensor of the bulk
$\boldsymbol{Z}$	fundamental matrix
$\boldsymbol{\epsilon}$	Ferroelectric Continuum Tangent Tensor: electric part, permittivity tensor
$\boldsymbol{\varepsilon}$	strain tensor
$\boldsymbol{\varepsilon}^{e}$	elastic part of the strain tensor
$\boldsymbol{\varepsilon}^{p}$	plastic part of the strain tensor
$\boldsymbol{\sigma}$	stress tensor

Third Order Quantities

$\mathfrak{e}$	Ferroelectric Continuum Tangent Tensor: coupling part, piezoelectric tensor
$\mathfrak{e}^*$	ferroelectric auxiliary tensor
$\mathfrak{e}^{\triangle}$	ferroelectric auxiliary tensor

Fourth Order Quantities

$\mathbb{C}$	incremental constitutive operator of the bulk
$\mathbb{C}^{el}$	Elastic Continuum Tangent Stiffness Tensor
$\mathbb{C}^{ep}$	Prandtl-Reuss Tensor
$\mathbb{C}^{ep}_{alg}$	algorithmic tangent modulus of bulk elastoplasticity
$\mathbb{C}^{fer}$	Ferroelectric Continuum Tangent Tensor: mechanical part, stiffness tensor
$\mathbb{C}^{iso}$	isotropic Elastic Continuum Tangent Stiffness Tensor
$\mathbb{C}^{ort}$	orthotropic Elastic Continuum Tangent Stiffness Tensor
$\mathbb{C}^{tra}$	transversal isotropic Elastic Continuum Tangent Stiffness Tensor
$\mathbb{M}$	transversal isotropic auxiliary tensor
$\mathbb{M}_1$, $\mathbb{M}_2$	orthotropic auxiliary tensors

Miscellaneous Quantities

$\mathcal{B}$	configuration of a body of interest
$\mathcal{B}^-$	part of $\mathcal{B}$, complementing to $\mathcal{B}^+$
$\mathcal{B}^+$	part of $\mathcal{B}$, complementing to $\mathcal{B}^-$
$\mathcal{B}_{ce}$	part of $\mathcal{B}$ related to a continuum element
$\partial\mathcal{B}_D$	electrical Neumann boundary of $\mathcal{B}$
$\partial\mathcal{B}_u$	mechanical Dirichlet boundary of $\mathcal{B}$
$\partial\mathcal{B}_\Phi$	electrical Dirichlet boundary of $\mathcal{B}$
$\partial\mathcal{B}_\sigma$	mechanical Neumann boundary of $\mathcal{B}$
$\mathcal{C}$	set of complex numbers
$\mathcal{C}^n$	n-dimensional complex vector space
const.	some constant quantity
$\mathrm{d}A$	infinitesimal surface element
$\mathrm{d}S$	infinitesimal line element
$\mathrm{d}V$	infinitesimal volume element
$\mathrm{d}A_{ce}$	infinitesimal surface element of a continuum element
$\mathrm{d}V_{ce}$	infinitesimal volume element of a continuum element
$\mathrm{d}A_{ie}$	infinitesimal surface element of an interface element
$\mathrm{d}S_{ie}$	infinitesimal line element of an interface element
$\mathcal{E}$	closure of the elastic range
$\mathcal{E}_s^{if}, \mathcal{E}_t^{if}, \mathcal{E}_n^{if}$	decoupled closures of the interfacial elastic ranges
i_{Em_0}, $i_{\varepsilon Em_0}$	sets of invariants $\Rightarrow$ ferroelectricity
$i_{[\![u]\!]}$	set of coefficients $\Rightarrow$ interfacial elasticity
i_{En}, $i_{[\![u]\!]En}$	sets of coefficients $\Rightarrow$ interfacial ferroelectricity
i_ε	set of invariants $\Rightarrow$ isotropic elasticity
$i_{\varepsilon M_0}$	set of invariants $\Rightarrow$ transversal isotropic elasticity
$i_{\varepsilon M_1}$, $i_{\varepsilon M_2}$	sets of invariants $\Rightarrow$ orthotropic elasticity
Γ	centre line of an interface
Γ^-	boundary of $\mathcal{B}^-$ towards the interface
Γ^+	boundary of $\mathcal{B}^+$ towards the interface
Γ_{ie}	part of Γ related to an interface element
$\mathcal{R}^n$	n-dimensional real-valued vector space
$\mathcal{S}$, $\mathcal{S}^*$	thermodynamic forces
$\mathcal{S}_s^{if}, \mathcal{S}_t^{if}, \mathcal{S}_n^{if}$	interfacial thermodynamic forces
$\mathcal{S}_s^{if,*}, \mathcal{S}_t^{if,*}, \mathcal{S}_n^{if,*}$	interfacial thermodynamic forces

Bibliography

[1] G. Alfano and M.A. Crisfeld. Finite element interface models for the delamination analysis of laminated composites: mechanical and computational issues. *Int. J. Numer. Methods Engng.*, 50:1701–1736, 2001.

[2] I. Arias, S. Serebrinsky, and M. Oritz. A phenomenologial cohesive model of ferroelectric fatigue. *Acta Mater.*, 54:975–985, 2006.

[3] A. Arockiarajan and A. Menzel. On the modelling of rate-dependent domain switching in piezoelectric materials under superimposed stresses. *Comput. Model. Eng. Sci.*, 19:163–180, 2007.

[4] A. Arockiarajan, A. Menzel, B. Delibas, and W. Seemann. Computational modeling of rate–dependent domain switching in piezoelectric materials. *Euro. J. Mech. A/Solids*, 25:950–964, 2006.

[5] H. Askes, T. Bennett, and E.C. Aifantis. A new formulation and $\mathcal{C}^0$-implementation of dynamically consistent gradient elasticity. *Int. J. Numer. Methods Engng.*, 72:111–126, 2007.

[6] F. Balle, G. Wagner, and D. Eifler. Ultrasonic spot welding of aluminum sheet/carbon fiber reinforced polymer–joints. *Materialwissenschaft und Werkstofftechnik*, 38:934–938, 2007.

[7] G.I. Barenblatt. The mathematical theory of equilibrium cracks in brittle fracture. *Advances in Applied Mechanics*, 7:55–129, 1962.

[8] O.H. Basquin. The exponential law of endurance tests. *Proceedings of ASTM*, 10:625–630, 1910.

[9] U. Bast. *Eigenschaften der Sekundärphase $Ba_6Ti_{17}O_{40}$ und ihr Einfluss auf $BaTiO_3$-Keramik*. PhD thesis, Universität Erlangen-Nürnberg, 1985.

[10] K.J. Bathe. *Finite Element Procedures*. Prentice Hall, 1996.

[11] Z.P. Bažant. Why continuum damage is nonlocal: Micromechanics arguments. *J. Engrg. Mech.*, 117:1070–1087, 1991.

[12] Z.P. Bažant and G. Pijaudier-Cabot. Nonlocal damage, localization, instability and convergence. *ASME J. Appl. Mech.*, 55:287–293, 1988.

[13] G. Beer. An isoparametric joint/interface element for finite element analysis. *Int. J. Numer. Methods Engng.*, 21:585–600, 1985.

[14] T. Belytschko and T. Black. Elastic crack growth in finite elements with minimal remeshing. *Int. J. Numer. Methods Engng.*, 45:601–620, 1999.

[15] T. Belytschko, J. Fish, and B.E. Engelmann. A finite element with embedded localization zones. *Int. J. Numer. Methods Engng.*, 70:59–89, 1988.

[16] T. Belytschko, W.K. Liu, and B. Moran. *Nonlinear Finite Elements for Continua and Structures*. Wiley, 2000.

[17] A. Benallal. *Ill-posedness and Localization in Solids Structures. Computational Plasticity, Ed. D.R.J. Owen et al.* Pineridge Press, 1992.

[18] A. Benallal. L.M.T. Cachan, France. Private communication, 2006.

[19] A. Benallal, R. Billardon, and G. Geymonat. Conditions de bifurcation à l'intérieur et aux frontières pour une classe de matériaux non standards. *C. R. Acad. Sci., Paris, Série II*, 308:893–898, 1989.

[20] A. Benallal, R. Billardon, and G. Geymonat. Phénomènes des localization à la frontière d'un solide. *C. R. Acad. Sci., Paris, Série II*, 310:679–684, 1990.

[21] A. Benallal, R. Billardon, and G. Geymonat. *Bifurcation and Localization in Rate-Independent Materials. Some General Considerations*, volume 327 of *CISM Courses and Lectures*. Springer, 1992.

[22] A. Benallal and C. Comi. On interfacial properties in gradient damaging continua. *C. R. Mecanique*, 333:319–324, 2005.

[23] H.P. Beringer, G. Heinke, and E. Strickle. Lösung tribotechnischer Probleme mit Hilfe von Polymerwerkstoffen. *Materialwissenschaften und Werkstofftechnik*, 22:168–173, 1991.

[24] D. Bertsekas. *Nonlinear Programming*. Athena Scientific, 2003.

[25] D. Bigoni and M. Gei. Bifurcations of a coated, elastic cylinder. *Int. J. Solids Struct.*, 38:5117–5148, 2001.

[26] D. Bigoni, M. Ortiz, and A. Needleman. Effect of interfacial compliance on bifurcation of a layer bonded to a substrate. *Int. J. Solids Struct.*, 34:4305–4326, 1997.

[27] M.A. Biot. *Mechanics of Incremental Deformations*. John Wiley and Sons, 1965.

[28] D. Braess. *Finite Elemente*. Springer, 1991.

[29] G. Busse, B.-H. Kröplin, and F.K. Wittel (Eds.). *Damage and its Evolution in Fiber-Composite Materials: Simulation and Non-Destructive Evaluation*. ISD Verlag, 2006.

[30] H.-J. Butt, K. Graf, and M. Kappl. *Physics and Chemistry of Interfaces*. Wiley-VCH, 2006.

[31] G.T. Camacho and M. Ortiz. Computational modelling of impact damage in brittle failure. *Int. J. Solids Struct.*, 33:2899–2938, 1996.

[32] P. Cannmo, L. Mähler, and K. Runesson. Modelling of interfacial viscoplastic slip coupled to damage in a polycrystalline microstructure. *Comput. Mech.*, 20:12–19, 1997.

[33] P. Cannmo, K. Runesson, and M. Ristinmaa. Modelling of plasticity and damage in a polycrystalline microstructure. *Int. J. Plasticity*, 11:949–970, 1995.

[34] J.L. Chaboche. Viscoplastic constitutive equations for the description of cyclic and anisotropic behaviour of metals. *Bulletin de l'Académie Polonaise des Sciences Série Sc. et Tech.*, 25:33–42, 1977.

[35] J.L. Chaboche. Continuum damage mechanics: Parts 1/2 - 2/2. *ASME J. Appl. Mech.*, 55:59–72, 1988.

[36] F. Cirak, M. Ortiz, and A. Pandolfi. A cohesive approach to thin-shell fracture and fragmentation. *Comput. Methods Appl. Mech. Engrg.*, 194:2604–2618, 2005.

[37] G. Cloud. *Optical Methods of Engineering Analysis*. Cambridge, 1995.

[38] B.D. Coleman and V.J. Mizel. Norms and semi-groups in the theory of fading memory. *Arch. Rational Mech. Anal.*, 23:87–274, 1966.

[39] B.D. Coleman and W. Noll. An approximation theorem for functionals, with application in continuum mechanics. *Arch. Rational Mech. Anal.*, 6:355–370, 1960.

[40] B.D. Coleman and W. Noll. Foundations of linear viscoelasticity. *Rev. Mod. Phys.*, 33:239–249, 1961.

[41] B.D. Coleman and W. Noll. The thermodynamics of elastic materials with heat conduction and viscosity. *Arch. Rational Mech. Anal.*, 13:167–178, 1963.

[42] A. Corigliano, S. Mariani, and A. Pandolfi. Numerical analysis of rate-dependent dynamic composite delamination. *Compos. Struct.*, 66:766–775, 2006.

[43] F. Daining, B. Liu, and C.T. Sun. Fatigue crack growth in ferroelectric ceramics driven by alternating electric fields. *J. Am. Ceram. Soc.*, 87:840–846, 2004.

[44] R. de Borst and H. Mühlhaus. Gradient-dependent plasticity: Formulation and algorithmic aspects. *Int. J. Numer. Methods Engng.*, 35:521 – 539, 1992.

[45] M.J. Van den Bosch, P.J.G Schreurs, and M.G.D. Geers. An improved description of the exponential Xu and Needleman cohesive zone law for mixed-mode decohesion. *Engng. Fract. Mech.*, 73:1220 – 1234, 2006.

[46] J. Dolbow, N. Moës, and T. Belytschko. An extended finite element method for modelling crack growth with frictional contact. *Comput. Methods Appl. Mech. Engrg.*, 190:6825–6846, 2001.

[47] M.A. Dowaikh and R.W. Ogden. On surface waves and deformations in a pre-stressed incompressible elastic solid. *IMA J. Appl. Math.*, 44:261–284, 1990.

[48] D.S. Dugdale. Yielding of steel sheets containing slits. *Journal of Mechanics and Solids*, 8:100–104, 1960.

[49] G.W. Ehrenstein, G. Riedel, and P. Trawiel. *Praxis der thermischen Analyse von Kunststoffen*. Carl Hanser, 2003.

[50] M. Erinc, P. Schreurs, and M. Geers. Integrated numerical-experimental analysis of interfacial fatigue fracture in SnAgCu solder joints. *Int. J. Solids Struct.*, 44:5680–5694, 2007.

[51] A.C. Eringen and G.A. Maugin. *Electrodynamics of Continua I. Foundations and Solid Media*. Springer, 1989.

[52] H.D. Espinosa, H.-C. Lu, P.D. Zavattieri, and S. Dwivedi. A 3-d finite deformation anisotropic visco-plasticity model for fiber composites. 35:369–410, 2001.

[53] H.D. Espinosa and P.D. Zavattieri. Modeling of ceramic microstructures: dynamic damage initiation and evolution. *Shock Compression of Condensed Matter – 1999*, pages 333–338, 1999.

[54] M.L. Falk, A. Needleman, and J.R. Rice. A critical evaluation of cohesive zone models of dynamic fracture. *J. Phys. IV*, 11:43–52, 2001.

[55] H. Friebe and D. Winter. Raster- und Moireverfahren, Grauwertkorrelation - Stand der Technik und Entwicklungspotential. *GESA-Symposium, Schliersee, GMA-Bericht*, 29:169–180, 1996.

[56] K. Friedrich, Z. Lu, and A.M. Häger. Overview on polymer composites for friction and wear application. *Theor. Appl. Fract. Mech.*, 19:1–11, 1993.

[57] M. Gei, F. Genna, and D. Bigoni. An interface model for the periodontal ligament. *J. Biomech. Eng.*, 124:538–546, 2002.

[58] A. Gens, I. Carol, and E.E. Alonso. An interface element formulation for the analysis of soil-reinforcement interaction. *Computers and Geotechnics*, 7:133–151, 1988.

[59] A.M. Häger and K. Friedrich. Aufbau und Eigenschaften von Polymer- Verbundwerkstoffen für reibungs- und verschleissbelastete Bauteile. *10th Int. Colloquium: Tribology - Solving Friction and Wear Problems, Bartz, W. J. (Ed.), Techn. Akademie Esslingen, Ostfildern*.

[60] A. Hansbo and P. Hansbo. A finite element method for the simulation of strong and weak discontinuities in solid mechanics. *Comput. Methods Appl. Mech. Engrg.*, 193:3523–3540, 2004.

[61] P. Hansbo and M.G. Larson. Discontinous Galerkin methods for incompressible and nearly incompressible elasticity by Nitsche's method. *Comput. Methods Appl. Mech. Engrg.*, 191:1895–1908, 2002.

[62] J.H. Hanson, T.N. Bittencourt, and A.R. Ingraffea. Three-dimensional influence coefficient method for cohesive crack simulations. *Engng. Fract. Mech.*, 71:2109–2124, 2004.

[63] E.W. Hart. Constitutive relations for the nonelastic deformation of metals. *ASME J. Eng. Mat. Tech.*, 98:193–202, 1976.

[64] P. Haupt. *Continuum Mechanics and Theory of Materials*. Springer, 2000.

[65] R. Hill. *The Mathematical Theory of Plasticity*. Oxford University Press, 1950.

[66] R. Hill. A general theory of uniqueness and stability of elastic plastic solids. *J. Mech. Phys. Solids*, 6:236–249, 1958.

[67] R. Hill. Acceleration waves in solids. *J. Mech. Phys. Solids*, 10:1–16, 1962.

[68] C.T. Hua and D.F. Socie. Fatigue damage in 1045 steel under constant amplitude biaxial loading. *Fatigue Eng. Mat. Struct.*, 7:165–179, 1984.

[69] T.J.R. Hughes. *The Finite Element Method – Linear Static and Dynamic Finite Element Analysis*. Dover, 2000.

[70] A. Ibrahimbegovic, L. Chorfi, and F. Gharzeddine. Thermomechanical coupling at finite elastic strain: covariant formulation and numerical implementation. *Commun. Numer. Methods Engng.*, 17:275–289, 2001.

[71] T. Ikeda. *Fundamentals of Piezoelectricity*. Oxford University Press, 1996.

[72] N.E. Jansson and R. Larsson. A damage model for simulation of mixed-mode delamination growth. *Compos. Struct.*, 53:409–417, 2001.

[73] Z.H. Jin, G.H. Paulino, and R.H. Dodds. Finite element investigation of quasi-static crack-growth in functionally graded materials using a novel cohesive zone fracture model. *ASME J. Appl. Mech.*, 69:370–379, 2002.

[74] M. Kaliske. A formulation of elasticity and viscoelasticity for fibre reinforced material at small and finite strains. *Comput. Methods Appl. Mech. Engrg.*, 185:225–243, 2000.

[75] M. Kaliske and H. Rothert. Formulation and implementation of three-dimensional viscoelasticity at small and finite strains. *Comput. Mech.*, 19:228–239, 1997.

[76] M. Kamlah. Ferroelectric and ferroelastic piezoceramics - modeling of electromechanical hysteresis phenomena. *Continuum Mech. Thermodyn.*, 13:219–268, 2001.

[77] M. Kamlah and U. Böhle. Finite element analysis of piezoceramic components taking into account ferroelectric hysteresis behaviour. *Int. J. Solids Struct.*, 38:605–633, 2001.

[78] S. Klinkel. A phenomenological constitutive model for ferroelastic and ferroelectric hysteresis effects in ferroelectric ceramics. *Int. J. Solids Struct.*, 43:7197–7222, 2006.

[79] S. Klinkel. A thermodynamic consistent 1d model for ferroelastic and ferroelectric hysteresis effects in piezoceramics. *Commun. Numer. Methods Engng.*, 22:727–739, 2006.

[80] M. Klisinski, K. Runesson, and S. Sture. Finite element with inner softening band. *J. Engrg. Mech.*, 117:575–587, 1991.

[81] U. Knauer. *Submikronanalyse von $BaTiO_3$-Keramik im Elektronenmikroskop zum Studium von Gefügeausbildung und elektrischen Eigenschaften*. PhD thesis, Universität Erlangen-Nürnberg, 1982.

[82] R. Kornmann and B. Kröplin. Objektrasterverfahren zur räumlichen Verformungsmessung an Hochtemperaturbauteilen. *Technisches Messen*, 67:267–273, 2000.

[83] E. Krempl. An experimental study of room-temperature rate-sensitivity, creep and relaxation of AISI type 304 stainless steel. *J. Mech. Phys. Solids*, 27:363–375, 1979.

[84] E. Krempl and C.M. Bordonaro. Non-proportional loading of nylon 66 at room temperature. *Int. J. Plasticity*, 14:245–258, 1998.

[85] O. Krol. *Thermo-Mechanical Modelling of Solids and Interfaces – Theory, Numerics and Applications*. PhD thesis, TU Kaiserslautern, 2007.

[86] M. Kroon and J. Faleskog. Micromechanics of cleavage fracture initiation in ferritic steels by carbide cracking. *J. Mech. Phys. Solids*, 53:171–196, 2005.

[87] G. Krüger and U. Meyer. Kunststoff-Metall-Verbindungen ohne Klebstoffeinsatz. *Adhäsion - Kleben und Dichten*, 42:31–34, 1998.

[88] R. Larsson and N. Jansson. Geometrically non-linear damage interface based on regularized strong discontinuity. *Int. J. Numer. Methods Engng.*, 54:473–497, 2002.

[89] J. Lemaitre. Coupled elasto-plasticity and damage. Constitutive equations. *Comput. Methods Appl. Mech. Engrg.*, 51:31–49, 1985.

[90] J. Lemaitre. *A Course on Damage Mechanics*. Springer, 1994.

[91] J. Lemaitre and J.-L. Chaboche. *Mechanics of Solid Materials*. Cambridge University Press, 1994.

[92] J. Lemaitre and A. Plumtree. Application of damage concepts to predict creep-fatigue failures. *ASME J. Eng. Mat. Tech.*, 101:284–292, 1979.

[93] S. Li, M.D. Thouless, A.M. Waas, J.A. Schroeder, and P.D. Zavattieri. Use of a cohesive-zone model to analyze the fracture of a fiber-reinforced polymer-matrix composite. *Compos. Sci. Technol.*, 65:537–549, 2005.

[94] S. Li, M.D. Thouless, A.M. Waas, J.A. Schroeder, and P.D. Zavattieri. Use of mode-I cohesive zone models to describe the fracture of an adhesively-bonded polymer-matrix composite. *Compos. Sci. Technol.*, 65:281–293, 2005.

[95] T. Liebe, A. Menzel, and P. Steinmann. Theory and numerics of a thermodynamically consistent framework for geometrically non-linear gradient plasticity. *Int. J. Engng. Sci.*, 41:1603–1629, 2003.

[96] H.R. Lofti and P.B. Shing. Embedded representation of fracture in concrete with mixed finite elements. *Int. J. Numer. Methods Engng.*, 38:1307–1325, 1995.

[97] R. Lohkämper, H. Neumann, and G. Arlt. Internal bias in acceptor-doped $BaTiO_3$ ceramics: Numerical evaluation of increase and decrease. *J. Appl. Phys.*, 68:4220–4224, 1990.

[98] J. Lubliner. A maximum-dissipation principle in generalized plasticity. *Acta Mech.*, 52:225–237, 1984.

[99] D.C. Lupascu. *Fatigue in Ferroelectric Ceramics and Related Issues*. Springer, 2004.

[100] C.S. Lynch. On the development of multiaxial phenomenological constitutive laws for ferroelectric ceramics. *J. Intelligent Mat. Systems Struct.*, 9:555–563, 1998.

[101] C.S. Lynch and R.M. McMeeking. Finite strain ferroelectric constitutive laws. *Ferroelectrics*, 160:177–184, 1994.

[102] R. Mahnken and E. Stein. A unified approach for parameter identification of inelastic material models in the frame of the finite element method. *Comput. Methods Appl. Mech. Engrg.*, 136:225–258, 1996.

[103] R. Mahnken and E. Stein. Parameter identification for finite deformation elasto-plasticity in principal directions. *Comput. Methods Appl. Mech. Engrg.*, 147:17–39, 1997.

[104] S.S. Manson and M.H. Hirschberg. *Fatigue: An Interdisciplinary Approach*. Syracuse University Press, 1964.

[105] J.E. Marsden and T.J.R. Hughes. *Mathematical Foundations of Elasticity*. Dover, 1994.

[106] G.A. Maugin. *Continuum Mechanics of Electromagnetic Solids*. North-Holland, 1988.

[107] G. Mehlhorn. *Der Ingenieurbau, Band 4: Werkstoffe, Elastizitätstheorie*. Ernst & Sohn, 1997.

[108] V. Mehling, Ch. Tsakmakis, and D. Gross. Phenomenological model for the macroscopical material behavior of ferroelectric ceramics. *J. Mech. Phys. Solids*, 55:2106–2141, 2007.

[109] J.M. Melenk and I. Babuška. The partition of unity finite element method: basic theory and applications. *Comput. Methods Appl. Mech. Engrg.*, 139:289–314, 1996.

[110] A. Menzel, A. Arockiarajan, and S.M. Sivakumar. Two models to simulate rate-dependent domain switching effects – application to ferroelastic polycrystalline ceramics. *Smart Mater. Structures*, 2008.

[111] A. Menzel, M. Ekh, K. Runesson, and P. Steinmann. A framework for multiplicative elastoplasticity with kinematic hardening coupled to anisotropic damage. *Int. J. Plasticity*, 21:397–434, 2005.

[112] A. Menzel and P. Steinmann. On the continuum formulation of higher gradient plasticity for single and polycrystals. *J. Mech. Phys. Solids*, 48(8):1777–1796, 2000. Erratum 49(5):1179-1180, 2001.

[113] J. Mergheim. *Computational Modelling of Strong and Weak Discontinuities*. PhD thesis, TU Kaiserslautern, 2006.

[114] J. Mergheim, E. Kuhl, and P. Steinmann. Towards the algorithmic treatment of 3d strong discontinuities. *Commun. Numer. Methods Engng.*, 23:97–108, 2007.

[115] J. Mergheim and P. Steinmann. A geometrically nonlinear FE approach for the simulation of strong and weak discontinuities. *Comput. Methods Appl. Mech. Engrg.*, 195:5037–5052, 2006.

[116] K. Meyberg and P. Vachenauer. *Höhere Mathematik 2: Differentialgleichungen, Funktionentheorie, Fourier-Analysis, Variationsrechnung*. Springer, 2001.

[117] C. Miehe. Entropic thermoelasticity at finite strains. Aspects of the formulation and numerical implementation. *Comput. Methods Appl. Mech. Engrg.*, 120:243–269, 1995.

[118] C. Miehe and J. Schröder. Post-critical discontinuous localization analysis of small-strain softening elastoplastic solids. *Arch. Appl. Mech.*, 64:267 – 285, 1994.

[119] A.K. Miller. *Unified Constitutive Equations for Plastic Deformation and Creep of Engineering Alloys*. Elsevier, 1987.

[120] V.J. Mizel and C.-C. Wang. A fading memory hypothesis which suffices for chain rules. *Arch. Rational Mech. Anal.*, 23:124–134, 1966.

[121] N. Moës, J. Dolbow, and T. Belytschko. A finite element method for crack growth without remeshing. *Int. J. Numer. Methods Engng.*, 46:131–150, 1999.

[122] H. Mühlhaus and E.C. Aifantis. A variational principle for gradient plasticity. *Int. J. Solids Struct.*, 28:845 – 857, 1991.

[123] J.J. Munoz, U. Galvanetto, and P. Robinson. On the numerical simulation of fatigue driven delamination with interface elements. *Internat. J. Fatigue.*, 28:1136–1146, 2006.

[124] S.A.R. Naga. Effect of glass fibre content on the frictional behaviour of glass fibre reinforced polyamide 66. *Tribologie 2000, 8. Int. Kolloquium, Technische Akademie Esslingen*, pages 25.7.1–25.7.6, 1992.

[125] A. Needleman. A continuum model for void nucleation by inclusion debonding. *ASME J. Appl. Mech.*, 54:525 – 531, 1987.

[126] A. Needleman and M. Ortiz. Effect of boundaries and interfaces on shear-band localization. *Int. J. Solids Struct.*, 28:859 – 877, 1991.

[127] O. Nguyen, E.A. Repetto, M. Ortiz, and R.A. Radovitzky. A cohesive model of fatigue crack growth. *Internat. J. Frac.*, 110:351–369, 2001.

[128] J. Nitsche. Über ein Variationsprinzip zur Lösung von Dirichlet-Problemen bei Verwendung von Teilräumen, die keinen Randbedingungen unterworfen sind. *Commun. Numer. Methods Engng.*, 36:9–15, 1970.

[129] J. Nuffer, D.C. Lupascu, and J. Rödel. Damage evolution in ferroelectric PZT induced by bipolar electric cycling. *Acta Mater.*, 48:3783–3794, 2000.

[130] R.W. Ogden. *Non-Linear Elastic Deformations*. Dover Publications, 1984.

[131] M. Ortiz, Y. Leroy, and A. Needleman. A finite element method for localized failure analysis. *Comput. Methods Appl. Mech. Engrg.*, 61:189–214, 1987.

[132] M. Ortiz and A. Pandolfi. Finite-deformation irreversible cohesive elements for three-dimensional crack-propagation analysis. *Int. J. Numer. Methods Engng.*, 44:1267–1282, 1999.

[133] M. Ortiz and L. Stainier. The variational formulation of viscoplastic constitutive updates. *Comput. Methods Appl. Mech. Engrg.*, 171:419–444, 1999.

[134] F. Oster, F. Haupert, and K. Friedrich. Experimentelle Bestimmung der tribologischen Eigenschaften von faserverstärkten Kunststoffbeschichtungen auf metallischen Substraten mittels Ring-Platte-Prüfanordnung. *Tribologie-Fachtagung Göttingen*, pages 31/1–31/10, 2000.

[135] M. Paas, P. Schreurs, and W.A.M. Brekelmans. A continuum approach to brittle and fatigue damage: Theory and numerical procedures. *Int. J. Solids Struct.*, 30:579–599, 1993.

[136] A. Pandolfi, P. Krysl, and M. Ortiz. Finite element simulation of ring expansion and fragmentation: The capturing of length and time scales through cohesive models of fracture. *Internat. J. Frac.*, 95:279–297, 1999.

[137] A. Pandolfi and M. Ortiz. Solid modeling aspects of three-dimensional fragmentation. *Engng. Comput.*, 14:287–308, 1998.

[138] A. Pandolfi and M. Ortiz. An efficient adaptive procedure for three-dimensional fragmentation simulations. *Engng. Comput.*, 18:148–159, 2002.

[139] R.H.J. Peerlings. *Enhanced Damage Modelling for Fracture and Fatigue*. PhD thesis, TU Delft, 1999.

[140] R.H.J. Peerlings, W.A.M. Brekelmans, R. de Borst, and M.G.D. Geers. Gradient-enhanced damage modelling of high-cycle fatigue. *Int. J. Numer. Methods Engng.*, 49:1547–1569, 2000.

[141] R.H.J. Peerlings, R. de Borst, W.A.M. Brekelmans, and J.H.P. de Vree. Gradient enhanced damage for quasi-brittle materials. *Int. J. Numer. Methods Engng.*, 39:3391–3403, 1996.

[142] P. Perzyna. The constitutive equations for rate sensitive plastic materials. *Quart. Appl. Math.*, 20:321–332, 1963.

[143] P. Perzyna and W. Wojno. Thermodynamics of a rate sensitive plastic material. *Archives of Mechanics*, 20:499–511, 1968.

[144] H. Potente. *Fügen von Kunststoffen*. Carl Hanser Verlag, 2004.

[145] E. Radi, D. Bigoni, and A. Tralli. On uniqueness for frictional contact rate problems. *J. Mech. Phys. Solids*, 47:275–296, 1999.

[146] J.N. Reddy. *An Introduction to the Finite Element Method*. McGraw-Hill, 1993.

[147] S. Reese and S. Govindjee. Multiplicative thermo-viscoplasticity: a thermodynamic model and its finite element implementation. *Technische Mechanik*, 18:209–216, 1998.

[148] S. Reese and S. Govindjee. A theory of finite viscoelasticity and numerical aspects. *Int. J. Solids Struct.*, 35:3455–3482, 1998.

[149] P. Robinson, U. Galvanetto, D. Tumino, G. Bellucci, and D. Violeau. Numerical simulation of fatigue-driven delamination using interface elements. *Int. J. Numer. Methods Engng.*, 63:1824–1848, 2005.

[150] M. Rühle. Struktur und chemische Zusammensetzung von inneren Grenzflächen in verschiedenen Materialien. *Tätigkeitsbericht, Max-Planck-Institut für Metallforschung, Stuttgart*, pages 429–437, 2004.

[151] H. Schaumburg. *Werkstoffe und Bauelemente der Elektrotechnik Band 2: Keramik*. Teubner, 1994.

[152] J.C.J. Schellekens. *Computational Strategies for Composite Structures*. PhD thesis, TU Delft, 1992.

[153] J.C.J. Schellekens and R. De Borst. On the numerical integration of interface elements. *Int. J. Numer. Methods Engng.*, 36:43–66, 1993.

[154] P.J. Schorn, D. Bräuhaus, U. Böttger, R. Waser, G. Beitel, N. Nagel, and R. Bruchhaus. Fatigue effect in ferroelectric $PbZr_{1-x}Ti_xO_3$ thin films. *J. Appl. Phys.*, 99, 2006.

[155] J. Schröder and D. Gross. Invariant formulation of the electromechanical enthalpy function of transversely piezoelectric materials. *Arch. Appl. Mech.*, 73:533–552, 2004.

[156] J. Schröder, F. Gruttmann, and J. Löblein. A simple orthotropic finite elasto-plasticity model based on generalized stress-strain measures. *Comput. Mech.*, 30:48–64, 2002.

[157] J. Schröder, P. Neff, and D. Balzani. A variational approach for materially stable anisotropic hyperelasticity. *Int. J. Solids Struct.*, 42:4352–4371, 2005.

[158] J. Schröder and H. Romanowski. A thermodynamically consistent mesoscopic model for transversely isotropic ferroelectric ceramics in a coordinate-invariant setting. *Arch. Appl. Mech.*, 74:863–877, 2005.

[159] J. Segurado and J. LLorca. A new three-dimensional interface finite element to simulate fracture in composites. *Int. J. Solids Struct.*, 41:2977–2993, 2004.

[160] S. Serebrinsky and M. Ortiz. A hysteretic cohesive-law of fatigue-crack nucleation. *Scripta Materialia*, 53:1193–1196, 2005.

[161] G.K. Sfantos and M.H. Aliabadi. A boundary cohesive grain element formulation for modelling intergranular microfracture in polycrystalline brittle materials. *Int. J. Numer. Methods Engng.*, 69:1590–1626, 2007.

[162] J.C. Simo and F. Armero. Geometrically non-linear enhanced strain mixed methods and the method of incompatible modes. *Int. J. Numer. Methods Engng.*, 33:1414–1449, 1992.

[163] J.C. Simo, F. Armero, and R.L. Taylor. Improved versions of assumed enhanced strain tri-linear elements for 3d finite deformation problems. *Comput. Methods Appl. Mech. Engrg.*, 12:277–296, 1993.

[164] J.C. Simo and T.J.R. Huges. *Computational Inelasticity*, volume 7 of *Interdisciplinary Applied Mathematics*. Springer, 1998.

[165] R.C. Smith. *Smart Material Systems*, volume 7 of *Frontiers in Applied Mathematics*. SIAM, 2005.

[166] A.J.M. Spencer. *Continuum Mechanics*. Longman, 1980.

[167] A.J.M. Spencer. *Continuum Theory of the Mechanics of Fibre-Reinforced Composites*, volume 282 of *CISM Courses and Lectures*. Springer, 1984.

[168] P. Steinmann. Formulation and computation of geometrically non-linear gradient damage. *Int. J. Numer. Methods Engng.*, 46:757 – 779, 1999.

[169] P. Steinmann and P. Betsch. A localisation capturing FE-interface based on regularized strong discontinuities at large inelastic strains. *Int. J. Solids Struct.*, 37:4061 – 4082, 2000.

[170] P. Steinmann and O. Häsner. On material interfaces in thermomechanical solids. *Arch. Appl. Mech.*, 75:31 – 41, 2005.

[171] P. Steinmann, C. Miehe, and E. Stein. Comparison of different finite deformation inelastic damage models within multiplicative elastoplasticity for ductile materials. *Comput. Mech.*, 13:458–474, 1994.

[172] N. Sukumar, N. Moës, B. Moran, and T. Belytschko. Extended finite element method for three-dimensional crack modelling. *Int. J. Numer. Methods Engng.*, 48:1549–1570, 2000.

[173] Z. Suo, M. Ortiz, and A. Needleman. Stability of solids with interfaces. *J. Mech. Phys. Solids*, 40:613–640, 1992.

[174] T. Svedberg and K. Runesson. A thermodynamically consistent theory of gradient-regularized plasticity coupled to damage. *Int. J. Plasticity*, 13:669–696, 2003.

[175] M.G.A. Tijssens, L.J. Sluys, and E. van der Giessen. Simulation of fracture of cementitious composites with explicit modelling of microstructural features. *Engng. Fract. Mech.*, 68:1245–1263, 2001.

[176] M.G.A. Tijssens, E. van der Giessen, and L.J. Sluys. Modelling of crazing using a cohesive surface methodology. *Mechanics of Materials*, 32:19–35, 2000.

[177] T.C.T. Ting. *Anisotropic Elasticity*. Oxford University Press, 1996.

[178] C. Truesdell. Hypo-elasticity. *J. Rational Mech. Anal.*, 4:83–133, 1955.

[179] C. Truesdell and W. Noll. *The Non-Linear Field Theories of Mechanics*. Springer, 2nd edition, 1992.

[180] J. Utzinger, M. Bos, M. Floeck, A. Menzel, E. Kuhl, R. Renz, K. Friedrich, A. Schlarb, and P. Steinmann. Computational modelling of thermal impact welded peek/steel single lap tensile specimens. *Comput. Mater. Sci.*, 41:287–296, 2008.

[181] J. Utzinger, A. Menzel, P. Steinmann, and A. Benallal. Aspects of bifurcation in an isotropic elastic continuum with orthotropic inelastic interface. *Euro. J. Mech. A/Solids*, 27:532–547, 2008.

[182] J. Utzinger, P. Steinmann, and A. Menzel. Computational modelling of microcracking effects in polycrystalline piezoelectric ceramics. *Submitted for publication*, 2008.

[183] J. Utzinger, P. Steinmann, and A. Menzel. On the simulation of cohesive fatigue effects in grain boundaries of a piezoelectric mesostructure. *Int. J. Solids Struct.*, 45:4687–4708, 2008.

[184] W. Voigt. *Lehrbuch der Kristallphysik*. Teubner, 1966.

[185] M. Šilhavỳ. *The Mechanics and Thermodynamics of Continous Media*. Texts and Monographs in Physics. Springer, 1997.

[186] G.N. Wells and L.J. Sluys. A new method for modelling cohesive cracks using finite elements. *Int. J. Numer. Methods Engng.*, 50:2667–2682, 2001.

[187] I. Westram, W.S. Oates, D.C. Lupascu, J. Rödel, and C.S. Lynch. Mechanism of electric fatigue crack growth in lead zirconate titanate. *Acta Mater.*, 55:301–312, 2007.

[188] K. Willam, I. Rhee, and B. Shing. Interface damage model for thermomechanical degradation of heterogeneous materials. *Comput. Methods Appl. Mech. Engrg.*, 193:3327 – 3350, 2004.

[189] D. Winter. *Optische Verschiebungsmessung nach dem Objektrasterprinzip mit Hilfe eines flächenorientierten Ansatzes*. PhD thesis, TU Braunschweig, 1993.

[190] J. Wodara. *Ultraschallfügen*. DVS-Verlag, 2004.

[191] P. Wriggers. *Nichtlineare Finite-Element-Methoden*. Springer, 2001.

[192] P. Wriggers. *Computational Contact Mechanics*. John Wiley and Sons, 2002.

[193] X.P. Xu and A. Needleman. Void nucleation by inclusions debonding in a crystal matrix. *Modelling Simul. Mat. Sci. Engng.*, 1:111–132, 1993.

[194] L. Yang and A. Ettemeyer. Strain measurement by three-dimensional electronic speckle pattern interferometry: potentials, limitations, and applications. *Optical Engineering*, 42:1257 – 1266, 2003.

[195] O.C. Zienkiewicz. *Methode der Finiten Elemente*. Carl Hanser Verlag, 1975.

Curriculum Vitae

Name:	Johannes Utzinger
Geburtsdatum:	6. September 1978
Geburtsort:	Zweibrücken
Nationalität:	deutsch
Familienstand:	ledig

1985-1989	Grundschule Hilgardschule, Zweibrücken
1989-1998	Helmholtz-Gymnasium Zweibrücken, Abschluss: Allgemeine Hochschulreife
1998-1999	Zivildienst
1999-2004	Studium des Maschinenbaus, Technische Universität Kaiserslautern, Vertiefungsrichtung: Grundlagen des Maschinenbaus, Abschluss: Diplom-Ingenieur
2004-	Wissenschaftlicher Mitarbeiter, Bearbeitung von Teilprojekt 7 innerhalb der DFG-Forschergruppe 524 “Herstellung, Eigenschaftsanalyse und Simulation geschweißter Leichtbaustrukturen aus Metall/Faser-Kunststoff-Verbunden”, Lehrstuhl für Technische Mechanik, Technische Universität Kaiserslautern

UKL/LTM-Schriftenreihe

bereits veröffentlicht wurden:

1 Menzel, A.: Modelling and Computation of Geometrically Nonlinear Anisotropic Inelasticity.
2002, ISBN 3-925178-86-4

2 Betsch, P.: Computational Methods for Flexible Multibody Dynamics.
2002, ISBN 3-925178-92-9

3 Liebe, T.: Theory and numerics of higher gradient inelastic material behavior.
2003, ISBN 3-936890-09-9

4 Groß, M.: Conserving Time Integrators for Nonlinear Elastodynamics.
2004, ISBN 3-936890-37-4

5 Kuhl, E.: Theory and Numerics of Open System Continuum Thermodynamics – Spatial and Material Settings –.
2004, ISBN 3-936890-42-0

6 Sunyk, R.: On Aspects of Mixed Continuum-Atomistic Material Modelling.
2004, ISBN 3-936890-51-X

7 Arockiarajan, A.: Computational Modeling of Domain Switching Effects in Piezoceramic Materials – A Micro-Macro Mechanical Approach.
2005, ISBN 3-936890-92-7

8 Mergheim, J.: Computational Modeling of Strong and Weak Discontinuties.
2006, ISBN 3-939432-02-4; 978-3-939432-02-4-9

9 Delibas, B.: Rate dependent nonlinear properties of perovskite tetragonal piezoelectric materials using a micromechanical model.
2006, ISBN 3-939432-05-9; 978-3-939432-05-0

10 Leyendecker, S.: Mechanical integrators for constrained dynamical systems in flexible multibody dynamics.
2006, ISBN 3-939432-09-1; 978-3-939432-09-8

11 Denzer, R.: Computational Configurational Mechanics.
2006, ISBN 3-939432-12-1; 978-3-939432-12-8

12 Krol, O.: Thermo-Mechanical Modelling of Solids and Interfaces – Theory, Numerics and Applications. 2007, ISBN 978-3-939432-45-6

13 Kleuter, B.: Generalized Parameter Identification for Finite Viscoelasticity. 2007, ISBN 978-3-939432-53-1

14 Menzel, A.: Frontiers in Inelastic Continuum Mechanics. 2007, ISBN 978-3-939432-55-5

15 Himpel, G.: Computational Modeling of Biomechanical Phenomena – Remodeling, Growth and Reorientierung. 2008, ISBN 978-3-939432-62-3

16 Bargmann, S.: Theory and numerics of non-classical thermo-hyperelasticity. 2008, ISBN 978-3-939432-77-7

17 Hirschberger, C. B.: A Treatise on Micromorphic Continua. Theory, Homogenization, Computation. 2008, ISBN 978-3-939432-80-7

18 Mohr, R.: Consistent Time-Integration of Finite Elasto-Plasto-Dynamics. 2008, ISBN 978-3-939432-81-4

19 Utzinger, J.: Analysis and Computation of Solid Interfaces on the Meso Scale. 2008, ISBN 978-3-939432-85-2